



**The Use of Microscopy and Spectroscopy  
to Probe the Dynamic Behaviours of  
Metal-Organic Frameworks and their  
Guests.**

Alexander James Tansell

A thesis submitted for the Degree of Doctor of Philosophy

September 2019



## Acknowledgements

---

First and foremost, I have to give my utmost, sincerest thanks to Dr Timothy Easun, for his guidance, patience and assurance during the past four years, and for taking a chance on me – a boundary 2:1 chemist with questionable knowledge, limitless enthusiasm (back then, at least) and good references. I also owe him gratitude for encouraging me to develop my skills outside of the laboratory, and helping me become the gregarious science communicator I am today.

Next up, my work wife and smiling Welsh sunbeam, Corey. I couldn't have gotten the past four years without her. The extended lunchbreaks, shared snack draw and BBQs were exactly what was needed to deal with the day-to-day pitfalls of research. I'm glad to be leaving my PhD with (of course) a thorough knowledge of MOFs, but also, and more importantly, a friendship to last a lifetime.

I'd like to thank the rest of the Easun group (and by extension, the inhabitants of labs 2.84 and 2.91 and the wider inorganic chemistry sector at Cardiff) for shared merriments in times of success, and comfort in times of struggle. The Cardiff Analytical Services team (Tom, Robin, Simon and Rob) have been a priceless amenity during times of synthetic ineptitude. I'd like to show gratitude for their (occasional) impressive sub-5-minute turnaround time, and for training me on equipment so I'd stop badgering them. I'd also like to thank the Cardiff Catalysis Institute experimental officers, Greg Shaw and Nia Richards, for letting me loose on their already oversubscribed equipment and being on-call for my numerous queries and silly mishaps.

Finally, I need to thank those who have kept me grounded and helped me unwind – my friends in Cardiff and Birmingham, and my family (particularly my mom) who have listened to hours of tirades on the strains of science, and have held me up when I thought I'd had enough. I'd be even more of a quivering, exhausted wreck if I'd had to survive the last four years without you all.

## Abstract

---

This thesis describes the stimuli-responsive nature of metal-organic frameworks to light, solvent introduction and solvent loss.

Chapter 1 introduces metal-organic frameworks, highlighting the different components of the materials, and reviewing historic work into the development of stimuli-responsive MOFs. Approaches to post-synthetic modification (experimentally undertaken in Chapter 2) are introduced. Specialist experimental techniques and various approaches to the analysis of infrared spectra (used in Chapters 3 and 4) are also defined.

Chapter 2 describes how optical spectroscopy and microscopy has been employed to track fluorescent guest molecules through framework pores. As part of this work, size-optimised single crystals of NOTT-100 and  $\text{Sc}_2\text{BDC}_3$  were synthesised. In the process of investigating crystal size, damage to crystals upon exposure to the SEM sample chamber vacuum was observed. The effect of common laboratory solvents on crystal quality was qualitatively investigated, and solvent acceptor number and molar volume were found to correlate to crystal damage. Reaction conditions for the post-synthetic modification of frameworks with a monocarboxylate-functionalised dye were established through the use of UV-visible (UV-VIS) absorption spectroscopy and confocal laser scanning microscopy (CLSM). Frameworks were post-synthetically modified with both a spirooxazine-based and a hydrazone-based photoswitch. Solid-state photoswitching of the spirooxazine-based photoswitch was observed during *in situ* CLSM experiments and on 290 nm irradiation by UV-VIS-diffuse reflectance spectroscopy. The adsorption capabilities of modified materials were measured using  $\text{N}_2$  sorption isotherms, and modification of materials with dyes was found to hinder the adsorption of guests into frameworks in all cases.

Chapter 3 investigates the diffusion of therapeutic agents from MOF single crystals and bulk powders using *in situ* infrared microscopy and *in situ* diffuse reflectance infrared Fourier transform spectroscopy (DRIFTS). A sophisticated experimental technique was devised to establish the kinetics of guest loss from MOFs into a volatile solvent environment. The loss of caffeine from MIL-68(Ind) into acetonitrile (MeCN) was tracked at six temperatures, and an  $E_a$  of +144 kJ mol<sup>-1</sup> (calculated error <1 kJ mol<sup>-1</sup>) determined for the diffusion process. The loss of carbon monoxide (CO) from fully-desolvated NOTT-100 was tracked at low temperatures. Analysis of spectra confirmed the loss of CO from different Cu-paddlewheel sites to be interconnected processes, and not occurring in isolation from one another.

Chapter 4 employs IR microspectroscopy to probe the structural rearrangement of a solvent-switchable, breathing framework, SHF-61. Crystallographic experiments have reported that desolvation from CHCl<sub>3</sub> and DMF led to open- and closed-pore structures respectively. In this thesis, examination of the  $\nu(\text{NH})$  stretch using IR microspectroscopy was able to track the time-resolved pore-opening process during resolvation with DMF, identifying four states of the pore structure and monitoring their relative abundancies during the resolvation experiment. The open-pore structure was resolvated with and subsequently desolvated from: CHCl<sub>3</sub>, cyclopentanone and DMF. The rate of resolvation and subsequent desolvation was elucidated, using only  $\nu(\text{NH})$  stretches and respective solvent bands. The response of the material to CO<sub>2</sub> loading was investigated, and a gas uptake isotherm shape was recreated for one single crystal of material.

## List of abbreviations

---

IR	Infrared
7-DCCA	7-(Diethylamino)coumarin-3-carboxylic acid
ABDC	2-Aminoterephthalic acid
ad	Adeninate
Al(NO <sub>3</sub> ) <sub>3</sub>	Aluminium(III) nitrate
AN	Gutmann acceptor number
atm	Atmosphere
AzDC	Azobenzene-4,4'-dicarboxylic acid
BDC	Benzenedicarboxylic acid / Terephthalic acid
BET	Brunauer–Emmett–Teller
BODIPY	Boron-dipyrromethene
BPDC	4,4'-Biphenyldicarboxylic acid
4,4'-BPE	<i>trans</i> -1,2- <i>bis</i> (4-pyridyl)ethylene
BPTC	4,4'-Biphenyl-3,3',5,5'-tetracarboxylic acid
bpy	Bipyridine
Br <sub>2</sub>	Bromine
CA	Capping agent
ca.	Circa
CaF <sub>2</sub>	Calcium fluoride
CAU	Christian-Albrechts-University
CDCl <sub>3</sub>	Deuterated chloroform
CH <sub>4</sub>	Methane
CHCl <sub>3</sub>	Chloroform
CLSM	Confocal laser scanning microscopy
CO	Carbon monoxide
CO <sub>2</sub>	Carbon dioxide
conc.	Concentrated
CORM	Carbon monoxide release molecule
cm <sup>-1</sup>	Wavenumber
Cu(NO <sub>3</sub> ) <sub>2</sub> .3H <sub>2</sub> O	Copper(II) nitrate trihydrate
CyP	Cyclopentadiene
dabco	1,4-Diazabicyclo[2.2.2]octane
DCM	Dichloromethane
DDS	Drug delivery system

DEF	<i>N,N'</i> -Diethylformamide
dhbc	2,5-Dihydroxybenzoic acid
DLS	Diamond Light Source
DMF	<i>N,N'</i> -Dimethylformamide
DMSO	Dimethyl sulfoxide
DRIFTS	Diffuse reflectance infrared Fourier transform spectroscopy
DSCP	Disuccinatocisplatin
DUT	Dansk Universitetspædagogisk Tidsskrift
$E_a$	Activation energy
$\text{Et}_2\text{O}$	Diethyl ether
$\text{EtOH}$	Ethanol
FC	Ferrocene
FEG-SEM	Field emission gun scanning electron microscope
FTIR	Fourier transform infrared
$\text{H}_2\text{diol}$	2,2'-Dihydroxybiphenyl-4,4'-dicarboxylic acid
$\text{H}_2\text{O}$	Water
$\text{H}_2\text{SO}_4$	Sulfuric acid
HCl	Hydrochloric acid
HKUST	Hong Kong University of Science and Technology
$\text{HNO}_3$	Nitric acid
HPLC	High performance liquid chromatography
hr	Hours
$\text{In}(\text{NO}_3)_3$	Indium nitrate
$\text{iPrOH}$	Isopropyl alcohol
IRMOF	Isoreticular metal-organic framework
$\text{K}_2\text{CO}_3$	Potassium carbonate
KBr	Potassium bromide
$\text{kJ mol}^{-1}$	Kilojoules per mole
$\text{KMnO}_4$	Potassium permanganate
KOH	Potassium hydroxide
LC-MS	Liquid chromatography-mass spectrometry
LED	Light emitting diode
$\text{L-PrOH}$	<i>L</i> -Proline
M	$\text{mol dm}^{-3}$
MCN	Merocyanine
1-MCP	1-Methylcyclopropene

MCT	Mercury cadmium telluride
$\text{Me}_2\text{NH}_2^+$	Dimethylammonium
MeCN	Acetonitrile
MeOD	Deuterated methanol
MeOH	Methanol
$\text{MgSO}_4$	Magnesium sulfate
MIL	Materials of Institut Lavoisier
MIRIAM	Multimode Infrared Imaging And Microspectroscopy
$\text{mM}$	$\text{mmol dm}^{-3}$
MOF	Metal-organic framework
$M_r$	Molecular mass
MV	Molar volume
$\text{NaHCO}_3$	Sodium hydrogen carbonate
nanoMOF	Nanoscale metal-organic framework
NaOH	Sodium hydroxide
ndc	1,4-Naphthalene dicarboxylic acid
$\text{NEt}_3$	Triethylamine
$\text{NH}_2\text{OH.HCl}$	Ammonium hydroxide hydrochloride
NLDFT	Non-linear density functional theory
NMR	Nuclear magnetic resonance
NOTT	University of Nottingham
$\text{P}(\text{'Bu})_3$	Tri- <i>tert</i> -butylphosphine
PBS	Phosphate-buffered saline
$\text{Pd}_2(\text{dba})_3$	Tris(dibenzylideneacetone)dipalladium(0)
PGE2	Prostaglandin E <sub>2</sub>
PNIPAM	Poly( <i>N</i> -isopropylacrylamide)
ppm	Parts per million
proc	Procainamide
PSM	Post-synthetic modification
PXRD	Powder X-ray diffraction
RP	Polarity relative to water
S:N	Signal:noise
SALE	Solvent-assisted linker exchange
SBF	Simulated body fluid
SBU	Secondary building unit
$\text{Sc}(\text{NO}_3)_3$	Scandium(III) nitrate

SCCM	Square cubic centimetres
SCXRD	Single crystal X-ray diffraction
SEM	Scanning electron microscopy
SHF	University of Sheffield
SP <sub>c</sub>	Closed spiropyran
SP <sub>o</sub>	Open spiropyran
SPO	Spirooxazine
SPS	Solvent purification system
ST	Surface tension
SURMOF	Surface-anchored metal-organic framework
'BuOH	<i>tert</i> -Butyl alcohol
TEOS	Tetraethyl orthosilicate
TFA	Trifluoroacetic acid
TGA	Thermogravimetric analysis
THF	Tetrahydrofuran
TLC	Thin layer chromatography
UiO	Universitetet i Oslo
UV	Ultraviolet
UV-VIS	Ultraviolet-Visible
UV-Vis-DRS	UV-Visible-Diffuse reflectance spectra
VT	Variable temperature
wt%	Weight percent
XPS	X-ray photoelectron spectroscopy
ZIF	Zeolitic imidazolate frameworks
Zn(NO <sub>3</sub> ) <sub>2</sub> .xH <sub>2</sub> O	Zinc(II) nitrate hydrate
ZnSe	Zinc selenide
ZrCl <sub>4</sub>	Zirconium(IV) chloride

## List of figures

---

Figure 1.1	Example SBUs demonstrating possible geometries. Black, carbon; red, oxygen; one metal ion at the centre of each polyhedron.	1
Figure 1.2	Single-crystal structures of MOFs constructed from (top) 4,4'-bipyridine and (bottom) 4,4'-dicarboxylic acid linkers.	2
Figure 1.3	Mechanism for modulator action. ‘Lower pH’ and ‘Higher pH’ pathways involve addition of deprotonation modulators (HCl, NEt <sub>3</sub> , etc.) to the reaction mixture. Capping agents are binding modulators (benzoic, salicylic, formic, acetic acids, etc.).	3
Figure 1.4	Crystal structures of the framework ligand (5,5',5''-(1,3,5-triazine-2,4,6-triyltriamino)tris-isophthalate hexasodium) at 20 °C (top) and -80 °C (bottom). Structure at 20 °C shows an unbound carboxylate group, which binds to Eu <sup>3+</sup> cations at -80 °C. Temperature-dependent binding environments are circled in red.	4
Figure 1.5	SC-SC transformation of the framework between room temperature (left) and low temperature (right), instigated by Eu <sup>3+</sup> cation binding. Eu <sup>3+</sup> cation is represented by green polyhedral.	5
Figure 1.6	Schematic image of controlled release using of analytes from MOF–PNIPAM composite.	5
Figure 1.7	Evolution of the photoluminescence signal of Tb-GWMOF at varying pressures	6
Figure 1.8	(Left) Illustration of solvent-induced solvatochromism of Nile Blue loaded into DUT 25. Solvatochromism of Nile Blue is affected by acidity, and the exposure of DUT-25–Nile Blue solvents varying in acidity/basicity induced solvatochromic response. (Right) Fluorescence emission spectra of DUT-25 in different solvents. Increasing solvent polarity saw a red shift in $\lambda_{\text{max}}$ .	6
Figure 1.9	(Left) Illustration of the dynamic solvent-responsive behaviour of [Ni(H <sub>2</sub> diol)]. (Right) N <sub>2</sub> adsorption isotherms at 77 K for [Ni(H <sub>2</sub> diol)(DMF) <sub>2</sub> ] (red), [Ni(H <sub>2</sub> diol)(DEF) <sub>2</sub> ] (green) and [Ni(H <sub>2</sub> diol)] (blue). Filled and open circles represent adsorption and desorption points, respectively.	7

Figure 1.10	Photolysis and mapping of a single crystal of ReCu. (a) Crystal prior to irradiation, with Raman mapping area indicated in black. (b) Raman mapping, where red corresponds to the presence of the ground state Raman spectrum. (c) The crystal after “writing” and (d) the Raman map indicating presence of (red) ground-state Raman spectrum and (green) photoproduct Raman spectrum.	9
Figure 1.11	(Left) Schematic of SALE from bipy to dabco (2) and dabco and bipy (3). (Right) N <sub>2</sub> adsorption isotherms for different ligand combinations.	10
Figure 1.12	Schematic of post-synthetically modified frameworks. Linkers were brominated across the C≡C bond using N-bromosuccinimide (NBS) and N,N-diphenylthiourea (DPT).	11
Figure 1.13	(Left) Photograph and (right) schematic of Linkam FTIR600 stage.	13
Figure 1.14	Infrared spectrum of HKUST-1. Red circles indicate areas of band saturation.	15
Figure 1.15	Infrared spectrum of Sc <sub>2</sub> BDC <sub>3</sub> . The red line indicates oscillations in the spectral baseline, arising due to scattering of light around the single crystal sample.	16
Figure 1.16	Example spectrum of SHF-61-CHCl <sub>3</sub> after desolvation at 120 °C. Regions of overlapped peaks are indicated in red. Regions of saturation are indicated in purple.	17
Figure 1.17	Example spectral fits for SHF-61-CHCl <sub>3</sub> at higher energy (top).	18
Figure 1.18	Example baseline corrections for SHF-61-CHCl <sub>3</sub> .	19
Figure 1.19	Infrared spectra collected during CyP-resolvation of SHF-61 o, focussed on CyP carbonyl band region.	20
Figure 1.20	Baseline applied to integration process of CyP carbonyl bands during resolvation of SHF-61 o with CyP.	20
Figure 1.21	Example spectral composition plot of CO-loaded (orange) and unloaded (blue) NOTT-100 during -75 °C CO desorption experiments.	21
Figure 2.1	(a) Schematic drawing of a MOF-5 crystal in a solution of mixed dyes. The image on the right shows a fluorescence confocal microscopy cross-section images of the crystal. (b) Representation of MOF-5 crystal placed onto an organogel, presoaked in the DMF dye solution. The corresponding side-on confocal microscopy image illustrates the separation of the dyes into two distinct bands. All scale bars represent 200 μm.	21

Figure 2.2	(Left) Representations of BODIPY-dye surface-modified HKUST-1, (middle) CLSM images, and (right) transmission images of dye-modified HKUST-1 at $z = A-E$ . The sequential Z-stack slicing from the bottom of crystal ( $z = A$ ) to the top of crystal ( $z = E$ ) reveal the octahedral crystal morphology of the framework.	30
Figure 2.3	Closed-form <b>SPO</b> and open-form <b>MCN</b> .	31
Figure 2.4	Solutions of the spirooxazine shown in Figure 2.3, in MeOH.	31
Figure 2.5	UV-VIS absorption spectrum of spirooxazine (inset) in indicated solvents.	32
Figure 2.6	UV-VIS absorption spectra of spirooxazine (pictured) in MeOD at 243 K, before and after 210 s irradiation at $\lambda = 313$ nm.	32
Figure 2.7	Reaction scheme for synthesis of nitro-functionalised spiropyran in reference 22.	33
Figure 2.8	(Left) Ar adsorption (filled) and desorption (open) isotherms for indicated materials. (Right) $\text{CO}_2$ adsorption (filled) and desorption (open) isotherms for MOF-808-SP <sub>c</sub> and MOF 808-SP <sub>o</sub> .	33
Figure 2.9	$\text{CO}_2$ adsorption isotherms of $\text{Zn}(\text{AzDC})(4,4'\text{-BPE})_{0.5}$ at 303 K. Light intensity was fixed at 24.6 W cm <sup>-2</sup> in the wavelength range of 200–500 nm.	34
Figure 2.10	Crystal structures of metal-organic frameworks modified in this chapter.	36
Figure 2.11	SEM images of a) MIL-68(Ind), b) NOTT-100, c) $\text{Sc}_2\text{BDC}_3$ and d) UiO-67. Images are captured at x200, x100, x100 and x500 magnification respectively.	37
Figure 2.12	Structures of dyes discussed throughout this chapter.	38
Figure 2.13	UV-VIS-DRS spectra of dyes (top) and MOFs (bottom). Regions of spectral overlap are indicated in yellow and green.	39
Figure 2.14	Comparison of L-proline-containing reaction solutions; a) $\text{H}_2\text{SO}_4$ (55 °C), b) HCl + L-proline (55 °C), c) $\text{HNO}_3$ + L-proline (55 °C) and d) $\text{HNO}_3$ + L-proline (120 °C).	41
Figure 2.15	SEM images of the most promising NOTT-100 samples.	42
Figure 2.16	SEM images of (left) DMF-washed and (right) MeOH-exchanged NOTT-100. NB: scale bars are 2 mm and 1 mm respectively.	43
Figure 2.17a	SEM images of solvent-exchanged NOTT-100, ordered from best to worst left-to-right and top-to-bottom. Exchange solvent indicated in corners of images.	44

Figure 2.17b	SEM images of solvent-exchanged NOTT-100, ordered from best to worst left-to-right and top-to-bottom. Exchange solvent indicated in corners of images.	45
Figure 2.18	Plots of solvent properties vs NOTT-100 crystal ranking.	46
Figure 2.19	SEM images at x100 magnification of $\text{Sc}_2\text{BDC}_3$ crystals from simultaneous synthesis in three different vessels.	47
Figure 2.20	SEM images at x59/60 magnification of $\text{Sc}_2\text{BDC}_3$ , synthesised by the pre-doping method using the stated <i>R</i> factors. Reaction time was 48 hr in all cases.	49
Figure 2.21	SEM images at x100 magnification of $\text{Sc}_2\text{BDC}_3$ synthesised with <i>R</i> = 0.12 (top) and 0.17 (bottom) with indicated reaction times.	50
Figure 2.22	SEM images at x50 magnification of $\text{Sc}_2\text{BDC}_3$ synthesised from reaction solution at five-fold concentration, with indicated reaction times.	51
Figure 2.23	Structures of dyes discussed in this chapter.	52
Figure 2.24	Schematic of experimental approach for UV-VIS approach to establishing reaction timescales for post-synthetic modification of MOFs with monocarboxylate dye.	55
Figure 2.25	(Left) Solution-phase UV-VIS spectra of (top) SALE reaction solutions post-incubation [Stage 1] and (bottom) MOF washings to remove physisorbed dye [Stage 2]. (Right) Plots showing percentage of initial <b>7-DCCA</b> remaining in (top) reaction solutions post-incubation [Stage 1] and (bottom) MOF washings [Stage 2]. Points marked in red indicate >100% of initial <b>7-DCCA</b> concentration.	57
Figure 2.26	(Left) Solution-phase UV-VIS spectra of (top) SALE reaction solutions post-incubation [Stage 1] and (bottom) MOF washings to remove physisorbed dye [Stage 2]. (Right) Plots showing percentage of initial <b>7-DCCA</b> remaining in (top) reaction solutions post-incubation [Stage 1] and (bottom) MOF washings [Stage 2]. Points marked in red indicate <0% of initial <b>7-DCCA</b> concentration.	58
Figure 2.27	(Left) Solution-phase UV-VIS spectra of (top) SALE reaction solutions post-incubation [Stage 1] and (bottom) MOF washings to remove physisorbed dye [Stage 2]. (Right) Plots showing percentage of initial <b>7-DCCA</b> remaining in (top) reaction solutions post-incubation [Stage 1] and (bottom) MOF washings [Stage 2]. Points marked in red indicate <0% of initial <b>7-DCCA</b> concentration.	59
Figure 2.28	(Left) Solution-phase UV-VIS spectra of (top) SALE reaction solutions post-incubation [Stage 1] and (bottom) MOF washings to remove physisorbed dye [Stage 2]. (Right) Plots showing	60

	percentage of initial <b>7-DCCA</b> remaining in (top) reaction solutions post-incubation [Stage 1] and (bottom) MOF washings [Stage 2].	
Figure 2.29	Solution-phase UV-VIS spectra of reaction solutions following MIL-68(In) SALE reactions with <b>7-DCCA</b> .	62
Figure 2.30	Solution-phase UV-VIS spectra of combinations of <b>7-DCCA</b> with (left) linkers, (centre) metal salts and (right) modulators and solvents. Vertical red lines indicate position of only <b>7-DCCA</b> in MeOH (412 nm).	64
Figure 2.31	Structure of <b>7-DCCA</b> , with protonation sites (red) and deprotonation sites (blue) indicated.	65
Figure 2.32	Plot of deviance from initial <b>7-DCCA</b> peak position with addition of HCl (0.01 M) and NaOH (0.01 M) in (left) nm and (right) $\text{cm}^{-1}$ .	65
Figure 2.33	Plot of change in <b>7-DCCA</b> peak absorbance with addition of HCl (0.01 M) and NaOH (0.01 M).	66
Figure 2.34	UV-VIS absorption spectra of HCl-digested <b>7-DCCA</b> modified MOF washings.	68
Figure 2.35	Example of analysis procedure for UV-VIS-DRS spectra, indicated. Regions highlighted in blue are indicative of <b>7-DCCA</b> .	70
Figure 2.36	Plots of <b>7-DCCA</b> reflectance vs time for (left) MIL-68(In) and (right) UiO-67.	71
Figure 2.37	CLSM images, with histogram area outlined for each framework.	73
Figure 2.38	Plots of CLSM average fluorescence intensity of <b>7-DCCA</b> -modified MOFs. Error bars are the mean standard deviations of each average fluorescence intensity.	74
Figure 2.39	(a) Single and (b) Z-stack CLSM images of 4 hr <b>7-DCCA</b> -modified MIL-68(In).	74
Figure 2.40	PXRD patterns of UiO-67 collected from (orange) control and (blue) <b>7-DCCA</b> SALE experiments.	75
Figure 2.41	$^1\text{H}$ NMR spectra in MeOD of <b>phen-spiro</b> reaction mixtures with varying amounts of $\text{NEt}_3$ , as indicated.	77
Figure 2.42	$^1\text{H}$ NMR spectra in MeOD of <b>phen-spiro</b> reaction mixtures in 'bench' vs anhydrous solvent, as indicated.	80
Figure 2.43	Structures of (top) <b>phen-spiro</b> and (bottom) <b>m-hydrazone</b> , with their respective photoswitched states.	81
Figure 2.44	CLSM images of two separate single crystals of UiO-67 modified with 0.03 mM <b>phen-spiro</b> in MeCN at 60 °C for 24 hours.	83

Figure 2.45	CLSM Z-stack images of <b>phen-spiro</b> -modified $\text{Sc}_2\text{BDC}_3$ at 22.5 $\mu\text{m}$ steps (left to right). Blue and red shading indicates 428–508 nm and 642–695 nm fluorescence respectively. Purple shading indicates combined fluorescence.	84
Figure 2.46	CLSM Z-stack images of <b>phen-spiro</b> -modified $\text{Sc}_2\text{BDC}_3$ at 22.5 $\mu\text{m}$ steps (1; top of crystal and 6; bottom of crystal). Purple shading indicates combined 428–508 nm and 642–695 nm fluorescence.	85
Figure 2.47	UV-VIS-DR spectra of $\text{Sc}_2\text{BDC}_3$ (top), $\text{Sc}_2\text{BDC}_3\supset\text{phen-spiro}$ (middle) and <b>phen-spiro</b> (bottom).	85
Figure 2.48	CLSM images of $\text{Sc}_2\text{BDC}_3\supset\text{phen-spiro}$ after varying specified periods of irradiation with a 633 nm laser. Blue and red shading indicates 428–508 nm and 642–695 nm fluorescence respectively. Purple shading indicates combined fluorescence.	87
Figure 2.49	CLSM image of $\text{Sc}_2\text{BDC}_3\supset\text{phen-spiro}$ , with area used (25,893 pixels) to generate fluorescence intensity values indicated in green. Purple shading indicates combined 428–508 and 642–695 nm fluorescence.	88
Figure 2.50	Plot of mean fluorescence intensity with increasing 633 nm irradiation. Blue and red points indicate fluorescence detected between 428–508 nm and 642–695 nm respectively.	88
Figure 2.51	Plots of UV-VIS-DR spectra of $\text{Sc}_2\text{BDC}_3\supset\text{phen-spiro}$ (orange) without irradiation and (blue) after 24 hr irradiation (390 nm – red line).	89
Figure 2.52	CLSM Z-stack images of <b>phen-spiro</b> -modified UiO-67 at 7.5 $\mu\text{m}$ steps (left to right). Blue and red shading indicates 428–508 nm and 642–695 nm fluorescence respectively.	90
Figure 2.53	UV-VIS-DR spectra of UiO-67 (top), UiO-67 $\supset\text{phen-spiro}$ (middle) and <b>phen-spiro</b> (bottom).	91
Figure 2.54	CLSM image of UiO-67 $\supset\text{phen-spiro}$ , with area used (6,834 pixels) to generate fluorescence intensity values indicated in green. Blue shading indicates 428–508 nm fluorescence.	92
Figure 2.55	CLSM of UiO-67 $\supset\text{phen-spiro}$ after varying spells of irradiation with a 633 nm laser. Blue and red shading indicates 428–508 and 642–695 nm fluorescence respectively. Purple shading indicates combined fluorescence.	94
Figure 2.56	Plots of UV-VIS-DR spectra of UiO-67 $\supset\text{phen-spiro}$ without irradiation (orange), after 1 hr (green) and after 24 hr (blue) 390 nm irradiation.	95
Figure 2.57	CLSM Z-stack images of <b>m-hydrazone</b> -modified $\text{Sc}_2\text{BDC}_3$ at 7.5 $\mu\text{m}$ steps. Blue shading indicates 428–508 nm fluorescence.	96

Figure 2.58	UV-VIS-DR spectra of unmodified $\text{Sc}_2\text{BDC}_3$ (top), $\text{Sc}_2\text{BDC}_3 \supset \text{m-hydrazone}$ (middle) and $\text{m-hydrazone}$ (bottom).	97
Figure 2.59	CLSM Z-stack images of $\text{m-hydrazone}$ -modified UiO-67 at 2.5 $\mu\text{m}$ steps. Blue shading indicates 428–508 nm fluorescence.	98
Figure 2.60	UV-VIS-DR spectra of unmodified UiO-67 (top), UiO-67 $\supset \text{m-hydrazone}$ (middle) and $\text{m-hydrazone}$ (bottom).	99
Figure 2.61	Volumetric $\text{N}_2$ isotherms of (left) NOTT-100 and (right) NOTT-100 $\supset \text{7-DCCA}$ at 77 K.	100
Figure 2.62	Volumetric $\text{N}_2$ isotherms of (left) $\text{Sc}_2\text{BDC}_3$ and (right) $\text{Sc}_2\text{BDC}_3 \supset \text{phen-spiro}$ at 77 K.	101
Figure 2.63	Pore size distribution (left) and cumulative pore volume (right) of $\text{Sc}_2\text{BDC}_3$ and $\text{Sc}_2\text{BDC}_3 \supset \text{phen-spiro}$ , as indicated.	102
Figure 2.64	Volumetric $\text{N}_2$ isotherms of (top) UiO-67, (middle) UiO-67 $\supset \text{7-DCCA}$ and (bottom) UiO-67 $\supset \text{phen-spiro}$ at 77 K.	103
Figure 2.65	Pore size distribution (left) and cumulative pore volume (right) of UiO-67, UiO-67 $\supset \text{7-DCCA}$ and UiO-67 $\supset \text{phen-spiro}$ .	104
Figure 3.1	Two main cargo-loading strategies for MOFs, as indicated.	127
Figure 3.2	Schematic of cisplatin-enriched nanoMOFs synthesis.	128
Figure 3.3	Release of procainamide- $\text{H}^+$ into 0.1 M PBS buffer (blue) and ultrapure water (red) over 140 h.	129
Figure 3.4	Histological analysis of pig arteries 3 weeks after angioplasty. Sections were stained (C, E) or viewed under autofluorescence (D, F). C & D show surgically injured pig artery from a pig treated with oxygen. E & F show surgically injured pig artery from a pig treated with CO. Arrows indicate scar tissue.	131
Figure 3.5	<i>In situ</i> infrared spectra of (top) metal-organic frameworks, (middle) guest pharmaceuticals and (bottom) solvents considered for desorption experiments, as indicated. * region contains $\text{CO}_2$ background peaks, removed for clarity.	134
Figure 3.6	(Top) Crystal structures of (left-to-right) HKUST-1, MIL-68(Ind), MIL-101(Cr) and $\text{Sc}_2\text{BDC}_3$ . (Bottom) Metal nodes for the frameworks shown above.	135
Figure 3.7	ChemDraw structures of (a) caffeine, (b) ibuprofen and (c) paracetamol.	136
Figure 3.8	ChemDraw structures of (a) acetonitrile ( $\text{MeCN}$ ), (b) dichloromethane ( $\text{DCM}$ ), (c) ethanol ( $\text{EtOH}$ ) and (d) <i>n</i> -hexane.	136
Figure 3.9	Infrared spectra of single crystals of the MOFs studied.	137
Figure 3.10	Infrared spectra of guest pharmaceuticals studied.	138

Figure 3.11	Infrared spectra of diffusion solvents used.	139
Figure 3.12	Example spectral overlap comparison, with regions of interest indicated for caffeine (blue). * region contains CO <sub>2</sub> background peaks, removed for clarity	140
Figure 3.13	Schematic of solvent-saturated Linkam cell	142
Figure 3.14	Possible baseline corrections; (left) constant, (centre) no baseline (integral taken from y = 0) and (right) straight line.	144
Figure 3.15	Baseline applied to MIL-68(In)⊃caffeine spectra during integration at indicated temperatures.	145
Figure 3.16	Peak integral change of 1700 cm <sup>-1</sup> caffeine carbonyl band during diffusion from MIL-68(In) at 10 °C.	146
Figure 3.17	Peak integral change of 1700 cm <sup>-1</sup> caffeine carbonyl band during diffusion from MIL-68(In) at 15 °C.	146
Figure 3.18	Peak integral change of 1700 cm <sup>-1</sup> caffeine carbonyl band during diffusion from MIL-68(In) at 20 °C.	147
Figure 3.19	Peak integral change of 1700 cm <sup>-1</sup> caffeine carbonyl band during diffusion from MIL-68(In) at 25 °C.	147
Figure 3.20	Peak integral change of 1700 cm <sup>-1</sup> caffeine carbonyl band during diffusion from MIL-68(In) at 30 °C.	148
Figure 3.21	Peak integral change of 1700 cm <sup>-1</sup> caffeine carbonyl band during diffusion from MIL-68(In) at 35 °C.	148
Figure 3.22	Arrhenius plot of caffeine diffusion from MIL-68(In)⊃caffeine.	150
Figure 3.23	Plots of mass of caffeine desorbed from MIL-68(In)⊃caffeine at indicated temperatures.	152
Figure 3.24	(Left) Caffeine solutions in MeCN after MIL-68(In)⊃caffeine desorption experiments. (Right) Four samples of MIL-68(In)⊃caffeine post-desorption.	153
Figure 3.25	Crystal structures of (left) NOTT-100 and (right) Cu-paddlewheel metal node. Axial water molecules are circled.	155
Figure 3.26	DRIFT spectra of CO-loaded NOTT-100 CO region during -100 °C desorption experiments.	157
Figure 3.27	Integrated area intensity of CO-loaded NOTT-100 CO region during -100 °C desorption experiments.	158
Figure 3.28	Peak analysis fit of NOTT-100 CO desorption after 44 seconds at -75 °C.	159
Figure 3.29	Peak area fits of indicated peaks during NOTT-100 CO desorption experiments.	160

Figure 3.30	Composite model plots for CO desorption from NOTT-100 at indicated temperatures. Orange indicates CO-saturated NOTT-100 at the beginning of the experiment and blue indicates the end of the desorption experiment.	161
Figure 3.31	Change in peak area of $2123\text{ cm}^{-1}$ peak during CO-desorption from NOTT-100, with UV irradiation in indicated region in blue.	163
Figure 3.32	IR spectral assignment of NOTT-100 $\supset$ CO.	164
Figure 4.1	Structures of (left) MIL-53as, (middle) MIL-53 <i>ht</i> and (right) MIL-53 <i>lt</i> . Altered pore structure is clear in right-hand figure.	175
Figure 4.2	Proposed structures of (top) MIL-101(Cr) and (bottom) MIL-53(Cr) following adsorption of carbamazepine.	176
Figure 4.3	Distortion of the classic $M_3(\mu_3\text{-O})(\text{ldc})_3(L^T)_3$ cluster, leading to the reversed breathing directions for MIL-88 and MCF-18. $\text{ldc}$ = linear dicarboxylic acid; $L^T$ = terminating ligand.	177
Figure 4.4	The structure of $\text{Zn}_2(\text{BDC})_2(\text{DABCO})\supset$ benzene at 298 (left) and 100 K (right).	178
Figure 4.5	Microscope images of desolvated SHF-61-DMF (left) and SHF-61-CHCl <sub>3</sub> . Collected at x15 magnification. Scale bar represents 60 $\mu\text{m}$ .	180
Figure 4.6	a) In(O <sub>2</sub> CR) <sub>4</sub> tetrahedral network node. b) View down the <i>a</i> -axis that shows lozenge-shaped channels. c) Hydrogen-bonding interaction between the amino groups of adjacent networks. d) View down the <i>c</i> -axis that shows the helical arrangement of the two interpenetrated networks along the channel axis ( <i>a</i> -axis).	181
Figure 4.7	Overview of guest-related flexibility of SHF-61.	182
Figure 4.8	Example spectrum of SHF-61-CHCl <sub>3</sub> after desolvation at 120 °C. Regions indicated in red require deconvolution due to overlapping peaks; region indicated in purple is saturated.	183
Figure 4.9	Example spectral fits for SHF-61-CHCl <sub>3</sub> at higher energy (top) and lower energy (bottom).	184
Figure 4.10	Example baseline corrections for SHF-61-CHCl <sub>3</sub> .	185
Figure 4.11	Infrared spectra collected during CyP-resolvation of SHF-61 <i>o</i> , focussed on CyP $\nu(\text{CO})$ band region.	186
Figure 4.12	Baseline applied to integration process of CyP $\nu(\text{CO})$ bands during resolvation of SHF-61 <i>o</i> with CyP.	186
Figure 4.13	IR spectra of solvated (blue) and desolvated (red) crystals of SHF-61-CHCl <sub>3</sub> (left) and SHF-61-DMF (right).	190
Figure 4.14	Peak area (orange) and position (blue) changes of SHF-61-CHCl <sub>3</sub> (top) and SHF-61-DMF (bottom) higher energy (left) and lower energy (right) $\nu(\text{NH})$ following heating.	191

Figure 4.15	Illustration of solvent interactions with 2-aminoterephthalate linker in SHF-61.	192
Figure 4.16	Spectral composition plots of SHF-61-CHCl <sub>3</sub> (left) and SHF-61-DMF during staged desolvation experiments.	193
Figure 4.17	Spectral composition plot of SHF-61-DMF during staged desolvation experiments, when fit to four models.	194
Figure 4.18	Transition of DMF model states.	194
Figure 4.19	Photograph of SHF-61c measured in this experiment collected <i>in situ</i> on the IR microscope. Aperture size is 20 x 20 μm.	196
Figure 4.20	Peak area and position changes of SHF-61c following resolvation with DMF for (left) higher energy and (right) lower energy ν(NH) peaks. Data is absent for 199–249 mins (indicated by *) due to a detector coolant fill on the microscope spectrometer.	196
Figure 4.21	Composition plot of spectra during SHF-61c-DMF resolvation experiment. Data is absent for 199–249 mins (indicated by *) due to a detector coolant fill on the microscope spectrometer.	198
Figure 4.22	(Left) Infrared spectra of DMF ν(CO) stretch (1700–1650 cm <sup>-1</sup> ) in SHF-61c (orange) and SHF-61c-DMF (blue). (Right) Change in peak area of 1660 cm <sup>-1</sup> DMF carbonyl peak during DMF-resolvation of SHF-61c. Data is absent for SHF-61c-DMF resolvation for the period 199–249 mins (indicated by *) due to a detector coolant fill on the microscope spectrometer.	199
Figure 4.23	Photograph of SHF-61o (indicated), collected <i>in situ</i> on the IR microscope. Aperture size is 20 x 20 μm.	200
Figure 4.24	Infrared spectra of DMF ν(CO) stretch (1700–1650 cm <sup>-1</sup> ) in SHF-61o (orange) and SHF-61o-DMF (blue). (Right) Change in peak area of 1660 cm <sup>-1</sup> DMF ν(CO) band during SHF-61o DMF-resolvation.	201
Figure 4.25	(Left) Composition plot of spectra during SHF-61o-DMF resolvation experiment. (Right) Change in peak area of 1660 cm <sup>-1</sup> DMF ν(CO) band during SHF-61o DMF-resolvation. Points highlighted in green have been excluded from the fitting process.	202
Figure 4.26	Photograph of SHF-61o measured in this experiment (indicated), collected <i>in situ</i> on the IR microscope. Aperture size is 20 x 20 μm.	203
Figure 4.27	Peak area and position changes of SHF-61o following resolvation with CHCl <sub>3</sub> for (left) higher energy and (right) lower energy ν(NH) peaks.	204

Figure 4.28	(Left) Desolvated (green) and CHCl <sub>3</sub> -resolvated (blue) SHF-61 <b>o</b> . Peak at 1230–1215 cm <sup>-1</sup> is indicative of δ(CH) bend. (Right) Peak area of 1220 cm <sup>-1</sup> CHCl <sub>3</sub> δ(CH) bend during SHF-61 CHCl <sub>3</sub> -resolution fit to a biexponential curve (red).	205
Figure 4.29	Composition plot of spectra during SHF-61 <b>o</b> -CHCl <sub>3</sub> resolution experiment.	206
Figure 4.30	Photograph of SHF-61 <b>o</b> measured in this experiment (indicated), collected in situ on the IR microscope. Aperture size is 20 x 20 μm.	206
Figure 4.31	(Left) Infrared spectra of CyP ν(CO) stretches (1750–1710 cm <sup>-1</sup> ) in SHF-61 <b>o</b> and SHF-61 <b>o</b> -CyP	207
Figure 4.32	Baseline applied to integration process of CyP ν(CO) stretches during resolution of SHF-61 <b>o</b> with CyP.	208
Figure 4.33	(Left) 1727 cm <sup>-1</sup> and (right) 1744 cm <sup>-1</sup> CyP ν(CO) stretches fit to biexponential curve fits (red) during SHF-61 <b>o</b> CyP-resolvation.	208
Figure 4.34	Composition plot of spectra during SHF-61 <b>o</b> -CyP resolution experiment.	209
Figure 4.35	(Left) <b>o</b> Cys and (right) <b>od</b> model composition fit to biexponential curves (red) during SHF-61 <b>o</b> CyP-resolvation.	209
Figure 4.36	Peak area of 1660 cm <sup>-1</sup> DMF ν(CO) stretch fit to a biexponential curve (red) during SHF-61 <b>o</b> -DMF desolvation experiments.	214
Figure 4.37	Composition plot of spectra during desolvation of SHF-61 <b>o</b> -DMF.	215
Figure 4.38	Biexponential curve fits (red) of (left) <i>od</i> and (right) <i>oDs</i> model composition during desolvation of SHF-61 <b>o</b> -DMF.	216
Figure 4.39	Biexponential curve fit (red) of 1220 cm <sup>-1</sup> CHCl <sub>3</sub> δ(CH) bend peak integral during SHF-61 <b>o</b> -CHCl <sub>3</sub> desolvation experiments.	217
Figure 4.40	Composition plot of spectra during desolvation of SHF-61 <b>o</b> -CHCl <sub>3</sub> .	218
Figure 4.41	Biexponential curve fits (red) of <i>oCs</i> (left) and <i>od</i> (right) model composition plots during desolvation of SHF-61 <b>o</b> -CHCl <sub>3</sub> .	219
Figure 4.42	Biexponential curve fits (red) of (left) 1727 cm <sup>-1</sup> and (right) 1744 cm <sup>-1</sup> CyP ν(CO) stretches during desolvation of SHF-61 <b>o</b> -CyP.	220
Figure 4.43	Composition plot of spectra during desolvation of SHF-61 <b>o</b> -CyP.	221
Figure 4.44	Biexponential curve fits (red) of <i>oCys</i> (left) and <i>od</i> (right) model composition during desolvation of SHF-61 <b>o</b> -CyP.	221
Figure 4.45	Gravimetric CO <sub>2</sub> isotherms at 298 K of desolvated SHF-61 <b>o</b> (blue) and SHF-61 <b>c</b> (green).	224

Figure 4.46	IR spectrum of desolvated SHF-61-CHCl <sub>3</sub> (blue) and CO <sub>2</sub> -loaded SHF-61-CHCl <sub>3</sub> .	225
Figure 4.47	Peak area (orange) and position (blue) changes of SHF-61 <b>o</b> (top) and SHF-61 <b>c</b> (bottom) higher energy (left) and lower energy (right) $\nu(\text{NH})$ following CO <sub>2</sub> sorption.	226
Figure 4.48	Infrared spectrum (3700-2500 cm <sup>-1</sup> ) of CO <sub>2</sub> -loaded SHF-61-CHCl <sub>3</sub> , with CO <sub>2</sub> combination bands indicated.	228
Figure 4.49	Baseline correction applied during peak integration of CO <sub>2</sub> combination bands in SHF-61-CHCl <sub>3</sub> .	228
Figure 4.50	Plots of CO <sub>2</sub> combination band integral in SHF-61-CHCl <sub>3</sub> (left) and SHF-61-DMF (right) at varying partial pressures of CO <sub>2</sub> . Note, difference in y-axis scale.	229
Figure 4.51	Composition plot of spectra during CO <sub>2</sub> uptake into (left) SHF-61 <b>o</b> and (right) SHF-61 <b>c</b> .	230
Figure 4.52	(Left) Peak integrals of 3570 cm <sup>-1</sup> peak during CO <sub>2</sub> uptake in SHF-61 <b>o</b> (orange) and SHF-61 <b>c</b> (purple). (Right) Volumetric CO <sub>2</sub> isotherms of SHF-61 <b>o</b> (blue) and SHF-61 <b>c</b> (green).	231
Figure A2.1	Solution-phase UV-VIS spectra of metal salt–, solvent– and modulator–linker combinations of indicated MOF constituents in MeOH.	246
Figure A2.2	Solution-phase UV-VIS spectra of linker–, solvent– and modulator–metal salt combinations of indicated MOF constituents in MeOH.	246
Figure A2.3	Solution-phase UV-VIS spectra of metal salt–, linker–, solvent– modulator combinations of indicated MOF constituents in MeOH.	247
Figure A2.4	PXRD patterns of MIL-68(ln) collected from (orange) control and (blue) <b>7-DCCA</b> SALE experiments.	248
Figure A2.5	PXRD patterns of NOTT-100 collected from (orange) control and (blue) <b>7-DCCA</b> SALE experiments.	248
Figure A2.6	PXRD patterns of Sc <sub>2</sub> BDC <sub>3</sub> collected from (orange) control and (blue) <b>7-DCCA</b> SALE experiments.	249
Figure A2.7	LC-MS trace of crude <b>phen-spiro</b> .	249
Figure A2.8	MS fragments of crude <b>phen-spiro</b> LC trace.	250

## List of tables

---

Table 2.1	Qualitative crystal ranking of solvent-exchanged NOTT-100 with associated solvent parameters.	46
Table 2.2	Reagent masses and associated <i>R</i> factors for doping experiments. Reagents from the synthesis by Miller <i>et al.</i> are highlighted in blue.	48
Table 2.3	Solvent-assisted ligand exchange conditions taken or adapted from the references indicated.	53
Table 2.4	Estimation of unreacted and chemisorbed <b>7-DCCA</b> following SALE reactions.	61
Table 2.5	Pore dimensions of MOFs discussed herein.	61
Table 2.6	MOF constituent combinations, for which the UV-VIS absorption spectra were collected in MeOH.	62
Table 2.7	N <sub>2</sub> BET isotherm data collected at 77 K.	105
Table 3.1	Exponential curve fitting results from MIL-68(Ind)⊃caffeine diffusion experiments.	149
Table 4.1	Times for which SHF-61-DMF and SHF-61-CHCl <sub>3</sub> were held at specified temperatures during desolvation experiments. *The detector required a liquid N <sub>2</sub> fill at this stage and therefore we had to wait for the detector temperature to stabilise before further collection.	189
Table 4.2	Peak area and position changes for SHF-61 on desolvation.	191
Table 4.3	Changes in $\nu(\text{NH})$ bands after resolvation of SHF-61c with DMF.	197
Table 4.4	Changes in $\nu(\text{NH})$ bands after resolvation of SHF-61o with DMF.	200
Table 4.5	Changes in $\nu(\text{NH})$ bands after resolvation of SHF-61o with CHCl <sub>3</sub> .	204
Table 4.6	Changes in $\nu(\text{NH})$ bands after resolvation of SHF-61o with CyP.	207
Table 4.7.	Changes in $\nu(\text{NH})$ bands (top) after resolvation experiments (April 2018) and (bottom) after desolvation experiments (September 2016).	211
Table 4.8	Changes in $\nu(\text{NH})$ bands (top) after desolvation of SHF-61o-DMF (April 2018) and (bottom) after desolvation of SHF-61-DMF (September 2016).	214

Table 4.9	Changes in $\nu(\text{NH})$ bands (top) after desolvation of SHF-61 <sup><b>o</b></sup> -DMF (April 2018) and (bottom) after desolvation of SHF-61-DMF (September 2016).	217
Table 4.10	Changes in $\nu(\text{NH})$ bands (top) after desolvation of SHF-61 <sup><b>o</b></sup> -DMF (April 2018) and (bottom) after desolvation of SHF-61-DMF (September 2016).	219
Table 4.11	Changes in $\nu(\text{NH})$ bands after desolvation of resolvated SHF-61 <sup><b>o</b></sup> materials.	222
Table 4.12	Changes in $\nu(\text{NH})$ bands in SHF-61 <sup><b>o</b></sup> (top) and SHF-61 <sup><b>c</b></sup> (bottom) after $\text{CO}_2$ loading.	227
Table 4.13	Timescales for staged heating of SHF-61.	235
Table A2.1	Attempted combinations for NOTT-100 single crystal synthesis	243
Table A2.2	Peak positions for $\lambda_{\max}$ of <b>7-DCCA</b> peaks in UV-VIS-DR spectra during timed modification experiments.	247
Table A2.3	Assignment of MS fragments in crude <b>phen-spiro</b> .	251
Table A4.1	Peak analysis approach used for solvent bands during SHF-61 re/desolvation experiments.	251

## List of equations

---

Equation 2.1	<i>R</i> factor for control of crystal polydispersity.	48
Equation 3.1	Exponential curve decay equation.	149
Equation 3.2	Arrhenius equation.	150

## List of schemes

---

Scheme 2.1	<b>Phen-spiro</b> reaction scheme.	77
------------	------------------------------------	----

# Contents

---

Acknowledgements .....	i
Abstract.....	ii
List of abbreviations .....	iv
List of figures .....	viii
List of tables.....	xx
List of equations.....	xxi
List of schemes .....	xxi
Contents .....	xxii

## 1 Introduction.....1

1.1 Stimuli-responsive materials .....	1
1.2 Structure of metal-organic frameworks.....	1
1.3 Control of crystal size.....	3
1.4 Stimuli-responsive MOFs .....	4
1.5 Post-synthetic modification of MOFs .....	9
1.6 Specialised experimental methods.....	12
1.7 Experimental challenges .....	15
1.8 Approaches to spectral analysis.....	17
1.8.1 Peak fitting analysis .....	17
1.8.2 Peak integration.....	19
1.8.3 Composite spectral modelling .....	21
1.9 Scope of this thesis.....	23
1.10 References .....	24

## 2 Tracking fluorescent guests in metal-organic frameworks .....28

2.1 MOFs as hosts for mobile guests.....	28
2.1.1 Tracking fluorescent guests in MOFs .....	28
2.1.2 Spirooxazine molecular switches .....	31
2.1.3 Photoswitches in MOFs .....	33
2.2 Aims and Objectives .....	35
2.3 Results and Discussion.....	36
2.3.1 MOF selection.....	36
2.3.2 Optimisation of crystal size .....	40
2.3.2.1 NOTT-100 single crystal growth .....	40

2.3.2.2 Solvent effects on NOTT-100 crystal stability .....	43
2.3.2.3 Optimisation of $\text{Sc}_2\text{BDC}_3$ crystal size.....	47
2.3.3 Post-synthetic modification of MOFs with coordinating dyes.....	52
2.3.3.1 Optimisation of SALE reaction conditions.....	53
2.3.3.1.1 Stage 1 – SALE reaction solutions.....	56
2.3.3.1.2 Stage 2 – Physisorbed 7-DCCA .....	56
2.3.3.1.3 UV-VIS spectral absorption shifts of 7-DCCA as a result of reaction conditions.....	62
2.3.3.1.4 Effect of pH on 7-DCCA.....	65
2.3.3.1.5 Contributing factors to 7-DCCA peak position in SALE reaction ..	66
2.3.3.1.5 Stage 3 – Solution-phase UV-VIS.....	67
2.3.3.1.6 Stage 3 – UV-VIS-Diffuse Reflectance .....	69
2.3.3.1.7 Stage 3 – Confocal laser scanning microscopy.....	72
2.3.3.1.8 Framework stability in SALE control reaction conditions .....	75
2.3.3.1.9 Reaction time conclusions .....	76
2.3.3.4 Synthesis of phen-spiro photoswitch .....	77
2.3.3.5 Solid-state photoswitch behaviour.....	83
2.3.3.5.1 PSM of $\text{Sc}_2\text{BDC}_3$ with phen-spiro.....	83
2.3.3.5.2 Photoswitching of $\text{Sc}_2\text{BDC}_3$ -phen-spiro .....	86
2.3.3.5.3 PSM of UiO-67 with phen-spiro .....	90
2.3.3.5.4 Photoswitching of UiO-67-phen-spiro .....	92
2.3.3.5.5 PSM of $\text{Sc}_2\text{BDC}_3$ with <i>m</i> -hydrazone.....	96
2.3.3.5.6 PSM of UiO-67 with <i>m</i> -hydrazone.....	98
2.3.3.5.7 Summary of solid-state MOF-bound behaviour of photoswitches.	99
2.3.3.6 Comparison of uptake capabilities of modified MOFs.....	100
2.4 Conclusions and Outlook .....	106
2.5 Experimental .....	109
2.5.1 General methods .....	109
2.5.2 Phen-spiro synthetic route .....	110
2.5.3 MOF linker synthesis .....	113
2.5.4 MOF synthesis.....	118
2.5.5 Post-synthetic modification of MOFs.....	120
2.5.6 Irradiation experiments .....	122
2.6 References .....	123

<b>3 Tracking non-fluorescent therapeutic agents from metal-organic frameworks .....</b>	<b>127</b>
3.1 MOFs as Drug Delivery Systems .....	127
3.1.1 Therapeutic uses of carbon monoxide .....	130
3.2 Aims and Objectives .....	133
3.3 Choice of materials .....	133
3.4 IR spectral features.....	137
3.4.1 MOF IR spectral features.....	137
3.4.2 Guest pharmaceutical IR spectral features .....	138
3.4.3 Solvent IR spectral features .....	139
3.5 Results and Discussion.....	141
3.5.1 DLS B22 MIRIAM analyte diffusion experiments.....	141
3.5.1.1 Experimental development .....	141
3.5.1.1.1 Extrinsically bound analyte removal .....	141
3.5.1.1.2 Solvent evaporation during analyte diffusion.....	142
3.5.1.1.3 Choice of MOF and analyte .....	143
3.5.1.2 Spectral analysis .....	144
3.5.1.3 Diffusion from bulk powder .....	151
3.5.2 CO loss from NOTT-100 DRIFTS experiments .....	155
3.5.2.1 Spectral analysis .....	158
3.5.2.1.1 CO region integration.....	158
3.5.2.1.2 Peak fitting analysis .....	159
3.5.2.1.3 Composite spectral modelling .....	161
3.5.2.1.4 Cu–CO spectral assignment .....	164
3.6 Conclusions and Outlook .....	165
3.7 Experimental.....	167
3.7.1 DLS B22 MIRIAM analyte diffusion experiments.....	167
3.7.2 Bulk solid caffeine desorption experiments .....	169
3.7.3 CO release from NOTT-100 DRIFTS experiments .....	169
3.8 References .....	171
<b>4 Solvent-switchable behaviour of SHF-61 .....</b>	<b>175</b>
4.1 Flexible MOFs.....	175
4.2 Aims & Objectives.....	179
4.3 Results and Discussion.....	180
4.3.1 Approaches to spectral analysis.....	183
4.3.1.1 Peak fitting analysis.....	183

4.3.1.2	Peak integration .....	185
4.3.1.3	Composite spectral modelling .....	187
4.3.2	Desolvation of SHF-61.....	188
4.3.3	Resolvation of SHF-61 <i>o</i> and SHF-61 <i>c</i> .....	195
4.3.3.1	Resolvation of SHF-61 <i>c</i> with DMF .....	196
4.3.3.2	Resolvation of SHF-61 <i>o</i> with DMF .....	200
4.3.3.3	Resolvation of SHF-61 <i>o</i> with CHCl <sub>3</sub> .....	203
4.3.3.4	Resolvation of SHF-61 <i>o</i> with CyP .....	206
4.3.3.5	Comparison of results from resolvation experiments .....	211
4.3.4	Desolvation of resolvated SHF-61 <i>o</i> .....	213
4.3.4.1	Desolvation of SHF-61 <i>o</i> -DMF .....	213
4.3.4.2	Desolvation of SHF-61 <i>o</i> -CHCl <sub>3</sub> .....	216
4.3.4.3	Desolvation of SHF-61 <i>o</i> -CyP .....	219
4.3.4.4	Comparison of results from desolvation of resolvated SHF-61 <i>o</i> experiments .....	222
4.3.5	CO <sub>2</sub> loading in SHF-61 .....	224
4.3.5.1	Spectral analysis by peak fitting .....	225
4.3.5.2	Spectral analysis by peak integration .....	228
4.3.5.3	Spectral analysis by composite modelling .....	229
4.3.5.4	Comparison of results from CO <sub>2</sub> uptake experiments .....	231
4.4	Conclusions and Outlook.....	232
4.5	Experimental .....	234
4.5.1	Synthesis of SHF-61 materials .....	234
4.5.2	B22 MIRIAM experiments.....	235
4.5.3	Spectral analysis .....	237
4.6	References .....	239
<b>5</b>	<b>Concluding remarks.....</b>	<b>241</b>
<b>6</b>	<b>Appendix .....</b>	<b>243</b>

---

# **Chapter 1**

## **Introduction**

---

# 1 Introduction

---

## 1.1 Stimuli-responsive materials

Stimuli-responsive materials can respond to changes in their environment, including, but not limited to: temperature,<sup>1,2</sup> pressure,<sup>3–7</sup> pH<sup>8–10</sup> or light.<sup>11,12</sup> Advances in the area have often focussed on polymers or silica nanoparticles due to their applications in the medical and energy fields.<sup>13–18</sup> However, the capabilities of metal-organic framework-based responsive materials have not been neglected, and have also been extensively reviewed.<sup>19–23</sup>

## 1.2 Structure of metal-organic frameworks

The benefits of MOF-based stimuli-responsive materials lie in the versatility of their construction. MOFs are based on organic bridging ligands (mostly carboxylate, phosphonate or N-donating linkers<sup>24</sup>) and metal ions.<sup>25,26</sup> Interactions between these two components form secondary building units (SBUs), also known as metal nodes, which are able to direct the growth of the framework network by harnessing the preferred coordination number and geometry of the metal ion. Metal nodes primarily form *in situ* during the framework synthesis, and often include bridging groups, such as oxides or cyanides,<sup>27</sup> contributing to the stability and preferred geometry of the metal node. Figure 1.1 shows a variety of SBUs observed in MOFs.

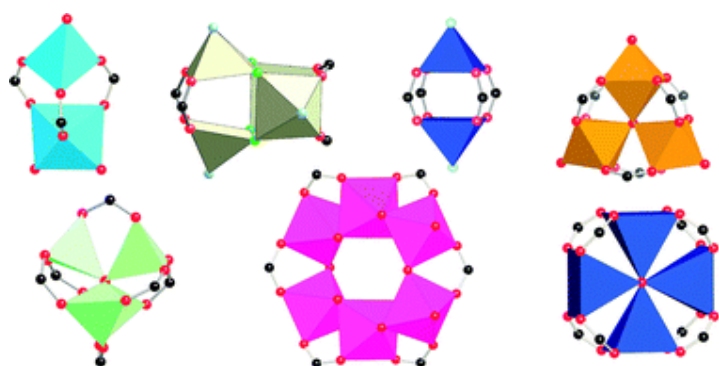


Figure 1.1. Example SBUs demonstrating possible geometries. Black, carbon; red, oxygen; one metal ion at the centre of each polyhedron. Reproduced from reference 27.

Organic linkers in MOFs play an important role in determining pore size and internal surface area,<sup>28</sup> but many other interesting properties of the framework can stem from flexibility,<sup>29,30</sup> functionalisation<sup>31,32</sup> or responsivity of the linker.<sup>31</sup> Linkers are often synthesised prior to MOF synthesis, or functionalised post-synthetically, after the synthesis of the parent MOF.<sup>34,35</sup> Structural motifs formed by combination of linkers and metal nodes are shown below in Figure 1.2.

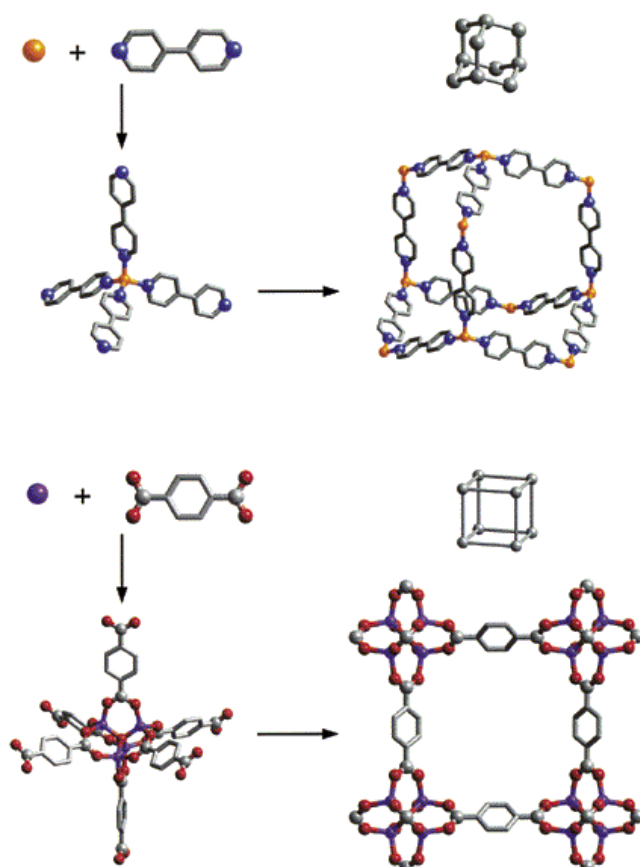


Figure 1.2. Single-crystal structures of MOFs constructed from (top) 4,4'-bipyridine and (bottom) 4,4'-dicarboxylic acid linkers. Adapted from reference 36.

MOFs are ideal candidates for an ‘intelligent design’ approach, as the inclusion of specific metals or linkers can bring desired properties and behaviour into the material.

## 1.3 Control of crystal size

Modulators are agents included to influence the growth of MOF crystals. There are two types of modulator, both with different mechanisms of activity. Binding modulators, such as acetic acid, benzoic acid, trifluoroacetic acid (TFA) and pyridine,<sup>37–40</sup> bind reversibly to the metal node during synthesis, inhibiting coordination sites and slowing the formation of nucleation sites.<sup>38,41</sup> Deprotonation modulators, such as hydrochloric (HCl) acid or triethylamine (NEt<sub>3</sub>),<sup>39,42,43</sup> affect the pH of the reaction solution, influencing the rate of linker deprotonation. A low pH results in slower deprotonation, and hence slower crystal nucleation and the formation of fewer, larger crystals. Conversely, a high pH will favour linker deprotonation, resulting in fast nucleation and the formation of a large number of small crystals. The mechanisms of modulator action are shown in Figure 1.3.

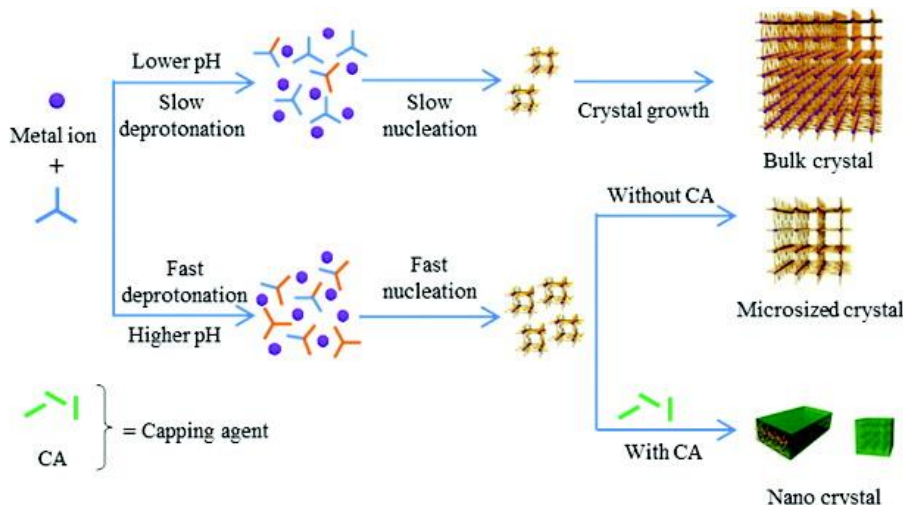


Figure 1.3. Mechanism for modulator action. ‘Lower pH’ and ‘Higher pH’ pathways involve addition of deprotonation modulators (HCl, NEt<sub>3</sub>, etc.) to the reaction mixture. Capping agents are binding modulators (benzoic, salicylic, formic, acetic acids, etc.).

Reproduced from reference 44.

## 1.4 Stimuli-responsive MOFs

As mentioned previously, stimuli-responsive MOFs have been reviewed by co-workers in the field<sup>19–22</sup> as well as by our group.<sup>23,45</sup> The stimuli-responsivity of these materials is associated with the ‘designability’ of the frameworks – specific responses can be anticipated for specific linkers and metal nodes, and this can influence the constituent parts and synthetic conditions used for framework synthesis.

The temperature-induced response of a Eu-based framework, capable of detecting explosives, was reported by Zhu *et al.* in 2015.<sup>1</sup> Luminescence from the Eu<sup>3+</sup> centre was quenched upon detection of explosive molecule 2,4,6-trinitrophenol at concentrations as low as 0.05 mM. The more interesting property of the framework was a low-temperature single-crystal to single-crystal transformation. The framework linker, shown in Figure 1.4, is hexadentate, but one carboxylic acid group remains unbound at room temperature. Upon cooling to -80 °C, the free carboxylic acid group binds to a residual, unreacted Eu<sup>3+</sup> cations that act as guests in the framework pore.

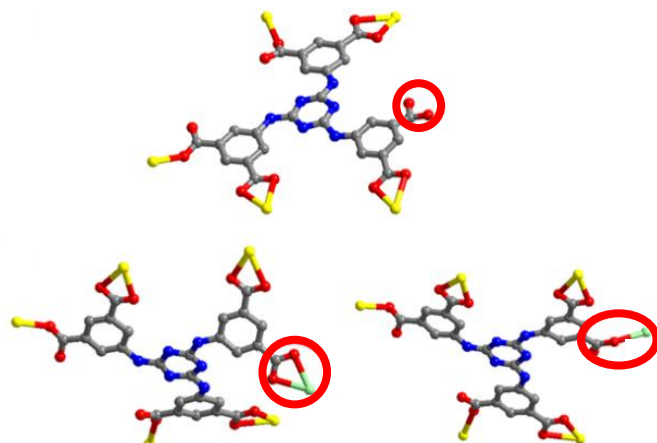


*Figure 1.4. Crystal structures of the framework ligand (5,5',5''-(1,3,5-triazine-2,4,6-triyltriimino)tris-isophthalate hexasodium) at 20 °C (top) and -80 °C (bottom). Structure at 20 °C shows an unbound carboxylate group, which binds to Eu<sup>3+</sup> cations at -80 °C. Temperature-dependent binding environments are circled in red. Adapted from reference 1.*

This cation binding led to an elongation of the pore along the *a*-axis of the unit cell (*a* = 23.8 Å at room temperature and 26.1 Å at -80 °C) and contraction along the *b*-axis (*b* = 24.5 Å at room temperature and 21.6 Å at -80 °C). The deformation of the pore structure upon Eu<sup>3+</sup> binding is shown in Figure 1.5.

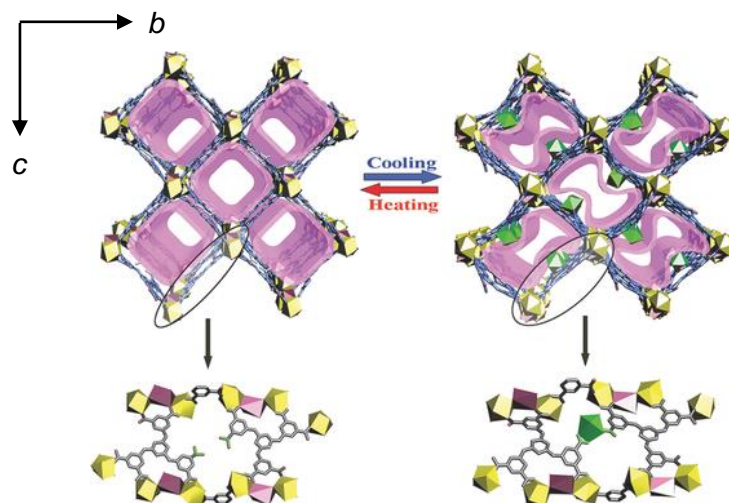


Figure 1.5. SC-SC transformation of the framework between room temperature (left) and low-temperature (right), instigated by Eu<sup>3+</sup> cation binding. Eu<sup>3+</sup> cation is represented by green polyhedral. Reproduced from reference 1.

Nagata *et al.* reported the synthesis of a thermoresponsive MOF–Poly(*N*-isopropylacrylamide) (PNIPAM) polymer composite.<sup>2</sup> UiO-66-NH<sub>2</sub> was post-synthetically modified with PNIPAM through covalent attachment at the NH<sub>2</sub> group, and loaded with caffeine, procainamide and resorufin. The polymer is able to undergo a conformation change and can be switched through ON (open) and OFF (closed) states by lower and higher temperatures respectively, allowing for controlled release of guest molecules, which is illustrated in Figure 1.6.

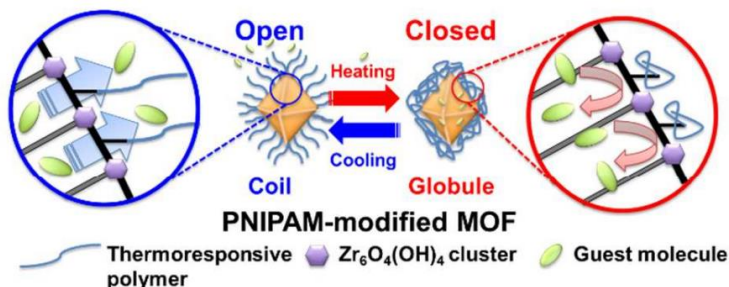
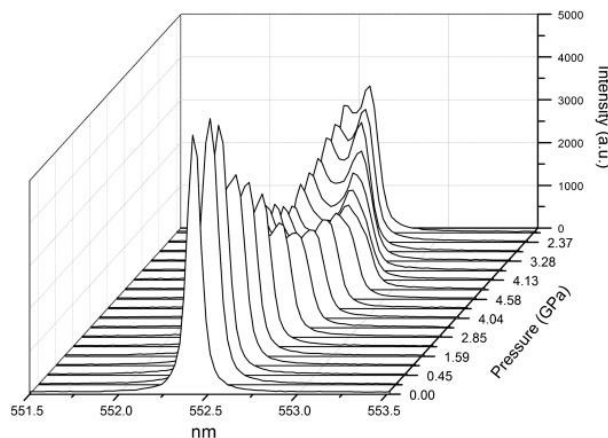


Figure 1.6. Schematic image of controlled release of analytes from MOF–PNIPAM composite. Reproduced from reference 2.

The pressure-stimulated photoluminescence behaviour of a terbium-adipate framework was explored by Spender *et al.* in 2013.<sup>5</sup> Three phase transitions were observed within the 0–4 GPa pressure range, inducing pronounced changes in the emission spectra of the complex. The change in photoluminescence signal is shown below in Figure 1.7.



*Figure 1.7. Evolution of the photoluminescence signal of Tb-GWMOF6 at varying pressures. Reproduced from reference 5.*

The response of MOFs to changes in solvent environment are known phenomena, but are not as widely investigated.<sup>46</sup> A Cu-based framework with a tetrazolate-carboxylate linker (DUT-25), reported by Grünker *et al.*, exhibits sustained solvatochromism of a loaded guest and solvent-stimulated changes in fluorescence emission.<sup>47</sup>

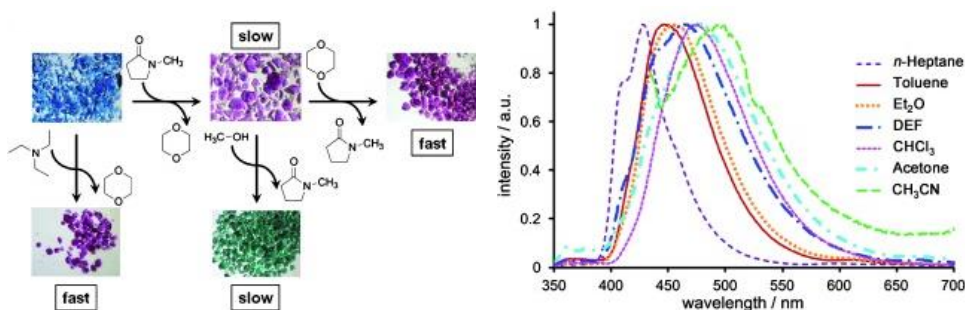


*Figure 1.8. (Left) Illustration of solvent-induced solvatochromism of Nile Blue loaded into DUT-25. Solvatochromism of Nile Blue is affected by acidity, and the exposure of DUT-25-Nile Blue solvents varying in acidity/basicity induced solvatochromic response. (Right) Fluorescence emission spectra of DUT-25 in different solvents. Increasing solvent polarity saw a red shift in  $\lambda_{\text{max}}$ . Adapted from reference 47.*

The sustained solvatochromism observed in Nile Blue-loaded DUT-25 (Figure 1.8, left) lends itself to potential applications as a multifunctional material for the visual detection and removal of undesirable materials. Increasing solvent polarity in the non-guest loaded framework induced a bathochromic shift of the emission maxima, as well as reduced emission intensity due to quenching, as shown in Figure 1.8 (right).

Sumby, Doonan and co-workers reported a Ni-framework with switchable Ni-centre geometry, induced by the solvent environment. The as-synthesised material,  $[\text{Ni}(\text{H}_2\text{diol})]$ , (where  $\text{H}_2\text{diol} = 2,2'\text{-dihydroxybiphenyl-4,4'-dicarboxylic acid}$ ) has an octahedral Ni-node, coordinated to two carboxylate groups in equatorial positions and two DMF molecules in the axial positions. Activation of the material to remove axial solvent molecules results in adoption of a distorted tetrahedral Ni(II) geometry.

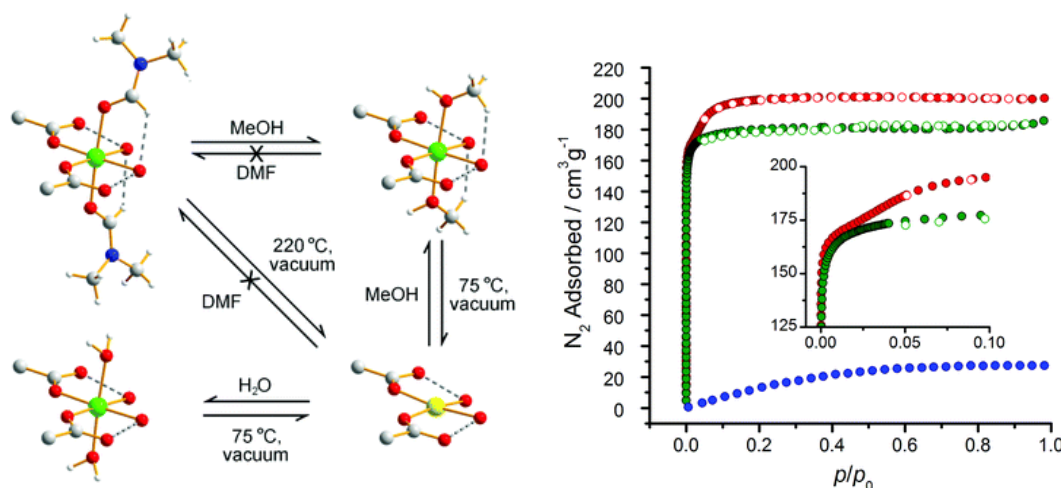


Figure 1.9. (Left) Illustration of the dynamic solvent-responsive behaviour of  $[\text{Ni}(\text{H}_2\text{diol})]$ . (Right)  $\text{N}_2$  adsorption isotherms at 77 K for  $[\text{Ni}(\text{H}_2\text{diol})(\text{DMF})_2]$  (red),  $[\text{Ni}(\text{H}_2\text{diol})(\text{DEF})_2]$  (green) and  $[\text{Ni}(\text{H}_2\text{diol})]$  (blue). Filled and open circles represent adsorption and desorption points, respectively. Adapted from reference 48.

The material was synthesised in DMF or DEF, forming  $[\text{Ni}(\text{H}_2\text{diol})(\text{S})_2] \cdot \text{S}$  (where  $\text{S} = \text{DMF}/\text{DEF}$ ). The activated material  $[\text{Ni}(\text{H}_2\text{diol})]$  was formed by solvent exchange into MeOH and heating for 4 hours under vacuum.

Solvation of the activated form with H<sub>2</sub>O or MeOH vapour leads to coordination of these solvents in the axial positions of the distorted tetrahedral Ni-node, and conversion to the octahedral Ni(II) geometry, as tracked by time-resolved magnetometry. Thermogravimetric analysis (TGA) confirmed that, after submersion of the activated material in DMF for 48 hours, there was no coordination of DMF molecules to the Ni-node (Figure 1.9, left). This phenomenon is yet to be explained.

Significant reduction in N<sub>2</sub> adsorption at 1 bar was observed following activation of the material (Figure 1.9, right). Examination of the crystal structure of the activated material saw the formation of a distorted tetrahedral Ni-node, preventing access to the polar parts of the framework, reducing available N<sub>2</sub> binding sites.

The photodriven response of framework materials is a broad and well-documented subject area, and will be explored further in Section 2.1. A notable example, however, was reported in 2013 by George, Champness and co-workers,<sup>49</sup> where an irreversible photoinduced charge transfer process was instigated in a Cu-based framework with a Re(CO)<sub>3</sub>Cl-functionalised 2,2'-bipyridine linker (Figure 1.10 overleaf).

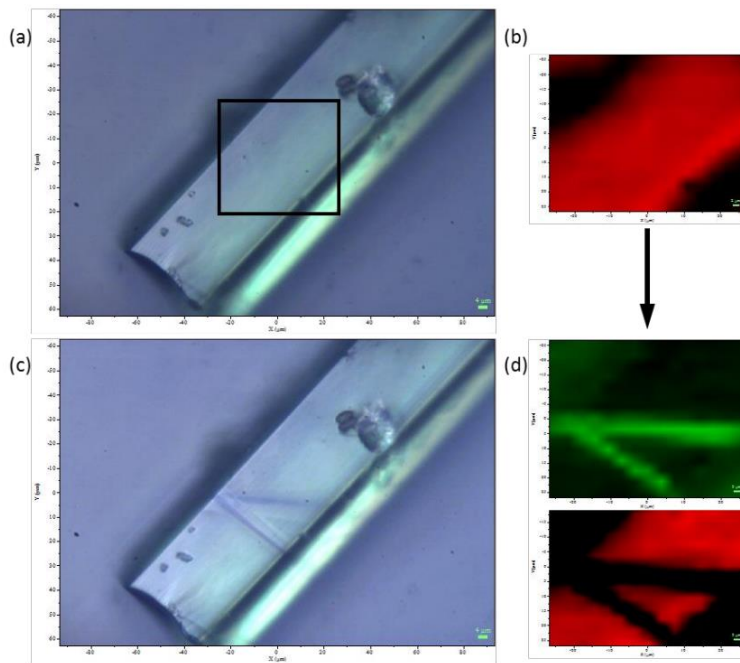


*Figure 1.10. Photolysis and mapping of a single crystal of ReCu. (a) Crystal prior to irradiation, with Raman mapping area indicated in black. (b) Raman mapping, where red corresponds to the presence of the ground state Raman spectrum. (c) The crystal after “writing” and (d) the Raman map indicating presence of (red) ground-state Raman spectrum and (green) photoproduct Raman spectrum. Reproduced from reference 49.*

A 325 nm laser was used to irreversibly “write” on the crystal surfaces, as shown in Figure 1.10(a). Photolysis of the material resulted in excitation of  $\{\text{Re}^{\text{I}}(\text{CO})_3\text{Cl}(\text{bpy})—\text{Cu}^{\text{II}}\}$  to the  $\{\text{Re}^{\text{II}}(\text{CO})_3\text{Cl}(\text{bpy})—\text{Cu}^{\text{I}}\}$  state, observed in Figure 1.10(d) in green.

## 1.5 Post-synthetic modification of MOFs

Post-synthetic modification (PSM) can be used to functionalise and enhance inherent properties of a MOF, or impart altogether new properties, by altering the physical and chemical properties.<sup>50</sup> Approaches to post-synthetic modification types include solvent-assisted ligand exchange (SALE), where a solvent medium is employed to substitute linkers within a MOF.

The pore size of frameworks can be altered using SALE by exchanging longer ligands with a shorter alternative. In 2013, Jeong *et al.* replaced the 4,4-bipyridine (bipy) pillaring ligand in the framework with a shorter 1,4-diazabicyclo[2.2.2]octane (dabco) ligand in a Ni-based framework to reduce the pore size.<sup>51</sup> The decrease in pore size was confirmed by N<sub>2</sub> adsorption isotherms, as shown below in Figure 1.11. By varying the concentration of the exchanging ligands, alternating layers of ligands of bipy and dabco were observed, as well as complete replacement of the bipy ligand with dabco.

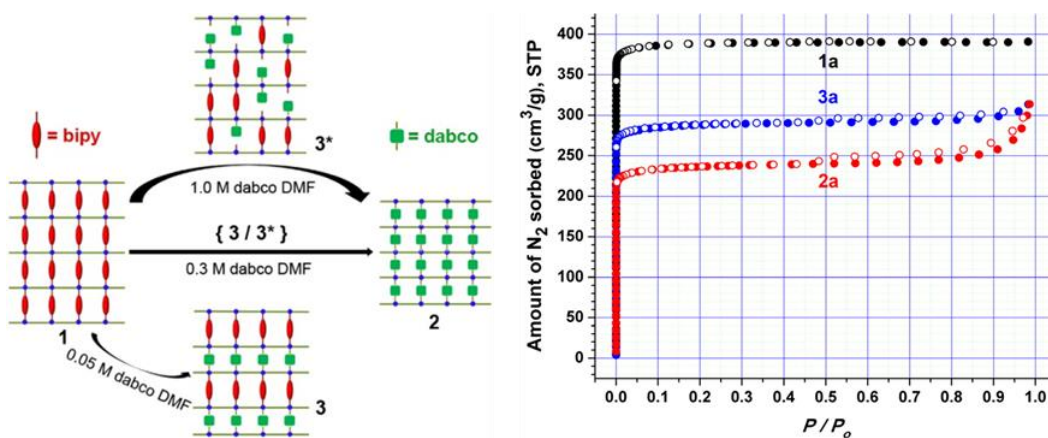


Figure 1.11. (Left) Schematic of SALE from bipy to dabco (2) and dabco and bipy (3). (Right) N<sub>2</sub> adsorption isotherms for different ligand combinations. Taken from reference 51.

An alternative PSM technique involves the modification, but not exchange, of the framework ligand. Forgan and co-workers reported the bromination of unsaturated bonds in the linkers of a Zr-framework.<sup>52</sup> The bromination occurred around the C≡C bond, shown in the linkers of Figure 1.12 overleaf.

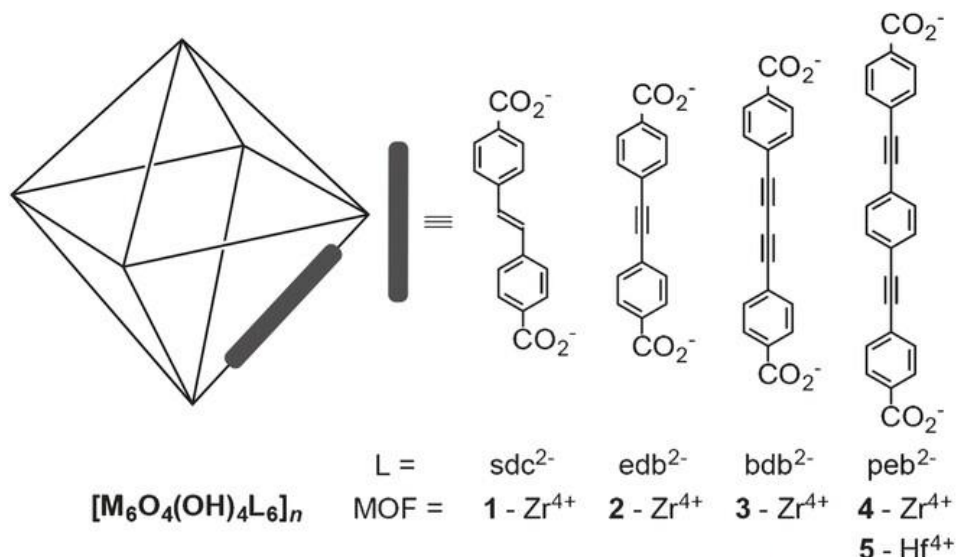


Figure 1.12. Schematic of post-synthetically modified frameworks. Linkers were brominated across the  $C\equiv C$  bond using *N*-bromosuccinimide (NBS) and *N,N'*-diphenylthiourea (DPT). Reproduced from reference 52.

Bromination of the linkers (pictured in Figure 1.12) across the  $C\equiv C$  bond resulted in shortening of the linker, and the unit cell decreased in size. Characterisation of the post-synthetic modification was carried out using  $^{13}C$  NMR and FT-IR to show the change of C-C bond type.

The post-synthetic modification of frameworks has often been employed to introduce additional functionality to the materials. Hatton and co-workers modified Mg-MOF-74 (magnesium 2,5-dihydroxyterephthalate) with tetraethylenepentamine, increasing  $CO_2$  uptake by 3.5 wt%. Increased  $CO_2$  adsorption was attributed to the  $CO_2$  binding sites in the amine functionality.

## 1.6 Specialised experimental methods

A variety of specialised techniques have been employed and developed throughout this thesis. These are described below, with details on the experiment each technique was employed for and where it is discussed within this thesis. Further specific details associated with each technique are given in appropriate sections.

### ***Confocal laser scanning microscopy (CLSM)***

CLSM samples were examined on a Zeiss LSM 880 Airyscan confocal microscope (Zeiss, Germany) under x10, x20, x40 and x63 objectives lens using Zeiss Zen software. Samples were imaged *via* confocal fluorescence and brightfield imaging modalities. Fluorescence was excited at 405 and 633 nm and emission collected at user defined ranges. Samples were optically sectioned through their volume using Nyquist sampling with the confocal pinhole set up 1 Airy unit. Images are presented either as single confocal optical sections or Z-stacks. *In situ* irradiation experiments were carried out using the on-board 405 and 633 nm excitation lasers (15.7 and 5.5 mW output respectively). This technique was used to image dye-modified MOF crystals in Chapter 2, and to irradiate and image MOF-bound photoswitches in the same chapter.

### ***In situ infrared microspectroscopy***

In order to interrogate single crystals, *in situ* IR spectroscopic measurements were carried out on the B22 MIRIAM (Multimode InfraRed Imaging And Microspectroscopy) beamline at the Diamond Light Source on a Bruker Hyperion 3000 microscope and Bruker Vertex spectrometer supplied with broadband infrared radiation from synchrotron source, using a 15x objective and a liquid N<sub>2</sub> controlled MCT (Mercury Cadmium Telluride) detector. Samples were loaded on to a 0.2 x 16 mm CaF<sub>2</sub> or ZnSe window and enclosed within a variable-temperature gas-tight Linkam FTIR600 cell fitted with 0.2 x 22 mm CaF<sub>2</sub> or ZnSe top and bottom windows (Figure 1.13).

The temperature of the Linkam cell body was controlled by water flow. This was to cool the cell body, minimising mechanical temperature drift, or to warm the stage body when cooling the sample to minimise condensation on the cell windows, which would block transmission of the IR beam.

Window material was selected depending on the region of interest required for experiments, due to the differing transmission ranges in the infrared for each material. Glass knife edge apertures were used to define the sample area as either 15 x 15 or 20 x 20 µm, depending on crystal size. Spectra were collected (128 scans) in the range 4000-500 cm<sup>-1</sup> with 4 cm<sup>-1</sup> resolution. CO<sub>2</sub> and N<sub>2</sub> gases were dried through zeolite filters between the gas cylinder and mass flow controllers before reaching the experimental stage.

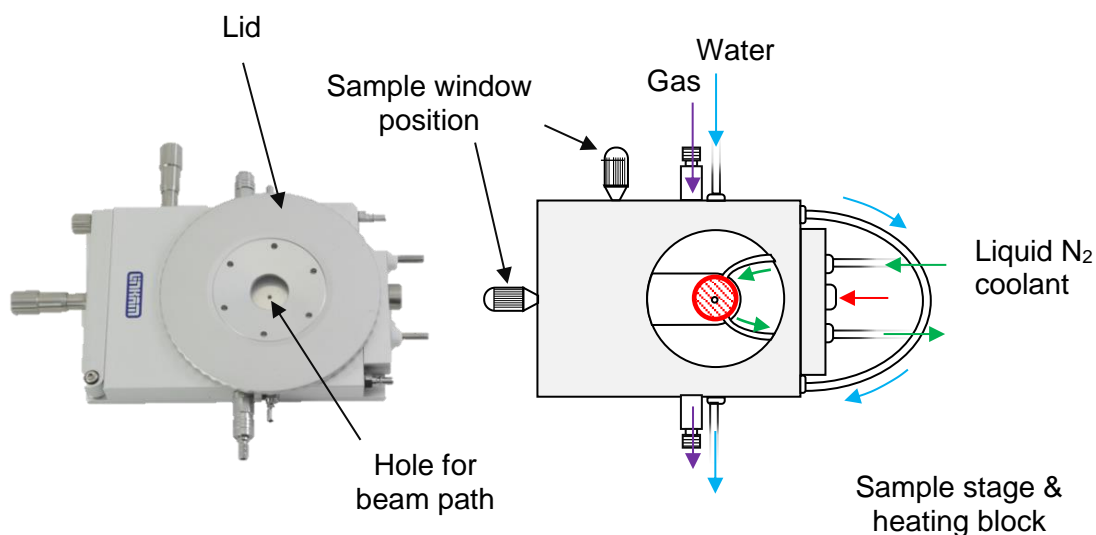


Figure 10.13. (Left) Photograph and (right) schematic of Linkam FTIR600 stage.

This technique was employed in Chapters 3 and 4. In Chapter 3, microspectroscopy was used to track the diffusion of MOF-bound caffeine into surrounding solvent. In Chapter 4, the technique was used to examine the changes in pore structure of a solvent-switchable framework with different guest molecules present.

### ***In situ diffuse reflectance infrared Fourier transform spectroscopy***

*In situ* DRIFTS measurements were undertaken in collaboration with Dr Paul Webb at the University of St Andrews. Measurements were carried out in Sasol laboratories by Dr Webb, using a variable temperature proprietary instrument housed in a N<sub>2</sub>-filled glovebox. Gas lines were connected to the spectrometer to allow control of the sample environment.

### ***Scanning electron microscopy***

Scanning electron microscopy (SEM) images were collected on two instruments. Samples collected using a HITACHI TM3030Plus Tabletop Microscope were prepared on adhesive tape. Alternatively, images were collected using a Tescan MAIA3 field emission gun scanning electron microscope (FEG-SEM). Samples were dry dispersed onto 300 mesh Cu-grid supported holey carbon film. This technique was used in Chapter 2, to determine the optimum growth conditions for MOF single crystals, and to examine the effect of different solvents on crystal damage upon exposure to the SEM vacuum chamber.

### ***UV-visible spectroscopy***

UV-VIS spectra were collected using a modular Ocean Optics Flame-S-UV-VIS-ES spectrometer and DH-mini deuterium-tungsten light source connected *via* fibre optic cables. Irradiation experiments were carried out in a custom-built aluminium sample holder and irradiated with seven 40 mW 390 nm UV LEDs housed in an aluminium holder. This technique was employed in Chapter 2 to examine the solid-state behaviour of MOF-bound photoswitches.

Experimental methods for more generalised techniques are detailed within associated chapters.

## 1.7 Experimental challenges

### ***Infrared band saturation***

Large single crystals are desirable for applications such as single crystal X-ray diffraction, but crystals that are too thick present challenges for infrared (IR) microspectroscopy. Thick crystals prevent the transmission of infrared light and produce spectra with ‘flattened’ or tapered peaks (Figure 1.14), known as *saturation*. The ideal crystal shape to prevent band saturation in synchrotron microspectroscopy are plates with a thickness of ca. 20 µm. Light intensity at the detector is a function of the beam intensity profile and losses in the system and is hence not uniform across the entire IR region. Due to this, saturation in one part of the spectrum is not detrimental to the experiment if the areas of interest are not affected. The beam intensity in specific infrared regions can also be optimised by altering the positions of mirrors which direct the synchrotron infrared beam, as the energy profile of the beam is not spatially uniform.

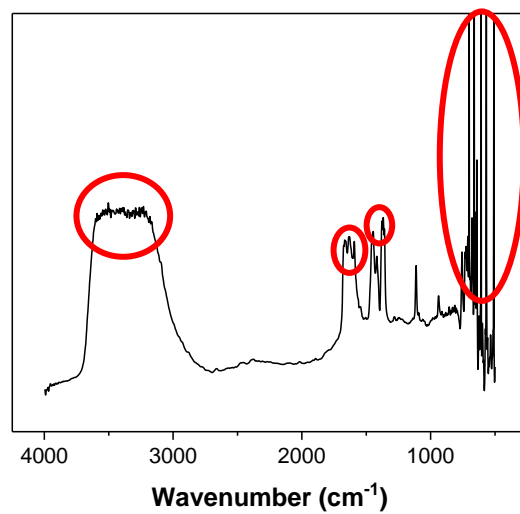


Figure 1.14. Infrared spectrum of HKUST-1. Red circles indicate areas of band saturation.

This necessitated developing a particular approach to sample preparation in Chapters 3 and 4 for *in situ* IR measurements. Samples were initially prepared by deposition of crystals from the first drop of crystal slurry from a glass Pasteur pipette, however these crystals were typically too large and caused band saturation.

Instead, the pipette was allowed to settle for a few seconds, and the first drop returned to the flask, removing the largest crystals. Smaller crystals were transferred to a 10  $\mu\text{L}$  pipette tip by lightly touching the tip to the solvent droplet at the end of the pipette, and surface tension carried the solvent and smaller crystals to the pipette tip. Crystals were then dispensed from the pipette tip to the Linkam cell window.

### **Crystal scattering in infrared**

Crystals that are too small will lead to scattering of IR radiation, resulting in deviation of the light path and less light reaching the instrument detector. Crystals in the region 2-10  $\mu\text{m}$  are most affected by scattering.

This often manifests in a disruption of the spectral baseline (Figure 1.15), often observed as wavelike oscillations, making analysis of spectra less straightforward. This can be overcome by; a) choosing/growing crystals that are large enough not to scatter or; b) decreasing the size of the experimental aperture to smaller than the crystal to avoid scattering off the crystal edges. A smaller aperture results in less light being detected and hence a lower signal:noise (S:N) ratio, so there is a trade-off when measuring smaller crystals using this technique.

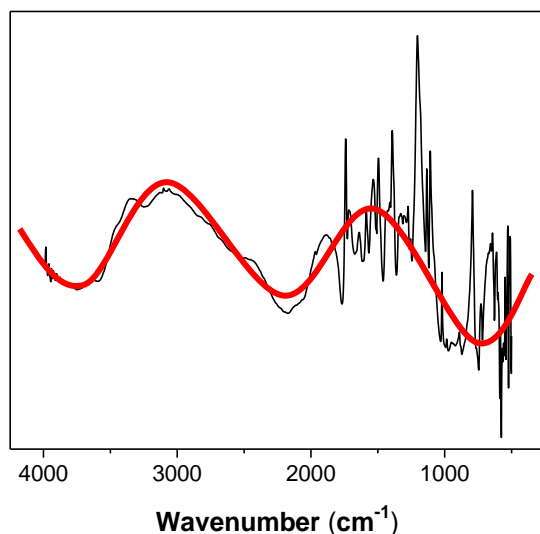


Figure 1.15. Infrared spectrum of  $\text{Sc}_2\text{BDC}_3$ . The red line indicates oscillations in the spectral baseline, arising due to scattering of light around the single crystal sample.

## 1.8        Approaches to spectral analysis

Various approaches to spectral analysis are detailed throughout this thesis, and an introduction to each approach is detailed in the next section. All data has been analysed in OriginPro 2017, unless otherwise stated. Specific details regarding each fitting process are detailed, where appropriate, later in the thesis.

### 1.8.1       Peak fitting analysis

A sample infrared spectrum collected during desolvation experiments is shown in Figure 1.16. Many peaks in the spectrum are overlapped and can be deconvoluted using peak fitting analysis in OriginPro 2017. Overlapped peaks are indicated in red in Figure 1.16.

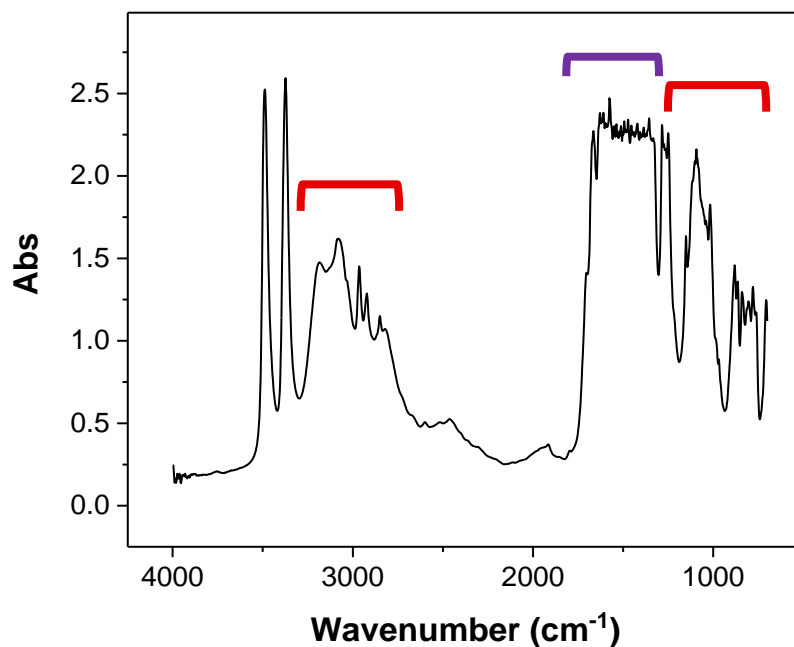


Figure 1.16. Example spectrum of SHF-61-CHCl<sub>3</sub> after desolvation at 120 °C. Regions of overlapped peaks are indicated in red. Regions of saturation are indicated in purple.

Peak fitting analysis deconvolutes overlapped spectral regions, determining the individual contribution of each infrared peak to the overall spectral shape, as shown overleaf in Figure 1.17.

Peaks can be fit to a variety of peak shapes, however only Gaussian and Lorentzian peak shapes are used throughout this thesis, as is customary for infrared peaks.<sup>53–56</sup> The peak shape is determined by visual inspection and identification of the most appropriate shape.

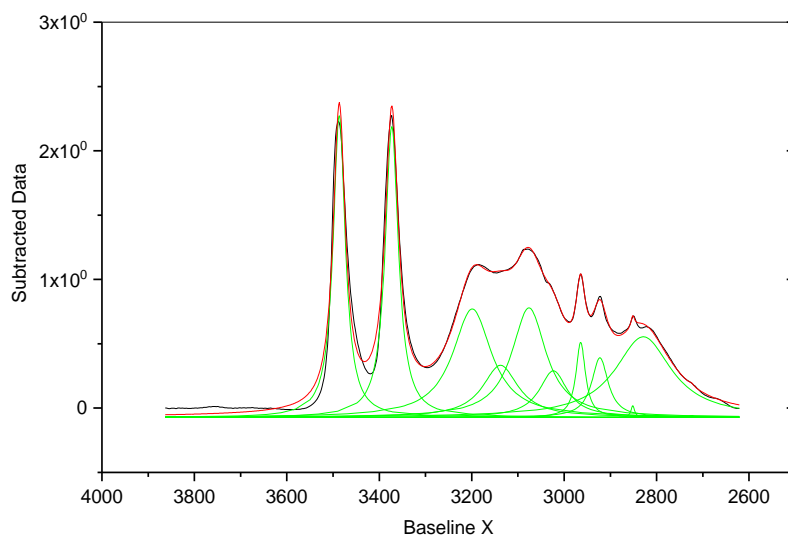


Figure 1.17. Example spectral fits for SHF-61-CHCl<sub>3</sub> at higher energy (top).

Regions of saturation within each spectrum can be masked, meaning that they are omitted from any fitting procedures. Alternatively, areas of the spectrum can be omitted entirely. Baseline correction is applied to the spectrum to combat the effects of an imperfect baseline, often due to small amounts of water present in most samples. Example baseline corrections for a specific spectral region are shown in Figure 1.18.

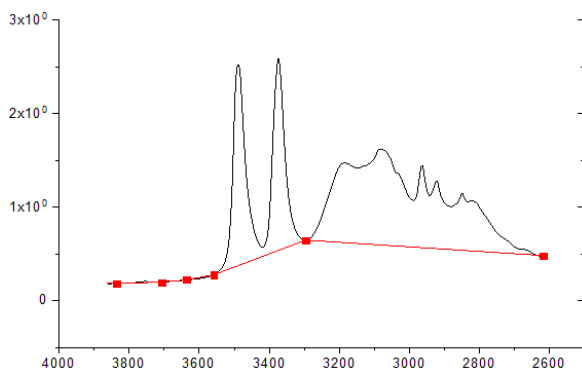


Figure 1.18. Example baseline corrections for SHF-61-CHCl<sub>3</sub>.

Baseline subtractions were deliberately kept simple to minimise the risk of inadvertently removing information or adding false data. Following baseline subtraction and selecting initial peak positions, peak fit properties (peak position, areas, width, etc.) are refined using a least-squares regression until convergence. If fits fail to converge, peak properties are fixed at specific values and consequently not used further for analysis of spectral change.

## 1.8.2 Peak integration

Peak integration is employed when failure to converge during peak fitting analysis was not solved by fixing peak properties. Peak integration provided the integral of the peak, but no peak positions, and hence is potentially less informative than peak fitting analysis. Figure 1.19 shows an example IR spectrum where peak integration was employed, focussing on solvent bands, collected during the CyP-resolvation of SHF-61 o.

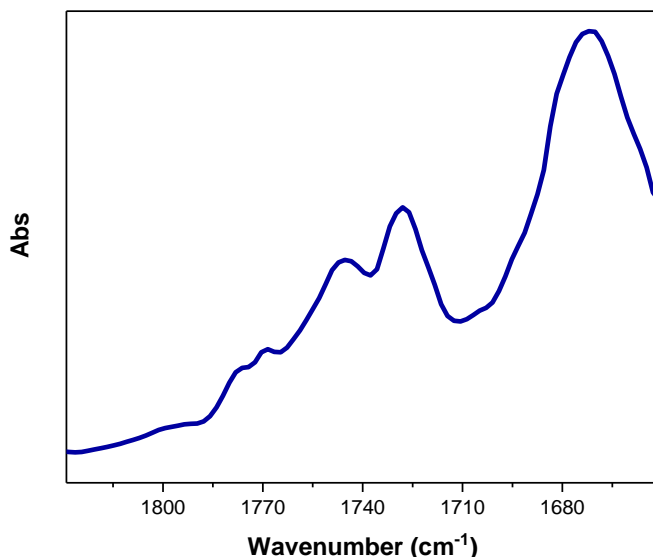


Figure 1.19. Infrared spectra collected during CyP-resolvation of SHF-61o, focussed on CyP carbonyl band region.

Figure 1.20 shows an example of the baseline correction applied during peak integration of the CyP bands resolvation of SHF-61o. Baseline positions are user-selected, but shifting baselines can complicate the choice of baseline positions. If this problem arises, straight line, constant, or no baseline can be applied.

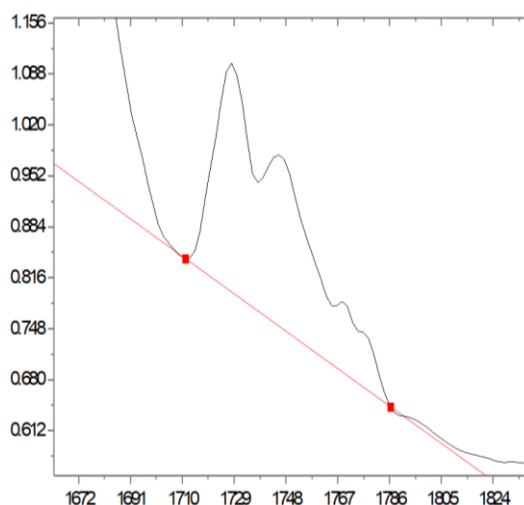


Figure 1.20. Baseline applied to integration process of CyP carbonyl bands during resolvation of SHF-61o with CyP.

Following baseline subtraction, integration boundaries were selected and the peak integral was calculated.

### 1.8.3 Composite spectral modelling

Composite spectrum modelling in OriginPro 2017 fits infrared spectra to multiple spectral models. The process reports the composition of a given spectrum as a sum of model spectra input by the user. It identifies the best fit percentage of each model spectrum and the residual spectral profile *via* a least-squares approach.

Model spectra are selected from key states identified during each experiment, which are identified by the user as likely components of any given IR spectrum. Spectral composition values are then generated, which can be plotted against time to give plots indicating the percentage composition of a spectrum as a sum of model spectra at any time point during the spectral series. An example spectral composition plot is shown in Figure 1.21.

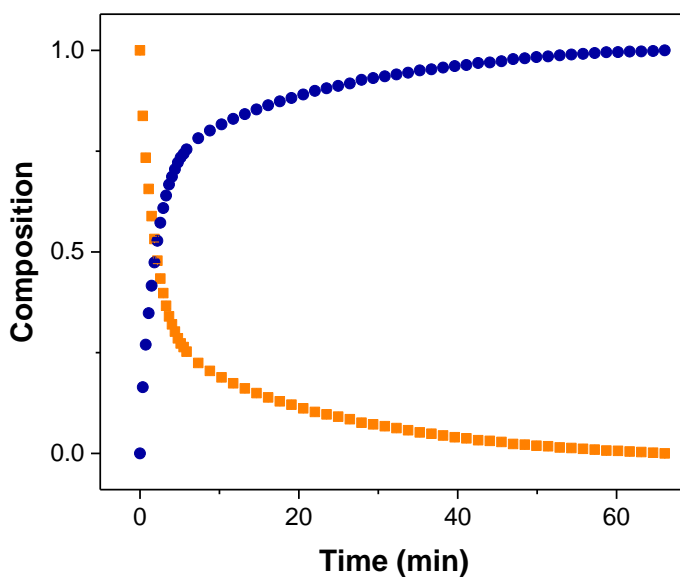


Figure 1.21. Example spectral composition plot of CO-loaded (orange) and unloaded (blue) NOTT-100 during -75 °C CO desorption experiments.

Although composite spectral modelling is an ideal approach to map the progression from one state to another, it does not identify any individual peaks

in the IR spectrum, or assign any parts of the spectrum to specific vibrations or interactions within the crystal. Additional errors in spectral interpretation are introduced if the model spectra are not ideal, *e.g.* models representing the beginning and end of a process may not be the definitive beginning and end of the process. Instances where this is a problem are noted throughout the thesis, where appropriate.

## 1.9 Scope of this thesis

This thesis examines the effect of different stimuli on various metal-organic frameworks, and how this affects guest diffusion processes within the framework pores.

The first results chapter (Chapter 2) discusses the post-synthetic modification of size-optimised MOF crystals with fluorescent dye molecules. Optical spectroscopy and microscopy were employed to track guest distribution, and the solid-state photolysis of photoswitch-modified materials was investigated.

In Chapter 3, the diffusion of two therapeutic guest agents from MOFs tracked by IR spectroscopies is detailed. The chapter investigates the diffusion of a small gaseous therapeutic agent and a large pharmaceutical molecule, the latter of which is induced by the addition of solvent to the sample. A brief introduction into the use of MOFs as drug delivery systems (DDSs) is given at the beginning of Chapter 3.

The final results chapter (Chapter 4) examines the response of a framework with a solvent-switchable pore structure. The new methods described in Chapter 3 have been developed further to study these structurally responsive crystals. Desolvation, resolvation and CO<sub>2</sub> uptake experiments are carried out, using IR microspectroscopy to track the changing solvent content and framework structures present throughout the experiments.

Several reproducible novel methods have been developed to track the diffusion of guest molecules through frameworks, with and without external stimuli. These methods are applicable to future studies in the field.

## 1.10 References

- 1 M. Zhu, X.-Z. Song, S.-Y. Song, S.-N. Zhao, X. Meng, L.-L. Wu, C. Wang and H.-J. Zhang, *Adv. Sci.*, 2015, **2**, 1500012.
- 2 S. Nagata, K. Kokado and K. Sada, *Chem. Commun.*, 2015, **51**, 8614–7.
- 3 E. C. Spencer, R. J. Angel, N. L. Ross, B. E. Hanson and J. A. K. Howard, *J. Am. Chem. Soc.*, 2009, **131**, 4022–6.
- 4 S. C. McKellar, J. Sotelo, A. Greenaway, J. P. S. Mowat, O. Kvam, C. A. Morrison, P. A. Wright and S. A. Moggach, *Chem. Mater.*, 2016, **28**, 466–473.
- 5 E. C. Spencer, J. Zhao, N. L. Ross, M. B. Andrews, R. G. Surbella and C. L. Cahill, *J. Solid State Chem.*, 2013, **202**, 99–104.
- 6 Z. Su, Y.-R. Miao, G. Zhang, J. T. Miller and K. S. Suslick, *Chem. Sci.*, 2017, **8**, 8004–8011.
- 7 A. U. Ortiz, A. Boutin, K. J. Gagnon, A. Clearfield and F.-X. Coudert, *J. Am. Chem. Soc.*, 2014, **136**, 11540–5.
- 8 E. Khodaverdi, H. A. Soleimani, F. Mohammadpour and F. Hadizadeh, *Chem. Biol. Drug Des.*, 2016, **87**, 849–857.
- 9 A. Madaan, P. Singh, A. Awasthi, R. Verma, A. T. Singh, M. Jaggi, S. K. Mishra, S. Kulkarni and H. Kulkarni, *Clin. Transl. Oncol.*, 2013, **15**, 26–32.
- 10 V. K. Seiler, K. Callebaut, K. Robeyns, N. Tumanov, J. Wouters, B. Champagne and T. Leyssens, *CrystEngComm*, 2018, **20**, 3318–3327.
- 11 A. B. Kanj, K. Müller and L. Heinke, *Macromol. Rapid Commun.*, 2017, **39**, 1700239.
- 12 A. Saad, O. Oms, J. Marrot, A. Dolbecq, K. Hakouk, H. El Bekkachi, S. Jobic, P. Deniard, R. Dessapt, D. Garrot, K. Boukheddaden, R. Liu, G. Zhang, B. Keita and P. Mialane, *J. Mater. Chem. C*, 2014, **2**, 4748–4758.
- 13 D. Roy, J. N. Cambre and B. S. Sumerlin, *Prog. Polym. Sci.*, 2010, **35**, 278–301.
- 14 M. Nakahata, Y. Takashima, H. Yamaguchi and A. Harada, *Nat. Commun.*, 2011, **2**, 511.
- 15 M. Wei, Y. Gao, X. Li and M. J. Serpe, *Polym. Chem.*, 2017, **8**, 127–143.
- 16 R. T. Shafranek, S. C. Millik, P. T. Smith, C.-U. Lee, A. J. Boydston and A. Nelson, *Prog. Polym. Sci.*, 2019, **93**, 36–67.
- 17 S. Giri, B. G. Trewyn, M. P. Stellmaker and V. S.-Y. Lin, *Angew. Chemie Int. Ed.*, 2005, **44**, 5038–5044.
- 18 S. Mura, J. Nicolas and P. Couvreur, *Nat. Mater.*, 2013, **12**, 991–1003.
- 19 L. Wang, M. Zheng and Z. Xie, *J. Mater. Chem. B*, 2018, **6**, 707–717.

- 20 K. Yang, G. Zhou and Q. Xu, *RSC Adv.*, 2016, **6**, 37506–37514.
- 21 F. X. Coudert, *Chem. Mater.*, 2015, **27**, 1905–1916.
- 22 S. Castellanos, F. Kapteijn and J. Gascon, *CrystEngComm*, 2016, **18**, 4006–4012.
- 23 C. L. Jones, A. J. Tansell and T. L. Easun, *J. Mater. Chem. A*, 2016, **4**, 6714–6723.
- 24 T. Devic and C. Serre, *Chem. Soc. Rev.*, 2014, **43**, 6097–6115.
- 25 H.-C. “Joe” Zhou and S. Kitagawa, *Chem. Soc. Rev.*, 2014, **43**, 5415–5418.
- 26 T. L. Easun and A. C. Nevin, in *Organometallic Chemistry: Volume 42*, eds. N. J. Patmore and P. I. P. Elliot, The Royal Society of Chemistry, 2018, 54–79.
- 27 D. J. Tranchemontagne, J. L. Mendoza-Cortés, M. O’Keeffe and O. M. Yaghi, *Chem. Soc. Rev.*, 2009, **38**, 1257.
- 28 D. Zhao, D. J. Timmons, D. Yuan and H.-C. Zhou, *Acc. Chem. Res.*, 2011, **44**, 123–133.
- 29 E. J. Carrington, C. A. McAnally, A. J. Fletcher, S. P. Thompson, M. Warren and L. Brammer, *Nat. Chem.*, 2017, **9**, 882–889.
- 30 C. L. Jones, E. A. Marsden, A. C. Nevin, B. M. Kariuki, M. M. Bhadbhade, A. D. Martin and T. L. Easun, *R. Soc. Open Sci.*, 2017, **4**, 171064.
- 31 F. Carson, E. Martínez-Castro, R. Marcos, G. G. Miera, K. Jansson, X. Zou and B. Martín-Matute, *Chem. Commun.*, 2015, **51**, 10864–10867.
- 32 L. Wu, W. Wang, R. Liu, G. Wu and H. Chen, *R. Soc. Open Sci.*, 2018, **5**, 181378.
- 33 T. L. Easun, J. Jia, J. A. Calladine, D. L. Blackmore, C. S. Stapleton, K. Q. Vuong, N. R. Champness and M. W. George, *Inorg. Chem.*, 2014, **53**, 2606–2612.
- 34 A. Modrow, D. Zargarani, R. Herges and N. Stock, *Dalton Trans.*, 2012, **41**, 8690–8696.
- 35 W.-M. Liao, J.-H. Zhang, Z. Wang, S.-Y. Yin, M. Pan, H.-P. Wang and C.-Y. Su, *J. Mater. Chem. A*, 2018, **6**, 11337–11345.
- 36 Mohamed Eddaoudi, David B. Moler, Hailian Li, Banglin Chen, Theresa M. Reineke, Michael O’Keeffe and Omar M. Yaghi, *Acc. Chem. Res.*, 2001, **34**, 319–330.
- 37 M. H. Rosnes, F. S. Nesse, M. Opitz and P. D. C. Dietzel, *Microporous Mesoporous Mater.*, 2019, **275**, 207–213.
- 38 T. Tsuruoka, S. Furukawa, Y. Takashima, K. Yoshida, S. Isoda and S. Kitagawa, *Angew. Chemie Int. Ed.*, 2009, **48**, 4739–4743.

- 39 F. Vermoortele, B. Bueken, G. Le Bars, B. Van de Voorde, M. Vandichel, K. Houthoofd, A. Vimont, M. Daturi, M. Waroquier, V. Van Speybroeck, C. Kirschhock and D. E. De Vos, *J. Am. Chem. Soc.*, 2013, **135**, 11465–11468.
- 40 M.-H. Pham, G.-T. Vuong, F.-G. Fontaine and T.-O. Do, *Cryst. Growth Des.*, 2012, **12**, 3091–3095.
- 41 S. Diring, S. Furukawa, Y. Takashima, T. Tsuruoka and S. Kitagawa, *Chem. Mater.*, 2010, **22**, 4531–4538.
- 42 X. Lin, I. Telepeni, A. J. Blake, A. Dailly, C. M. Brown, J. M. Simmons, M. Zoppi, G. S. Walker, K. M. Thomas, T. J. Mays, P. Hubberstey, N. R. Champness and M. Schröder, *J. Am. Chem. Soc.*, 2009, **131**, 2159–71.
- 43 D. J. Tranchemontagne, J. R. Hunt and O. M. Yaghi, *Tetrahedron*, 2008, **64**, 8553–8557.
- 44 H. Guo, Y. Zhu, S. Wang, S. Su, L. Zhou and H. Zhang, *Chem. Mater.*, 2012, **24**, 444–450.
- 45 A. J. Tansell, C. L. Jones and T. L. Easun, *Chem. Cent. J.*, 2017, **11**, 100.
- 46 M. Wriedt, A. A. Yakovenko, G. J. Halder, A. V. Prosvirin, K. R. Dunbar and H.-C. Zhou, *J. Am. Chem. Soc.*, 2013, **135**, 4040–4050.
- 47 R. Grünker, V. Bon, A. Heerwig, N. Klein, P. Müller, U. Stoeck, I. A. Baburin, U. Mueller, I. Senkovska and S. Kaskel, *Chem. - A Eur. J.*, 2012, **18**, 13299–13303.
- 48 T. D. Keene, D. Rankine, J. D. Evans, P. D. Sounthor, C. J. Kepert, J. B. Aitken, C. J. Sumby and C. J. Doonan, *Dalton Trans.*, 2013, **42**, 7871.
- 49 T. L. Easun, J. Jia, T. J. Reade, X.-Z. Sun, E. S. Davies, A. J. Blake, M. W. George and N. R. Champness, *Chem. Sci.*, 2014, **5**, 539–544.
- 50 C. Janiak and J. K. Vieth, *New J. Chem.*, 2010, **34**, 2366.
- 51 S. Jeong, D. Kim, X. Song, M. Choi, N. Park and M. S. Lah, *Chem. Mater.*, 2013, **25**, 1047–1054.
- 52 R. J. Marshall, S. L. Griffin, C. Wilson and R. S. Forgan, *Chem. - A Eur. J.*, 2016, **22**, 4870–4877.
- 53 L. Chen and M. Garland, *Appl. Spectrosc.*, 2003, **57**, 323–330.
- 54 S. A. Kirillov, in *Novel Approaches to the Structure and Dynamics of Liquids: Experiments, Theories and Simulations*, Springer Netherlands, Dordrecht, 2004, pp. 193–227.
- 55 J. T. Reilly, J. M. Walsh, M. L. Greenfield and M. D. Donohue, *Spectrochim. Acta Part A Mol. Spectrosc.*, 1992, **48**, 1459–1479.
- 56 H. Keles, A. Naylor, F. Clegg and C. Sammon, *Analyst*, 2014, **139**, 2355–2369.

---

# **Chapter 2**

**Tracking fluorescent guests in  
metal-organic frameworks**

---

## Tracking fluorescent guests in metal-organic frameworks

---

### 2.1 MOFs as hosts for mobile guests

The impressive adsorption properties and host-guest chemistry in MOFs has been highlighted and extensively reviewed within the scientific community.<sup>1–4</sup> Due to the large pore volume of most frameworks, guest molecules can undergo subsequent reactions whilst hosted in the pore, including photoinduced polymerisation,<sup>5</sup> hydrogen gas production<sup>6</sup> and the treatment of chemical warfare agents.<sup>7–9</sup> The mobility of pore-bound guest molecules is a key feature of the interesting behaviour often observed in guest-loaded frameworks.

#### 2.1.1 Tracking fluorescent guests in MOFs

The uptake and tracking of fluorescent guest molecules in MOFs has provided deeper understanding of mechanisms of guests diffusion within frameworks, and has also identified predominant factors that affect diffusion. Confocal laser scanning microscopy (CLSM) is often employed as it provides spatially-resolved maps of fluorescent guest distribution within single crystals.<sup>10–12</sup>

Han *et al.* highlighted the chromatographic separation capabilities of MOFs in 2010, where charged dyes Pyronin Y (red, 3 mM) and Azure A (green, 3 mM) were adsorbed by single crystals of MOF-5.<sup>13</sup> Figure 2.1 shows two methods of dye loading into the framework. Interestingly, DMF was used to prevent damage to MOF-5 crystals, as alternative solvents (DCM, H<sub>2</sub>O, MeCN, MeOH and THF) caused substantial cracking, due to the protic nature and/or volatility of the solvents. Solvent-induced crystal damage is explored in Section 2.3.2.2 on pp.43 later in this thesis.

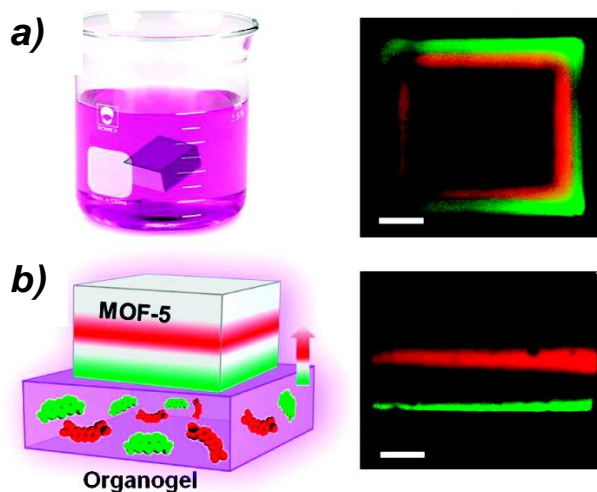


*Figure 2.11. (a) Schematic drawing of a MOF-5 crystal in a solution of mixed dyes. The image on the right shows a fluorescence confocal microscopy cross-section images of the crystal. (b) Representation of MOF-5 crystal placed onto an organogel, presoaked in the DMF dye solution. The corresponding side-on confocal microscopy image illustrates the separation of the dyes into two distinct bands. All scale bars represent 200  $\mu\text{m}$ . Adapted from reference 13.*

In method (a), crystals were submersed in a DMF dye solution, and uptake of dye was observed from crystal faces. In method (b), crystals were placed onto an organogel pre-soaked in DMF dye solution. CLSM images confirmed that both approaches to dye adsorption demonstrated the enhanced mobility of Pyronin 3 through the framework compared to Azure A, since the red fluorescence from Pyronin 3 is observed further into the crystal. Approach (b) was more akin to thin-layer chromatography, since the dye solutions diffuse into the MOF from only one side. The authors deemed dye size, diffusive and capillary transport mechanisms and the non-covalent interactions between dye molecules and the framework to be the main factors affecting the rate of transport.

Another notable study in this field is the post-synthetic modification of HKUST-1 by Kitagawa and co-workers.<sup>14</sup> A BODIPY-based dye was anchored to the surface of the material through a solvent-assisted ligand exchange reaction, in MeOH for 20 hr at 60 °C. Figure 2.2 shows CLSM images of the BODIPY-modified material, where modification has been restricted to the surface of the framework due to size exclusion from the framework pores. Modification was clearly seen along the octahedral morphology of the crystal.

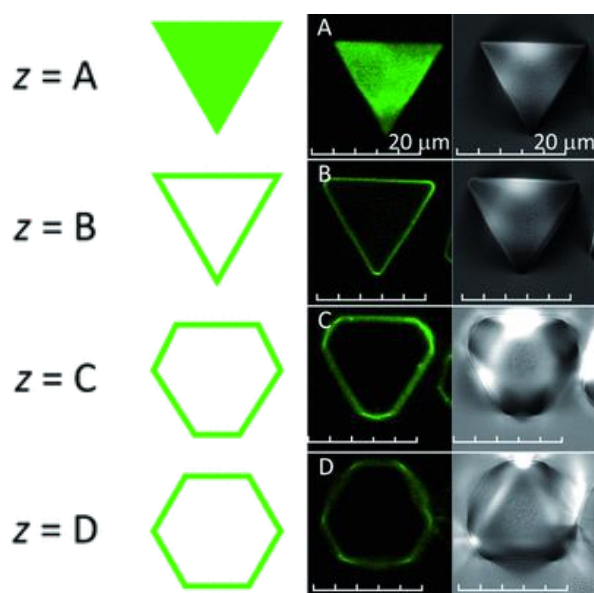


Figure 2.2 (Left) Representations of BODIPY-dye surface-modified HKUST-1, (middle) CLSM images, and (right) transmission images of dye-modified HKUST-1 at  $z = A-D$ . The sequential Z-stack slicing from the bottom of crystal ( $z = A$ ) to the middle of crystal ( $z = D$ ) reveal the octahedral crystal morphology of the framework. Adapted from reference 14.

### 2.1.2 Spirooxazine molecular switches

Spirooxazines are a class of compounds susceptible to stimuli-induced isomerisation. The equilibrium of isomers in these materials is affected by light, temperature, pH and solvent polarity,<sup>15–19</sup> making them a versatile and valuable molecular switch. Cleavage of the C–O bond (highlighted in red in Figure 2.3) instigates opening of the closed-form, spirooxazine (**SPO**) to open-form, planar merocyanine (**MCN**). The increase in structural conjugation (Figure 2.3) throughout the molecule leads to a highly coloured appearance due to strong absorption of visible light, shown in Figure 2.4.

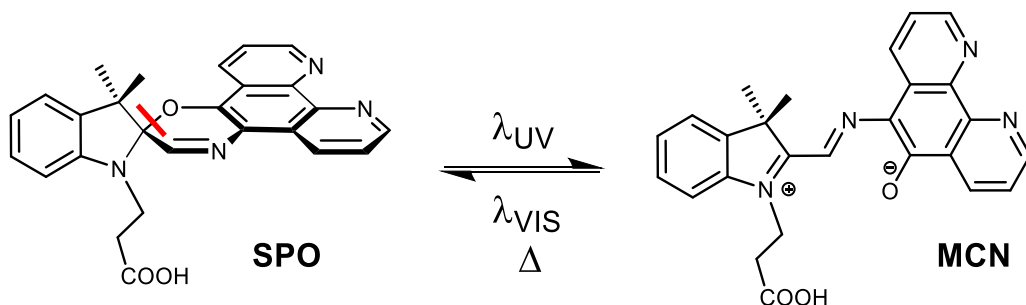


Figure 2.3. Closed-form **SPO** and open-form **MCN**.

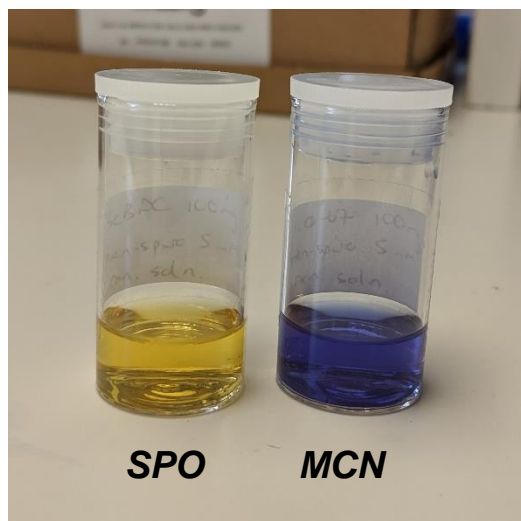
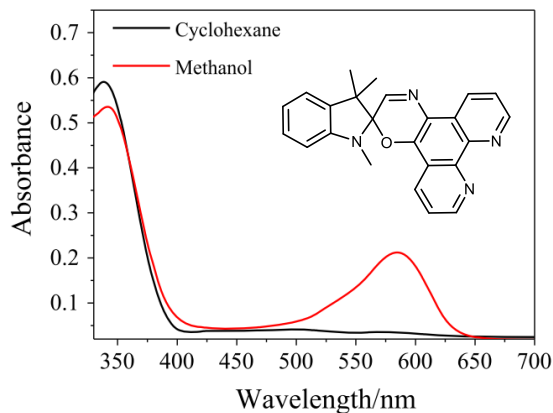


Figure 2.4. Solutions of the spirooxazine shown in Figure 2.3, both in MeOH.

The UV-VIS absorption spectra of **SPO** and **MCN** forms differ vastly. The effect of solvents on this equilibrium was investigated by Ji *et al.*, and Figure 2.5 shows spectra of the inset spirooxazine in cyclohexane and MeOH.<sup>20</sup> The spectrum of the MeOH solution showed a distinct band at ca. 550–650 nm, indicative of the open-form **MCN**. This shift in equilibrium, generating more **MCN** form, was attributed to the increased polarity of MeOH relative to cyclohexane.



*Figure 2.12. UV-VIS absorption spectrum of spirooxazine (inset) in indicated solvents. Reproduced from reference 20.*

The capabilities of spirooxazine as photoswitches has been explored previously, where they have been used in photochromic lenses.<sup>21</sup> Their photoswitchability was examined by Micheau and co-workers in 2007, where the UV-irradiation of a spirooxazine (inset in Figure 2.6) resulted in a significant increase in **MCN** form.<sup>19</sup>

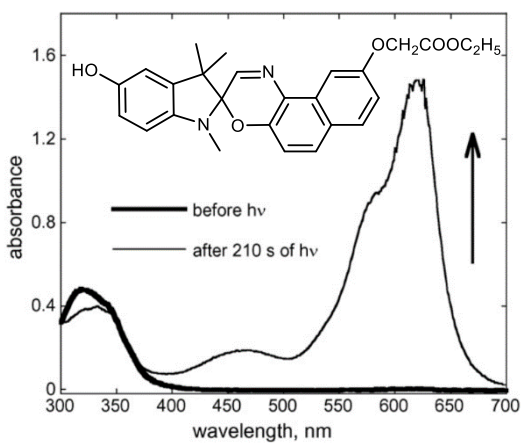


*Figure 2.13. UV-VIS absorption spectra of spirooxazine (pictured) in MeOD at 243 K, before and after 210 s irradiation at  $\lambda = 313$  nm. Reproduced from reference 19.*

### 2.1.3 Photoswitches in MOFs

Spiropyrans are structurally related to spirooxazines, and although they lack the nitrogen atom near the spiro-centre (the position of which is indicated in red in Figure 2.7), they exhibit similar properties. The spiropyran shown in Figure 2.7 was incorporated into Zr-based MOF-808 by D'Alessandro and co-workers, where compound **P** was grafted to the surface, followed by a condensation reaction to form MOF-bound **SP<sub>c</sub>**.

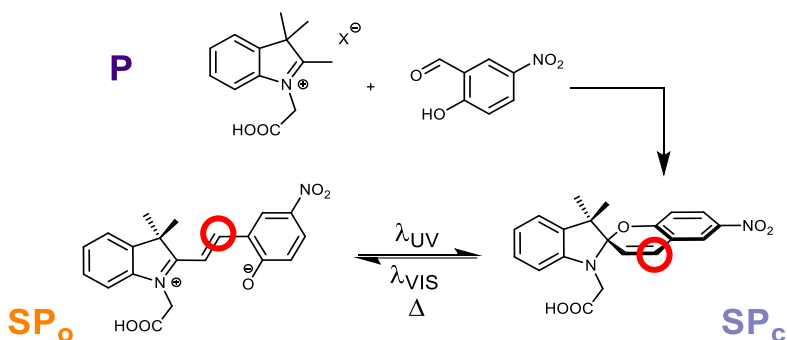


Figure 2.14. Reaction scheme for synthesis of nitro-functionalised spiropyran in reference 22.

Irradiation of MOF-808-**SP<sub>c</sub>** at 254 nm for 30 minutes formed the open-form **SP<sub>o</sub>**, which was confirmed by UV-VIS. Ar and CO<sub>2</sub> isotherms of MOF-808-**P**, MOF-808-**SP<sub>c</sub>** and MOF-808-**SP<sub>o</sub>** are shown in Figure 2.8.

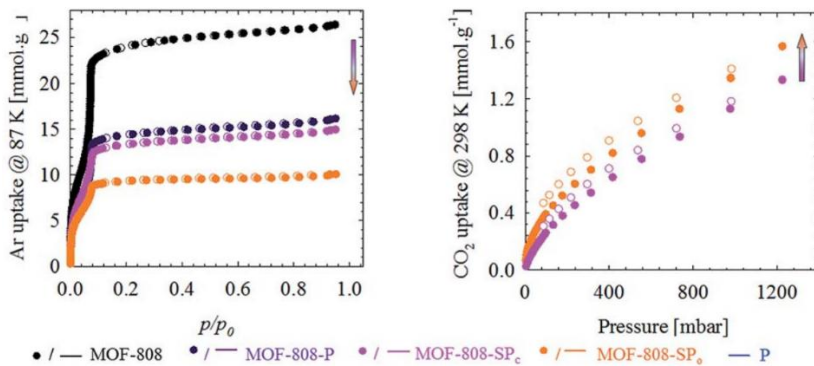


Figure 2.15. (Left) Ar adsorption (filled) and desorption (open) isotherms for indicated materials. (Right) CO<sub>2</sub> adsorption (filled) and desorption (open) isotherms for MOF-808-SP<sub>c</sub> and MOF-808-SP<sub>o</sub>. Reproduced from reference 22.

Reduced Ar uptake was observed following modification in all cases, but additional reduced uptake was observed following irradiation of **SP<sub>c</sub>** to form **SP<sub>o</sub>**, suggesting the larger **SP<sub>o</sub>** form affected the adsorption properties of the material.

Increased CO<sub>2</sub> uptake was observed following irradiation, likely due to the increase in strong CO<sub>2</sub> binding sites available in the charged **SP<sub>0</sub>** form.

Azobenzenes are another photoswitching group that have been shown to significantly impact the uptake properties of frameworks.<sup>23–28</sup> Lyndon, Hill and co-workers reported the synthesis of a framework with two photoisomerisable linkers, Zn(AzDC)(4,4'-BPE)<sub>0.5</sub> (where AzDC = azobenzene-4,4'-dicarboxylic acid and 4,4'-BPE = *trans*-1,2-bis(4-pyridyl)ethylene) which demonstrated significant differences in CO<sub>2</sub> uptake upon irradiation. Figure 2.9 shows the immediate and reversible reduction in uptake upon irradiation with 200–500 nm light.

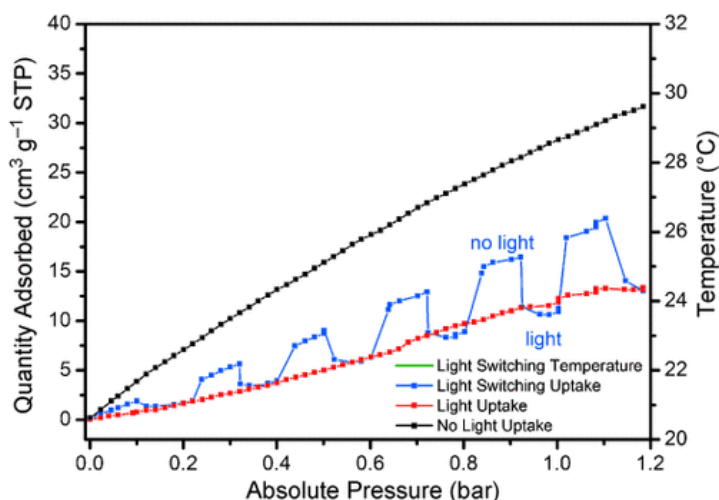


Figure 2.16. CO<sub>2</sub> adsorption isotherms of Zn(AzDC)(4,4'-BPE)<sub>0.5</sub> at 303 K. Light intensity was fixed at 24.6 W cm<sup>-2</sup> in the wavelength range of 200–500 nm. Adapted from reference 29.

The proven ability for MOF-incorporated photoswitches to impact guest uptake forms the basis for our study into the selective uptake and release of a variety of guest molecules.

## 2.2 Aims and Objectives

This chapter describes the post-synthetic modification of MOFs with coordinating fluorescent dyes and photoswitches. There are two main challenges in these experiments; primarily synthetic, but associated with this, the development of a methodology for post-synthetic modification with limited precedent in the scientific literature. Optical absorption spectroscopy and fluorescence microscopy have been employed throughout the chapter, generating useful images of modified materials and scientific data to elucidate the behaviour of MOF-bound photoswitches. The objectives of this chapter are:

1. Synthesise micron-scale metal-organic frameworks suitable for use in microscopy experiments
2. Establish reaction conditions for post-synthetic modification of chosen frameworks with coordinating dyes and photoswitches
3. Investigate solid-state photophysical behaviour of photoswitches
4. Determine the effect of modification on the guest uptake properties on porous frameworks

Section 2.3.2.2 (pp.43) details the effect of common laboratory solvents on crystal quality in SEM imaging. Although this was not a primary objective of the chapter, this study has considerable impact for research in the field and general laboratory and imaging practices around the world.

## 2.3 Results and Discussion

Work in this section involving the optimisation of crystal sizes (including NOTT-100 single crystal growth and solvent stability and  $\text{Sc}_2\text{BDC}_3$  single crystal growth optimisation) was undertaken with the assistance of MChem student Louisa Davis. The optimisation of SALE reaction conditions, including framework component control reactions and the pH study of **7-DCCA**, was carried out with the assistance of MChem student David Sowden. The synthesis and purification of **phen-spiro** was investigated with BSc project student Mitchell Davis and summer project students Joseph Paul-Taylor and Cameron Gray.

### 2.3.1 MOF selection

Frameworks that form sufficiently large crystals (upwards of a few micrometres) were chosen to ensure suitability for *in situ* infrared and confocal laser scanning fluorescence microscopy experiments described in this thesis. Among the frameworks commonly synthesised in the laboratory, the most promising candidates were MIL-68(Ind), NOTT-100,  $\text{Sc}_2\text{BDC}_3$  and UiO-67. The crystal structures of these frameworks are shown below in Figure 2.10. These frameworks form four distinct crystal morphologies and contain different metal nodes. SEM images of the DMF-washed materials are shown in Figure 2.11.

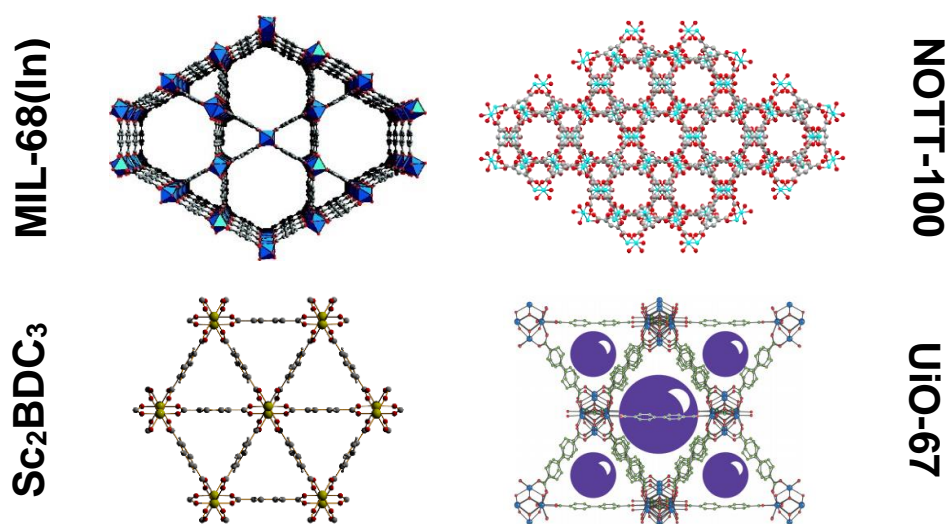
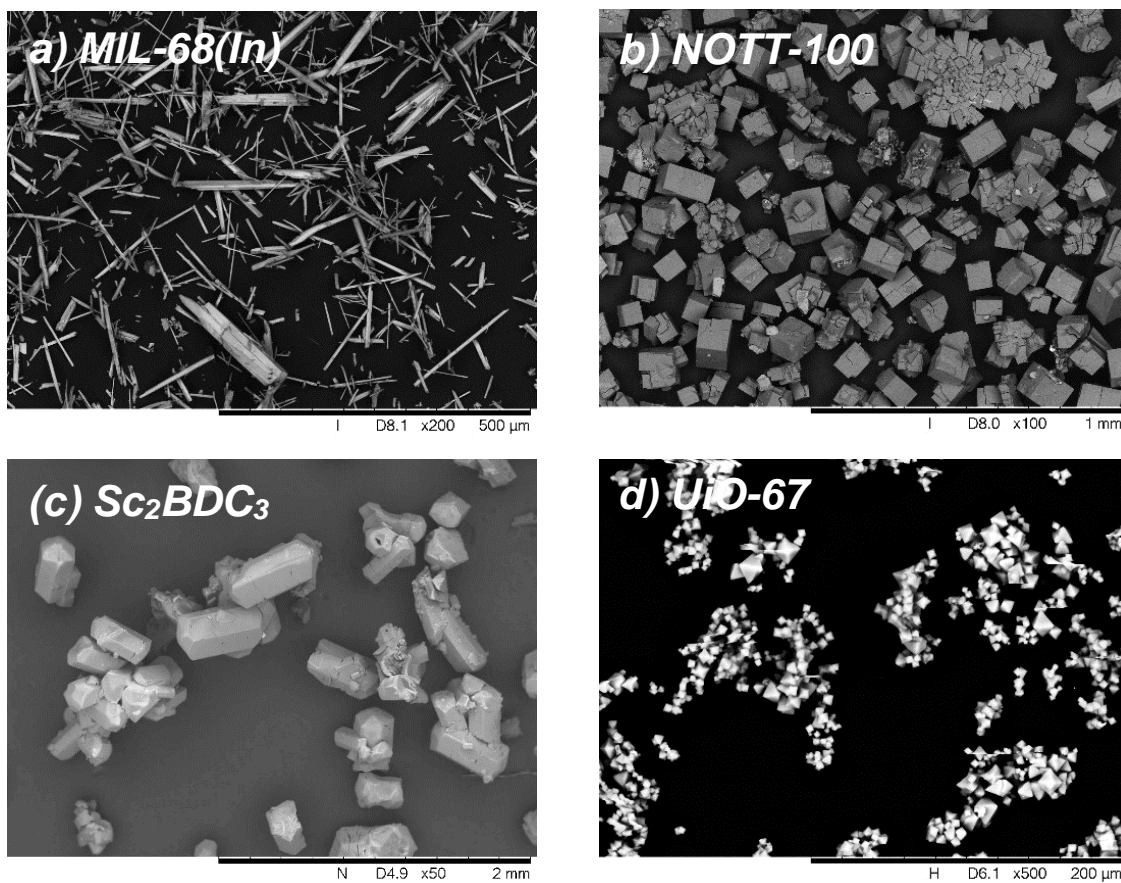


Figure 2.10. Crystal structures of metal-organic frameworks modified in this chapter.



*Figure 2.11. SEM images of a) MIL-68(*In*), b) NOTT-100, c) Sc<sub>2</sub>BDC<sub>3</sub> and d) UiO-67.  
Images are captured at x200, x100, x100 and x500 magnification respectively.*

Post-synthetic modification of these frameworks with photoactive moieties introduces new photophysics to the materials, and it was therefore important to carefully consider the absorption properties prior to modification. With the exception of NOTT-100, the frameworks do not absorb light in the visible part of the spectrum. NOTT-100 (blue crystals) absorbs at approximately 700 nm, due to the Cu(II)-based metal nodes.

The post-synthetic chemisorption of various dyes into the MOFs is described later in this chapter. The structures of the dyes are shown below in Figure 2.12.

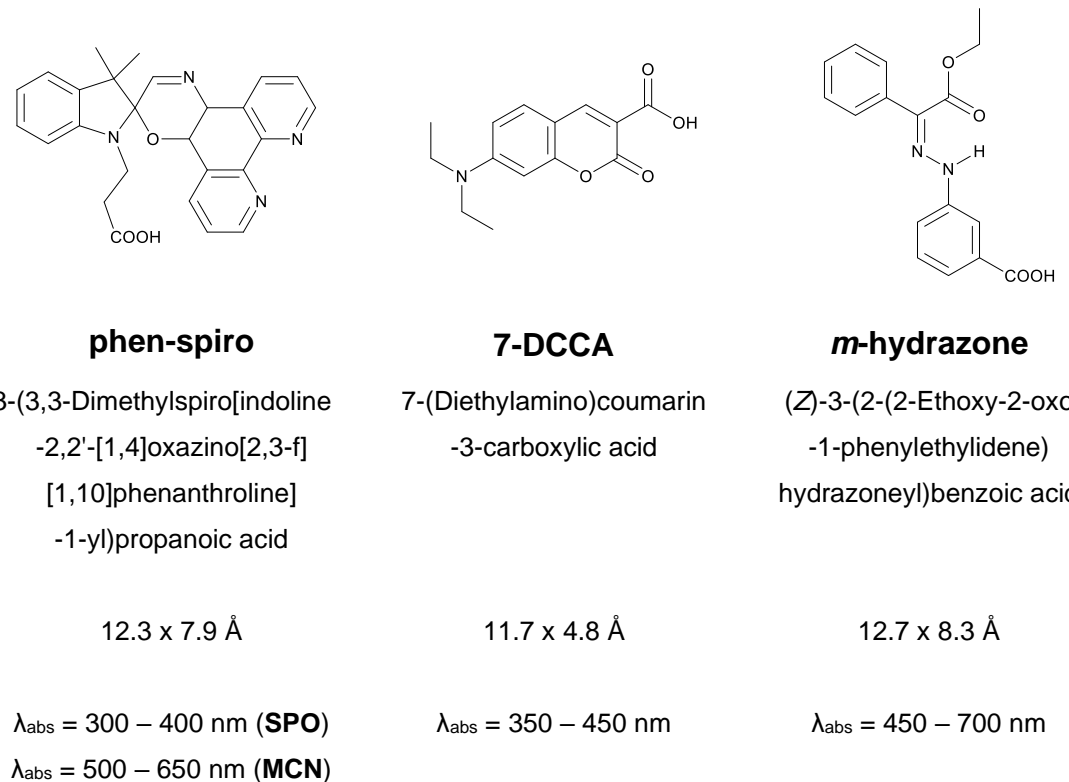


Figure 2.12. Structures of dyes discussed throughout this chapter.

The molecular dimensions of each photoswitch (Figure 2.11) are sufficiently similar that they should coordinate to frameworks in a similar fashion. The photoswitching spirooxazine **phen-spiro** absorbs UV light (300–400 nm) in the closed spirooxazine form and green-red light (500–650 nm) in the open merocyanine form. **7-DCCA**, a monocarboxylate coumarin-based dye, absorbs blue light (350–450 nm). The hydrazone-based photoswitch **m-hydrazone** absorbs green-red light (450–700 nm). The UV-VIS-diffuse reflectance spectroscopy (UV-VIS-DRS) spectra for all dyes and frameworks of interest are shown overleaf in Figure 2.13, with areas of overlap between dyes and frameworks indicated.

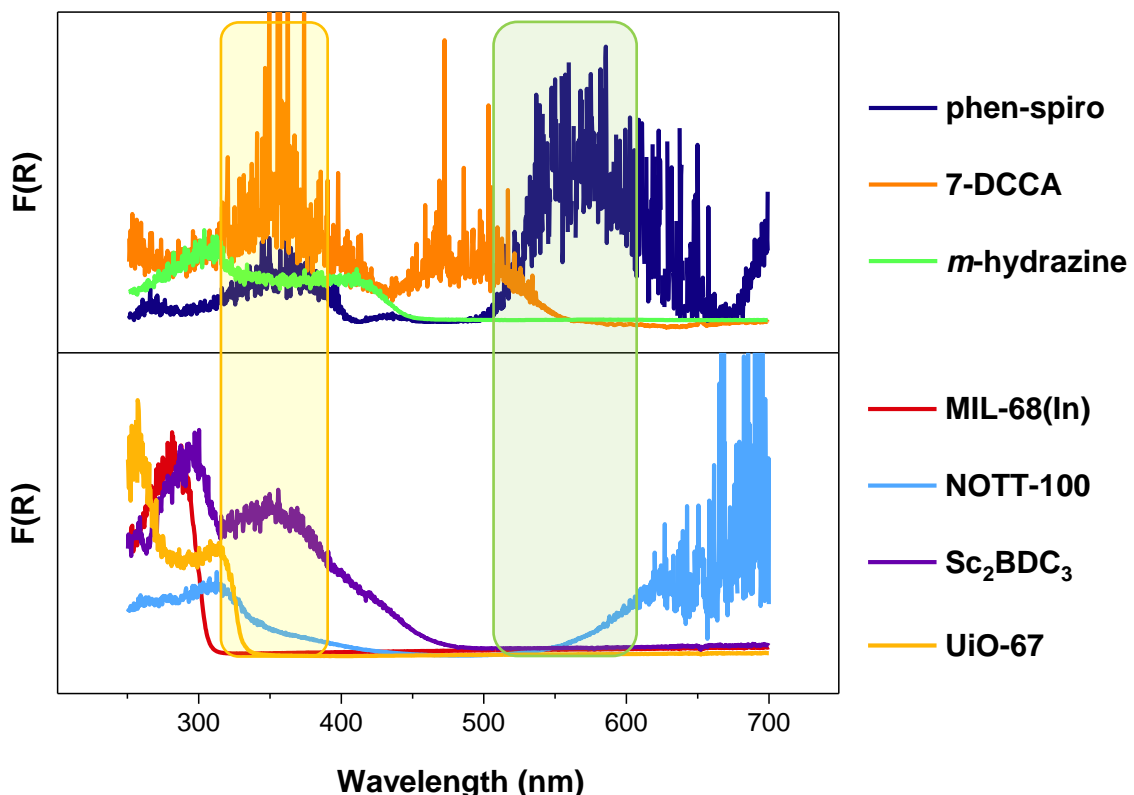


Figure 2.13. UV-VIS-DRS spectra of dyes (top) and MOFs (bottom). Regions of spectral overlap are indicated in yellow and green.

The region highlighted in Figure 2.13 in yellow indicates overlap of Sc<sub>2</sub>BDC<sub>3</sub> with **7-DCCA**, **m-hydrazone** and the closed spirooxazine form of **phen-spiro**. The green-highlighted area shows partial overlap between the open merocyanine form of **phen-spiro** and NOTT-100. Therefore, UV-VIS-DRS was a suitable technique to confirm successful modification of some frameworks with the aforementioned dyes, but it was not viable for all reactions. Therefore, confocal laser scanning fluorescence microscopy (CLSM) was also employed to evidence modification and optimise reaction conditions. The modification of frameworks is discussed later in Section 2.3.3 on pp.52.

## 2.3.2 Optimisation of crystal size

### 2.3.2.1 NOTT-100 single crystal growth

NOTT-100 was available in the laboratory due to a collaborative project undertaken with Dr Paul Webb at the University of St Andrews. This project is detailed further in Section 3.5.2 on pp.155.

The synthesis of NOTT-100 by Lin *et al.*, detailed in Section 2.5.4 on pp.118, described the formation of turquoise powder,<sup>30</sup> which is of insufficient size for single crystal microscopy-based experiments discussed herein. Adjustments to the original synthesis were made in our laboratory in order to grow larger crystals. The altered parameters were: starting material concentration, acid choice and concentration, solvents and co-solvents, temperature and heating time. Experimental details for all attempted reactions are reported in Appendix 1.

Crystal size and quality was evaluated using optical microscopy and the reactions that produced the most promising results were repeated with minor variations. The inclusion of EtOH, DMSO and DEF (independently) in any of the reactions prevented the formation of any solid, and adjusting the concentration of starting materials had no visible effect on crystal size or quality. Lower temperatures (55 and 65 °C) formed larger crystals. The effect of modulator appeared to have the greatest impact on the NOTT-100 produced.

A range of 5.24 µmol – 314 mmol of HCl, H<sub>2</sub>SO<sub>4</sub>, HNO<sub>3</sub>, *L*-proline, benzoic, formic and salicylic acids were introduced to the reactions with varying success. *L*-Proline was attempted following a report by Forgan and co-workers of success in modulating single-crystal growth of Zr-MOFs.<sup>31</sup> Binding modulators; *L*-proline, benzoic, formic and salicylic acids, inhibited the formation of crystals, with many experiments containing undissolved starting material after five days. Figure 2.14 shows examples of the impact of *L*-proline on reaction solutions.

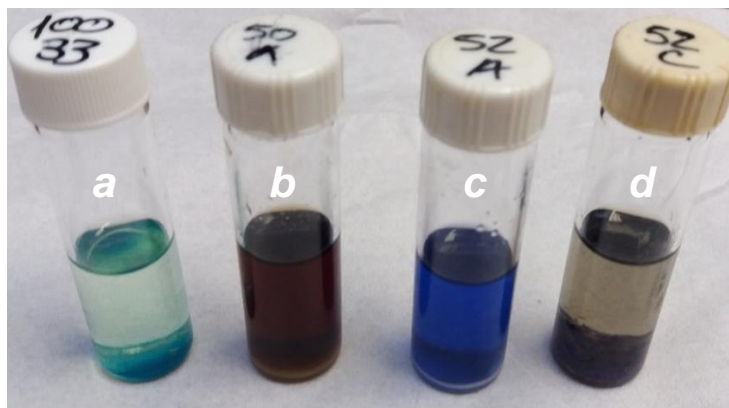


Figure 2.14. Comparison of *L*-proline-containing reaction solutions; a)  $\text{H}_2\text{SO}_4$  (55 °C), b)  $\text{HCl} + \text{L-proline}$  (55 °C), c)  $\text{HNO}_3 + \text{L-proline}$  (55 °C) and d)  $\text{HNO}_3 + \text{L-proline}$  (120 °C).

The above figure illustrates the unsuccessful modulation of NOTT-100 with *L*-proline. The darkened solution in vial **b** suggests the reduction of the active Cu(II) species to Cu(I). Red-brown precipitate in vial **d** indicates the formation of  $\text{Cu}_2\text{O}$ . PXRD analysis confirmed that solids formed in vials **b**, **c** and **d** were not NOTT-100.

The largest, most uniform crystals were obtained using i)  $\text{H}_2\text{SO}_4$  (8  $\mu\text{L}$ , 5 day synthesis); ii)  $\text{H}_2\text{SO}_4$  (30  $\mu\text{L}$ , 5 day synthesis); iii)  $\text{HNO}_3$  (90  $\mu\text{L}$ , 5 day synthesis) and iv)  $\text{HNO}_3$  (90  $\mu\text{L}$ , 6 day synthesis). Scanning electron microscopy (SEM) images were collected of these four samples, shown in Figure 2.15 overleaf.

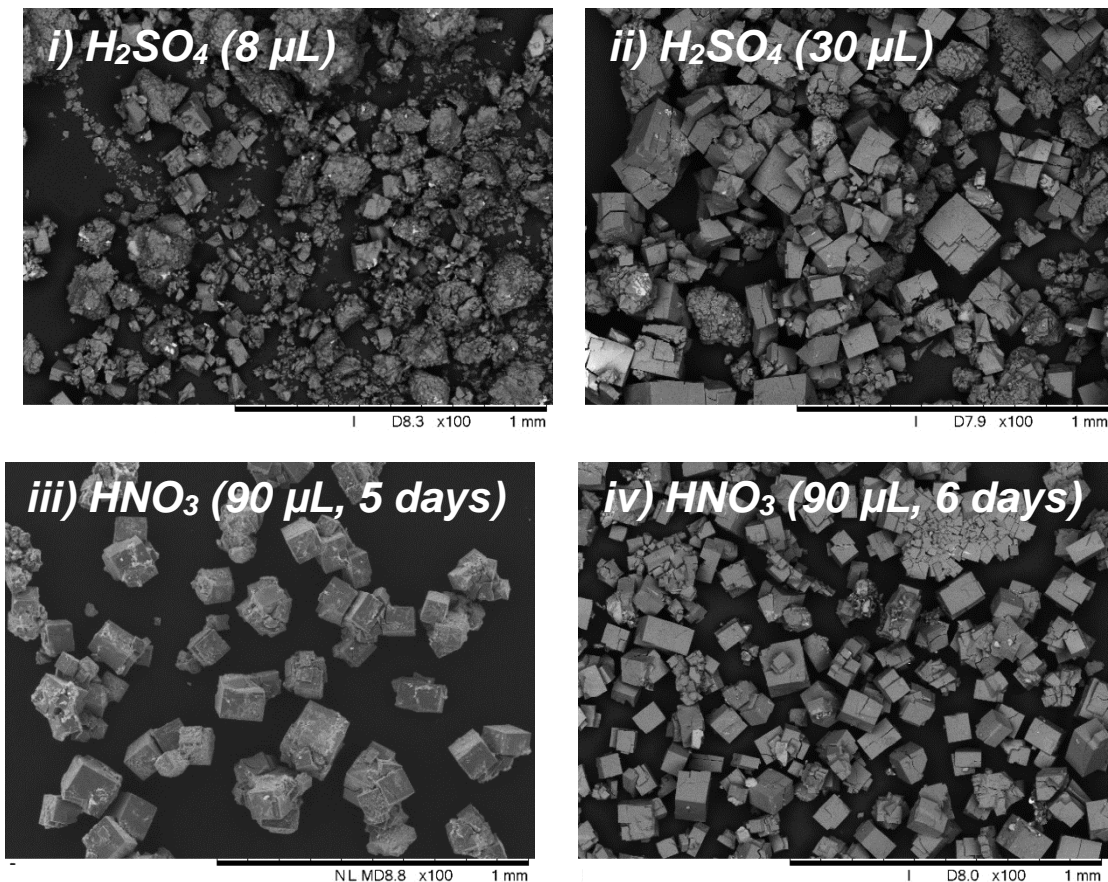


Figure 2.15. SEM images of the most promising NOTT-100 samples.

SEM images in Figure 2.15 indicate that HNO<sub>3</sub> encourages the formation of reasonably uniform cubic crystals (Figures 2.15iii and 2.15iv), whereas a larger variation of crystal size and morphology is present in reactions where H<sub>2</sub>SO<sub>4</sub> has been employed as modulator (Figures 2.15i and 2.15ii). A larger number of discrete, cubic NOTT-100 crystals can be seen as a fraction of the amount of visible sample in Figure 2.15iv (6-day synthesis) than Figure 2.15iii (5-day synthesis), despite the presence of larger crystal clusters resulting from the longer synthesis. Due to the need for discrete single crystals for microscopy experiments described herein, the longer heating time was employed for subsequent synthesis of NOTT-100 single crystals.

### 2.3.2.2 Solvent effects on NOTT-100 crystal stability

The post-synthetic solvent-exchange of MOFs is commonplace in laboratories around the world, displacing typical, high boiling point solvents used in the synthesis of the material, such as DMF and DMSO, with more volatile and more easily removed alternatives.<sup>32–34</sup> Solvent exchange was initially carried out using MeOH, and SEM images were collected of the as-synthesised and MeOH-solvent exchanged materials (Figure 2.16).

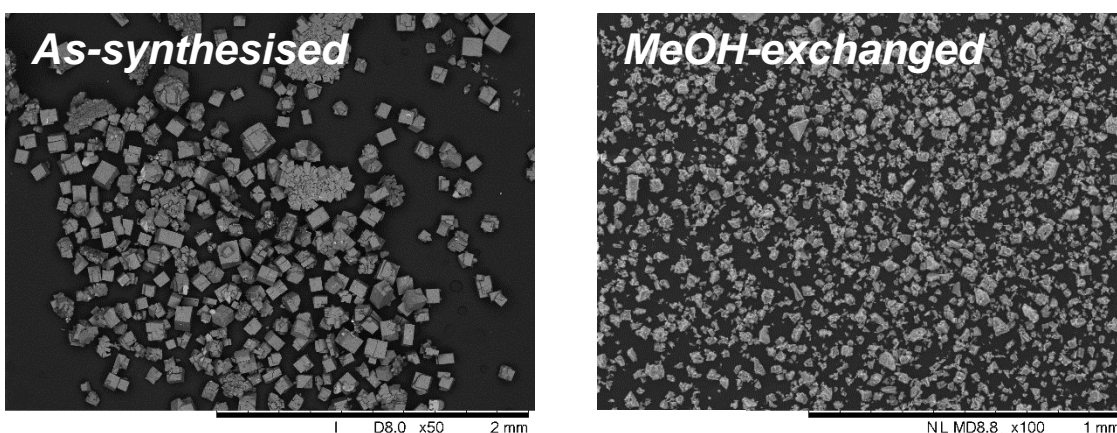


Figure 2.16. SEM images of (left) DMF-washed and (right) MeOH-exchanged NOTT-100.  
NB: scale bars are 2 mm and 1 mm respectively.

Figure 2.16 illustrates how single crystals of NOTT-100 appear to have shattered following solvent exchange into MeOH and SEM analysis.

In order to investigate the effects of different solvents on the stability of the crystals to solvent exchange and/or the SEM vacuum, NOTT-100 was solvent exchanged into a variety of commonly available ‘bench’ laboratory solvents. No solvents were specially dried and all were stored under air, emulating conditions in laboratories around the world. SEM images of solvent-exchanged materials are shown in Figures 2.17a and 2.17b, collected after allowing the samples to dry in air.

Samples were ranked qualitatively from best to worst based on visible crystal fragmentation, average crystallite size, agglomeration and surface cracking.

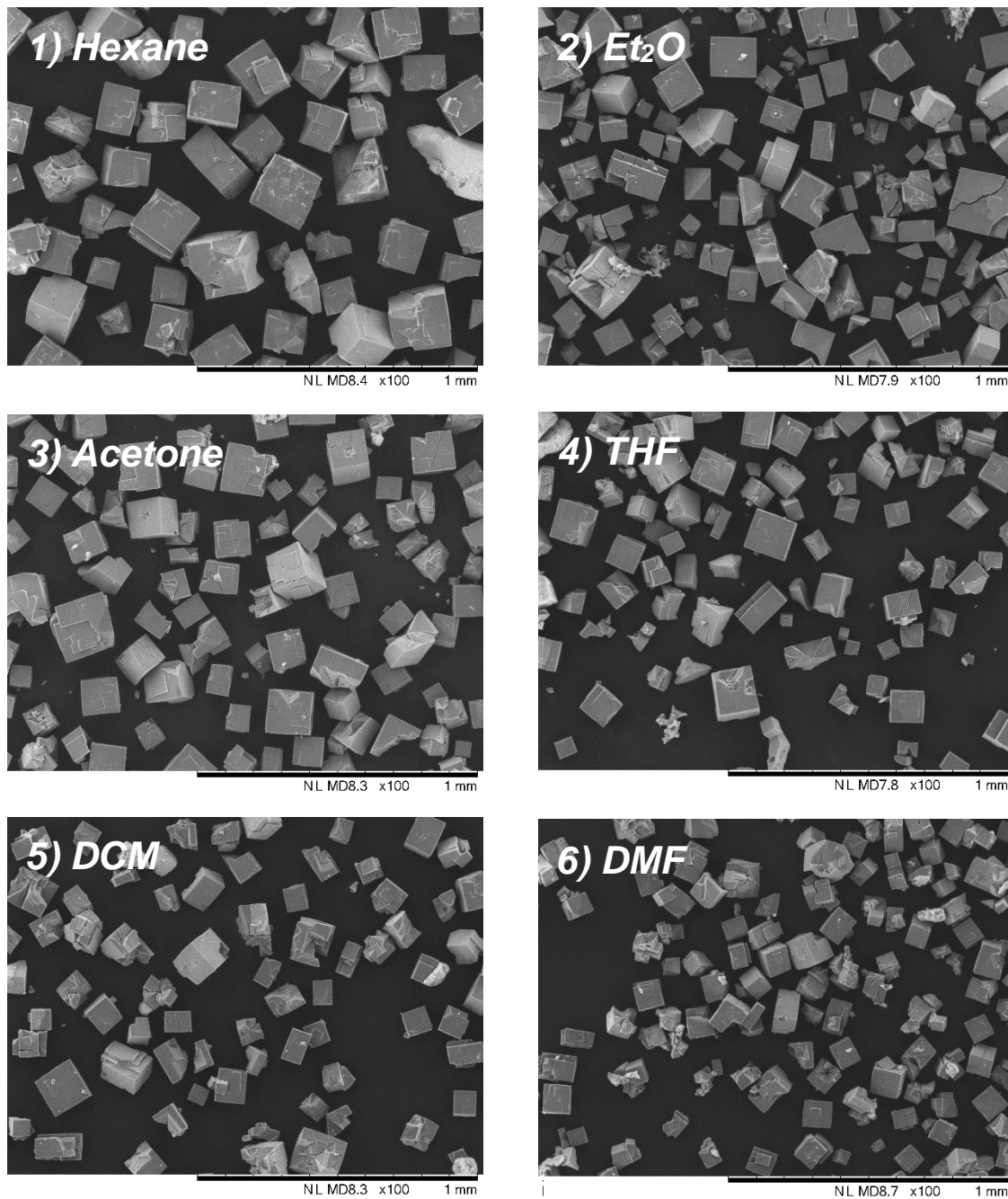


Figure 2.17a. SEM images of solvent-exchanged NOTT-100, ordered from best to worst left-to-right and top-to-bottom. Exchange solvent indicated in corners of images.

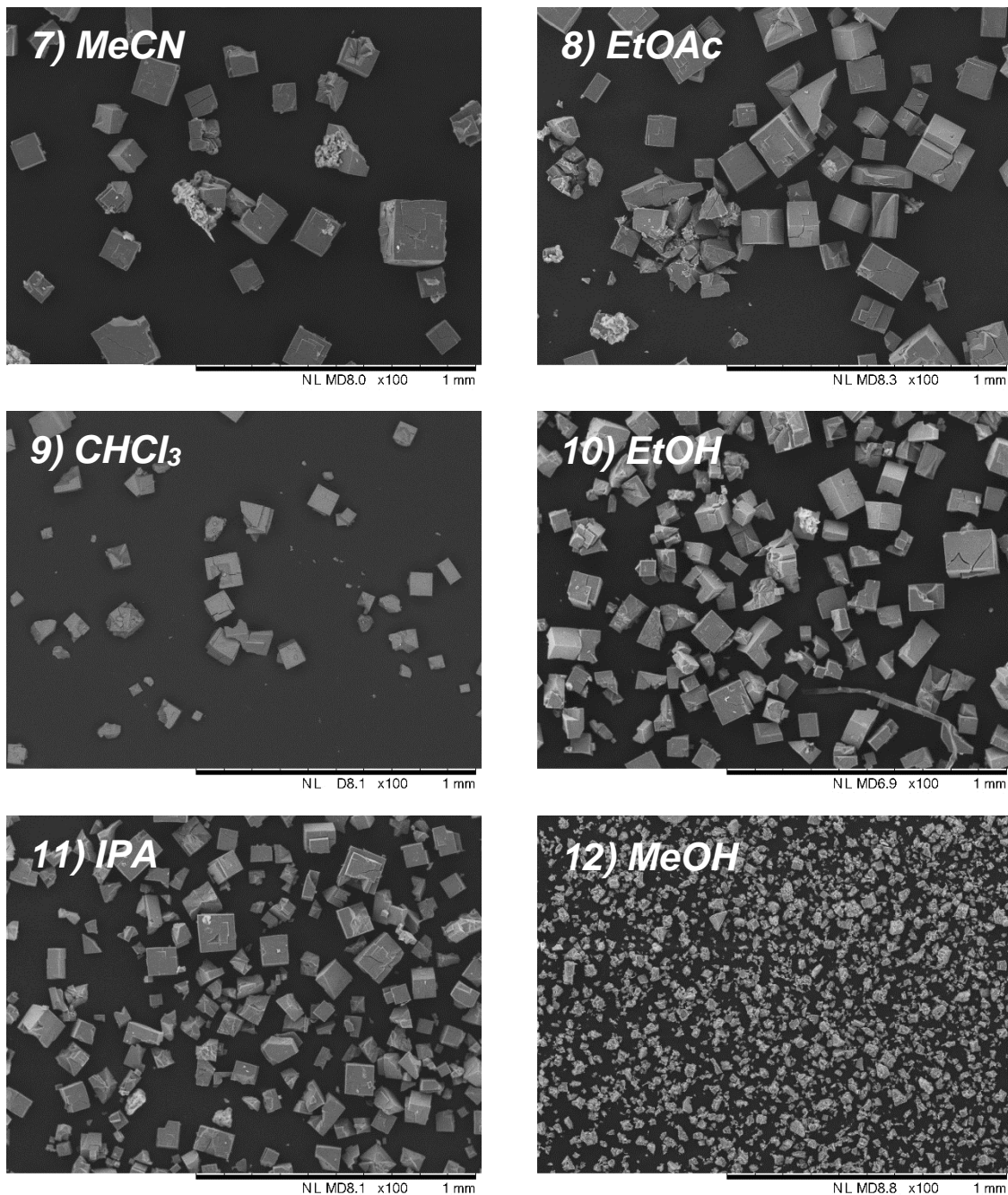
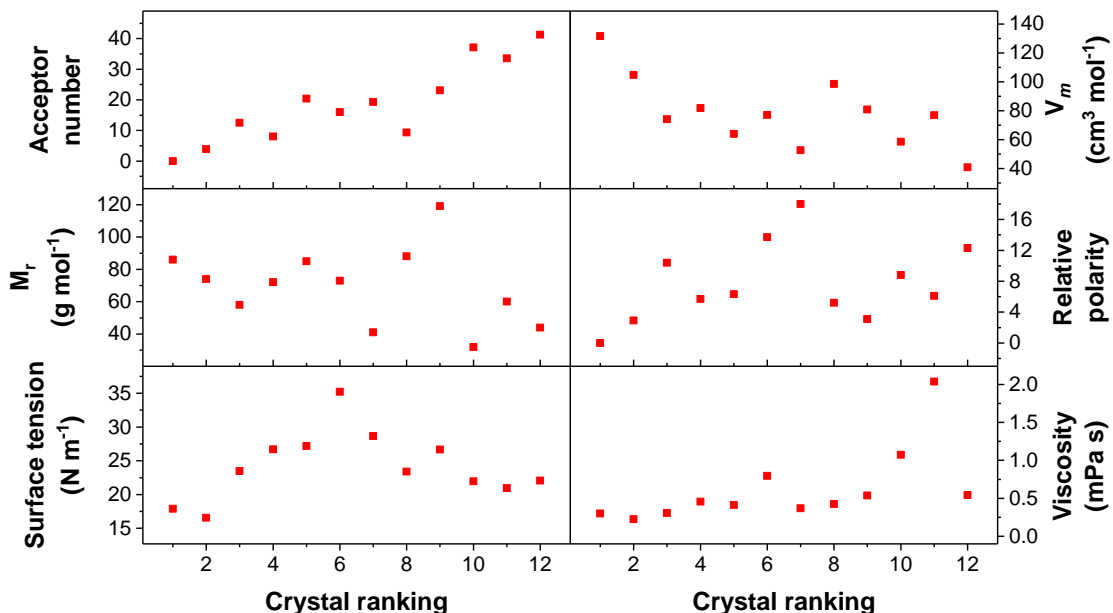


Figure 2.17b. SEM images of solvent-exchanged NOTT-100, ordered from best to worst left-to-right and top-to-bottom. Exchange solvent indicated in corners of images.

The qualitatively ranked outcome was compared against the following solvent properties: Gutmann acceptor number (AN; where a higher value indicates greater Lewis acidity),<sup>35,36</sup> molar volume ( $V_m$ ),<sup>37</sup> molecular mass ( $M_r$ ),<sup>38</sup> polarity relative to water (RP),<sup>37</sup> surface tension (ST)<sup>38</sup> and viscosity.<sup>38</sup> These values are shown for each solvent in Table 2.1.

*Table 2.1. Qualitative crystal ranking of solvent-exchanged NOTT-100 with associated solvent parameters.*

Solvent	Qualitative crystal ranking	AN	$V_m$ (cm <sup>3</sup> mol <sup>-1</sup> )	$M_r$ (g mol <sup>-1</sup> )	RP	ST (N m <sup>-1</sup> )	Viscosity (mPa s)
Hexane	1	0.0	131.6	86	0.0	17.9	0.30
Et <sub>2</sub> O	2	3.9	104.8	74	2.9	16.6	0.22
Acetone	3	12.5	74.0	58	10.4	23.5	0.31
THF	4	8.0	81.7	72	5.7	26.7	0.46
DCM	5	20.4	63.9	85	6.3	27.2	0.41
DMF	6	16.0	77.0	73	13.7	35.2	0.79
MeCN	7	19.3	52.6	41	18.0	28.7	0.37
EtOAc	8	9.3	98.5	88	5.2	23.4	0.42
CHCl <sub>3</sub>	9	23.1	80.7	119	3.1	26.7	0.54
EtOH	10	37.1	58.5	32	8.8	22.0	1.07
IPA	11	33.5	76.8	60	6.1	20.9	2.04
MeOH	12	41.3	40.7	44	12.3	22.1	0.54



*Figure 2.18. Plots of solvent properties vs NOTT-100 crystal ranking.*

The damaging effects of solvents on MOF crystals was also noted by Grzybowski and co-workers in 2010.<sup>13</sup> The plots shown in Figure 2.18 indicate that solvent acceptor number and molar volume have the greatest correlation to final qualitative crystal size and quality. Quantitative assessment using image analysis software is underway and will be completed by members of the group in the future.

We have shown that sample preparation can have significant impact on the appearance of the SEM images. The research group are currently processing more samples to assess this qualitative observation and have identified that the cause of crystallite breakdown is exposure to the SEM vacuum, *not* simply exchanging the initial solvent with other solvents. This could therefore have importance for all SEM images collected in the literature. Following investigation into the effects of solvent exchange, NOTT-100 single crystals were subsequently exchanged with hexane to prevent crystal damage.

### 2.3.2.3 Optimisation of $\text{Sc}_2\text{BDC}_3$ crystal size

$\text{Sc}_2\text{BDC}_3$  prepared by Miller *et al.* formed yellow crystals in excess of 160  $\mu\text{m}$  along the z-axis.<sup>39</sup> Figure 2.19 below shows SEM images of  $\text{Sc}_2\text{BDC}_3$ , synthesised simultaneously from the same procedure in one oven in three different reaction vessels, which show polydisperse crystallites within the range of 50–700  $\mu\text{m}$  across the three batches.

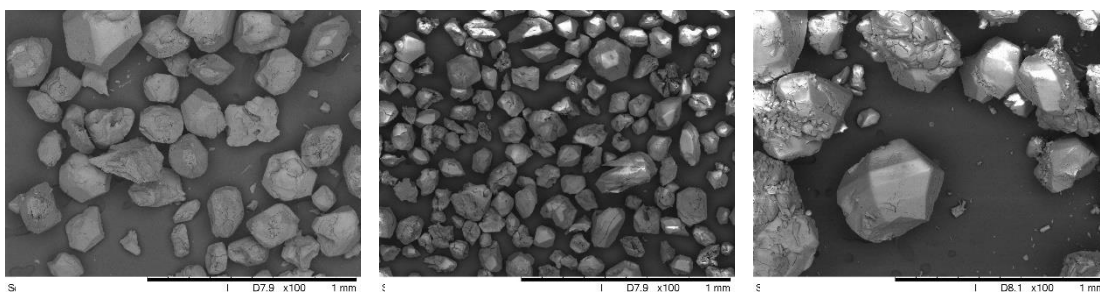


Figure 2.19. SEM images at 100x magnification of  $\text{Sc}_2\text{BDC}_3$  crystals from simultaneous synthesis in three different vessels.

The images in Figure 2.19 do not show reproducible production of consistently sized crystals, even under the same conditions. Ideal  $\text{Sc}_2\text{BDC}_3$  crystals for subsequent analyses were 100–250  $\mu\text{m}$  in length and ~50  $\mu\text{m}$  deep, preferably with significantly reduced polydispersity than those shown on the previous page.

In order to control the range of sizes of  $\text{Sc}_2\text{BDC}_3$  crystals, we employed a doping method, first described by Wang and co-workers to regulate crystal growth of ZIF-8.<sup>40</sup> The doping method involves a variable  $R$  factor, described below in Equation 2.1, which is a molar ratio of metal salt that is pre-heated with the linker before combining it with the remaining metal salt. Here, the approach pre-binds the carboxylate groups of the terephthalic acid linker with a  $\text{Sc}^{3+}$  cation in order to control nucleation of the desired product. Equation 2.1 defines  $R$ , where  $n$  is number of moles and *pre-M<sup>+</sup>* refers to the metal being pre-heated with the linker.

$$R = \frac{n_{(\text{pre-}M^+)} }{n_{(\text{organic ligand})}}$$

*Equation 2.1. R factor for control of crystal polydispersity.*

Experiments varying  $R$  (*i.e.* the mass of  $\text{Sc}(\text{NO}_3)_3$  introduced prior to combination of linker and bulk metal salt) and final heating time were carried out to examine the effects of both factors on particle size. Variations in experimental parameters are shown below in Table 2.2.

*Table 2.2. Reagent masses and associated R factors for doping experiments.*

*Reagents from the synthesis by Miller et al are highlighted in blue, and are taken from reference 39.*

BDC (mg)	$\text{Sc}(\text{NO}_3)_3$ (mg)	[pre- $M^+$ ] $\text{Sc}(\text{NO}_3)_3$ (mg)	R	Volume (mL)
<b>166.2</b>	<b>340.6</b>	<b>0</b>	<b>0</b>	<b>5</b>
108	100	2.5	0.017	2
108	100	10	0.067	2
108	100	18	0.12	2
108	100	25	0.17	2
108	100	18	0.12	2
270	250	45	0.12	1

The doping experiments were performed by introducing a precise amount of  $\text{Sc}(\text{NO}_3)_2$  (indicated in Table 2.2) to a slurry of terephthalic acid linker in water and heating at 70 °C with stirring for 2 hours. The remaining  $\text{Sc}(\text{NO}_3)_2$  was heated in water at 70 °C with stirring for 2 hours. The solution and slurry were subsequently combined and heated at 220 °C for 48 hours.

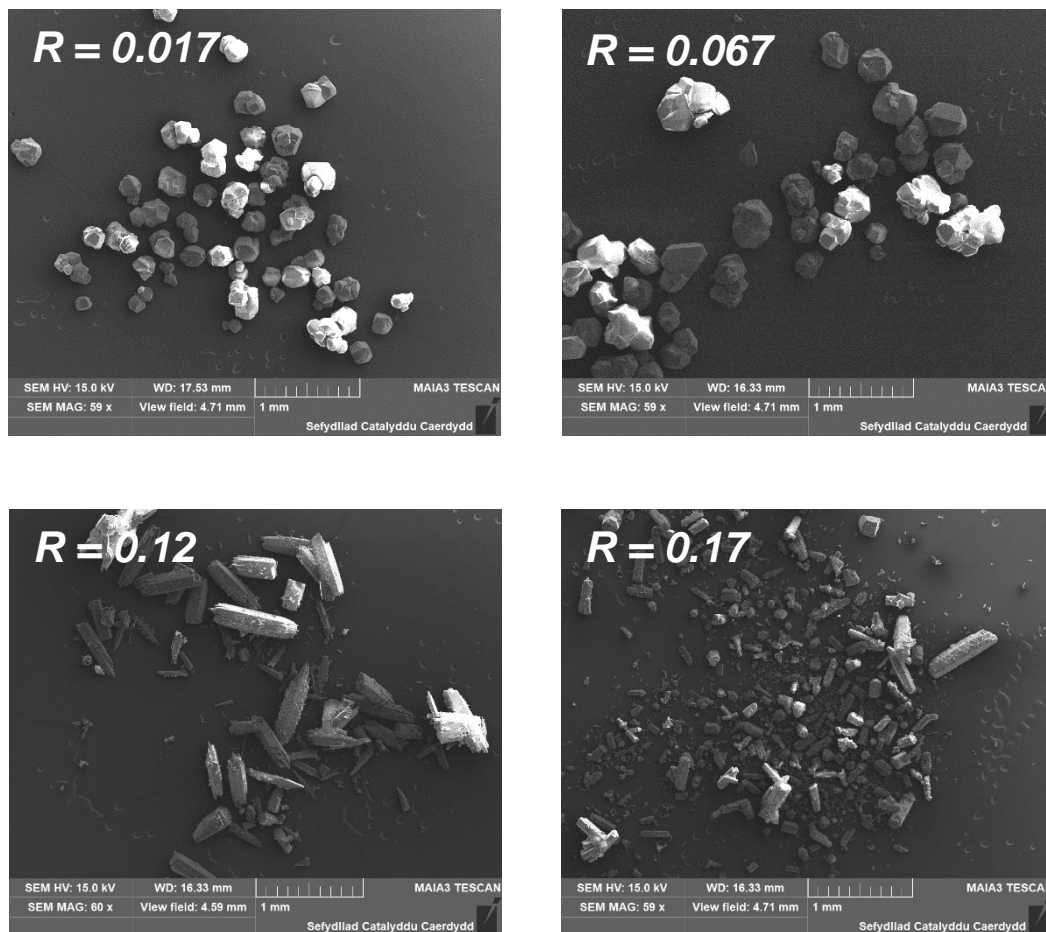


Figure 2.20. SEM images at 59/60x magnification of  $\text{Sc}_2\text{BDC}_3$ , synthesised by the pre-doping method using the stated  $R$  factors. Reaction time was 48 hr in all cases.

Figure 2.20 shows that pre-doping the linker slurry with different amounts of  $\text{Sc}(\text{NO}_3)_3$  heavily influences the size of crystals that grow. SEM images illustrate how lower  $R$  factors of 0.017 and 0.067 encourage the formation of cuboctahedra up to ca. 400  $\mu\text{m}$  in size. The larger doping ratios, 0.12 and 0.17, promote the growth of hexagonal rods up to ca. 800  $\mu\text{m}$  in length. Crystal size variation was qualitatively lowest in the sample with the smallest  $R$  factor of 0.017, where crystals range from 150–300  $\mu\text{m}$ .

Optimum crystals for single-crystal infrared microscopy experiments, described in Section 1.7 on pp.15, are plates with a thickness of up to 20  $\mu\text{m}$ . The cuboctahedra shown in Figure 2.20, synthesised using  $R = 0.017$  and  $0.067$ , are therefore too large in all directions. Similarly, even across the shorter axes, the hexagonal rods synthesised using  $R = 0.12$  are also too thick. Smaller cuboctahedra in the region of 20  $\mu\text{m}$  would be more likely to exhibit scattering effects, described in Section 1.7 on pp.16. Hexagonal rods minimise both saturation and scattering effects due to differing distances along the  $a$ ,  $b$  and  $c$  crystal axes. Doping ratios  $R = 0.12$  and  $0.17$  were therefore selected for experiments investigating the effect of reaction time on crystal formation. SEM images of as-synthesised materials from 24- and 48-hour syntheses are shown in Figure 2.21.

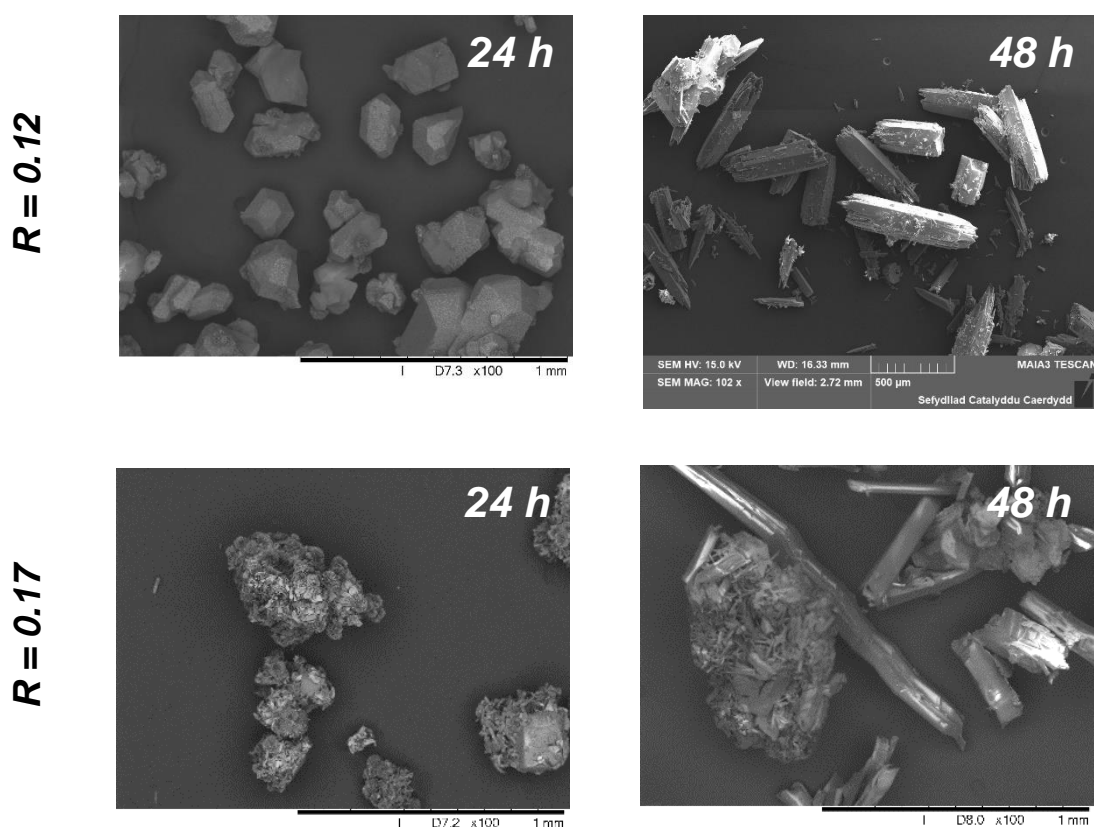


Figure 2.21. SEM images at x100 magnification of  $\text{Sc}_2\text{BDC}_3$  synthesised with  $R = 0.12$  (top) and  $0.17$  (bottom) with indicated reaction times.

Figure 2.21 does not appear to indicate any trends in polydispersity and discrete crystals in these images are of widely varying sizes. Crystals grown with  $R = 0.17$  show a higher degree of clustering, while crystals grown with  $R = 0.12$  appear more discrete. All crystals shown are far too large for IR microscopy experiments.

In an attempt to decrease the overall average crystal size produced, the total metal and ligand concentration in the reaction mixture used for the aforementioned  $R = 0.12$  synthesis was increased, from 0.00087 and 0.0013 mM to 0.0011 and 0.0017 mM, for  $\text{Sc}(\text{NO}_3)_3$  and terephthalic acid respectively.

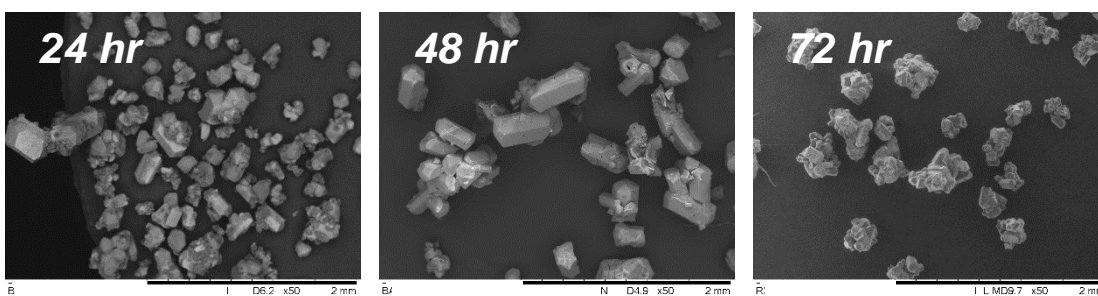


Figure 2.22. SEM images at 50x magnification of  $\text{Sc}_2\text{BDC}_3$  synthesised from reaction solution at five-fold concentration, with indicated reaction times.

We also investigated the time evolution of crystal size at three time points during the synthesis. The SEM images in Figure 2.22 show  $\text{Sc}_2\text{BDC}_3$  crystals of varying sizes and extents of aggregation. The reaction heated for 24 hr contains mainly smaller hexagonal rods, often in clusters. The 48 hr reaction also contains clusters of hexagonal rods, however the rods herein are significantly larger than the shorter timescale reaction. The longer 72 hr reaction time appears to fracture the longer rods, forming instead numerous clusters of smaller crystallites.

Given the outcomes of qualitative analysis of SEM images of the materials, a doping factor of  $R = 0.12$  in the more concentrated reaction solution was used to synthesise size-optimised  $\text{Sc}_2\text{BDC}_3$  crystals. An experimental procedure for the final synthesis is in Section 2.5.4 on pp.121.

### 2.3.3 Post-synthetic modification of MOFs with coordinating dyes

Post-synthetic modification (PSM) of MOFs enables a plethora of potential chemical transformations. In this work, we have investigated the solvent-assisted ligand exchange (SALE) of several literature-known frameworks with a range of coordinatively non-innocent dyes (Figure 2.23). The carboxylic acid functionality was chosen to facilitate straightforward exchange at the metal–carboxylate bonding site. Metal-bound carboxylate groups of framework linkers were exchanged with the carboxylate groups present in each dye molecule, imparting additional chemisorbed fluorescence to each framework.

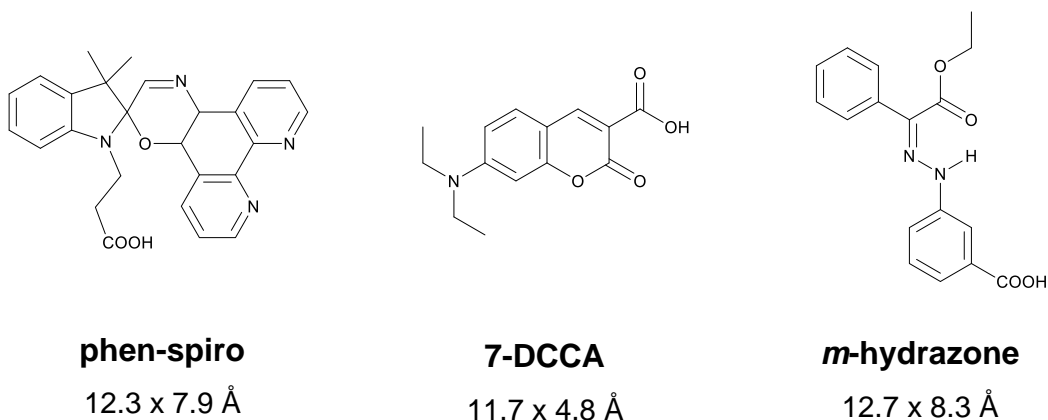


Figure 2.23. Structures of dyes discussed in this chapter.

**7-DCCA** is commercially available at £18/250 mg (Fluorochem UK), while both **phen-spiro** and ***m*-hydrazone** are research samples. **phen-spiro** was synthesised in our laboratory and is detailed further in Sections 2.3.3.4 and 2.5.2 on pp.77 and 111 respectively. ***m*-hydrazone** was provided by a collaborator, Ivan Aprahamian from Dartmouth College, USA.

Of the four frameworks discussed previously, (MIL-68(In), NOTT-100, Sc<sub>2</sub>BDC<sub>3</sub> and UiO-67), SALE has been successfully reported only in MIL-68(In), by Cohen and co-workers in 2012.<sup>41</sup> Forgan and co-workers have extensively reviewed PSM of Zr-MOFs in 2016,<sup>42</sup> including several examples of transmetalation in UiO-67.

The PSM of several frameworks (including Cu-based framework HKUST-1) with organic dye molecules was reported by Kitagawa and co-workers in 2010,<sup>14</sup> which inspired the use of optical spectroscopies to track fluorescent guests in MOFs explored in this chapter.

### 2.3.3.1 Optimisation of SALE reaction conditions

As SALE had been previously reported for MIL-68(Ind) and in Cu- and Zr-frameworks, experiments were carried out to establish optimised reaction conditions for linker exchange in all frameworks discussed herein. Optimisation reactions were carried out using **7-DCCA** as the molecule does not photoswitch, unlike **phen-spiro** and **m-hydrazone**, making it a simpler molecule, in addition to its commercial availability. In order to track the modification using UV-VIS spectroscopy, 0.03 mM **7-DCCA** solution was used, as this was the highest concentration achievable without saturating the detector of our spectrophotometer.

Initial reaction conditions, shown in Table 2.3, were either reproduced or adapted from the references indicated. The conditions noted for NOTT-100 were originally used for the modification of HKUST-1 by Kitagawa and co-workers,<sup>14</sup> and were reproduced here due to the same Cu paddlewheel-carboxylate bonding environment. As no literature precedent for the post-synthetic modification of Sc<sub>2</sub>BDC<sub>3</sub> was found, SALE reactions were incubated at 180 °C, due to the high thermal stability of the framework.

Table 2.3. Solvent-assisted ligand exchange conditions taken or adapted from the references indicated.

MOF	Carrier solvent	Temperature (°C)	Time (h)	Ref.
MIL-68(Ind)	DMF	55	3	41
NOTT-100	MeOH	100	20	14
UiO-67	MeOH	60	24	43
Sc <sub>2</sub> BDC <sub>3</sub>	MeOH	180	72	This work

The literature-adapted conditions offered starting points, but further experiments indicated that more dye was exchanged by the framework in MeOH than DMF. Upon visual inspection of MIL-68(Ind) and UiO-67 crystals after SALE reactions carried out in both DMF and MeOH, materials yielded when employing MeOH as a carrier solvent qualitatively appeared more strongly coloured, suggesting a higher incorporation of dye. This could be due to competition between the monocarboxylate dye and DMF solvent molecules. Therefore, MeOH was employed as a carrier solvent for modification reactions.

The extent of visual colouration of MIL-68(Ind) following incubation with methanolic **7-DCCA** was increasing with longer reaction time, so the incubation temperature was increased from 55 °C to 110 °C in order to increase the rate of ligand exchange. Similarly, the extent of dye exchange in NOTT-100 was increasing with increasing timescale (determined by UV-VIS-DRS) and hence the incubation temperature was increased from 100 °C to 130 °C. Incubation of NOTT-100 at 180 °C led to the decomposition of the framework to Cu<sub>2</sub>O.

Solution-phase UV-VIS spectroscopy was employed to determine the timescale for **7-DCCA** exchange. Figure 2.24 shows a schematic of the experimental approach for this characterisation method. **7-DCCA** incubation experiments were conducted at regular time intervals for all frameworks, and the reaction solution, framework washings and resulting MOF $\supset$ **7-DCCA** materials were analysed with UV-VIS and CLSM. The expectation of this approach was that UV-VIS analysis of a) the SALE reaction solution (Stage 1), b) a solution made up from the washings of the reaction solid to remove physisorbed **7-DCCA** from MOF pores (Stage 2) and c) acid-digested modified material (Stage 3) should collectively contain the amount of **7-DCCA** initially introduced via the stock dye solution.

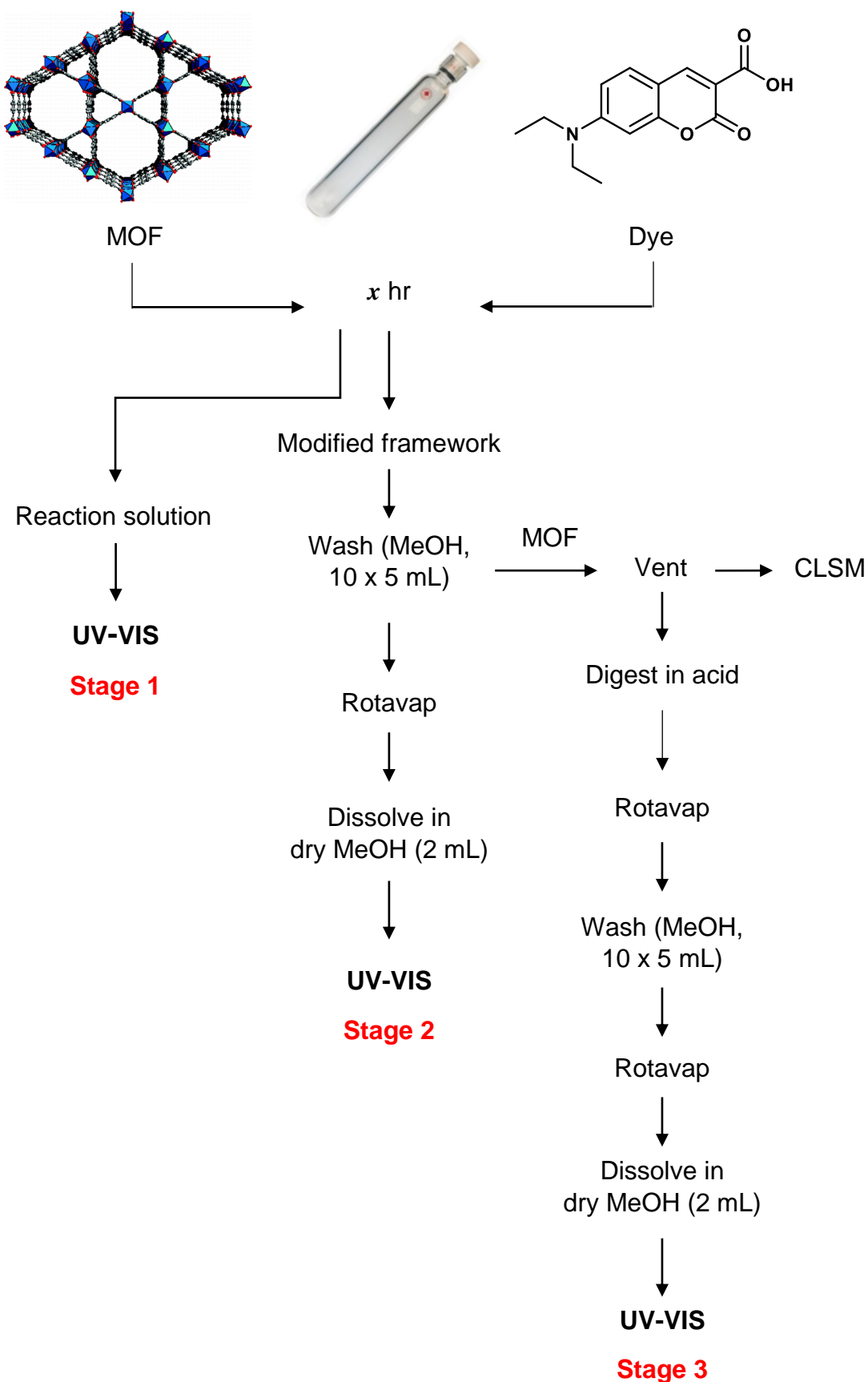


Figure 2.24. Schematic of experimental approach for UV-VIS approach to establishing reaction timescales for post-synthetic modification of MOFs with monocarboxylate dye.

Figures 2.25–2.28 across pp.57–60 show UV-VIS absorption spectra of SALE reaction solutions (Stage 1 of Figure 2.24) and reaction washings (Stage 2, showing the amount of weak physisorbed dye). In addition, these figures also show plots of the amount of **7-DCCA** in the reaction/washings solutions as a percentage of the initial amount of dye introduced from the stock dye solution. Two stock dye solutions were used in SALE reactions (0.0282 and 0.0252 mM) and hence plots throughout Figures 2.25–2.28 show the dye remaining as a percentage of the initial amount of dye introduced in the stock dye solution, as opposed to absolute mass of dye.

### 2.3.3.1.1 Stage 1 – SALE reaction solutions

As the schematic in Figure 2.24 shows, the reaction solution for each timed SALE experiment was retained and the UV-VIS absorption spectrum recorded. A selection of these spectra for all frameworks are shown in Figures 2.25–2.28. Each spectrum was baseline corrected by averaging ten points between 700.3–703.2 nm (where no absorbance is observed) and adding/subtracting this value from the whole spectrum as appropriate. The absorbance at each  $\lambda_{\text{max}}$  was taken from the baseline-corrected spectrum and plotted against time in Figures 2.25–2.28.

### 2.3.3.1.2 Stage 2 – Physisorbed 7-DCCA

To remove physisorbed dye post-SALE reaction, the frameworks were washed ten times with MeOH (5 mL). These washings were then dried and re-dissolved into dry MeOH (2 mL), and the UV-VIS absorbance spectrum collected. Each spectrum was baseline corrected, using the same procedure as discussed above for Stage 1. A selection of these spectra are shown in Figures 2.25–2.28. Due to the lower **7-DCCA** peak intensity in these spectra than the reaction solution spectra discussed in Stage 1, if a  $\lambda_{\text{max}}$  could not be identified, the absorbance was taken from 412 nm, which is the characteristic wavelength of **7-DCCA**. These absorbance values are plotted against time in Figures 2.25–2.28.

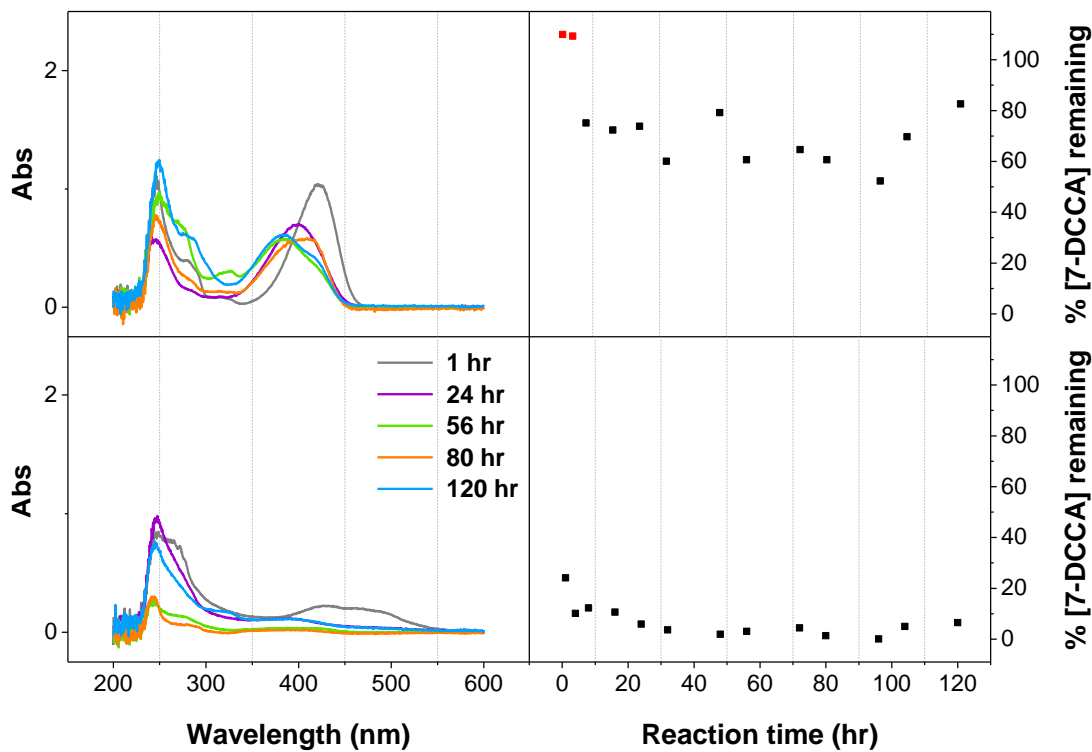
**MIL-68(In)**

Figure 2.25. (Left) Solution-phase UV-VIS spectra of (top) SALE reaction solutions post-incubation [Stage 1] and (bottom) MOF washings to remove physisorbed dye [Stage 2]. (Right) Plots showing percentage of initial **7-DCCA** remaining in (top) reaction solutions post-incubation [Stage 1] and (bottom) MOF washings [Stage 2]. Points marked in red indicate >100% of initial **7-DCCA** concentration.

In MIL-68(In), ~75% of **7-DCCA** remained in solution after 24 hours (Stage 1), ~5% of initial dye quantity was removed from the MOF by washing (Stage 2), which suggested the remaining 20% dye was chemisorbed to the framework.

## NOTT-100

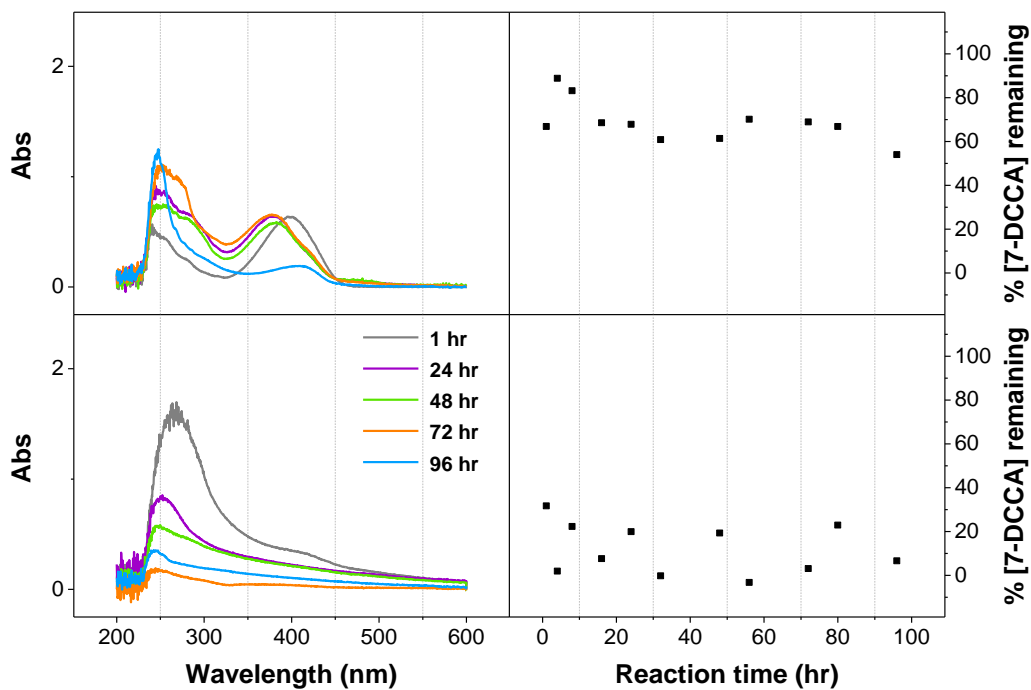


Figure 2.26. (Left) Solution-phase UV-VIS spectra of (top) SALE reaction solutions post-incubation [Stage 1] and (bottom) MOF washings to remove physisorbed dye [Stage 2]. (Right) Plots showing percentage of initial **7-DCCA** remaining in (top) reaction solutions post-incubation [Stage 1] and (bottom) MOF washings [Stage 2].

In NOTT-100, ~70% of **7-DCCA** remained in solution after 24 hours (Stage 1), ~20% of initial dye quantity was removed from the MOF by washing (Stage 2), which suggested the remaining 10% dye was physisorbed to the framework.

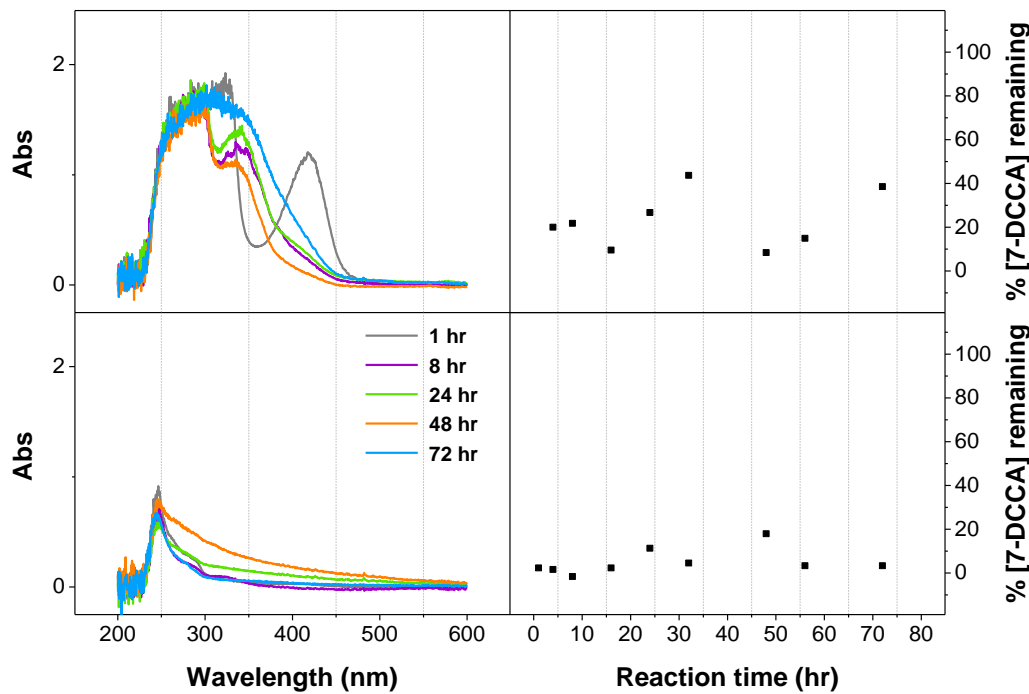
**Sc<sub>2</sub>BDC<sub>3</sub>**

Figure 2.27. (Left) Solution-phase UV-VIS spectra of (top) SALE reaction solutions post-incubation [Stage 1] and (bottom) MOF washings to remove physisorbed dye [Stage 2]. (Right) Plots showing percentage of initial **7-DCCA** remaining in (top) reaction solutions post-incubation [Stage 1] and (bottom) MOF washings [Stage 2].

In Sc<sub>2</sub>BDC<sub>3</sub>, ~25% of **7-DCCA** remained in solution after 24 hours (Stage 1), ~10% of initial dye quantity was removed from the MOF by washing (Stage 2), which suggested the remaining 65% dye was physisorbed to the framework.

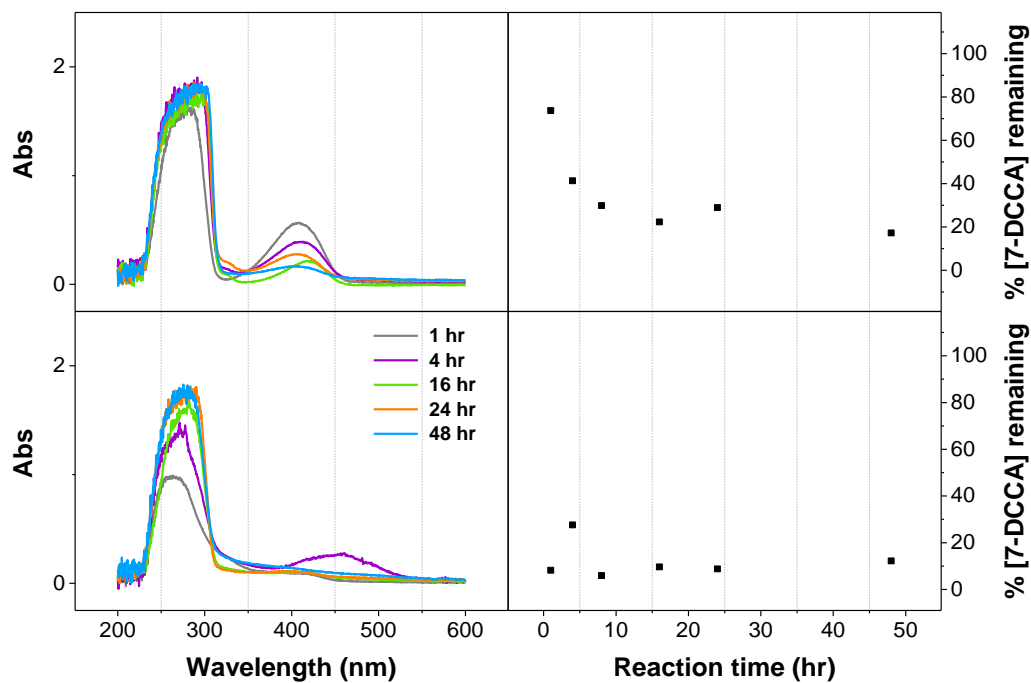
**UiO-67**

Figure 2.28. (Left) Solution-phase UV-VIS spectra of (top) SALE reaction solutions post-incubation [Stage 1] and (bottom) MOF washings to remove physisorbed dye [Stage 2]. (Right) Plots showing percentage of initial **7-DCCA** remaining in (top) reaction solutions post-incubation [Stage 1] and (bottom) MOF washings [Stage 2].

In UiO-67, ~30% of **7-DCCA** remained in solution after 24 hours (Stage 1), ~10% of initial dye quantity was removed from the MOF by washing (Stage 2), which suggested the remaining 20% dye was physisorbed to the framework.

*Table 2.4. Estimation of unreacted and chemisorbed **7-DCCA** following SALE reactions.*

<b>MOF</b>	<b>Dye remaining in solution</b>	<b>Physisorbed dye</b>	<b>Estimated chemisorbed dye</b>
MIL-68(In)	75%	5%	20%
NOTT-100	70%	20%	10%
Sc <sub>2</sub> BDC <sub>3</sub>	25%	10%	65%
UiO-67	30%	10%	60%

Table 2.4 shows the estimated **7-DCCA** chemisorbed to each framework, calculated as a percentage of the initial **7-DCCA** introduced in the stock dye solution. These values were calculated from the  $\lambda_{\text{max}}$  of peaks in the region of the characteristic **7-DCCA** peak (412 nm) in each UV-VIS spectrum. Some spectra (e.g. of reaction solutions from MIL-68(In) and NOTT-100 modification reactions, shown in Figures 2.25 and 2.26 respectively) show a blueshift of this peak. This blueshift is significantly more pronounced in the reaction solution spectra, which could be attributed to interactions between **7-DCCA** and unreacted starting materials retained after the synthesis of each framework, or due to the pH of the reaction solution. These hypotheses are discussed in Sections 2.3.3.1.3 and 2.3.3.1.4 on pp.62 and 65 respectively.

The estimated chemisorbed dye values in Table 2.4 suggest that, after 24 hours, more dye was chemisorbed to Sc<sub>2</sub>BDC<sub>3</sub> and UiO-67 than MIL-68(In) and NOTT-100. These values indicate that only a limited amount of physisorbed dye is retained within the framework pores. These values are disputable, however, as the 3 Å pores in Sc<sub>2</sub>BDC<sub>3</sub> (Table 2.5) should prevent the uptake of **7-DCCA**.

*Table 2.5. Pore dimensions of MOFs discussed herein*

<b>MOF</b>	<b>Pore dimensions (Å)</b>	<b>MOF</b>	<b>Pore dimensions (Å)</b>
MIL-68(In) <sup>44</sup>	Triangular; 6 Hexagonal; 16–17	Sc <sub>2</sub> BDC <sub>3</sub> <sup>39</sup>	3
NOTT-100 <sup>45</sup>	8.3 10.1	UiO-67 <sup>46</sup>	Tetrahedral; 11.5 Octahedral; 23

### 2.3.3.1.3 UV-VIS spectral absorption shifts of 7-DCCA as a result of reaction conditions

As mentioned on pp.61 in Section 2.3.3.1.2, a significant peak shift was observed in the **7-DCCA** peak of the reaction solution following SALE reactions. The greatest changes were observed in MIL-68(Ind) reactions, where the peak shifted across a range of 382–421 nm from the original 412 nm of the stock dye solution. These spectra are shown below in Figure 2.29.

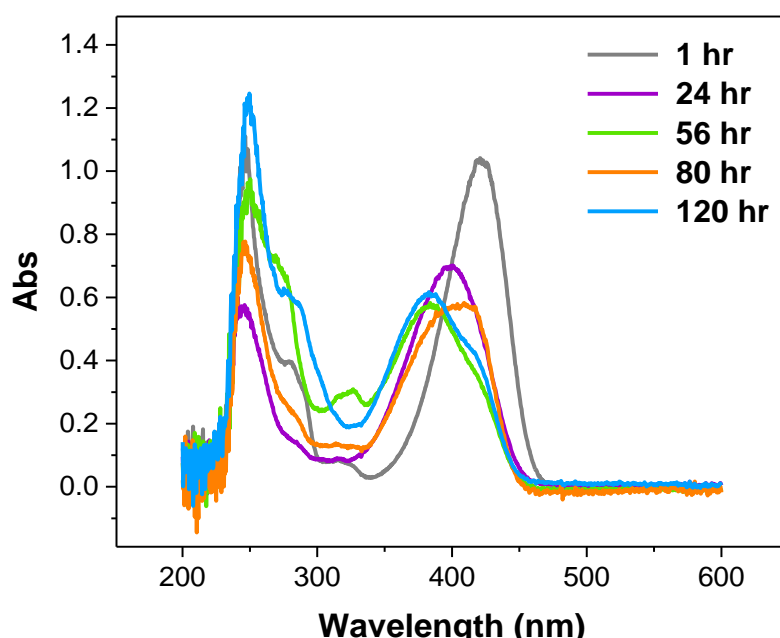


Figure 2.29. Solution-phase UV-VIS spectra of reaction solutions following MIL-68(Ind) SALE reactions with **7-DCCA**.

The shift in peak positions could be attributed to unreacted framework starting materials that were not removed during washing and solvent exchange of the frameworks.

Therefore, experiments were carried out to investigate combinations of these constituent materials with **7-DCCA** to identify which combination caused a peak shift. Table 2.6 shows all combinations of starting materials that were analysed.

*Table 2.6. MOF constituent combinations, for which the UV-VIS absorption spectra were collected in MeOH.*

<b>MIL-68(In)</b>		<b>NOTT-100</b>	
In(NO <sub>3</sub> ) <sub>3</sub>	BDC	Cu(NO <sub>3</sub> ) <sub>2</sub>	H <sub>4</sub> BPTC
In(NO <sub>3</sub> ) <sub>3</sub>	DMF	Cu(NO <sub>3</sub> ) <sub>2</sub>	DMF
In(NO <sub>3</sub> ) <sub>3</sub>	Dye	Cu(NO <sub>3</sub> ) <sub>2</sub>	Dye
BDC	DMF	Cu(NO <sub>3</sub> ) <sub>2</sub>	HNO <sub>3</sub>
BDC	Dye	H <sub>4</sub> BPTC	DMF
DMF	Dye	H <sub>4</sub> BPTC	Dye
		H <sub>4</sub> BPTC	HNO <sub>3</sub>
		DMF	Dye
		DMF	HNO <sub>3</sub>
		Dye	HNO <sub>3</sub>
<b>Sc<sub>2</sub>BDC<sub>3</sub></b>		<b>UiO-67</b>	
Sc(NO <sub>3</sub> ) <sub>2</sub>	BDC	ZrCl <sub>4</sub>	<i>L</i> -Proline
Sc(NO <sub>3</sub> ) <sub>2</sub>	Dye	ZrCl <sub>4</sub>	Dye
BDC	Dye	ZrCl <sub>4</sub>	HCl
		<i>L</i> -Proline	Dye
		<i>L</i> -Proline	HCl

Experiments were carried out by preparing solutions (0.06 mM in MeOH) of each component listed above and combining them in equal volumes to produce 0.03 mM concentrations of each component in a total 2 mL solution. The linker for UiO-67, 4,4'-biphenyldicarboxylic acid, was insoluble in MeOH at 0.06 mM and was therefore not tested. Figure 2.30 overleaf shows the solution-phase UV-VIS spectra of all dye-containing combinations; the non-dye containing combinations are shown in Appendix 1

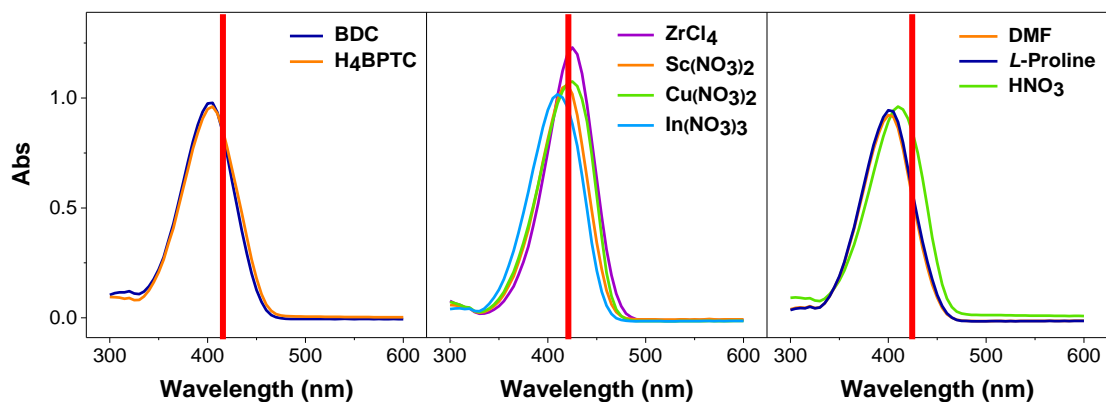


Figure 2.30. Solution-phase UV-VIS spectra of combinations of **7-DCCA** with (left) linkers, (centre) metal salts and (right) modulators and solvents. Vertical red lines indicate position of only **7-DCCA** in MeOH (412 nm).

Figure 2.30 indicates that a shift of the **7-DCCA** peak can be attributed to interactions with the free framework linkers (11 nm blue shift), metal salts (13 nm red shift for  $\text{ZrCl}_4$ ) and DMF/*L*-Proline (11 nm blue shift). The greatest shift observed is a 13 nm red shift in the combination of **7-DCCA** and  $\text{ZrCl}_4$  (the metal salt used for the synthesis of UiO-67). This suggests that the shift in peak in **7-DCCA** position in the SALE reaction solutions is either evidence of unreacted metal salt (incompletely removed during synthetic work-up) interacting with the dye, or the framework leaching metal into solution. Although **7-DCCA** was not predicted to damage the framework crystallinity during ligand exchange, the framework leaching metal under the harsh solvothermal conditions would indicate that the dye is not as innocent as initially thought. The stability of frameworks to SALE reaction conditions is discussed further in Section 2.3.3.1.8 on pp.75.

### 2.3.3.1.4 Effect of pH on 7-DCCA

**7-DCCA** contains four sites readily susceptible to pH effects, indicated in Figure 2.31. To examine the effect of pH on the UV-VIS spectrum of **7-DCCA**, and hence identify factors contributing to the peak changes in the reaction solution spectra of **7-DCCA** SALE reactions discussed on pp.61 of Section 2.3.3.1.2, the effects of aqueous solutions of HCl (0.1 M) and NaOH (0.01 M) on **7-DCCA** were investigated.

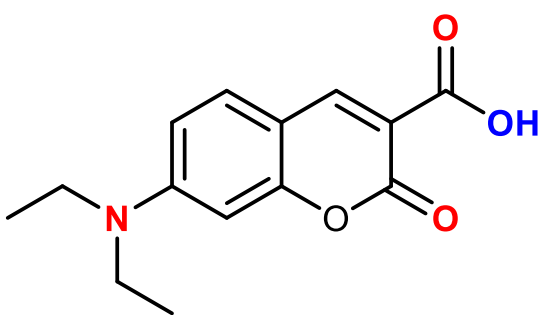


Figure 2.31. Structure of **7-DCCA**, with protonation sites (red) and deprotonation sites (blue) indicated.

50  $\mu$ L aliquots of these solutions were added to a solution of **7-DCCA** in MeOH (0.1 mL, 0.03 mM). The pH range for an equivalent aqueous solution would be 1-14. The UV-VIS spectrum was recorded immediately and after 24 hours. Deviations in peak position and peak absorbance from the **7-DCCA** peak ( $\lambda = 412$  nm,  $A = 0.88$  in pure MeOH) are shown in Figures 2.32 and 2.33 respectively.

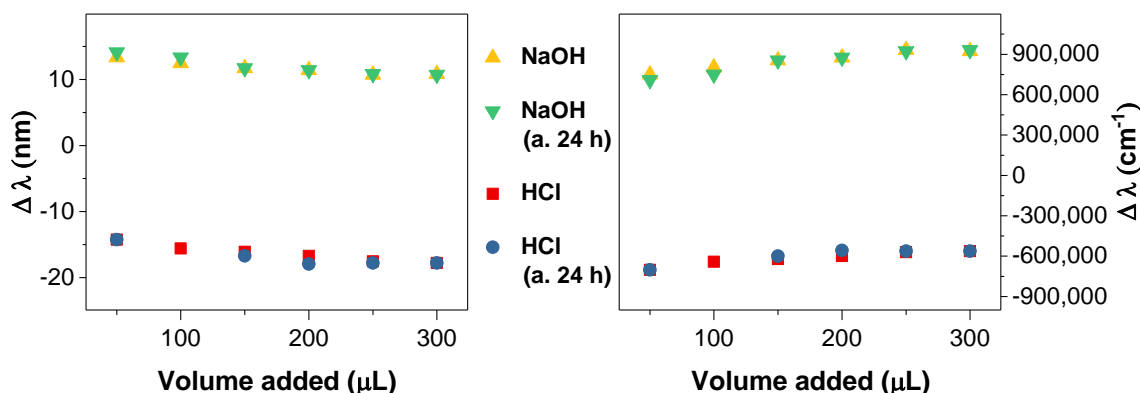


Figure 2.32. Plot of deviance from initial **7-DCCA** peak position with addition of HCl (0.01 M) and NaOH (0.01 M) in (left) nm and (right)  $\text{cm}^{-1}$ .

Figure 2.32 (left) shows a maximum of a 14 nm red shift and an 18 nm blue shift from 412 nm for NaOH (50  $\mu$ L) and HCl (300  $\mu$ L) addition respectively. The figure shown on the right displays the shift of the **7-DCCA** peak in wavenumbers, illustrating how great an effect the pH of the dye environment contributes to changes in energy of the system.

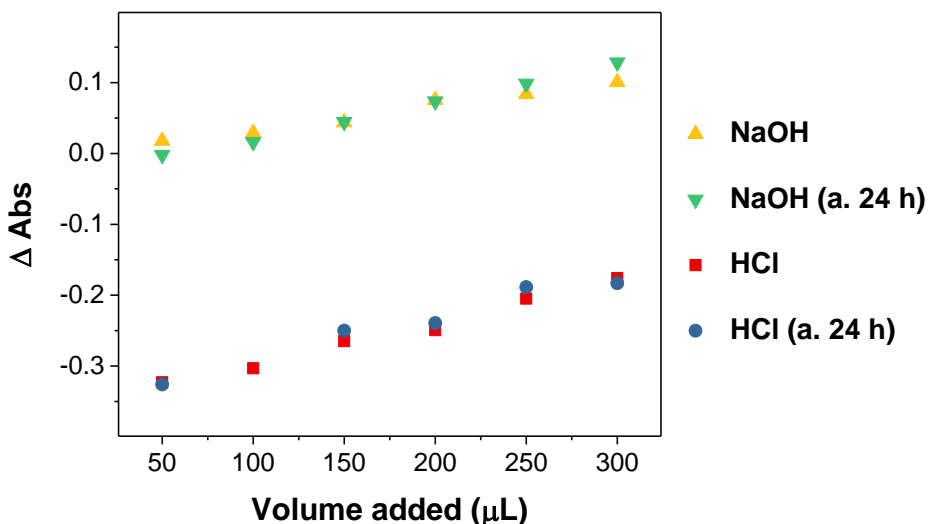


Figure 2.33. Plot of change in 7-DCCA peak absorbance with addition of HCl (0.01 M) and NaOH (0.01 M).

Figure 2.33 illustrates that the addition of base to the dye solution increases the absorbance and associated extinction coefficient of the dye peak, whilst addition of acid to the dye significantly reduces these values.

### 2.3.3.1.5 Contributing factors to 7-DCCA peak position in SALE reaction

There is a combination of factors the shifts observed in the **7-DCCA** SALE reaction solutions could be attributed to. Interaction of metal ions with **7-DCCA** (discussed in Section 2.3.3.1.3 on pp.64) prompted a maximum red shift of 13 nm, and red shifts of up to 14 nm were observed in the basification of **7-DCCA** solution. Blue shifts of 11 nm were observed in solutions containing **7-DCCA** and framework linkers (terephthalic acid and H<sub>4</sub>BPTC) and 13 nm following the acidification of **7-DCCA** solution.

As the MOF linkers discussed herein are carboxylic acids, and modulators used are all acids, the pH of reaction solutions are likely to be affected by these following exchange and release of these into solution. Due to the considerable number of variables that could contribute to shifting the position of the **7-DCCA** peak, further investigation into the mechanism of SALE is required to establish the most influential components of the reaction.

### 2.3.3.1.5 Stage 3 – Solution-phase UV-VIS

Acid-digestion of the modified materials was carried out to investigate the amount of dye present. Digestion of the framework would allow dissolution of the dye and subsequent analysis by solution-phase UV-VIS. We predicted that the concentration of **7-DCCA** would plateau and indicate a precise timescale for the exchange process when using ~0.03 mM dye solution.

Acid-digestion of the **7-DCCA** modified frameworks was carried out *via* sonication in conc. HCl (1 mL). The slurry was dried, however attempted re-dissolution of the residual solids was unsuccessful. Solids were therefore washed with MeOH (10 x 5 mL) to dissolve any **7-DCCA** present in the digested material. These washings were dried and then dissolved into dry MeOH (2 mL). As longer timescale SALE reactions were expected to have undergone the greatest extent of modification, the solids from these reactions were digested initially to explore viability of this approach. Figure 2.34 overleaf shows the UV-VIS absorption spectra of solutions made up from the washings of digested solids.

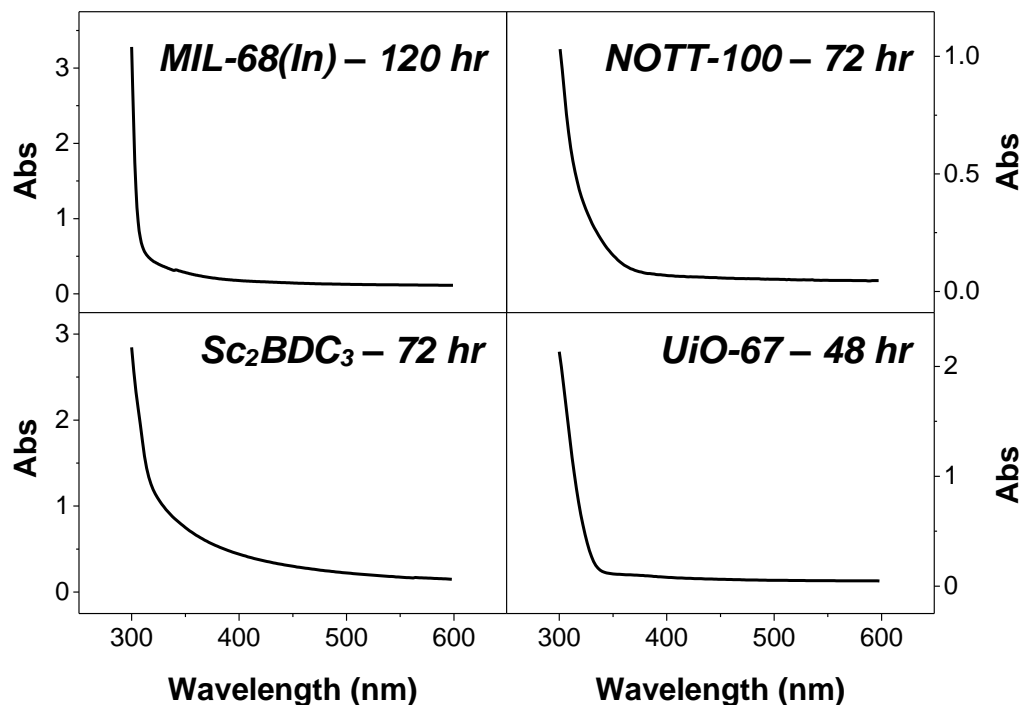


Figure 2.34. UV-VIS absorption spectra of HCl-digested **7-DCCA** modified MOF washings.

The spectra in Figure 2.34 show no characteristic **7-DCCA** peak. There are two possible reasons for this observation. Firstly, the concentration of **7-DCCA** incorporated into the framework was of such low concentration that it could not be observed. This is unlikely, as the absorbance of the lower concentration **7-DCCA** stock solution (0.0252 mM) was 0.83. The lowest estimated chemisorbed dye was 10% of the initial **7-DCCA** concentration (as summarised in Table 2.4 on pp.61), which would give an absorbance of detectable magnitude. The second reason is that **7-DCCA** was not stable to sonication in conc. HCl, and prolonged exposure to this process instigated decomposition of the fluorophore. The effects of pH on **7-DCCA** are discussed further in Section 2.3.3.1.4 on pp.65.

### 2.3.3.1.6 Stage 3 – UV-VIS-Diffuse Reflectance

As solution-phase UV-VIS spectroscopy was inconclusive in determining an accurate reaction timescale, UV-VIS-DRS was employed. This technique eliminated the exposure of the modified MOF to harsh conditions which could affect the fluorophore. A custom-built aluminium sample holder was used, facilitating quantitative comparison of the extent of modification between samples as the same amount of sample was in the measurement region. Similarly to the approach employed during the solution-phase UV-VIS measurements, we predicted that the reflectance of **7-DCCA** would plateau and indicate an accurate modification timescale.

All spectra were converted to  $F(R)$ , according to the Kubelka-Munk function.<sup>47</sup> A difference spectrum was generated for each UV-VIS-DR spectrum, where the unmodified framework UV-VIS-DR spectrum was subtracted from the UV-VIS-DR spectrum of modified materials. Spectral manipulations for all frameworks are shown overleaf in Figure 2.35.

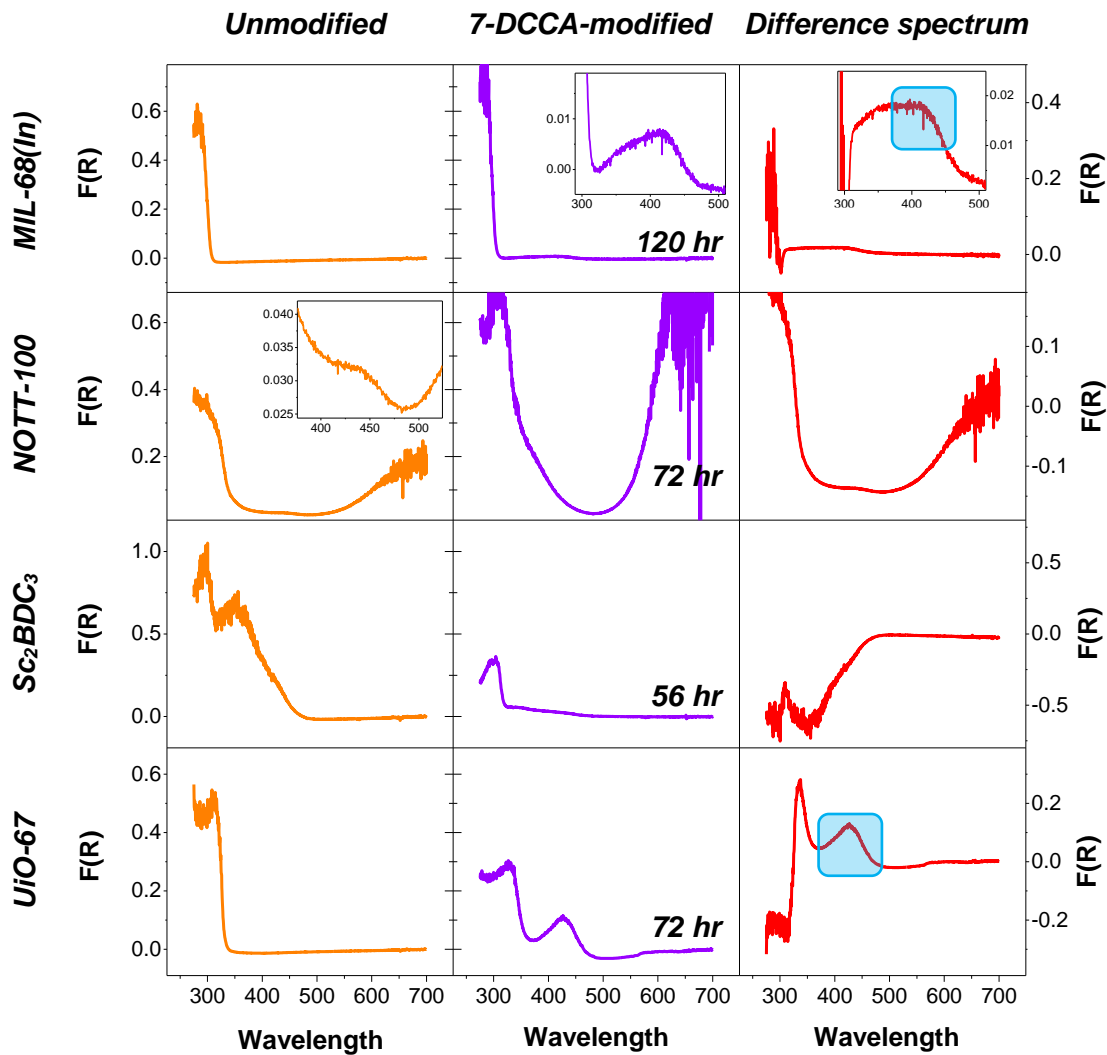


Figure 2.35. Example of analysis procedure for UV-VIS-DRS spectra, indicated. Regions highlighted in blue are indicative of 7-DCCA.

Figure 2.35 shows UV-VIS-DR spectra of all unmodified and modified frameworks and their difference spectra for the unmodified and final spectrum in each experiment.

As can be seen from the highlighted regions, peaks indicative of 7-DCCA were only discernible in UV-VIS-DR spectra for MIL-68(In) and UiO-67. In NOTT-100 and  $\text{Sc}_2\text{BDC}_3$ , 7-DCCA peaks were too heavily overlapped with reflectance bands from the framework so this technique was unsuitable for quantifying modification for these frameworks.

Each sample was modified over a range of timescales. All difference spectra for MIL-68(Indium) and UiO-67 were baseline corrected *via* an average of ten points (over the range 600.30–603.35 nm) and the reflectance of peaks in the region 412 nm (indicative of **7-DCCA**) collected from each spectrum. Plots of these values are shown below in Figure 2.36 and specific wavelengths chosen are tabulated in Appendix 1.

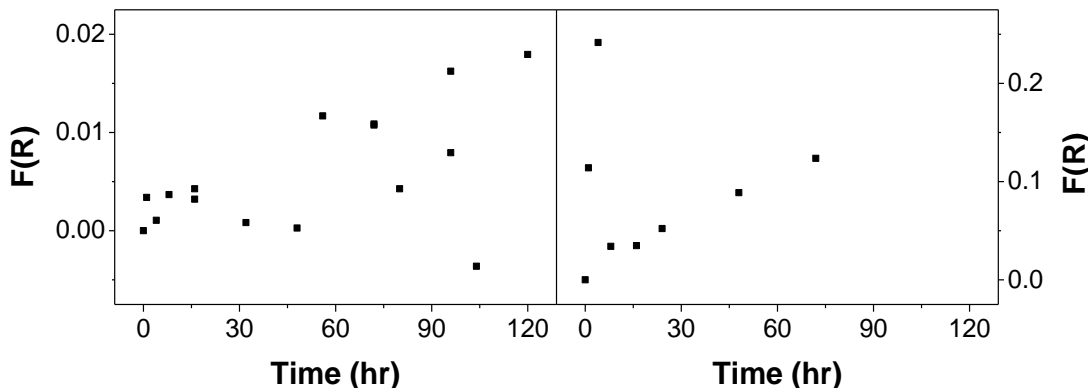


Figure 2.36. Plots of **7-DCCA** reflectance vs time for (left) MIL-68(Ind) and (right) UiO-67.

In both cases, there is an overall increase in the overall intensity of fluorescence originating from **7-DCCA**. The data have a high degree of scatter, particularly in the case of MIL-68(Indium), and because of the large apparent experimental error, and the lack of a clear plateau, this technique is inconclusive. There are two possible sources of error in this measurement. Firstly, our attempt to experimentally control the amount of material exposed to the measurement was unsuccessful, due to different crystallite sizes within samples and different packing arrangements of the material.

Secondly, the materials may have experienced structural change over time upon exposure to SALE reaction conditions, which were unpredictable and inconsistent across experiments. MOFs were also synthesised in several batches and therefore particle size may be inconsistent. The changes we are observing in the materials may be artefacts from different batches. This technique did, however, successfully confirm the presence of **7-DCCA** in the modified materials.

### 2.3.3.1.7 Stage 3 – Confocal laser scanning microscopy

Confocal laser scanning microscopy (CLSM) was employed as a technique to quantify reaction times following inconclusive results from UV-VIS-DRS. CLSM can interrogate single crystals of materials, whereas UV-VIS-DRS is appropriate for the analysis of bulk solids. Therefore, CLSM is not indicative of the bulk of a material, and several measurements of samples are required for data to be comparable with UV-VIS-DRS.

Single crystals were loaded to glass microscope slides, topped with a glass cover slip and sealed. Samples were excited using a 405 nm visible laser with a detector collection range of 429–549 nm. The power of the laser was varied for each sample to prevent saturation at the detector (MIL-68(In), 0.7%; NOTT-100, 100.0%; Sc<sub>2</sub>BDC<sub>3</sub>, 10.0%; UiO-67, 7.0%). Significant fluorescence quenching was observed during the collection of images for NOTT-100, likely due to the presence of Cu(II)-based metal nodes,<sup>48–50</sup> hence a substantially higher laser power was used for excitation. Z-stack images were collected on all samples to establish position of modification (*i.e.* surface-restricted or throughout the pore).

CLSM images were processed in Zen Blue 2.3, in which the fluorescence intensity within user selected areas can be interrogated with individual pixel resolution. Figure 2.37 overleaf shows the areas selected for the analysis of fluorescence in each framework. For each type of MOF, the same size spatial region was measured on each sample of that MOF across all reaction times, to enable direct comparison between the fluorescence intensity across a range of single crystals. The analysis generates an average and a standard deviation of fluorescence intensity for every pixel within the selected area.

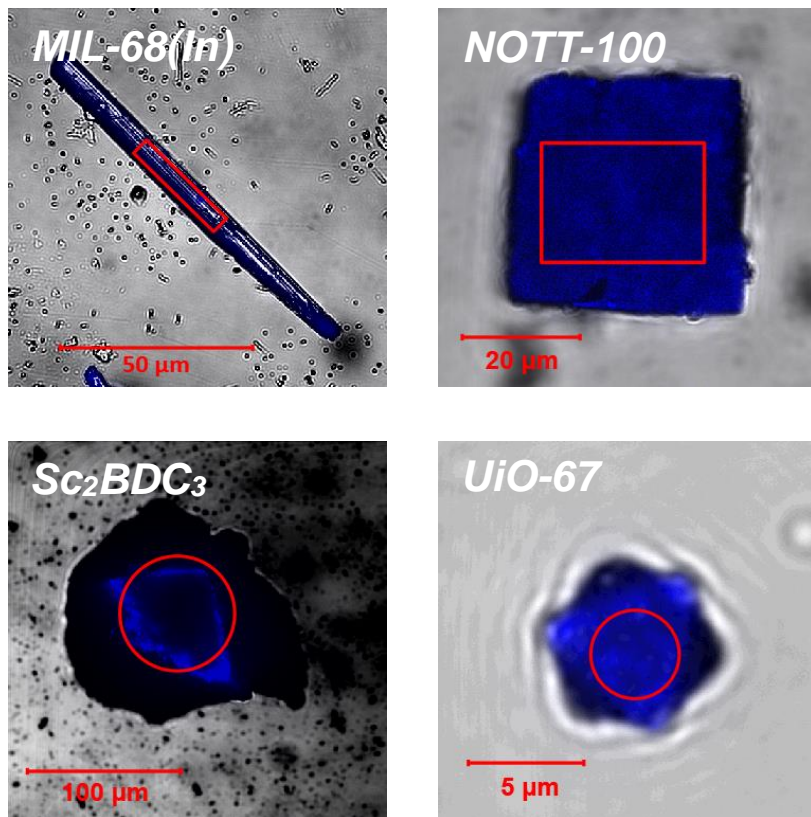


Figure 2.37. CLSM images, with histogram area outlined for each framework.

In each Z-stack, the image with the highest average fluorescence intensity detected (given by Zen Blue) in the chosen detector range (429–549 nm) was chosen for mapping. Between 3 – 7 crystals were mapped within each sample and the means of all average fluorescence intensities and associated standard deviations were calculated. These values are plotted for each framework overleaf in Figure 2.38.

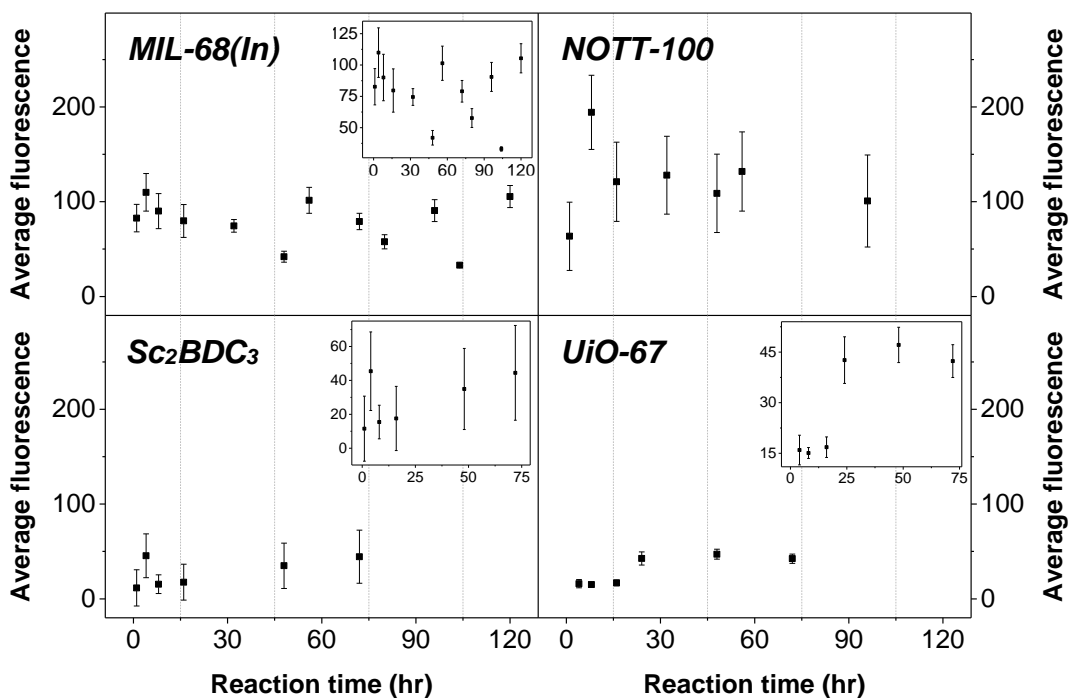


Figure 2.38. Plots of CLSM average fluorescence intensity of 7-DCCA-modified MOFs. Error bars are the mean standard deviations of each average fluorescence intensity.

The above plots indicate that for NOTT-100 and UiO-67, average fluorescence intensity did not increase after 24 hr. In Sc<sub>2</sub>BDC<sub>3</sub>, average fluorescence intensity was gradually increasing with time. The average fluorescence intensity in MIL-68(In) did not appear to stabilise at any point, and this is likely due to the significant photobleaching of the sample we observed during image collection, particularly during the collection of Z-stack images. Photobleaching was observed even when the samples were prepared using an anti-fade mounting media. Figure 2.39 shows reduced fluorescence intensity in the Z-stack images (Figure 2.39b) following prolonged excitation at 405 nm compared to the first image collected (Figure 2.39a).

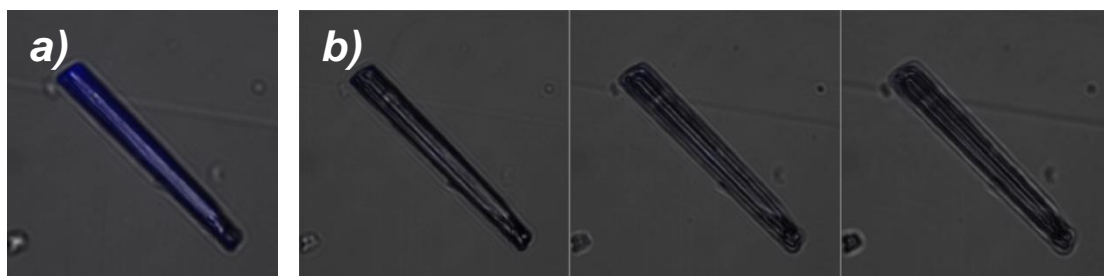


Figure 2.39. (a) Single and (b) Z-stack CLSM images of 4 hr 7-DCCA-modified MIL-68(In).

As the photobleaching mechanism was beyond the scope of this project, further experiments and techniques would need to be explored to investigate this.

According to this measurement, despite the significant variation in data points, it appears that by 24 hr, all of the modifications (except  $\text{Sc}_2\text{BDC}_3$ ) have reached their endpoint.

### 2.3.3.1.8 Framework stability in SALE control reaction conditions

Due to the forcing conditions employed for the modification of frameworks with **7-DCCA**, the frameworks were subjected to the SALE reaction conditions in the absence of the dye to investigate the stability of the frameworks in these conditions. All control reactions were carried out in anhydrous MeOH for 24 h and temperatures were as follows for each framework: MIL-68(Ind), 110 °C; NOTT-100, 130 °C;  $\text{Sc}_2\text{BDC}_3$ , 180 °C and UiO-67, 60 °C. Solids were collected via centrifugation, washed with MeOH (10 x 5 mL), dried in air and then analysed with PXRD to determine whether crystallinity had been retained.

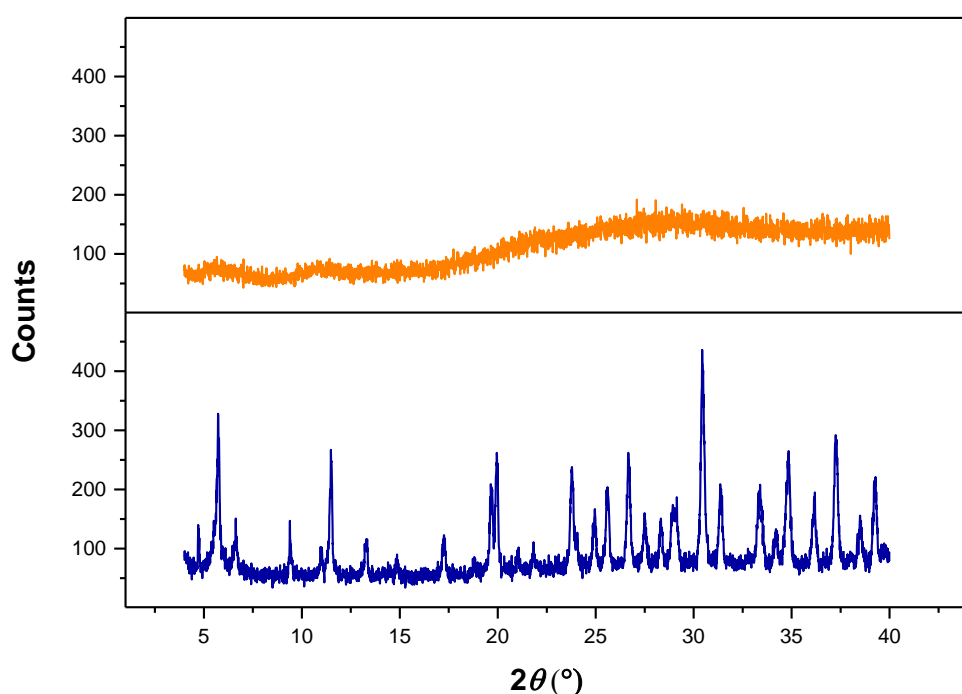


Figure 2.40. PXRD patterns of UiO-67 collected from (orange) control and (blue) **7-DCCA** SALE experiments.

Crystallinity was retained for all frameworks except UiO-67. Figure 2.40 shows two powder diffraction patterns – the top pattern (orange) is collected following heating UiO-67 in MeOH for 24 h at 60 °C in the absence of dye, and the bottom pattern (blue) is collected following heating the SALE reaction of UiO-67 with **7-DCCA**. Unexpectedly, these patterns show that crystallinity was retained in the presence of the dye, but not without it. Equivalent PXRD patterns for MIL-68(Ind), NOTT-100 and Sc<sub>2</sub>BDC<sub>3</sub> are shown in Appendix 1.

This could be due to attack of the Zr-node by either MeOH or **7-DCCA**, depending on the system. In the SALE reaction system, the exchange of the linker carboxylate binding group by the carboxylate group of **7-DCCA** results in retention of the ordered crystalline network present in the pristine MOF. We hypothesise that in the control experiment, MeOH attacks and coordinates to the node, disrupting the carboxylate binding environment throughout the structure and promoting the transition to an amorphous material.

### 2.3.3.1.9 Reaction time conclusions

UV-VIS-DRS was unsuitable for quantifying modification with **7-DCCA** in NOTT-100 and Sc<sub>2</sub>BDC<sub>3</sub> due to overlapping regions of the framework spectrum with the dye. Even though this was not anticipated for NOTT-100 (see Figure 2.13 and accompanying discussion in Section 2.3.1 on pp.39), the levels of modification observed in MIL-68(Ind) and UiO-67 suggest that **7-DCCA** peaks are significantly small enough to be obscured by the framework spectrum.

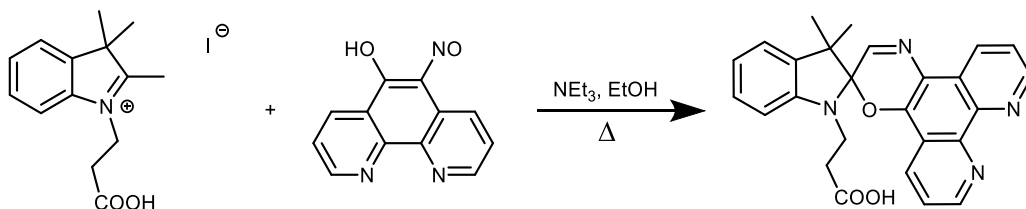
CLSM experiments demonstrate that 24 hr was sufficient for NOTT-100, Sc<sub>2</sub>BDC<sub>3</sub> and UiO-67 to chemisorb **7-DCCA**. Further SALE reactions with **phen-spiro** and **m-hydrazone** were therefore incubated for 24 hr. As the SALE reaction time for MIL-68(Ind) could not be quantified by either characterisation method, further modification of this framework with additional dyes was not investigated.

Photobleaching observed in MIL-68(In) hinders the reliability of any data extracted from CLSM experiments, as the amount of **7-DCCA** present could be vastly larger than the amount indicated in CLSM images.

Due to the significant issues of fluorescence quenching during the collection of CLSM images of NOTT-100-**7-DCCA**, additional modification of NOTT-100 with **phen-spiro** and **m-hydrazone** was not carried out. The next section will discuss the modification of  $\text{Sc}_2\text{BDC}_3$  and UiO-67 with **phen-spiro** and **m-hydrazone**.

### 2.3.3.4 Synthesis of phen-spiro photoswitch

**phen-spiro** is a spiroxazine-containing molecule synthesised within our laboratory. The synthetic reaction scheme is shown below in Scheme 2.1.



Scheme 2.1. *Phen-spiro* reaction scheme

Several synthetic difficulties presented themselves during the synthesis of this molecule. The initial reaction conditions employed were inspired by Meng and co-workers,<sup>51</sup> and the first reproduction of these reaction conditions yielded precipitation of pale yellow solid of moderate purity (analysed via  $^1\text{H}$  NMR spectroscopy) from the reaction mixture, which was collected via filtration. Upon extensive recreation of these reaction conditions, no solid ever precipitated again. The formation of the target molecule in the reaction mixture was confirmed by  $^1\text{H}$  NMR spectroscopic analysis, and the presence of the target was suggested when the initially pale yellow ethanolic reaction mixture turned deep blue, indicating the formation of open-form merocyanine (Figure 2.3, Section 2.1.2, pp.31).

Various approaches to purification were attempted, including;

- 1) Recrystallisation in a variety of solvents
- 2) Column chromatography (on both silica and alumina)
- 3) Automated column chromatography (on both silica and reverse-phase C<sub>8</sub> silica)
- 4) Preparative thin layer chromatography
- 5) High pressure liquid chromatography (HPLC)
- 6) Vapour diffusion crystallisation
- 7) Sublimation under reduced pressure
- 8) Complexation of carboxylic acid tail group, extraction into polar solvent

Purity was primarily assessed by <sup>1</sup>H NMR spectroscopy. Due to the effect of solvent polarity on the sensitive equilibrium of spirooxazine-merocyanine isomers (as discussed in Section 2.1.2 on pp.31–32), the separation of peaks indicating impurities and those indicating open-form **phen-spiro** was not always trivial. Following these difficulties, liquid chromatography-mass spectrometry (LC-MS) was often employed to assess sample purity.

Approach (1) yielded a variety of results. Due to the high solubility of the target in alcohols, these were commonly employed as the dissolution solvent. Addition of anti-solvents to this solution led to no precipitation (in the case of hexane and MeCN) or the precipitation of still impure solid (in the case of H<sub>2</sub>O). Hot-cold recrystallisations in any solvent did not lead to the precipitation of solid on cooling. Approach (2) failed due to the decomposition of the target molecule on silica, as confirmed by 2D TLC, and failure of the product to travel on alumina using a variety of solvent systems. Approach (3) led to the discharge of **phen-spiro** in all column fractions, unfortunately with several reaction impurities in all cases. Due to the decomposition of the target on silica, approach (4) was also unsuitable. Approach (5) failed in a similar manner to approach (3) and approach (6) led to the precipitation of still impure solid. In approach (7), the crude solid decomposed before pure **phen-spiro** sublimed.

Approach (8), the substitution of the carboxylic acid group proton with  $\text{Na}^+$  and  $\text{K}^+$  cations from  $\text{NaPF}_6$  and  $\text{KPF}_6$  and subsequent aqueous extraction, did not lead to the formation of pure **phen-spiro**.

Since purification of the target molecule was extremely difficult, the synthetic aim shifted to producing a crude material which was as pure as possible. Therefore, the conditions of synthesis were individually examined in an attempt to reduce the formation of side products during reaction.

Experiments were carried out to investigate the effects of changing the base concentration in the synthesis.  $\text{NEt}_3$  was employed as the base of choice throughout these experiments and was varied between 1 and 5 equivalents. In these experiments, purity of each crude reaction product was analysed *via*  $^1\text{H}$  NMR spectroscopy. A selection of  $^1\text{H}$  NMR spectra are shown in Figure 2.41. These spectra show the effect that varying base concentration in the reaction had on the purity of the crude material.

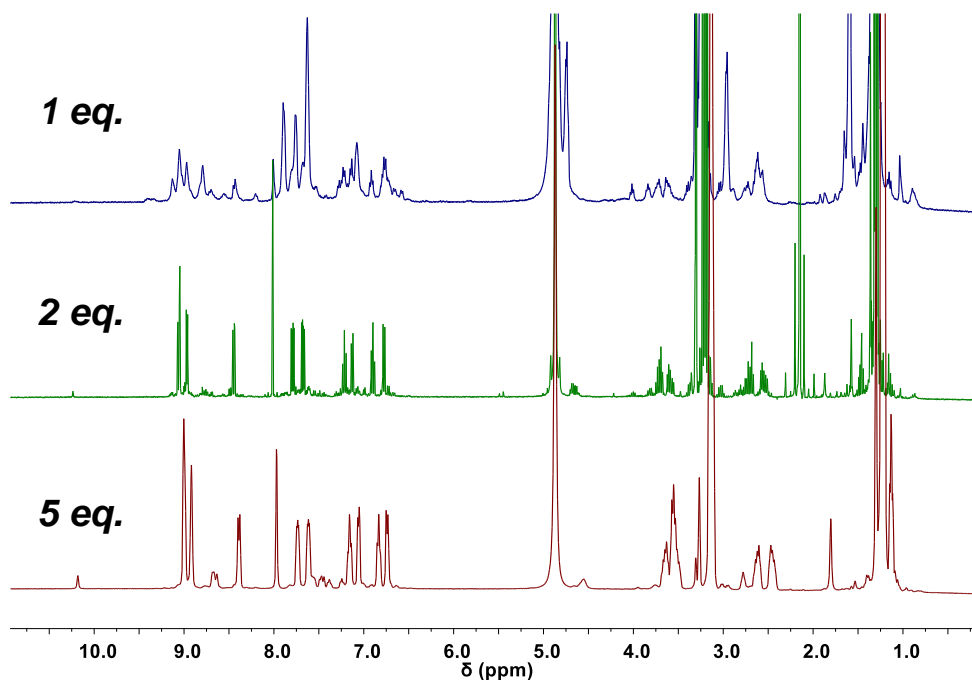


Figure 2.41.  $^1\text{H}$  NMR spectra in  $\text{MeOD}$  of **phen-spiro** reaction mixtures with varying amounts of  $\text{NEt}_3$ , as indicated.

Inspection of these spectra indicated that 5 equivalents of  $\text{NEt}_3$  led to the crude product with fewest impurities. These reactions were collected using anhydrous solvents with air sensitive techniques.

To investigate the effect of employing air-sensitive reaction techniques, a second reaction was performed using 5 equivalents of base using ‘bench’ solvents under air. The  $^1\text{H}$  NMR spectra of crude reaction mixtures are shown in Figure 2.42.

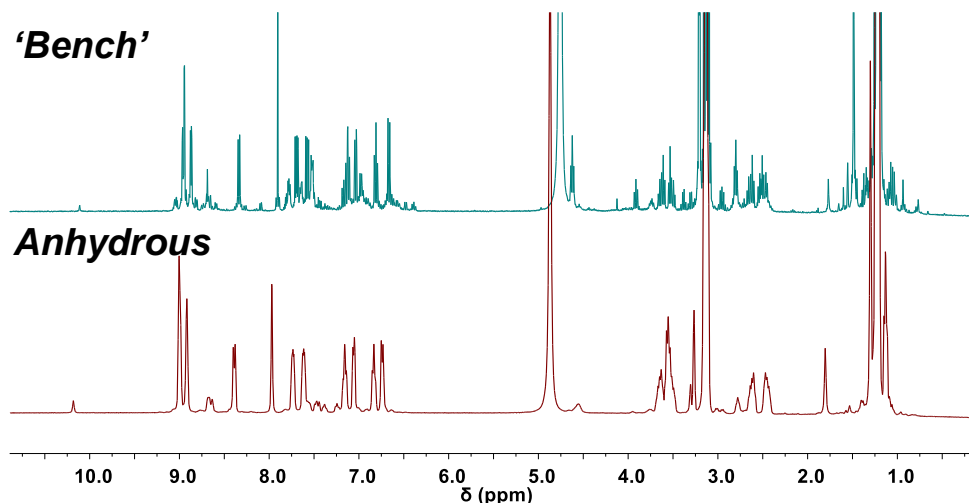


Figure 2.42.  $^1\text{H}$  NMR spectra in  $\text{MeOD}$  of **phen-spiro** reaction mixtures in ‘bench’ vs anhydrous solvent, as indicated.

These spectra indicate that performing **phen-spiro** synthesis under inert conditions in anhydrous solvents produces fewer unwanted side products.

To obtain more **phen-spiro** for additional experiments, **phen-spiro** synthesis was repeated under inert conditions, in anhydrous  $\text{EtOH}$  with 5 equivalents of anhydrous  $\text{NEt}_3$ . The reaction solution was dried under reduced pressure, redissolved into ‘bench’  $\text{EtOH}$  and stirred with activated charcoal ( $\sim 0.2$  g) for 30 minutes in an attempt to remove unknown impurities. The mixture was filtered and evaporated to dryness to yield a blue viscous oil. Sonication of this oil in  $\text{Et}_2\text{O}$  for 15 minutes followed by filtration and washing with cold  $\text{Et}_2\text{O}$  yielded dark blue solid. The solid was dissolved in a 1:1 ratio of  $^i\text{PrOH}:\text{H}_2\text{O}$ , and  $^i\text{PrOH}$  was removed under reduced pressure to precipitate blue solid. This solid was collected by filtration and washed with cold  $\text{Et}_2\text{O}$ .

The purity of **phen-spiro** obtained from these reaction conditions was inconsistent, even when using the same batches of starting materials and solvents. None of the **phen-spiro** batches synthesised were pure, and hence the batch used for the post-synthetic modification of frameworks (discussed in Section 2.3.3.5) is not pure. Analysis of the mass fragments in LC-MS traces (shown in Appendix 1) suggested that the material was contaminated primarily with the nitrosophenanthrolinol starting material.

### 2.3.3.5 Post-synthetic modification with photoswitches

After establishing conditions for the SALE of frameworks with **7-DCCA**, frameworks were modified with two photoswitches; **phen-spiro** and **m-hydrazone** (Figure 2.43). **phen-spiro**, a spirooxazine-based material, was synthesised in our laboratory (detailed previously in Section 2.3.3.4) and **m-hydrazone** was provided by Ivan Aprahamian, a collaborator from Dartmouth College, USA.

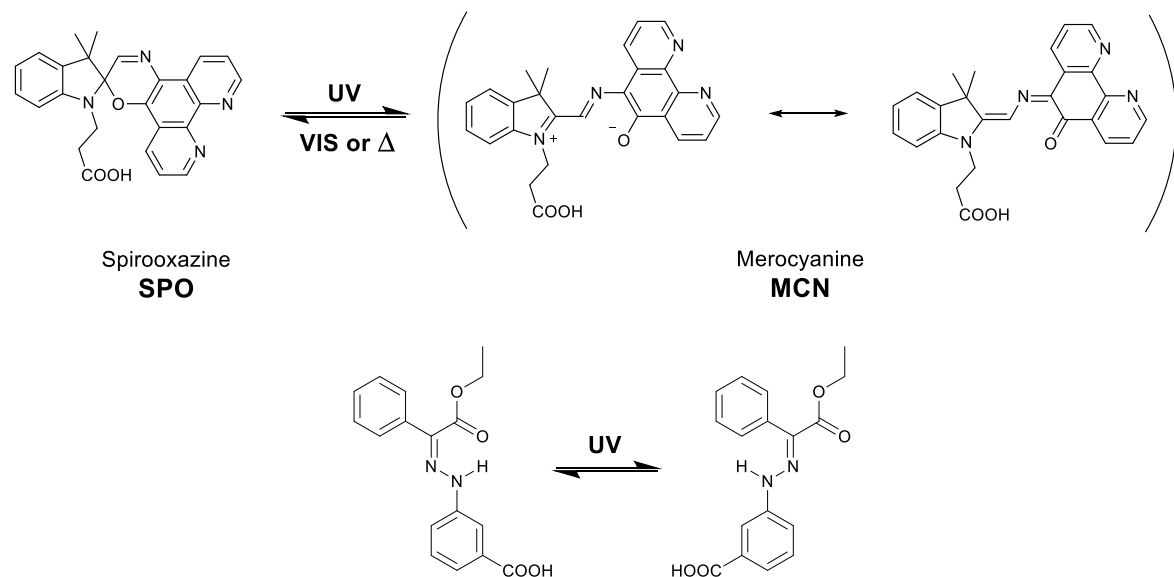


Figure 2.43. Structures of (top) **phen-spiro** and (bottom) **m-hydrazone**, with their respective photoswitched states.

There were two main aims of modifying frameworks with photoswitches. Firstly, to assess whether the modification inhibited guest uptake by blocking access to the pores of the framework. Secondly, to investigate whether framework-bound switches were still active in the solid state. If they were, this gives potential for the phototriggered release of pore-bound guest molecules.

SALE reactions were carried out using 100 mg of MOF and 10 mL of dye solution to ensure sufficient material was obtained for N<sub>2</sub> BET isotherms, discussed later in Section 2.3.3.6 on pp.100.

Frameworks were initially modified with 0.03 mM solutions of **phen-spiro** and **m-hydrazone** in anhydrous MeOH (except for UiO-67, when anhydrous MeCN was used) in solvothermal reaction vessels for 24 hours at different temperatures (NOTT-100, 130 °C; Sc<sub>2</sub>BDC<sub>3</sub>, 180 °C, UiO-67, 60 °C). Following incubation, solids were collected *via* centrifugation, washed with MeOH (10 x 10 mL) – or MeCN for UiO-67 – and dried in air. Solids were then analysed by UV-VIS-DRS and CLSM. Note that UiO-67 modification was attempted in MeOH, however all samples amorphized, unlike in the presence of **7-DCCA**.

In the case of the modification of UiO-67 with **phen-spiro**, CLSM images (Figure 2.44) showed no fluorescence in the ranges of 428–508 or 642–695 nm, despite excitation with both 405 and 633 nm lasers (63.2 and 100.0% power respectively), indicating that modification with a detectable amount of **phen-spiro** had failed.

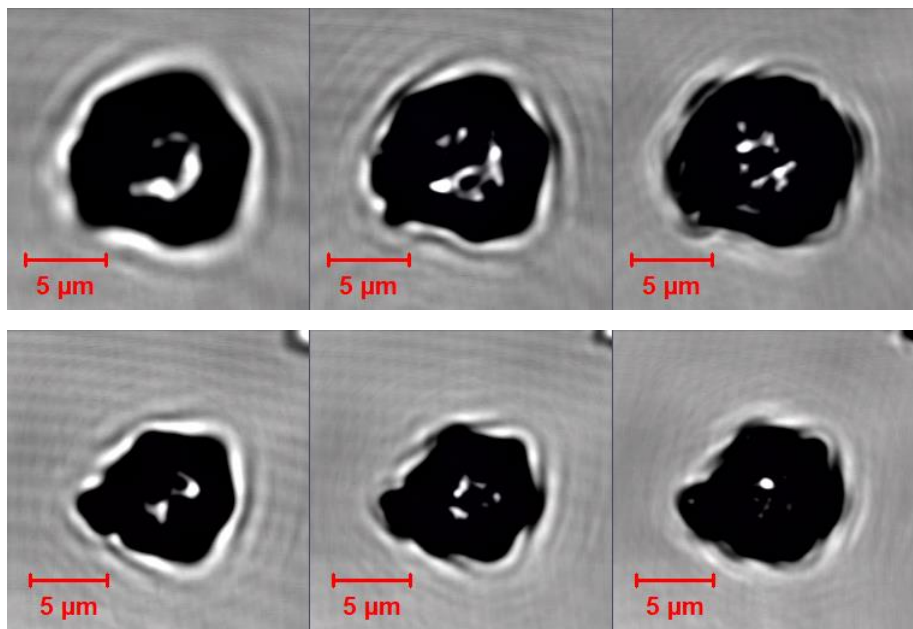


Figure 2.44. CLSM images of two separate single crystals of *UiO*-67 modified with 0.03 mM **phen-spiro** in MeCN at 60 °C for 24 hours.

As a result of this experiment, all subsequent MOF modifications were performed with a more concentrated solution of **phen-spiro** (5 mM) to ensure sufficient dye was introduced to the framework. CLSM images of **phen-spiro** modified materials are shown and discussed below.

### 2.3.3.5 Solid-state photoswitch behaviour

#### 2.3.3.5.1 PSM of $\text{Sc}_2\text{BDC}_3$ with phen-spiro

Modification of  $\text{Sc}_2\text{BDC}_3$  was characterised using CLSM and UV-VIS-DRS. More conclusions regarding position and extent of modification could be extracted from CLSM than UV-VIS-DRS. For CLSM experiments, samples were excited simultaneously with 405 and 633 nm lasers (18.0 and 40.0% power respectively) and fluorescence was detected in the regions 428–508 and 642–695 nm. Z-stack images of  $\text{Sc}_2\text{BDC}_3\text{-phen-spiro}$  are shown in Figure 2.45.

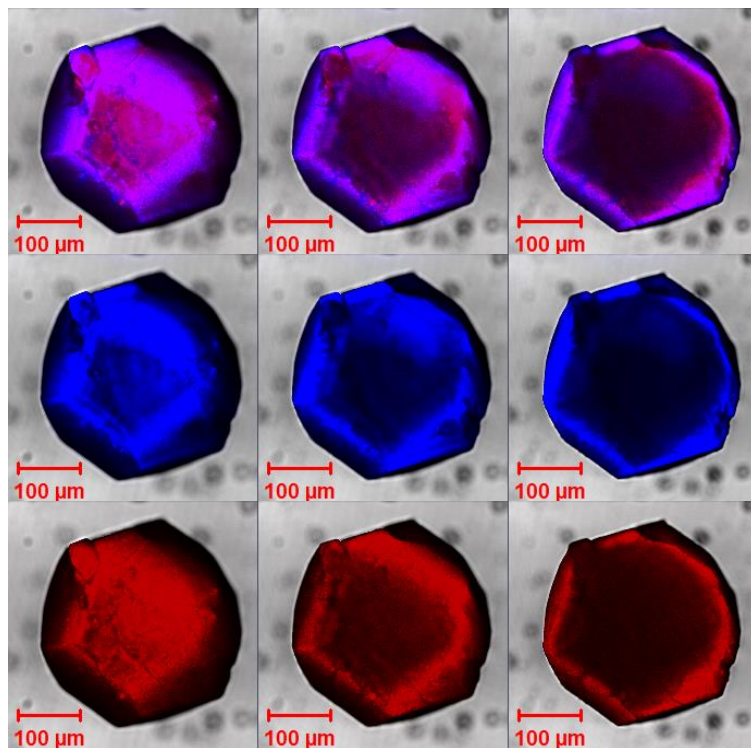


*Figure 2.45. CLSM Z-stack images of **phen-spiro**-modified  $\text{Sc}_2\text{BDC}_3$  at 22.5  $\mu\text{m}$  steps (left to right). Blue and red shading indicates 428–508 nm and 642–695 nm fluorescence respectively. Purple shading indicates combined fluorescence.*

The above images confirm successful modification of  $\text{Sc}_2\text{BDC}_3$  single crystals with **phen-spiro**. The blue and red fluorescence indicates the open **SPO** and closed **MCN** forms respectively. The difference in the blue and red fluorescence seems to be that blue emission is observed to a greater depth in the crystal (although the core is still non-emissive) and qualitatively the surface has more even red fluorescence than blue. This could be either due to different penetrations of **SPO** and **MCN** forms in the framework upon modification, or different degrees of photoswitching forming a photostationary equilibrium during the dual irradiation of the measurement. Figures 2.45 (above) and 2.46 (overleaf) show that modification is primarily at the surface, as confirmed by several single crystals, in the same manner as for **7-DCCA** modification.

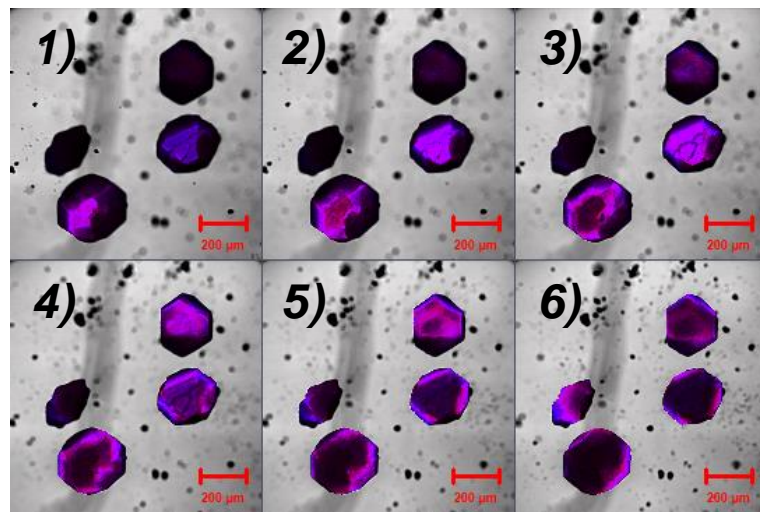


Figure 2.46. CLSM Z-stack images of **phen-spiro**-modified  $\text{Sc}_2\text{BDC}_3$  at  $22.5 \mu\text{m}$  steps (1; top of crystal and 6; bottom of crystal). Purple shading indicates combined  $428\text{--}508 \text{ nm}$  and  $642\text{--}695 \text{ nm}$  fluorescence.

UV-VIS-DRS spectra of  $\text{Sc}_2\text{BDC}_3$ ,  $\text{Sc}_2\text{BDC}_3\supset\text{phen-spiro}$  and **phen-spiro** are shown in Figure 2.47. The spectrum of  $\text{Sc}_2\text{BDC}_3\supset\text{phen-spiro}$  (middle) shows peaks indicative of **phen-spiro** modification at  $430\text{--}500$  and  $520\text{--}700 \text{ nm}$ , where the latter indicates the closed **MCN** form. The higher energy band indicates a protonated merocyanine form,<sup>19</sup> as the region of the open **SPO** form is overlapped by  $\text{Sc}_2\text{BDC}_3$  reflectance bands.

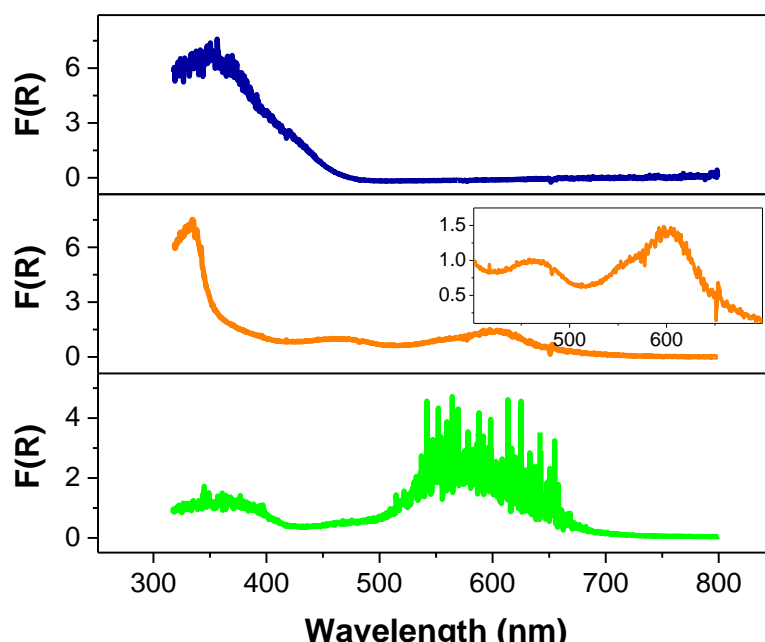


Figure 2.47. UV-VIS-DR spectra of  $\text{Sc}_2\text{BDC}_3$  (top),  $\text{Sc}_2\text{BDC}_3\supset\text{phen-spiro}$  (middle) and **phen-spiro** (bottom).

### 2.3.3.5.2 Photoswitching of $\text{Sc}_2\text{BDC}_3\text{-phen-spiro}$

To investigate the photoswitching capabilities of **phen-spiro** when covalently bound to  $\text{Sc}_2\text{BDC}_3$ , irradiation experiments were carried out *in situ* during CLSM and UV-VIS-DRS analysis.

#### **CLSM**

Samples of  $\text{Sc}_2\text{BDC}_3\text{-phen-spiro}$  were irradiated *in situ* on the confocal microscope with a 633 nm laser (100.0% power) for periods of time ranging from 90–300 sec, and Z-stack images were collected following each irradiation period. For image collection, samples were excited simultaneously with 405 and 633 nm lasers (18.0 and 40.0% power respectively) and fluorescence was detected in the regions 428–508 and 642–695 nm. Images collected following each timed irradiation step are shown overleaf in Figure 2.48.

Simultaneous excitation potentially instigates photoconversion in both forward and reverse directions. This will affect the photostationary equilibrium established during irradiation with the 633 nm laser, and hence introduces an additional layer of complexity to the system and associated measurements. Dual excitation was performed in order to collect measurements of both species simultaneous, and, for the purpose of these experiments, we were interested in the proportion of change of each species as opposed to absolute kinetics of photoconversion between the two states.

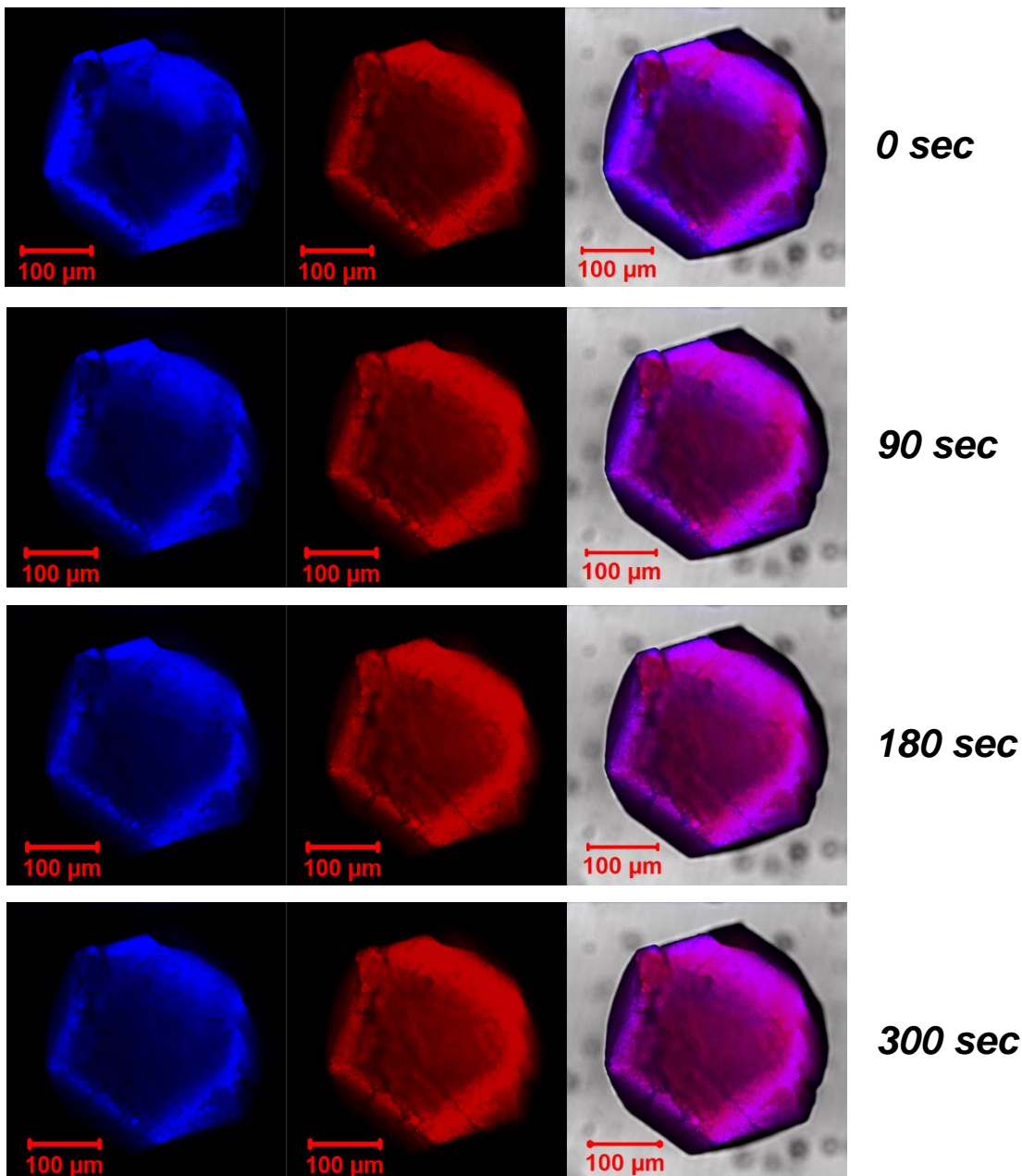


Figure 2.48. CLSM images of  $\text{Sc}_2\text{BDC}_3\text{-phen-spiro}$  after varying specified periods of irradiation with a 633 nm laser. Blue and red shading indicates 428–508 nm and 642–695 nm fluorescence respectively. Purple shading indicates combined fluorescence.

Figure 2.48 shows reducing blue fluorescence and increasing red fluorescence with increasing irradiation time. The increase in red MCN fluorescence gives rise to the observed reddening of the combined fluorescence (Figure 2.48, purple) from 0 to 300 seconds of irradiation.

Dual irradiation with both 405 and 633 nm lasers in this experiment instigates a shift in the equilibrium of photostationary states, where part of the blue, closed-form **SPO** state switches to the red, open-form **MCN**. The area on the crystal used to generate fluorescence intensity values is shown below in Figure 2.49. This area covers both core and shell parts of the crystal, and at no point during the measurement was fluorescence emission saturating the microscope detector.

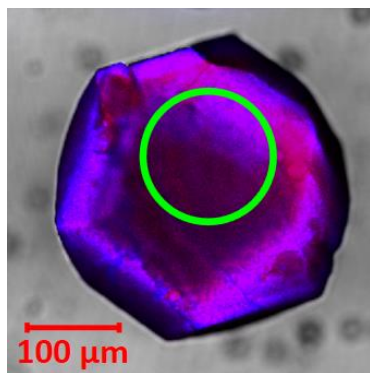


Figure 2.49. CLSM image of  $\text{Sc}_2\text{BDC}_3\text{-phen-spiro}$ , with area used (25,893 pixels) to generate fluorescence intensity values indicated in green. Purple shading indicates combined 428–508 and 642–695 nm fluorescence.

Figure 2.50 shows a plot of the average fluorescence intensity measured in ranges of 428–508 and 642–695 nm within the sampled area with increasing time of irradiation with a full-power 633 nm laser.

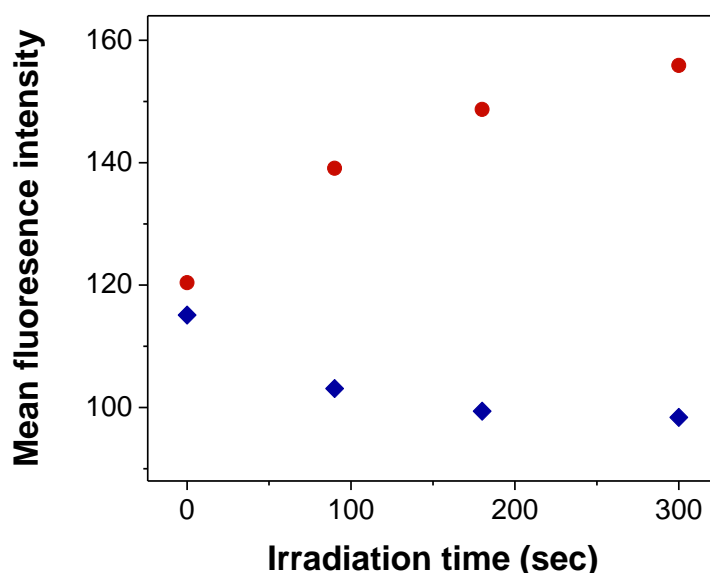


Figure 2.50. Plot of mean fluorescence intensity with increasing 633 nm irradiation. Blue and red points indicate fluorescence detected between 428–508 nm and 642–695 nm respectively.

The above plot confirms the qualitative visual observation of an increase in red **MCN** fluorescence and associated decrease in blue **SPO** fluorescence with increasing irradiation time. This demonstrates that changes in the ratio of these species can be detected by this method.

Samples of  $\text{Sc}_2\text{BDC}_3\text{-phen-spiro}$  were irradiated *in situ* in the UV-VIS-DRS sample holder using a custom-built 390 nm light source. UV-VIS-DR spectra were collected before and after irradiation and are shown in Figure 2.51.

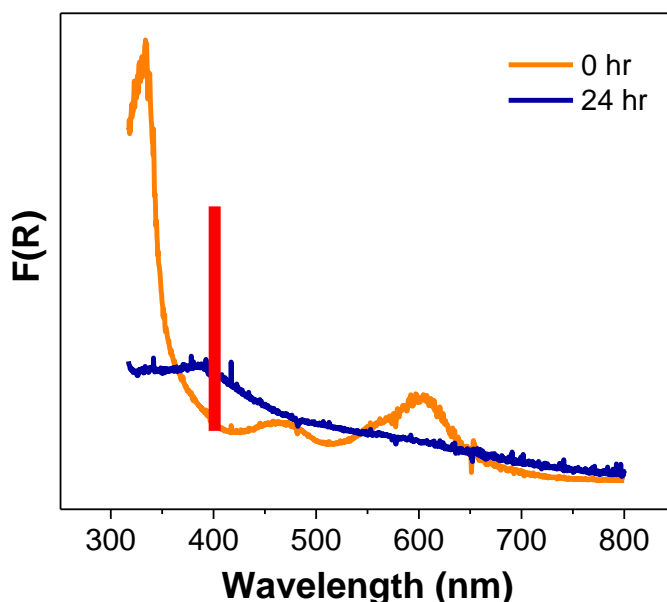


Figure 2.51. Plots of UV-VIS-DR spectra of  $\text{Sc}_2\text{BDC}_3\text{-phen-spiro}$  (orange) without irradiation and (blue) after 24 hr irradiation (390 nm – red line).

The post-irradiation UV-VIS-DR spectra (Figure 2.51) suggest that the photoswitch suffered from significant photobleaching during the 24 hr irradiation. Further work is required to establish the mechanism of photobleaching and conditions to investigate photoswitchability.

### 2.3.3.5.3 PSM of UiO-67 with phen-spiro

Modification of UiO-67 was characterised using CLSM and UV-VIS-DRS. More conclusions regarding position and extent of modification could be gathered from CLSM than UV-VIS-DRS. Given the difficulty disentangling the bimodal excitation employed during photoswitching experiments discussed in Section 2.2.3.5.2, **UiO-67 $\supset$ phen-spiro** samples were not excited simultaneously. Samples for CLSM experiments were excited separately with either 405 or 633 nm lasers (63.2 and 100.0% power respectively) and fluorescence detected in the regions 428–508 and 642–695 nm. Z-stack images of **UiO-67 $\supset$ phen-spiro** are shown in Figure 2.52.

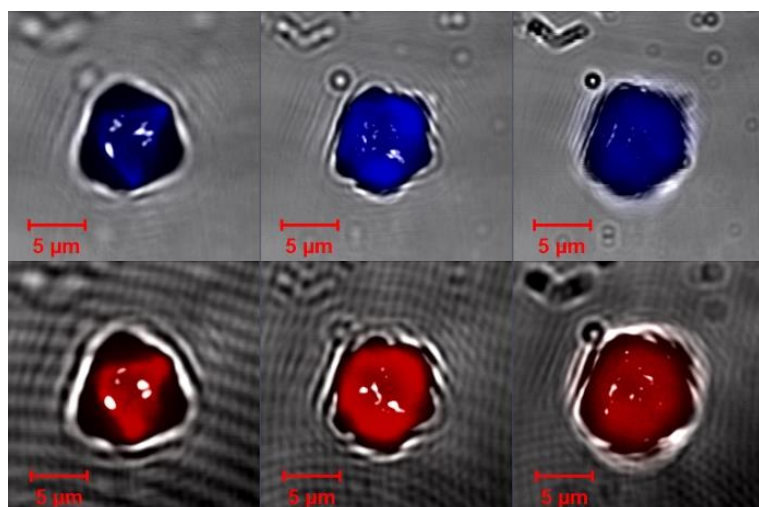


Figure 2.52. CLSM Z-stack images of **phen-spiro**-modified **UiO-67** at 7.5  $\mu\text{m}$  steps (left to right). Blue and red shading indicates 428–508 nm and 642–695 nm fluorescence respectively.

CLSM images above (Figure 2.52) show that modification of **UiO-67** with **phen-spiro** occurred throughout the whole crystal, consistent with **7-DCCA** modification. Fluorescence intensity from **SPO** and **MCN** forms appeared comparable across the sample, with no evidence of detector saturation.

UV-VIS-DRS spectra of UiO-67, UiO-67 $\supset$ **phen-spiro** and **phen-spiro** are shown in Figure 2.53. The spectrum of UiO-67 $\supset$ **phen-spiro** (middle) showed peaks indicative of **phen-spiro** modification at 320–400 and 520–700 nm, indicative of the open **SPO** and closed **MCN** forms respectively.

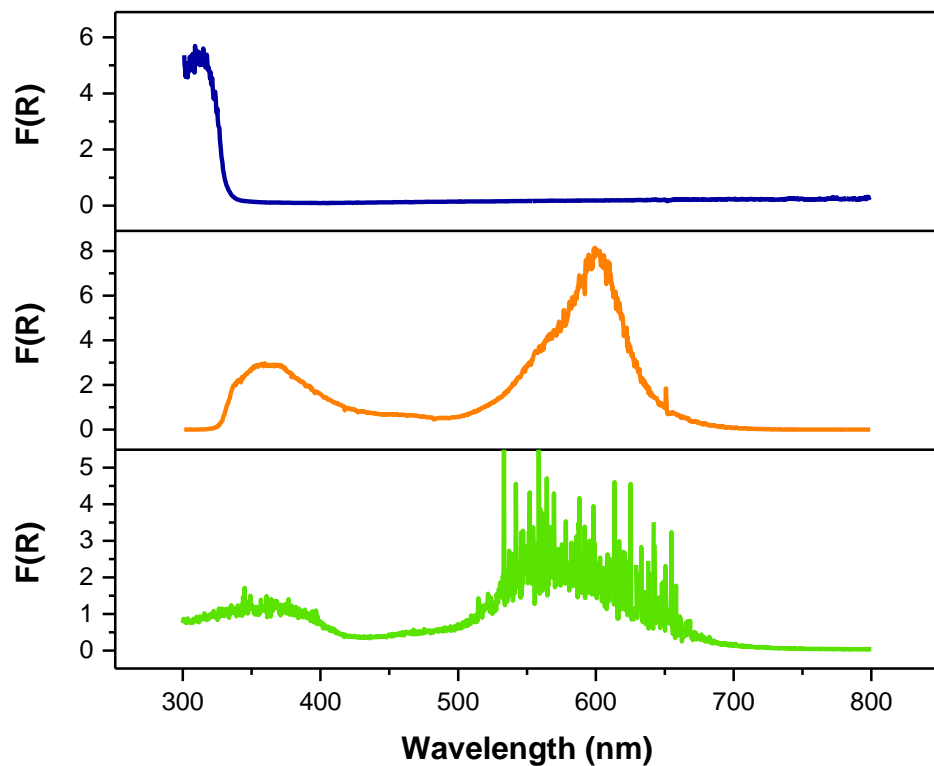


Figure 2.53. UV-VIS-DR spectra of UiO-67 (top),  
UiO-67 $\supset$ **phen-spiro** (middle) and **phen-spiro** (bottom).

### 2.3.3.5.4 Photoswitching of UiO-67 $\supset$ phen-spiro

To investigate the photoswitching capabilities of **phen-spiro** when covalently bound to UiO-67, irradiation experiments were carried out as part of CLSM and UV-VIS-DRS.

#### CLSM

Samples of UiO-67 $\supset$ **phen-spiro** were irradiated *in situ* on the confocal microscope, initially using a 405 nm laser (100.0% power), and subsequently using a 633 nm laser (100.0% power). Z-stack images were collected following each irradiation period, with separate 405 and 633 nm excitation. Fluorescence was collected in the ranges 428–508 nm (for 405 nm excitation) and 642–695 nm (633 nm excitation).

The average fluorescence intensity of each detection range (between 428–508 and 642–695 nm) was extracted from the area illustrated in Figure 2.54. To do this, Zen Blue 2.3 software is used to plot the intensity histogram of all the pixels in the chosen region. From this histogram, a mean fluorescence intensity per pixel is obtained.

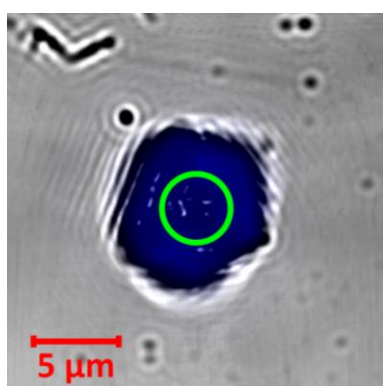


Figure 2.54. CLSM image of UiO-67 $\supset$ **phen-spiro**, with area used (6,834 pixels) to generate fluorescence intensity values indicated in green.  
Blue shading indicates 428–508 nm fluorescence.

In the first part of the experiment, after 90 sec irradiation with a 405 nm laser (100.0% power), blue average fluorescence intensity from the closed **SPO** form collected between 428–508 nm (measured with 405 nm excitation) decreased slightly from 135.0 to 129.6 counts per pixel, consistent with a small degree of conversion of **SPO** to **MCN** form. In comparison, red average fluorescence intensity from the open **MCN** form collected between 642–695 nm (measured with 633 nm excitation) fell significantly from 176.1 to 77.6. This is surprising, as we had anticipated that 405 nm irradiation would not induce back conversion of **MCN** to **SPO** form. There are two possible explanations; (i) irradiation at 405 nm is causing **MCN** to **SPO** conversion but the emission at 428–508 is not **SPO** emission, or (ii) the sample is experiencing photobleaching due to the high laser power. The latter possibility is consistent with the photobleaching observed during UV irradiation of  $\text{Sc}_2\text{BDC}_3\text{-phen-spiro}$  in UV-VIS-DRS experiments. Photobleaching of  $\text{UiO-67-phen-spiro}$  is discussed briefly further below.

In the second part of the experiment, irradiation of the material for 90 sec with a 633 nm laser (100.0% power) increased the blue average fluorescence intensity ascribed to the closed **SPO** form (collected 428–508 nm and excited at 405 nm) from 129.6 to 150.7 counts per pixel, where it remained constant following a further 300 sec of 633 nm irradiation. The red average fluorescence intensity (collected 642–692 nm and excited at 633 nm) decreased markedly from 176.1 to 14.5 counts per pixel from the beginning to the end of the experiment (390 seconds in total). The overall drop in red fluorescence is consistent with the anticipated conversion of the **MCN** form into **SPO**. The initial rise in blue fluorescence is also indicative of laser-induced formation of **SPO** from **MCN**. However, the lack of increased blue fluorescence on further irradiation may be indicating some degree of photobleaching in a similar manner to that potentially observed on 405 nm irradiation in the first part of this experiment.

Figure 2.55 shows a wide field of view on another sample of  $\text{UiO-67}\square\text{phen-spiro}$  also subjected to laser photolysis at 633 nm. There is a reduction in overall fluorescence in both detector channels (428–508 and 642–692 nm) after extended irradiation, strongly suggesting that again, laser irradiation at full power is causing photobleaching in these samples. Further work is needed to minimise photobleaching by measurement using lower laser powers and therefore weaker irradiation, and clearly more time points are required to understand the photoconversion process.

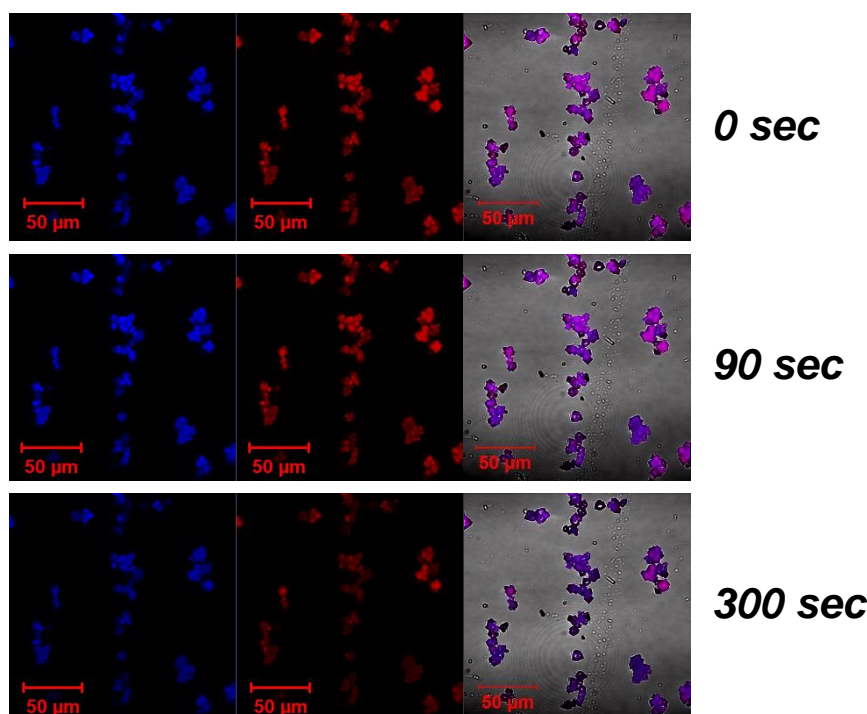


Figure 2.55. CLSM of  $\text{UiO-67}\square\text{phen-spiro}$  after varying spells of irradiation with a 633 nm laser. Blue and red shading indicates 428–508 nm and 642–692 nm fluorescence respectively. Purple shading indicates combined fluorescence.

Data from  $\text{Sc}_2\text{BDC}_3\square\text{phen-spiro}$  and  $\text{UiO-67}\square\text{phen-spiro}$  *in situ* CLSM irradiation experiments have shown that irradiation with the CLSM systems excitation lasers can prompt switching between **SPO** and **MCN** states. Unfortunately, the samples can suffer from photobleaching, rendering quantitative data regarding the amount of each state unreliable. To prevent photobleaching of **phen-spiro** in future CLSM experiments, lower laser powers with longer irradiation times should be used.

## UV-VIS-DRS

Samples of  $\text{UiO-67}\square\text{phen-spiro}$  were irradiated *in situ* in the UV-VIS-DRS sample holder using a custom-built 390 nm light source. UV-VIS-DR spectra were collected before, after 1 hr irradiation and after 24 hr irradiation and are shown in Figure 2.56.

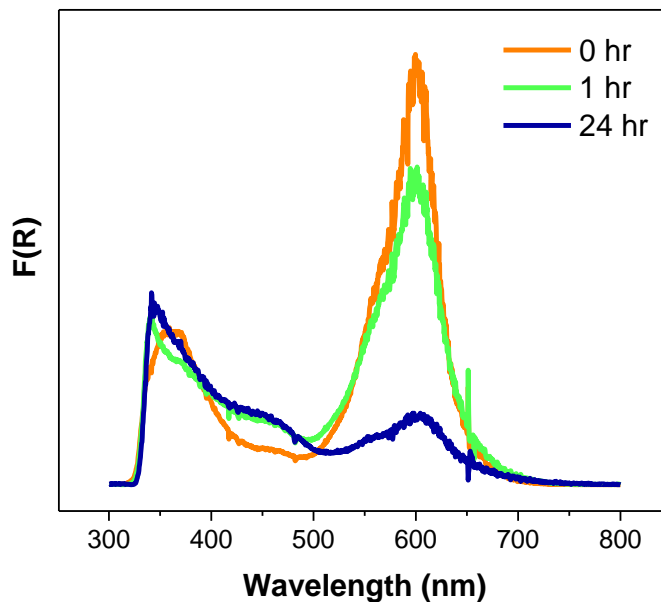


Figure 2.56. Plots of UV-VIS-DR spectra of  $\text{UiO-67}\square\text{phen-spiro}$  without irradiation (orange), after 1 hr (green) and after 24 hr (blue) 390 nm irradiation.

Similarly to  $\text{Sc}_2\text{BDC}_3\square\text{phen-spiro}$ , significant photobleaching of **phen-spiro** was observed following irradiation, identified by the significant reduction in the open-form **MCN** band at ca. 600 nm, with no identifiable increase in  $F(R)$  at ca. 360 nm, associated with closed-form **SPO**.

Photobleaching in both of these experiments with  $\text{UiO-67}\square\text{phen-spiro}$  is in contrast to  $\text{Sc}_2\text{BDC}_3\square\text{phen-spiro}$ , in which photobleaching was only observed during *in situ* irradiation of the UV-VIV-DRS experiments. Given the duration of irradiation of both samples was comparable in the CLSM experiments, we tentatively propose that **phen-spiro** moiety has become less photostable upon binding to the Zr-node than when bound to  $\text{Sc}_2\text{BDC}_3$ .

### 2.3.3.5.5 PSM of $\text{Sc}_2\text{BDC}_3$ with *m*-hydrazone

$\text{Sc}_2\text{BDC}_3$  was modified using a solution of ***m*-hydrazone** in anhydrous MeOH (10 mL, 0.03 mM) for 24 hr at 180 °C. Solids were collected by centrifugation, washed with MeOH (10 x 10 mL) and dried in air. Modification was confirmed using CLSM and images are shown in Figure 2.57.

CLSM images were excited with a 405 nm laser (10.6%) and fluorescence detected in the regions 428–508 and 642–695 nm. The Z-isomer of ***m*-hydrazone** fluoresces at 340 nm, and the photoswitched state fluoresces at 370 nm. This unpublished data was provided in communication with our collaborator, Ivan Aprahamian. Due to the relatively narrow window between the Z-isomer and photoswitched state of ***m*-hydrazone** compared to the CLSM detector settings, it is likely that any fluorescence detected from either state was being detected in the same detection range (428–508 nm) and hence could not be separated.

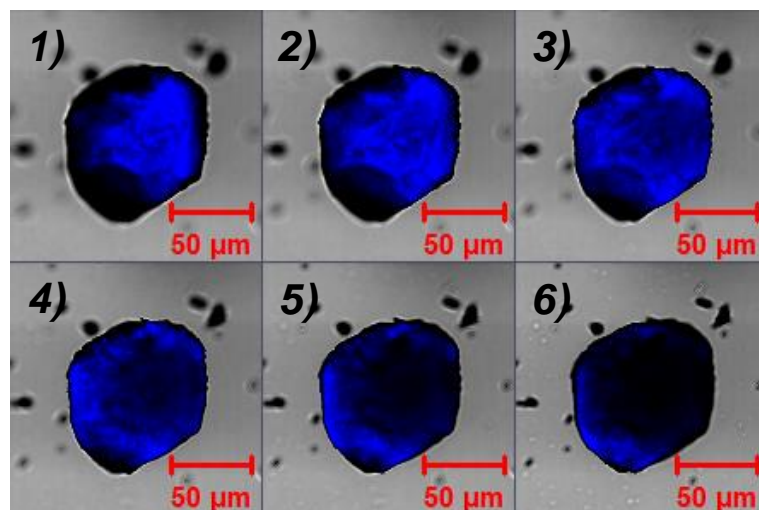


Figure 2.57. CLSM Z-stack images of ***m*-hydrazone**-modified  $\text{Sc}_2\text{BDC}_3$  at 7.5  $\mu\text{m}$  steps. Blue shading indicates 428–508 nm fluorescence.

Similarly to the modification of  $\text{Sc}_2\text{BDC}_3$  with **phen-spiro** and **7-DCCA**, this modification was limited to the surface of the crystal and did not occur throughout the pore, as suggested by Figure 2.57. This is particularly visible in images 4–6, where the blue fluorescence significantly diminishes in the core of the crystal.

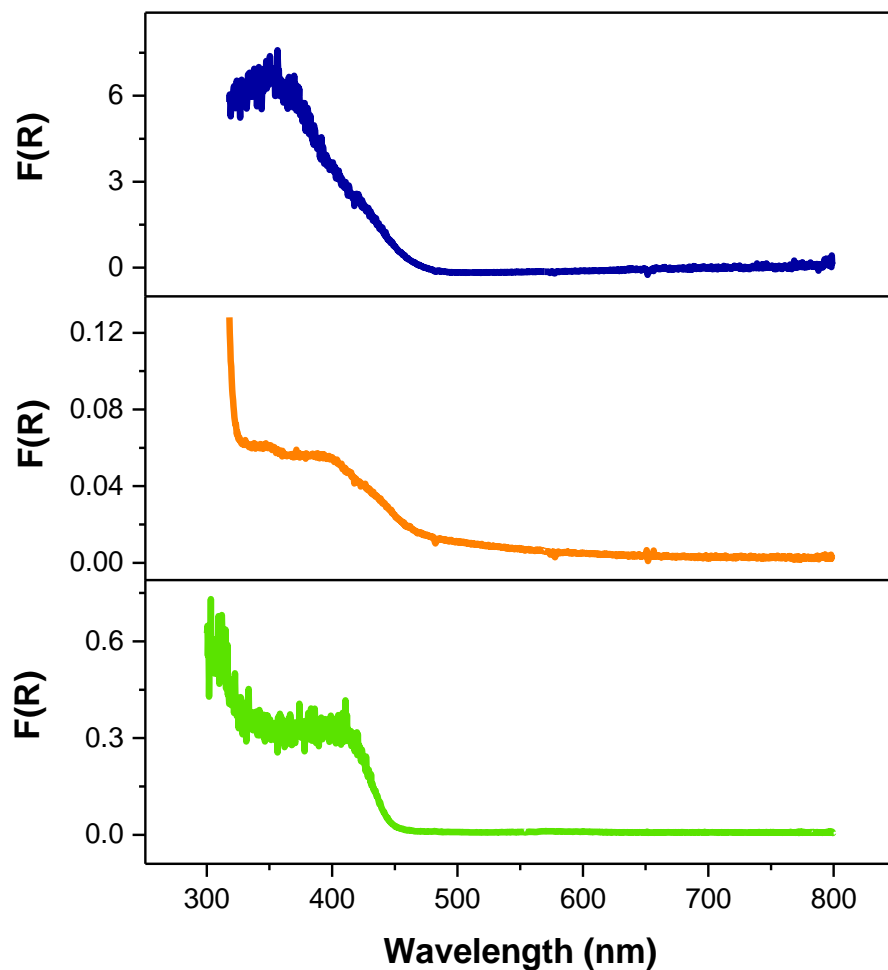


Figure 2.58. UV-VIS-DR spectra of unmodified  $\text{Sc}_2\text{BDC}_3$  (top),  $\text{Sc}_2\text{BDC}_3 \supset \text{m-hydrazone}$  (middle) and  $\text{m-hydrazone}$  (bottom).

The reflectance spectra of  $\text{Sc}_2\text{BDC}_3$ , **m-hydrazone** and  $\text{Sc}_2\text{BDC}_3 \supset \text{m-hydrazone}$  are shown in Figure 2.58. The framework and **m-hydrazone** clearly absorb in the same region of the spectra, making UV-VIS-DRS unsuitable for confirming the successful modification of the framework. Given this spectral overlap, photoconversion experiments were not carried out on this sample, as irradiation in the confocal microscopy equipment at 405 nm is not selective for the **m-hydrazone**.

### 2.3.3.5.6 PSM of UiO-67 with *m*-hydrazone

UiO-67 was modified using a solution of ***m*-hydrazone** in anhydrous MeCN (10 mL, 0.03 mM) for 24 hr at 60 °C. Solids were collected by centrifugation, washed with MeCN (10 x 10 mL) and dried in air. Modification was confirmed using CLSM and UV-VIS-DRS. CLSM images and UV-VIS-DR spectra and accompanying discussions are shown in Figures 2.59 and 2.60 respectively.

CLSM images were excited with a 405 nm laser (25.5%) and fluorescence detected in the regions 428–508 and 642–695 nm. The emission of the sample in the blue region is approximately 8x greater than the weak emission of unmodified UiO-67, indicative of the presence of ***m*-hydrazone**. The lower laser power was used for two reasons: avoid photobleaching and ***m*-hydrazone** has a higher quantum yield of emission than the **phen-spiro** and therefore lower laser power was needed to avoid saturation of the detector. Due to the narrow window between the *Z*-isomer and photoswitched state of ***m*-hydrazone** (340 and 370 nm respectively), the large blue fluorescence detection range would have detected fluorescence from both states cumulatively. Therefore, it would not have been possible to identify which fluorescence originated from which state. Similarly to the modification of UiO-67 with **phen-spiro** and **7-DCCA**, this modification occurred throughout the crystal, as suggested by the *Z*-stack images in Figure 2.59.

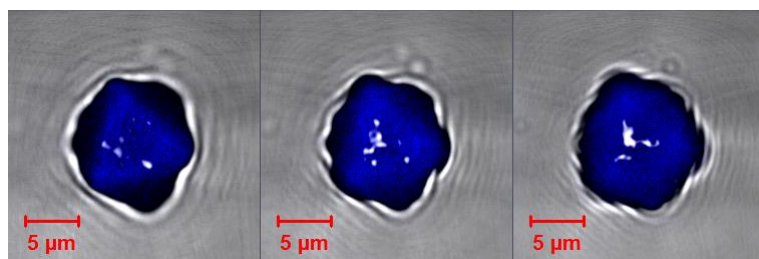


Figure 2.59. CLSM Z-stack images of ***m*-hydrazone**-modified UiO-67 at 2.5  $\mu\text{m}$  steps.  
Blue shading indicates 428–508 nm fluorescence.

The UV-VIS-DR spectra of  $\text{UiO-67}\supset\text{m-hydrazone}$  (Figure 2.60; overleaf) does not show evidence of modification with ***m*-hydrazone**, but this method analyses the bulk material, compared to the single crystal analysis available from CLSM.

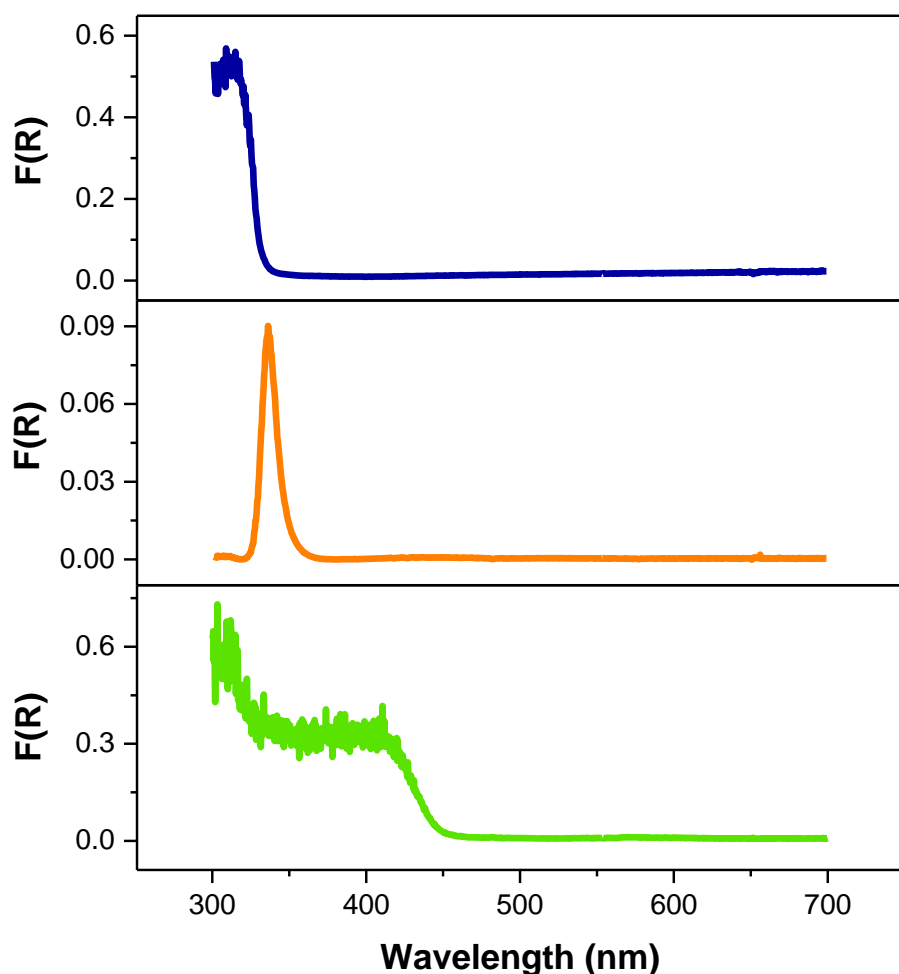


Figure 2.60. UV-VIS-DR spectra of unmodified *UiO*-67 (top), *UiO*-67-*m*-hydrazone (middle) and *m*-hydrazone (bottom).

### 2.3.3.5.7 Summary of solid-state MOF-bound behaviour of photoswitches

*In situ* irradiation during CLSM and UV-VIS-DRS experiments for both  $\text{Sc}_2\text{BDC}_3\supset\text{phen-spiro}$  and  $\text{UiO}-67\supset\text{phen-spiro}$  resulted in changes in the ratio of **SPO** and **MCN** states of **phen-spiro**, as discussed through Sections 2.3.3.5.2 and 2.3.3.5.4.

The spectral overlap of the framework and ***m*-hydrazone** absorption ( $\text{Sc}_2\text{BDC}_3 \supset \text{m-hydrazone}$ ) and the low observed uptake of ***m*-hydrazone** ( $\text{UiO-67} \supset \text{m-hydrazone}$ ) meant that irradiation experiments of this MOF-bound photoswitch have not yet been undertaken.

### 2.3.3.6 Comparison of uptake capabilities of modified MOFs

To assess whether modification of frameworks with **7-DCCA** and **phen-spiro** affected their uptake capabilities, volumetric  $\text{N}_2$  adsorption was recorded on unmodified and modified materials at 77 K. Solvent was removed from samples prior to the experiments by heating to 423 K under high vacuum. Pore size distribution and cumulative pore volume were calculated within Micromeritics 3flex software using a two-dimensional non-linear density functional theory (NLDFT) model ( $\text{N}_2$  on carbon at 77 K, with a finite slit pore geometry and a diameter-to-width aspect ratio of 4).<sup>52</sup>

#### **NOTT-100 vs NOTT-100 $\supset$ 7-DCCA**

$\text{N}_2$  isotherms for NOTT-100 and NOTT-100 $\supset$ 7-DCCA are shown in Figure 2.61.

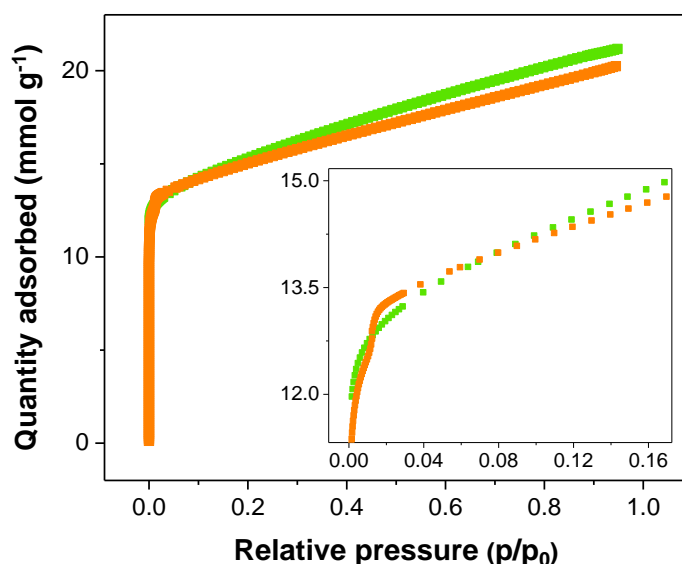


Figure 2.61. Volumetric  $\text{N}_2$  isotherms of NOTT-100 (green) and NOTT-100 $\supset$ 7-DCCA (orange) at 77 K.

The N<sub>2</sub> isotherms in Figure 2.61 suggest that the uptake properties of NOTT-100 did not greatly differ following modification with **7-DCCA**, where a small percentage decrease of only 0.46 mmol g<sup>-1</sup> (2.1% of the uptake of unmodified NOTT-100) of N<sub>2</sub> at 1 bar was observed in the modified materials. Interestingly, the isotherm of the NOTT-100-**7-DCCA** presents a step at low pressure that is yet to be explained, and is not observed in the unmodified framework.

### **Sc<sub>2</sub>BDC<sub>3</sub> vs Sc<sub>2</sub>BDC<sub>3</sub>-phen-spiro**

N<sub>2</sub> isotherms for Sc<sub>2</sub>BDC<sub>3</sub> and Sc<sub>2</sub>BDC<sub>3</sub>-**phen-spiro** are shown in Figure 2.62.

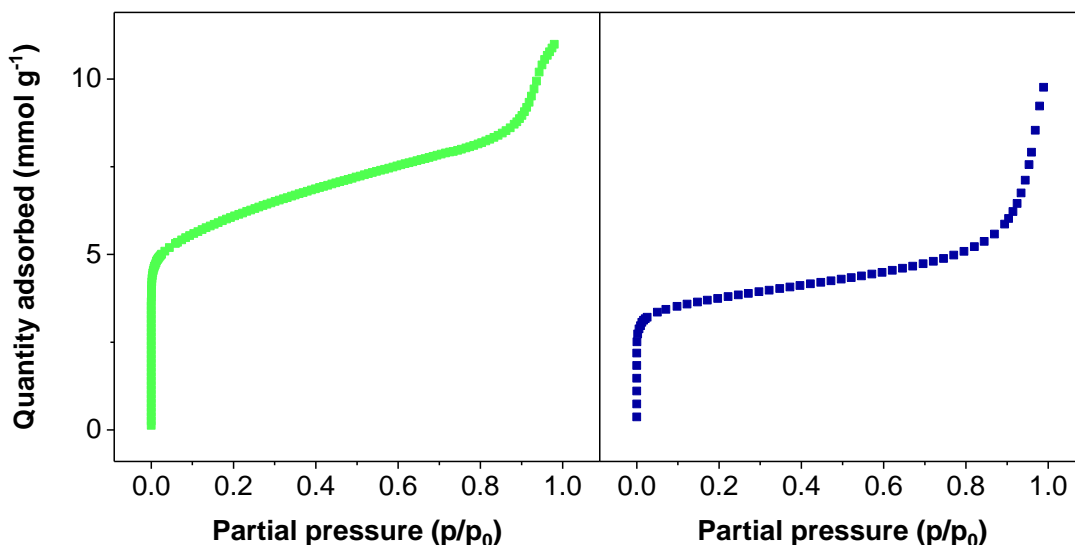


Figure 2.62. Volumetric N<sub>2</sub> isotherms of (left) Sc<sub>2</sub>BDC<sub>3</sub> and (right) Sc<sub>2</sub>BDC<sub>3</sub>-**phen-spiro** at 77 K.

N<sub>2</sub> isotherms in Figure 2.62 indicate that modification of Sc<sub>2</sub>BDC<sub>3</sub> with **phen-spiro** reduces the uptake of N<sub>2</sub> into the modified material by 1.2 mmol g<sup>-1</sup> (10.9% of the total uptake of unmodified Sc<sub>2</sub>BDC<sub>3</sub>).

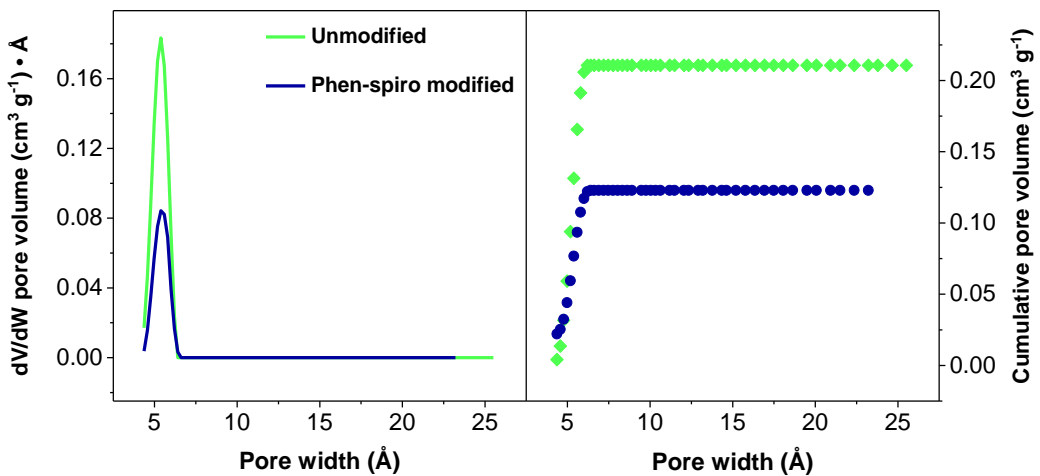


Figure 2.63. Pore size distribution (left) and cumulative pore volume (right) of  $\text{Sc}_2\text{BDC}_3$  and  $\text{Sc}_2\text{BDC}_3\supset\text{phen-spiro}$ , as indicated.

NLDFT model calculations (Figure 2.63) suggest that the pore size distribution remains the same following modification. The pore size distribution appears much the same, but the cumulative pore volume is reduced by  $0.088 \text{ cm}^3 \text{ g}^{-1}$  (41.7%).

***UiO-67 vs. UiO-67 $\supset$ 7-DCCA and UiO-67 $\supset$ phen-spiro***

$N_2$  isotherms for **UiO-67**, **UiO-67 $\supset$ 7-DCCA** and **UiO-67 $\supset$ phen-spiro** are shown in Figure 2.64.

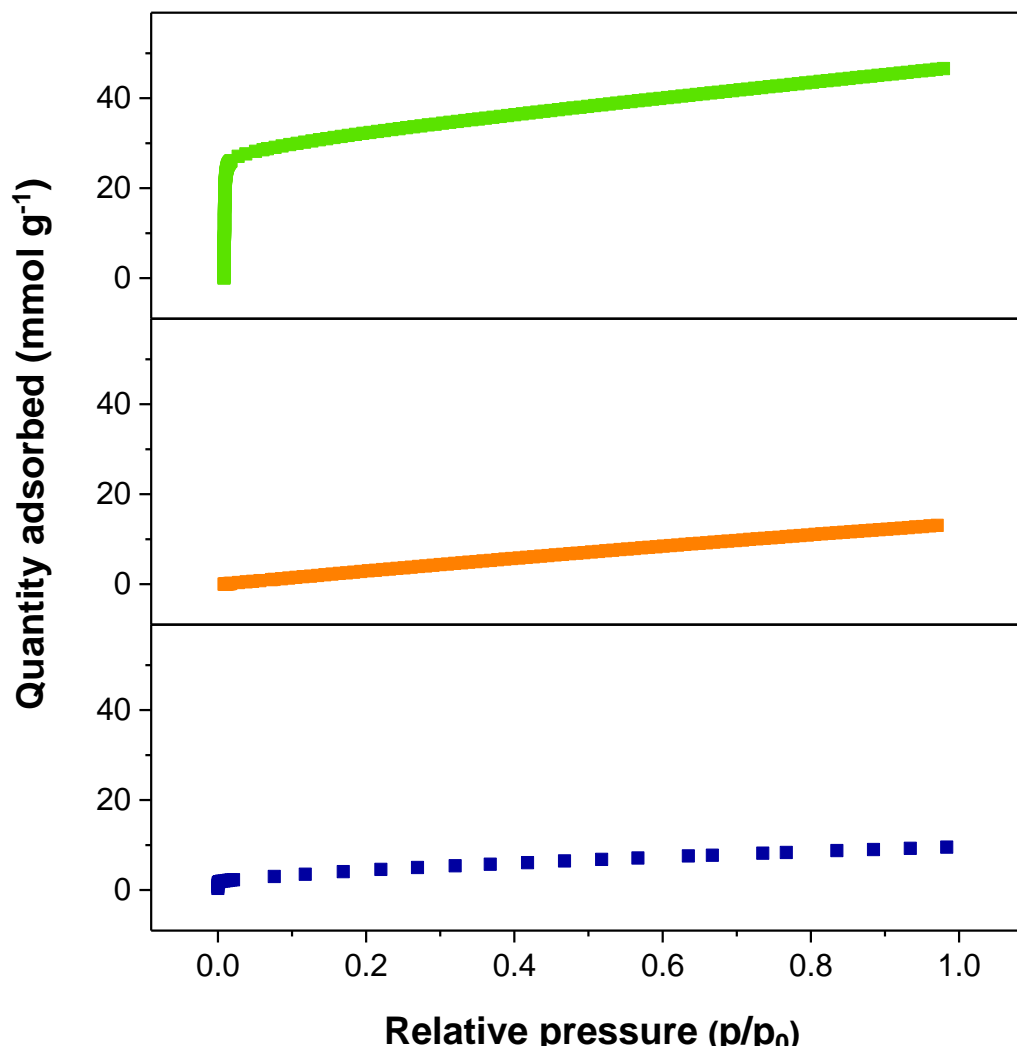


Figure 2.64. Volumetric  $N_2$  isotherms of (top) **UiO-67**, (middle) **UiO-67 $\supset$ 7-DCCA** and (bottom) **UiO-67 $\supset$ phen-spiro** at 77 K.

The modification of **UiO-67** with both **7-DCCA** and **phen-spiro** led to significant reduction of  $N_2$  uptake at 1 bar by 33.5 (71.9%) and 37.0 mmol g<sup>-1</sup> (79.5%) respectively, as indicated by Figure 2.64.

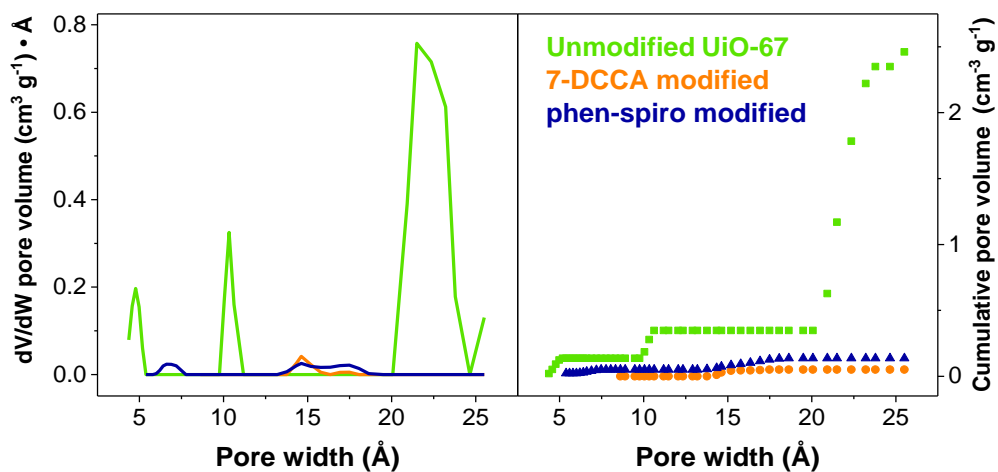


Figure 2.65. Pore size distribution (left) and cumulative pore volume (right) of **UiO-67**, **UiO-67 $\supset$ 7-DCCA** and **UiO-67 $\supset$ phen-spiro**, as indicated.

NLDFT model calculations (Figure 2.65) suggest that there are also significant changes in both pore size distribution and cumulative pore volume following modification. **UiO-67** used throughout this project was synthesised according to the procedure reported by Forgan and co-workers, and included amino acid modulators (*L*-proline) to increase particle size.<sup>31</sup> They reported 10 Å pores, however Figure 2.65 indicates pore sizes of 23, 11 and 5 Å, which more closely match the original report by Hupp and Farha and co-workers of 23 and 11.5 Å pores.<sup>46</sup> Modification of the framework with **7-DCCA** and **phen-spiro** reduces pore size to the 23 Å pore size to 13–18 Å for both materials, and an additional decrease of the 11 Å pore to 7 Å for the **phen-spiro** functionalised materials. Cumulative pore volume has also been significantly reduced in both cases.

### **Comparison of dye-modified MOFs**

Table 2.7 shows that modification of NOTT-100,  $\text{Sc}_2\text{BDC}_3$  and UiO-67 with either **7-DCCA** or **phen-spiro** reduced the BET surface area. This decrease was most significant in UiO-67, which could be attributed to modification occurring throughout the pore structure, as opposed to being confined primarily to the surface as in  $\text{Sc}_2\text{BDC}_3$ .

Table 2.7.  $N_2$  BET isotherm data collected at 77 K.

MOF	Modifier	BET Surface Area ( $\text{m}^2 \text{ g}^{-1}$ )	% decrease
NOTT-100	-	$1238 \pm 2$	
	<b>7-DCCA</b>	$1224 \pm 2$	1.1 %
$\text{Sc}_2\text{BDC}_3$	-	$460 \pm 2$	
	<b>Phen-spiro</b>	$292 \pm 0$	36.5%
UiO-67	-	$2646 \pm 1$	
	<b>7-DCCA</b>	$61 \pm 6$	97.7%
	<b>Phen-spiro</b>	$197 \pm 0$	92.6%

## 2.4 Conclusions and Outlook

Throughout this chapter, we have successfully tracked fluorescent guest species in MOF materials, quantifying and studying post-synthetic modification with these guests using spectro- and microscopic techniques.

This process first involved the manipulation of MOF crystal sizes through synthetic approach, where cubic single crystals of NOTT-100 were grown up to 200 µm in size. This was achieved through substitution of the modulator from the initial synthesis (conc. HCl) with conc. HNO<sub>3</sub>, alteration of the molar ratio of linker and metal salt and concentration of the reaction solution, and reduction of reaction temperature and increase of the reaction length. SEM analysis of this modified material revealed a qualitative correlation between fragmentation of crystals upon exposure to the vacuum of the SEM chamber and the Gutmann-Beckett solvent acceptor number and solvent molar volume. This phenomenon is currently undergoing quantitative assessment by other members of the research group, where the effect of common laboratory solvents on the SEM images of several well-studied MOFs is being investigated. A publication is in preparation.

Manipulation of Sc<sub>2</sub>BDC<sub>3</sub> crystal sizes was also achieved. Synthesis according to the procedure published by Miller *et al.* yielded polydisperse crystals of between 50–200 µm.<sup>39</sup> A doping method, first reported by Lan *et al.*, involved heating a small amount of metal salt (in this case, Sc(NO<sub>3</sub>)<sub>2</sub>) with the framework linker prior to solvothermal synthesis. This method produced hexagonal rods of 400 x 200 µm with significantly reduced range of particle sizes.

The aforementioned size optimised NOTT-100 and Sc<sub>2</sub>BDC<sub>3</sub>, as well as MIL-68(In) and UiO-67, were post-synthetically modified with carboxylic acid-functionalised dye molecules; **7-DCCA**, **phen-spiro** and **m-hydrazone**. Reaction conditions for SALE were optimised using results from timed reactions, where materials were modified with coumarin-based **7-DCCA**.

SALE reaction solutions and framework washings were analysed using UV-VIS spectroscopy and modified framework materials were analysed using both UV-VIS-DRS and CLSM. From these experiments, 24 hr was deemed sufficient for linker exchange to take place in NOTT-100,  $\text{Sc}_2\text{BDC}_3$  and UiO-67. Data analysed from MIL-68(Ind)  $\supset$  **7-DCCA** modification experiments were inconclusive, and further modification of MIL-68(Ind) was not carried out. Successful modification of  $\text{Sc}_2\text{BDC}_3$  and UiO-67 with **phen-spiro** and **m-hydrazone** was confirmed using CLSM and UV-VIS-DRS.

Following the modification of  $\text{Sc}_2\text{BDC}_3$  and UiO-67 with photoswitch **phen-spiro**, *in situ* irradiation experiments were carried out as part of CLSM and UV-VIS-DRS experiments to instigate photoisomerism of the spirooxazine moiety. Between 90–300 seconds of irradiation of the samples with a 633 nm laser, as part of CLSM experiments, resulted in switching from the closed **SPO** form to the open **MCN** form. It is worth noting that both 405 and 633 nm lasers were employed for excitation during the collection of CLSM images of **phen-spiro** modified frameworks, and therefore the photostationary equilibrium established during *in situ* irradiation experiments may have been further disturbed.

Irradiation of both samples with 390 nm UV LEDs for 24 hours, as part of UV-VIS-DRS experiments, resulted in a switch of **SPO** and **MCN** forms in  $\text{Sc}_2\text{BDC}_3$ . Unfortunately, both samples suffered photobleaching as a result of extended irradiation, but a shift in the amount of states present is clear in all experiments. The photostability of **phen-spiro** is highly complicated, and binding of the moiety to different metal centres further convolutes the system. In order to understand the photophysics of the system, further experiments, including extensive luminescence studies, solvent- and temperature-variable UV-VIS and additional irradiation experiments are required.

The  $\text{N}_2$  uptake of materials following modification with **7-DCCA** and **phen-spiro** was investigated *via* BET isotherm measurements. The modification of materials with both moieties resulted in reduced  $\text{N}_2$  uptake in NOTT-100,  $\text{Sc}_2\text{BDC}_3$  and UiO-67.

The most significant adsorption change was observed in UiO-67, where modification with **7-DCCA** resulted in a reduction of 97.7%. Uptake was hindered to a greater extent in UiO-67 than  $\text{Sc}_2\text{BDC}_3$  and NOTT-100 due to modification occurring throughout the whole crystal, whereas modification in  $\text{Sc}_2\text{BDC}_3$  was confined to the crystal surface.

CLSM images were inconclusive as to the position of modification in NOTT-100, but the small reduction in  $\text{N}_2$  uptake suggest that modification only took place on the crystal surface. Subsequent isotherm experiments should examine the capabilities of **phen-spiro** to selectively block access to the framework pores, either by *in situ* irradiation of materials during the measurement or ensuring conversion to either the **SPO** or **MCN** form prior to measurement.

## 2.5 Experimental

Compounds **6-11** and **16** were synthesised with the assistance of MChem project student Louisa Davis. Compound **12** was synthesised with the assistance of MChem project student Christopher Ashling. All **7-DCCA** modified materials were synthesised with the assistance of BSc project student James Bywater.

### 2.5.1 General methods

All starting materials were obtained from commercial sources and used without further purification. Specialist methods (CLSM, SEM, *in situ* UV-VIS-DRS) are detailed further in Section 1.6 on pp.12–14.

<sup>1</sup>H and <sup>13</sup>C NMR were recorded on Bruker DPX spectrometers operating at 300, 400 or 500 MHz. Spectrometer frequencies are indicated with each spectral assignment.

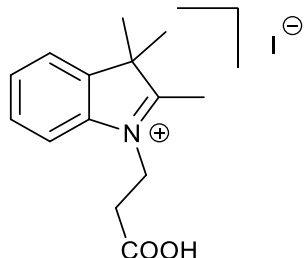
LC-MS was performed on a Thermo Ultimate 3000 with a C<sub>18</sub> column. The column is held at 40 °C and the gradient is from 95% A to 5% B over 20 min. Mobile phases are A: H<sub>2</sub>O (0.1% formic acid) and B: MeCN (0.1% formic acid). Mass spectrometry analysis was performed by in-house staff at Cardiff University using Bruker Amazon SL ion trap and Waters SYNAPT-Si G2 spectrometers.

Powder X-ray diffraction patterns were collected between 4° and 40° 2θ using an X’Pert Pro PAN Analytical powder diffractometer employing a Cu-K<sub>α</sub> radiation source operating at 40 keV and 40 mA.

UV-VIS spectra were collected using a modular Ocean Optics Flame-S-UV-VIS-ES spectrometer and DH-mini deuterium-tungsten light source connected *via* fibre optic cables.

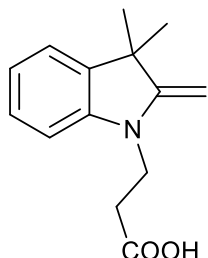
## 2.5.2 Phen-spiro synthetic route

### **1-(2-Carboxyethyl)-2,3,3-trimethyl-3H-indol-1-i um iodide (1)**

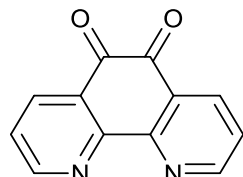


3-Iodopropionic acid (4.3 g, 21.7 mmol) and 2,3,3-trimethylindolenine (3.4 mL, 21.2 mmol) were dissolved in water (10 mL) and heated to 100 °C for 16 hr under  $\text{N}_2$ . The solution was cooled to ambient temperature (25 °C), water added (50 mL), and washed with  $\text{CHCl}_3$  (6 x 50 mL). Solvent was removed from the aqueous layer *in vacuo*. The reddish solid was dissolved into acetone *via* Soxhlet extraction for 16 hr. Product **1** precipitated on addition of  $\text{Et}_2\text{O}$  and the pale cream solid filtered under vacuum and washed with  $\text{Et}_2\text{O}$ . Yield 5.1 g (66.9%).  $^1\text{H}$  NMR ( $\text{D}_2\text{O}$ , 400 MHz)  $\delta$ (ppm) 7.7 (d, 1H,  $J$  = 9 Hz), 7.6 (d, 1H,  $J$  = 9 Hz), 7.5 (dd, 1H,  $J$  = 3, 6 Hz), 4.6 (t, 2H,  $J$  = 7 Hz), 3.0 (t, 2H,  $J$  = 7 Hz), 1.4 (s, 6H). MS (ES)  $m/z$  232.13 [M-I] $^+$ .

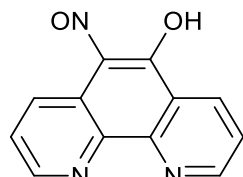
### **3-(3,3-Dimethyl-2-methyleneindolin-1-yl)propanoic acid (2)**



Compound **1** (10.8 g, 30.1 mmol) in water (50 mL) was added to KOH (8.0 g, 142.9 mmol) in water (150 mL) and stirred at room temperature for 5 days. The reaction mixture was neutralised with HCl (6 M and 1 M) and extracted into 1:1  $\text{iPrOH:DCM}$  (ca. 1.5 L), dried ( $\text{MgSO}_4$ ) and solvent removed *in vacuo*. Product **2** was collected as purple oil. Yield 4.5 g (64.8%).  $^1\text{H}$  NMR ( $\text{D}_2\text{O}$ , 400 MHz)  $\delta$ (ppm) 1.1 (d, 1H,  $J$  = 6 Hz), 1.5 (s, 6H), 2.8 (t, 2H,  $J$  = 7 Hz), 4.6 (t, 2H,  $J$  = 7 Hz), 7.6 (m, 2H), 7.7 (m, 1H), 7.8 (m, 1H). MS (EI)  $m/z$  232.12 [M+H] $^+$ .

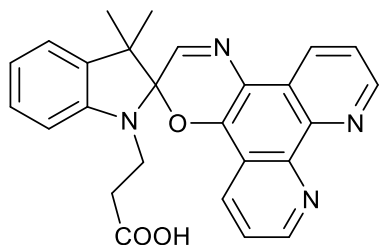
**1,10-Phenanthroline-5,6-dione (3)<sup>53</sup>**

1,10-Phenanthroline (20.0 g, 95.2 mmol) was dissolved in conc. H<sub>2</sub>SO<sub>4</sub> (160 mL) at 0 °C. KBr (40.3 g, 338.7 mmol) was added in ca. 5 g portions. Conc. HNO<sub>3</sub> (80 mL) was added in ca. 10 mL aliquots, liberating Br<sub>2</sub>, and the solution heated at 100 °C for 40 hr. The reaction was cooled to ambient temperature, poured into ice and neutralised using NaOH (10 M and 1 M) and saturated NaHCO<sub>3</sub> solution, forming yellow solid. The yellow solid was collected under vacuum and dissolved into EtOH via Soxhlet extraction for 16 hr. The solution was cooled to 0 °C and product **3** was collected under vacuum as yellow needle-like crystals. Yield 9.4 g (43.9%). <sup>1</sup>H NMR (CDCl<sub>3</sub>, 400 MHz) δ(ppm) 9.1 (dd, 1H, J = 5, 2 Hz), 8.5 (dd, 1H, J = 8, 2 Hz), 7.6 (dd, 1H, J = 8, 5 Hz). MS (EI) m/z 210.04 [M+H]<sup>+</sup>.

**6-Nitroso-1,10-phenanthrolin-5-ol (4)<sup>54</sup>**

NH<sub>2</sub>OH.HCl (0.7 g, 9.5 mmol) in water (5 mL) was added dropwise to compound **3** (2.0 g, 8.8 mmol) in EtOH (40 mL) and heated to 80 °C for 16 hr. The reaction mixture was then cooled, filtered under vacuum and washed with cold EtOH to give **4** as yellow-green powder. Yield 1.9 g (91.7%). <sup>1</sup>H NMR (CDCl<sub>3</sub>, 400 MHz) δ(ppm) 9.2 (dd, 1H, J = 5, 2 Hz), 9.0 (dd, 1H, J = 5, 2 Hz), 8.7 (ddd, 2H, J = 16, 8, 2 Hz), 7.6 (dd, 1H, J = 8, 5 Hz), 7.5 (dd, 1H, J = 8, 5 Hz). MS (ES) m/z 226.04 [M+H]<sup>+</sup>.

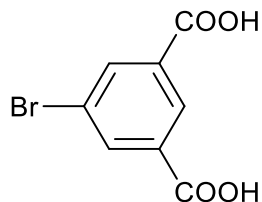
**3-(3,3-Dimethylspiro[indoline-2,2'-[1,4]oxazino[2,3-f][1,10]phenanthrolin]-1-yl) propanoic acid (5)**



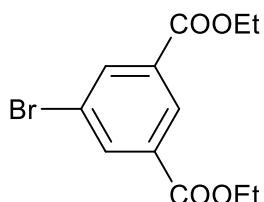
Compound **1** (250.9 mg, 0.7 mmol) and compound **4** (159.4 mg, 0.7 mmol) were dissolved in EtOH (15 mL) to give an orange solution. NEt<sub>3</sub> (0.1 mL, 0.7 mmol) was added and the reaction heated at 80 °C for 6 hr, forming a dark blue solution after 20 minutes. The reaction mixture was filtered whilst hot and washed with cold water and EtOH, giving compound **5** as pale yellow solid. Yield 82.5 mg (27.4%). <sup>1</sup>H NMR (400 MHz, MeOD) δ(ppm) 9.0 (s, 2H), 8.9 (s, 1H), 8.4 (d, 1H, *J* = 8 Hz), 8.0 (s, 1H), 7.8–7.7 (*m*, 1H), 7.8–7.6 (*m*, 1H), 7.2 (*t*, 1H, *J* = 7 Hz, 1H), 7.1 (d, 1H, *J* = 7 Hz), 6.8 (d, 1H, *J* = 7 Hz), 6.7 (d, 1H, *J* = 7 Hz), 3.6–3.5 (*m*, 2H), 2.7–2.4 (*m*, 2H), 1.3 (s, 3H). MS (ESI) *m/z* 439.18 [M+H]<sup>+</sup>.

### 2.5.3 MOF linker synthesis

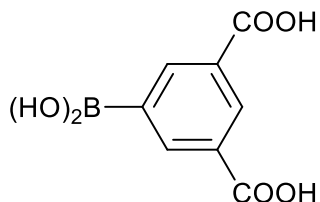
#### **5-Bromoisophthalic acid (6)**



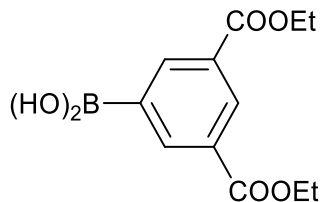
5-Bromo-*m*-xylene (7.4 mL, 54.5 mmol) and NaOH (7.7 g, 192.5 mmol) were dissolved in *t*BuOH (65 mL) and water (200 mL) and heated to 50 °C. KMnO<sub>4</sub> (35.2 g, 222.7 mmol) was added in *ca.* 5 g portions, as the solution turned from purple to brown. The reaction mixture was then heated to 70 °C and additional KMnO<sub>4</sub> (17.6 g, 111.4 mmol) was added in *ca.* 5 g portions. The reaction mixture was heated for 16 hr at 70 °C. When a consistent purple colour was seen, *i*PrOH (32 mL) was added and the reaction mixture heated at 80 °C for 2 hr. The reaction mixture was filtered whilst hot and washed with boiling water. The filtrate was reduced *in vacuo* until precipitate was seen and the mixture acidified to pH 1 with HCl (12 M) to produce a white precipitate, which was then filtered under vacuum and washed with water. The sticky white solid was dissolved into Et<sub>2</sub>O and dried (MgSO<sub>4</sub>) and solvent removed *in vacuo* to give product **6** as white solid. Yield 10.8 g (82%). <sup>1</sup>H NMR (DMSO-*d*<sub>6</sub>, 400 MHz) δ(ppm) 8.4 (t, 1H, *J* = 2 Hz), 8.2 (d, 2H, *J* = 2 Hz). MS (ASAP) *m/z* 327.0060 [M+2MeCN+H]<sup>+</sup>.

**5-Bromoisophthalyl ethanoate (7)**

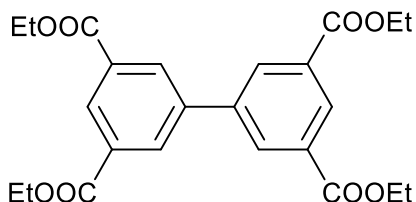
Compound **6** (3.2 g, 130.6 mmol) was dissolved in EtOH (100 mL) before the addition of conc. H<sub>2</sub>SO<sub>4</sub> (2 mL, 18 M). The reaction was then heated at 80 °C for 12 hr and solvent evaporated *in vacuo* until precipitation was observed. Water was added to form a white suspension, which was extracted into Et<sub>2</sub>O. The organic layer was dried (MgSO<sub>4</sub>) and solvent removed *in vacuo* to yield a colourless oil, which solidified upon standing to form product **7** as a white solid. Yield 2.3 g (63%) <sup>1</sup>H NMR (DMSO-*d*<sub>6</sub>, 400 MHz) δ(ppm) 8.4 (*t*, 1H, *J* = 2 Hz), 8.3 (*d*, 2H, *J* = 1 Hz), 4.4 (*q*, 4H, *J* = 7 Hz), 1.3 (*t*, 6H, *J* = 7 Hz). MS (EI) *m/z* 338.18 [M+K]<sup>+</sup>.

**5-Boronoisophthalic acid (8)**

3,5-Dimethylphenylboronic acid (10.0 g, 666.8 mmol) and NaOH (9.2 g, 230.0 mmol) were stirred in <sup>i</sup>BuOH (70 mL) and water (220 mL) and heated to 50 °C. KMnO<sub>4</sub> (60.0 g, 379.7 mmol) was added in four portions over 2 days, as the purple colour subsided. The reaction mixture was heated to 70 °C for 16 hr. When a consistent purple colour was seen, <sup>i</sup>PrOH (35 mL) was added and the mixture heated for 2 hr at 80 °C. The reaction mixture was filtered whilst hot and washed with boiling water. The filtrate was reduced *in vacuo* until precipitate was seen and the solution acidified to pH 1 with HCl (12 M), yielding a white precipitate which was filtered under vacuum and washed with water to give product **8** as white solid. Yield 4.2 g (30%) <sup>1</sup>H NMR (DMSO-*d*<sub>6</sub>, 400 MHz) δ(ppm) 8.6 (*d*, 2H, *J* = 2 Hz), 8.5 (*t*, 1H, *J* = 2 Hz). MS (ESI) *m/z* 209.01 [M-H]<sup>-</sup>.

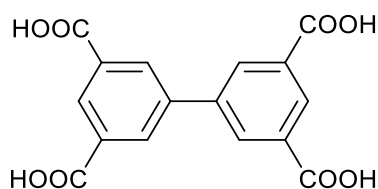
**(3,5-Bis(ethoxycarbonyl)phenyl)boronic acid (9)**

Compound **8** (12.66 g, 0.0604 mol) was dissolved in EtOH (450 mL) and conc.  $\text{H}_2\text{SO}_4$  (9 mL). The reaction was heated for 2 days at 80 °C, then solvent evaporated *in vacuo* until precipitation occurred. Water was added to yield a white precipitate which was then filtered under vacuum and washed with water until the filtrate reached pH 7 to give **9** as white solid. Yield 10.6 g (66%).  $^1\text{H}$  NMR (DMSO- $d_6$ , 400 MHz)  $\delta$ (ppm) 8.6 (d, 2H,  $J$  = 2 Hz), 8.5 (t, 1H,  $J$  = 2 Hz), 4.4 (q, 4H,  $J$  = 10 Hz), 1.3 (t, 6H,  $J$  = 9 Hz). MS (ES)  $m/z$  267.10 [M+H]<sup>+</sup>.

**Tetraethyl(biphenyl)-3,3',5,5'-tetracarboxylate (10)**

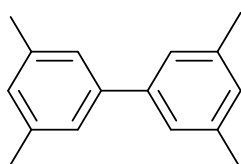
Compound **7** (1.7 g, 5.6 mmol), compound **9** (1.7 g, 6.4 mmol) and  $\text{K}_2\text{CO}_3$  (2.7 g, 19.2 mmol) were dissolved in toluene (250 mL) and water (60 mL) and degassed with nitrogen for 15 min at 60 °C.  $\text{P}(^3\text{Bu})_3$  (1 M solution in toluene, 1.9 mL, 1.9 mmol) was added followed by  $\text{Pd}_2(\text{dba})_3$  (0.6 g, 10 mol%). The reaction was then heated at 80 °C for 16 hr. The biphasic mixture was filtered and the resulting solid washed with DCM. The filtrate was added to water and extracted with DCM (5 x 25 mL). The organic phase was dried ( $\text{MgSO}_4$ ) and solvent removed *in vacuo* to yield an orange oil, which was recrystallised from DCM and MeOH to produce compound **10** as a white powder. Yield 1.3 g (52%).  $^1\text{H}$  NMR (DMSO- $d_6$ , 300 MHz)  $\delta$ (ppm) 8.5 (t, 2H,  $J$  = 2 Hz), 8.4 (d, 4H,  $J$  = 2 Hz), 4.4 (q, 8H,  $J$  = 7 Hz), 1.4 (t, 12H,  $J$  = 7 Hz). MS (ASAP)  $m/z$  460.3315 [M+NH<sub>4</sub>]<sup>+</sup>.

**1,1'-Biphenyl-3,3',5,5'-tetracarboxylic acid [Esterification method] (11)**



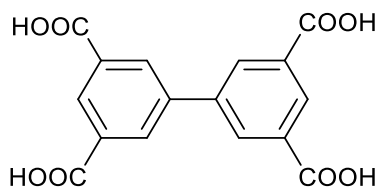
Compound **10** (1.1 g, 2.4 mmol) was heated in NaOH (2 M, 100 mL), THF (100 mL) and EtOH (100 mL) at 80 °C for 16 hr. THF and EtOH were removed *in vacuo*. The resulting aqueous solution was acidified to pH 6 with HCl (2 M and 1 M) to yield a pale brown precipitate which was washed with acetone and dried to give compound **11** as a cream powder. Yield 0.7 g (82.7%).  
¹H NMR (DMSO-*d*<sub>6</sub>, 400 MHz) δ(ppm) 8.5 (s, 2H), 8.4 (s, 4H).  
MS (ES) *m/z* 329.02 [M-H]<sup>-</sup>.

**1,1'-Biphenyl-3,3',5,5'-tetracarboxylic acid [Direct coupling method] (12)**



3,5-Dimethylphenylboronic acid (10.0 g, 66.7 mmol), 5-bromo-*m*-xylene (12.4 g, 66.9 mmol) and Cs<sub>2</sub>CO<sub>3</sub> (23.4 g, 66.8 mmol) were dissolved in EtOH (200 mL) with sonication and degassed for 2 hr. The mixture was heated to 80 °C and Pd(PPh<sub>3</sub>)<sub>4</sub> (0.77 g, 1 mol%) was added in small portions over 48 hr. Reaction solvent was removed *in vacuo* and the solid dissolved in chloroform (100 mL), washed with water (3 x 150 mL), dried (MgSO<sub>4</sub>) and solvent removed *in vacuo*. Product was purified by column chromatography (hexane) to produce **12** as white crystals. Yield 3.5 g (64.1%). <sup>1</sup>H NMR (CDCl<sub>3</sub>, 400 MHz) δ(ppm) 7.2 (s, 4H), 7.0 (s, 2H) and 2.4 (s, 12H). MS (ES) *m/z* 211.89 [M+H]<sup>+</sup>.

**1,1'-Biphenyl-3,3',5,5'-tetracarboxylic acid [Direct oxidation method] (13)**



Compound **11** (186.6 mg, 0.9 mmol) and NaOH (1.4 g, 35.0 mmol) were stirred in  $\text{tBuOH}$  (30 mL) and water (90 mL) and heated to 50 °C.  $\text{KMnO}_4$  (1.7 g, 10.8 mmol) was added and the reaction mixture heated to 70 °C for 4 days.  $\text{iPrOH}$  (40 mL) was added and the mixture heated for 2 hr at 90 °C. The reaction mixture was filtered whilst hot and washed with boiling water. The filtrate was reduced *in vacuo* until precipitate was seen and the solution acidified to pH 1 with HCl (12 M), yielding a white precipitate which was filtered under vacuum and washed with water to give product **13** as white solid. Yield 262.7 mg (89.7%).  
 $^1\text{H NMR}$  ( $\text{DMSO}-d_6$ , 400 MHz)  $\delta$ (ppm) 13.5 (s, 4H), 8.5 (s, 2H), 8.4 (s, 4H).  
MS (ASAP)  $m/z$  329.03 [M-H]<sup>-</sup>.

## 2.5.4 MOF synthesis

All materials were dried in air and characterised by PXRD, using an X'Pert PRO PANalytical diffractometer.

### **MIL-68(In),<sup>44</sup> In(OH)(O<sub>2</sub>C-C<sub>6</sub>H<sub>4</sub>-CO<sub>2</sub>)**

In(NO<sub>3</sub>)<sub>3</sub> (408.5 mg, 1.4 mmol), terephthalic acid (200.1 mg, 1.2 mmol) and DMF (5 mL) were heated for 48 hr at 100 °C in a Teflon-lined Parr autoclave. Solids were collected via centrifugation, washed with DMF (3 x 5 mL) and dried in air to yield **MIL-68(In)** as white crystalline powder. Yield 125.0 mg.

### **NOTT-100 bulk powder,<sup>30</sup>**

#### **[Cu<sub>2</sub>((O<sub>2</sub>C)<sub>2</sub>-C<sub>12</sub>H<sub>6</sub>-(CO<sub>2</sub>)<sub>2</sub>)(H<sub>2</sub>O)<sub>2</sub>(DMF)<sub>3</sub>(H<sub>2</sub>O)]**

Cu(NO<sub>3</sub>)<sub>2</sub>.3H<sub>2</sub>O (5.1 g, 21.0 mmol) and compound **11** (1.7 g, 5.0 mmol) were heated without stirring in 2:1 mixture of DMF and water (350 mL) and conc. HCl (1 mL) at 85 °C for 24 hr. The solution was filtered whilst hot and washed with warm DMF (15 mL) and Et<sub>2</sub>O (10 mL) to afford **NOTT-100** as a turquoise powder. The material was solvent exchanged with DMF and MeOH. Yield 2.6 g.

### **NOTT-100 single crystal,**

#### **[Cu<sub>2</sub>((O<sub>2</sub>C)<sub>2</sub>-C<sub>12</sub>H<sub>6</sub>-(CO<sub>2</sub>)<sub>2</sub>)(H<sub>2</sub>O)<sub>2</sub>(DMF)<sub>3</sub>(H<sub>2</sub>O)]**

Cu(NO<sub>3</sub>)<sub>2</sub>.3H<sub>2</sub>O (20.3 mg, 0.08 mmol) and compound **11** (13.9 mg, 0.04 mmol) were heated in a Wheaton vial with water (1 mL), DMF (2 mL) and conc. HNO<sub>3</sub> (90 µL) in an aluminium block at 55 °C for 5 days. Solids were collected via centrifugation, washed with DMF (3 x 5 mL) and hexane (3 x 5 mL) and dried in air. **NOTT-100** was collected as turquoise cubic crystals. Yield 18.6 mg.

***Sc<sub>2</sub>BDC<sub>3</sub>,<sup>39</sup> [Sc<sub>2</sub>(O<sub>2</sub>C-C<sub>6</sub>H<sub>4</sub>-CO<sub>2</sub>)<sub>3</sub>]***

Terephthalic acid (166.2 mg, 1.0 mmol) and Sc(NO<sub>3</sub>)<sub>3</sub> (340.6 mg, 1.2 mmol) were combined in water (5 mL) and heated in a Teflon-lined Parr autoclave at 220 °C for 3 days. Solids were collected *via* centrifugation, washed with DMF (3 x 5 mL) and DCM (3 x 5 mL) and dried in air to yield **Sc<sub>2</sub>BDC<sub>3</sub>** as yellow crystals. Yield 212.9 mg.

***Optimised Sc<sub>2</sub>BDC<sub>3</sub>, [Sc<sub>2</sub>(O<sub>2</sub>C-C<sub>6</sub>H<sub>4</sub>-CO<sub>2</sub>)<sub>3</sub>]***

Terephthalic acid (1.37 g, 8.2 mmol) and Sc(NO<sub>3</sub>)<sub>3</sub> (0.22 g, 1.0 mmol) in water (2.5 mL), and Sc(NO<sub>3</sub>)<sub>3</sub> (1.21 g, 5.2 mmol) in water (2.5 mL) were heated whilst stirring at 70 °C for 2 hr in two separate Wheaton vials. The metal salt solution was added to the linker slurry in a 23 mL Teflon-lined Parr autoclave and heated at 220 °C for 48 hr. The solids were collected *via* centrifugation, washed with DMF (3 x 5 mL) and THF (3 x 5 mL) and dried in air to yield **Sc<sub>2</sub>BDC<sub>3</sub>** as yellow hexagonal rods. Yield 619.7 mg.

***UiO-67,<sup>31</sup> [Zr<sub>6</sub>O<sub>4</sub>(OH)<sub>4</sub>(O<sub>2</sub>C-C<sub>12</sub>H<sub>8</sub>-CO<sub>2</sub>)<sub>6</sub>]<sub>n</sub>***

Biphenyl-4,4'-dicarboxylic acid (126.0 mg, 0.5 mmol) in DMF (5 mL) and ZrCl<sub>4</sub> (111.8 mg, 0.5 mmol) and *L*-proline (259.4 mg, 2.3 mmol) in DMF (5 mL) and conc. HCl (40 µL) were sonicated for ten minutes. The linker slurry and metal salt solution were transferred to a Teflon-lined Parr autoclave and heated at 100 °C for 48 hr. The solids were collected *via* centrifugation, washed with DMF (3 x 5 mL) and DCM (3 x 5 mL) and dried in air to yield **UiO-67** as white solid. Yield 117.7 mg.

## 2.5.5 Post-synthetic modification of MOFs

### **MIL-68(*In*) $\supset$ 7-DCCA**

MIL-68(*In*) (24.9 mg) was suspended in a solution of 7-DCCA in MeOH (4 mL, 0.05 mM) and heated in an Ace pressure tube at 110 °C for 5 days. The resulting yellow crystals were collected *via* centrifugation and washed with anhydrous MeOH (10 x 5 mL) to yield **MIL-68(*In*) $\supset$ 7-DCCA** as pale yellow crystalline powder.

### **NOTT-100 $\supset$ 7-DCCA**

NOTT-100 (25.1 mg) was suspended in a solution of 7-DCCA in MeOH (4 mL, 0.05 mM) and heated in an Ace pressure tube at 130 °C for 4 days. The resulting turquoise crystals were collected *via* centrifugation and washed with anhydrous MeOH (10 x 5 mL) to yield **NOTT-100 $\supset$ 7-DCCA** as turquoise crystals.

### **Sc<sub>2</sub>BDC<sub>3</sub> $\supset$ 7-DCCA**

Sc<sub>2</sub>BDC<sub>3</sub> (25.1 mg) was suspended in a solution of 7-DCCA in MeOH (4 mL, 0.05 mM) and heated in a Teflon-lined Parr autoclave at 180 °C for 3 days. The yellow crystals were collected *via* centrifugation and washed with anhydrous MeOH (10 x 5 mL) to yield **Sc<sub>2</sub>BDC<sub>3</sub> $\supset$ 7-DCCA** as yellow crystals.

### **UiO-67 $\supset$ 7-DCCA**

UiO-67 (25.2 mg) was suspended in a solution of 7-DCCA in MeCN (4 mL, 0.05 mM) and heated in an Ace pressure tube at 60 °C for 24 hr. The resulting yellow crystals were collected *via* centrifugation and washed with anhydrous MeOH (10 x 5 mL) to yield **UiO-67 $\supset$ 7-DCCA** as yellow crystals.

### ***NOTT-100 $\supset$ phen-spiro***

NOTT-100 (100.6 mg) was suspended in a solution of compound **5** in MeOH (10 mL, 5 mM) and heated in an Ace pressure tube at 130 °C for 24 hr. The crystals were collected *via* centrifugation and washed with anhydrous MeOH (10 x 10 mL) to yield **NOTT-100 $\supset$ phen-spiro** as turquoise crystals.

### ***Sc<sub>2</sub>BDC<sub>3</sub> $\supset$ phen-spiro***

Sc<sub>2</sub>BDC<sub>3</sub> (102.4 mg) was suspended in a solution of compound **5** in MeOH (10 mL, 5 mM) and heated in a Teflon-lined Parr autoclave at 180 °C for 24 hr. The turquoise crystals were collected *via* centrifugation and washed with anhydrous MeOH (10 x 10 mL) to yield **Sc<sub>2</sub>BDC<sub>3</sub> $\supset$ phen-spiro**.

### ***UiO-67 $\supset$ phen-spiro***

UiO-67 (99.4 mg) was suspended in a solution of compound **5** in MeCN (10 mL, 5 mM) and heated in an Ace pressure tube at 60 °C for 24 hr. The crystals were collected *via* centrifugation and washed with anhydrous MeOH (10 x 10 mL) to yield **UiO-67 $\supset$ phen-spiro** as dark blue crystals.

### ***Sc<sub>2</sub>BDC<sub>3</sub> $\supset$ m-hydrazone***

Sc<sub>2</sub>BDC<sub>3</sub> (100.9 mg) was suspended in a solution of *m*-hydrazone in MeOH (10 mL, 0.05 mM) and heated in a Teflon-lined Parr autoclave at 180 °C for 24 hr. The yellow crystals were collected *via* centrifugation and washed with anhydrous MeOH (10 x 5 mL) to yield **Sc<sub>2</sub>BDC<sub>3</sub> $\supset$ m-hydrazone**.

### ***UiO-67 $\supset$ m-hydrazone***

UiO-67 (102.6 mg) was suspended in a solution of *m*-hydrazone in MeCN (10 mL, 0.05 mM) and heated in an Ace pressure tube at 60 °C for 24 hr. The crystals were collected *via* centrifugation and washed with anhydrous MeOH (10 x 5 mL) to yield **UiO-67 $\supset$ m-hydrazone** as cream crystals.

## 2.5.6 Irradiation experiments

### ***UV-VIS-DRS irradiation of $\text{Sc}_2\text{BDC}_3\text{-phen-spiro}$ and $\text{UiO-67-phen-spiro}$***

$\text{Sc}_2\text{BDC}_3\text{-phen-spiro}$  and  $\text{UiO-67-phen-spiro}$  were lightly packed into a custom-built aluminium sample holder and irradiated with seven 40 mW 390 nm UV LEDs housed in an aluminium holder for 24 hr. UV-VIS-DR spectra were collected before and after irradiation.

### ***CLSM irradiation of $\text{Sc}_2\text{BDC}_3\text{-phen-spiro}$ and $\text{UiO-67-phen-spiro}$***

$\text{Sc}_2\text{BDC}_3\text{-phen-spiro}$  and  $\text{UiO-67-phen-spiro}$  were loaded from hexane slurries to glass microscope slides, before being topped with glass cover slips of 0.13–0.16 mm thickness and sealed with colourless fingernail adhesive. Samples were irradiated with a 630 nm laser line (100.0% power) for between 30–900 seconds. CLSM images were collected before and after irradiation.

## 2.6 References

- 1 A. Samokhvalov, *Chem. - A Eur. J.*, 2015, **21**, 16726–16742.
- 2 G. Tabacchi, *ChemPhysChem*, 2018, **19**, 1249–1297.
- 3 K. Hirai, P. Falcaro, S. Kitagawa, S. Furukawa, 'Host–Guest Metal–Organic Frameworks for Photonics.' in *Metal-Organic Frameworks for Photonics Applications. Structure and Bonding*, ed. B. Chen, G. Qian vol 157. Springer, Berlin, Heidelberg, 2013, **157**, 167–186.
- 4 A. J. Tansell, C. L. Jones and T. L. Easun, *Chem. Cent. J.*, 2017, **11**, 100.
- 5 S.-Y. Yang, X.-L. Deng, R.-F. Jin, P. Naumov, M. K. Panda, R.-B. Huang, L.-S. Zheng and B. K. Teo, *J. Am. Chem. Soc.*, 2014, **136**, 558–61.
- 6 Y. Kataoka, K. Sato, Y. Miyazaki, K. Masuda, H. Tanaka, S. Naito and W. Mori, *Energy Environ. Sci.*, 2009, **2**, 397.
- 7 J. E. Mondloch, M. J. Katz, W. C. Isley, P. Ghosh, P. Liao, W. Bury, G. W. Wagner, M. G. Hall, J. B. DeCoste, G. W. Peterson, R. Q. Snurr, C. J. Cramer, J. T. Hupp and O. K. Farha, *Nat. Mater.*, 2015, **14**, 512–6.
- 8 S.-Y. Moon, A. J. Howarth, T. Wang, N. A. Vermeulen, J. T. Hupp and O. K. Farha, *Chem. Commun.*, 2016, **52**, 3438–41.
- 9 Y. Liu, A. J. Howarth, J. T. Hupp and O. K. Farha, *Angew. Chemie Int. Ed.*, 2015, **54**, 9001–9005.
- 10 K. Hirai, S. Furukawa, M. Kondo, H. Uehara, O. Sakata and S. Kitagawa, *Angew. Chemie Int. Ed.*, 2011, **50**, 8057–8061.
- 11 I. Stassen, I. Boldog, C. Steuwe, D. De Vos, M. Roeffaers, S. Furukawa, R. Ameloot, J. Kärger, A. Kuhn, M. O'Keeffe, O. Yaghi and C. Wöll, *Chem. Commun.*, 2017, **54**, 14580–14583.
- 12 A. Karmakar, N. Kumar, P. Samanta, A. V. Desai and S. K. Ghosh, *Chem. - A Eur. J.*, 2016, **22**, 864–868.
- 13 S. Han, Y. Wei, C. Valente, I. Lagzi, J. J. Gassensmith, A. Coskun, J. F. Stoddart and B. A. Grzybowski, *J. Am. Chem. Soc.*, 2010, **132**, 16358–16361.
- 14 M. Kondo, S. Furukawa, K. Hirai and S. Kitagawa, *Angew. Chemie Int. Ed.*, 2010, **49**, 5327–5330.
- 15 V. A. Lokshin, A. Samat and A. V. Metelitsa, *Russ. Chem. Rev.*, 2002, **71**, 893–916.
- 16 Q. Zou, X. Li, J. Zhou, K. Bai and H. Ågren, *Dye. Pigment.*, 2014, **107**, 174–181.
- 17 S. Kumar, D. L. Watkins and T. Fujiwara, *Chem. Commun.*, 2009, **100**, 4369.
- 18 J. Bonefacino, M.-L. Vincent Tse, C.-F. Jeff Pun, X. Cheng, W. K. Edward Chan, A. Boersma and H.-Y. Tam, *Opt. Photonics J.*, 2013, **3**, 11–16.

- 19 E. B. Gaeva, V. Pimienta, S. Delbaere, A. V. Metelitsa, N. A. Voloshin, V. I. Minkin, G. Vermeersch and J. C. Micheau, *J. Photochem. Photobiol. A Chem.*, 2007, **191**, 114–121.
- 20 J. Ji, G. Song, X. Cai, J. Hu, L. Feng and H. Zhu, *Res. Chem. Intermed.*, 2016, **42**, 5597–5605.
- 21 US4915544, 1990.
- 22 K. Healey, W. Liang, P. D. Southon, T. L. Church and D. M. D'Alessandro, *J. Mater. Chem. A*, 2016, **4**, 10816–10819.
- 23 J. W. Brown, B. L. Henderson, M. D. Kiesz, A. C. Whalley, W. Morris, S. Grunder, H. Deng, H. Furukawa, J. I. Zink, J. F. Stoddart and O. M. Yaghi, *Chem. Sci.*, 2013, **4**, 2858–2864.
- 24 A. B. Kanj, K. Müller and L. Heinke, *Macromol. Rapid Commun.*, 2017, **39**, 1700239.
- 25 J. Park, L. B. Sun, Y. P. Chen, Z. Perry and H. C. Zhou, *Angew. Chemie Int. Ed.*, 2014, **53**, 5842–5846.
- 26 L. Heinke, M. Tu, S. Wannapaiboon, R. A. Fischer and C. Wöll, *Microporous Mesoporous Mater.*, 2015, **216**, 200–215.
- 27 J. Park, D. Yuan, K. T. Pham, J.-R. Li, A. Yakovenko and H.-C. Zhou, *J. Am. Chem. Soc.*, 2012, **134**(1), 99–102.
- 28 L. Heinke, M. Cakici, M. Dommaschk, S. Grosjean, R. Herges, S. Bräse and C. Wöll, *ACS Nano*, 2014, **8**, 1463–1467.
- 29 R. Lyndon, K. Konstas, B. P. Ladewig, P. D. Southon, P. C. J. Kepert and M. R. Hill, *Angew. Chemie Int. Ed.*, 2013, **52**, 3695–3698.
- 30 X. Lin, I. Telepeni, A. J. Blake, A. Dailly, C. M. Brown, J. M. Simmons, M. Zoppi, G. S. Walker, K. M. Thomas, T. J. Mays, P. Hubberstey, N. R. Champness and M. Schröder, *J. Am. Chem. Soc.*, 2009, **131**, 2159–71.
- 31 R. J. Marshall, C. L. Hobday, C. F. Murphie, S. L. Griffin, C. A. Morrison, S. A. Moggach and R. S. Forgan, *J. Mater. Chem. A*, 2016, **4**, 6955–6963.
- 32 A. J. Howarth, A. W. Peters, N. A. Vermeulen, T. C. Wang, J. T. Hupp and O. K. Farha, *Chem. Mater.*, 2017, **29**, 26–39.
- 33 H. Li, M. Eddaoudi, M. O'Keeffe and O. M. Yaghi, *Nature*, 1999, **402**, 276–279.
- 34 J. E. Mondloch, O. Karagiariidi, O. K. Farha and J. T. Hupp, *CrystEngComm*, 2013, **15**, 9258.
- 35 L. Malavolta, E. F. Poletti, E. H. Silva, S. Schreier and C. R. Nakae, *Int. J. Mol. Sci.*, 2008, **9**, 1321–32.
- 36 V. Gutmann, *Electrochim. Acta*, 1976, **21**, 661–670.
- 37 C. M. Hansen, *Hansen solubility parameters: a user's handbook*, CRC Press,

- 2007.
- 38 D. R. Lide, Ed., CRC Handbook of Chemistry and Physics.
- 39 S. R. Miller, P. A. Wright, C. Serre, T. Loiseau, J. Marrot and G. Férey, *Chem. Commun.*, 2005, **38**, 3850–3852.
- 40 X. Lan, N. Huang, J. Wang and T. Wang, *Chem. Commun.*, 2018, **54**, 584–587.
- 41 M. Kim, J. F. Cahill, H. Fei, K. A. Prather and S. M. Cohen, *J. Am. Chem. Soc.*, 2012, **134**, 18082–18088.
- 42 R. J. Marshall and R. S. Forgan, *Eur. J. Inorg. Chem.*, 2016, **2016**, 4310–4331.
- 43 F. Carson, E. Martínez-Castro, R. Marcos, G. G. Miera, K. Jansson, X. Zou and B. Martín-Matute, *Chem. Commun.*, 2015, **51**, 10864–10867.
- 44 C. Volkinger, M. Meddouri, T. Loiseau, N. Guillou, J. Marrot, G. Férey, M. Haouas, F. Tauelle, N. Audebrand and M. Latroche, *Inorg. Chem.*, 2008, **47**, 11892–11901.
- 45 B. Chen, N. W. Ockwig, A. R. Millward, D. S. Contreras and O. M. Yaghi, *Angew. Chemie Int. Ed.*, 2005, **44**, 4745–4749.
- 46 M. J. Katz, Z. J. Brown, Y. J. Colón, P. W. Siu, K. A. Scheidt, R. Q. Snurr, J. T. Hupp and O. K. Farha, *Chem. Commun.*, 2013, **49**, 9449–51.
- 47 K. E. Dekrafft, C. Wang and W. Lin, *Adv. Mater.*, 2012, **24**, 2014–2018.
- 48 J. Brunner and R. Kraemer, *J. Am. Chem. Soc.*, 2004, **126**, 13626–13627.
- 49 Y. Rahimi, A. Goulding, S. Shrestha, S. Mirpuri and S. K. Deo, *Biochem. Biophys. Res. Commun.*, 2008, **370**, 57–61.
- 50 S. L. Li and X. M. Zhang, *Inorg. Chem.*, 2014, **53**, 8376–8383.
- 51 X. Li, Y. Wang, T. Matsuura and J. Meng, *Heterocycles*, 1999, **51**, 2639.
- 52 J. Jagiello and J. P. Olivier, *J. Phys. Chem. C*, 2009, **113**, 19382–19385.
- 53 L. Li, N. Yuan, P. Wang, Y. Wu, Y. Song, Z. Chen and C. He, *J. Phys. Org. Chem.*, 2012, **25**, 872–877.
- 54 P. B. Terent'ev and A. P. Stankovichus, *Chem. Heterocycl. Compd.*, 1988, **24**, 1258–1262.

---

# **Chapter 3**

**Tracking non-fluorescent  
therapeutic agents from  
metal-organic frameworks**

---

### 3 Tracking non-fluorescent therapeutic agents from metal-organic frameworks

#### 3.1 MOFs as Drug Delivery Systems

Since the first example of pharmaceutical adsorption into MOFs in 2006,<sup>1</sup> interest in MOFs as potential drug delivery systems (DDSs) has grown. Their versatile and adaptable nature can lead to a variety of potential drug delivery mechanisms. The two main approaches to drug delivery from MOFs are illustrated in Figure 3.1, which are *via* post-synthetic encapsulation as guest molecules (*encapsulation strategy*) or by direct integration into framework building blocks (*direct assembly strategy*).

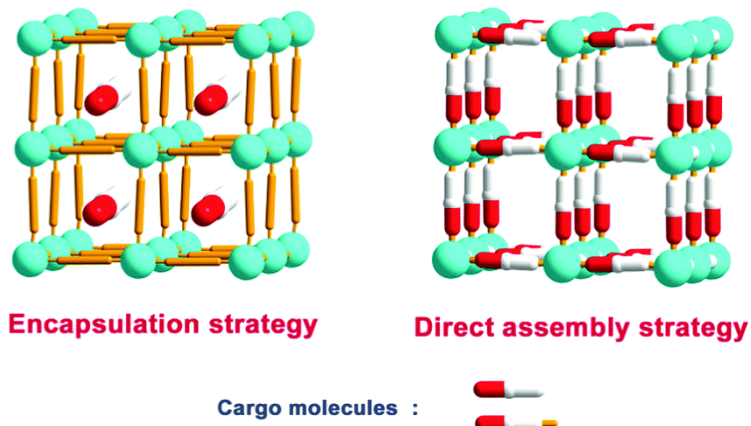


Figure 3.1. Two main cargo-loading strategies for MOFs, as indicated.  
Adapted from reference 2.

The first example of MOFs being used as hosts for therapeutic agents came from Horcajada *et al.* in 2006, where ibuprofen was encapsulated within MIL-100(Cr) and MIL-101(Cr) at 35 wt% and an impressive 140 wt% respectively. The difference in uptake was attributable to increased accessibility to larger pores in MIL-101(Cr). *In vitro* diffusion experiments into simulated body fluid (SBF) at 37 °C afforded complete ibuprofen loss after 3 and 6 days for MIL-100(Cr) and MIL-101(Cr) respectively. The increased retention time in MIL-101(Cr) was attributed to the larger number of aromatic rings present than in MIL-100(Cr), increasing the number of electrostatic interactions between ibuprofen and the host, and hence a longer retention time.

An early example of the *direct assembly* approach to MOF-therapeutic composites is from Lin and co-workers,<sup>3</sup> illustrated in Figure 3.2, who synthesised a framework consisting of a dicarboxylate bridging linker containing the anti-cancer drug *c,c,t*-(diamminedichlorodisuccinato)Pt(IV) (DSCP, abbreviated for disuccinatocisplatin) and Tb<sup>3+</sup> ions. The resulting amorphous nanoparticles were post-synthetically coated with a silica shell to increase stability and functionalised with c(RGDfK), a cyclic peptide sequence which demonstrates high binding affinity for an integrin upregulated in many angiogenic cancers. Uptake of the nanoparticles into cells was *via* receptor-mediated endocytosis upon surface modification with c(RGDfK), and subsequent reduction of the DSCP-functionalised linker led to the formation of the biologically active Pt(II) species. The thickness of the silica shell can be controlled by the length of reaction time and amount of tetraethyl orthosilicate (TEOS) starting material, affording a pharmaceutical-enriched nanoMOF with tuneable degradability.

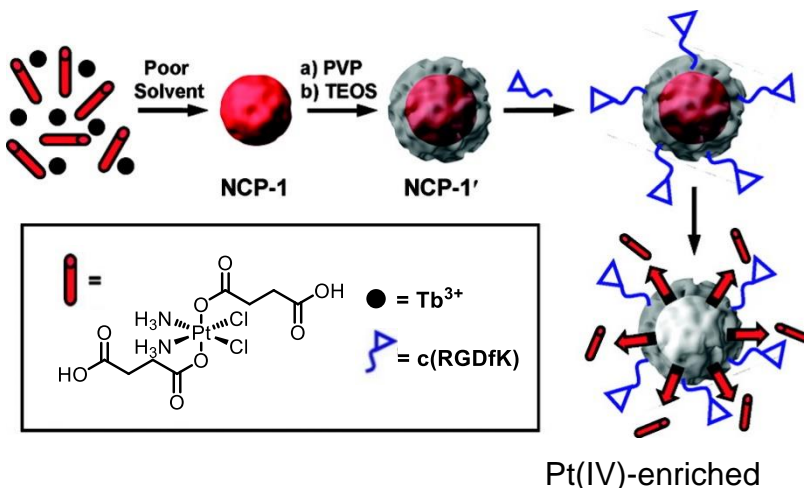


Figure 3.2. Schematic of cisplatin-enriched nanoMOFs synthesis.  
Taken from reference 3.

A persistent challenge in the design of DDSs is ensuring appropriate release and dosing of therapeutic to the patient, which can be tackled by triggered release DDSs. Drug release can be triggered by either intrinsic (e.g. biological pH, redox state, biomolecule availability) or extrinsic (e.g. irradiation or changes in magnetic field) stimuli, both with their own advantages and disadvantages.<sup>4</sup>

Internal stimuli exploit inherent physiological differences within damaged tissues, such as the reduced pH in tumour cells, while extrinsic stimuli can allow more control over the drug release.<sup>5</sup>

An example of intrinsically stimulated drug release was reported by Rosi and co-workers in 2009.<sup>6</sup> The synthesis of novel material bio-MOF-1 ( $[Zn_8(ad)_4(BPDC)_6O \cdot 2Me_2NH_2, 8DMF, 11H_2O]$ , where ad = adeninate and BPDC = biphenyldicarboxylate), was followed by post-synthetic exchange of the  $Me_2NH_2^+$  cations with the cationic drug procainamide HCl, a common antiarrhythmic, to form  $[Zn_8(ad)_4(BPDC)_6O \cdot 3.5(proc-H^+), 1.5Cl^-, 16.5H_2O]$  (where proc = procainamide). Procainamide has a short *in vivo* half-life and requires dosing every 3–4 h. It was therefore an ideal candidate for a controlled release study. Introduction of the drug-loaded bio-MOF-1 to phosphate-buffered saline (PBS) buffer leads to further cation exchange, triggering release of procainamide- $H^+$  as  $Na^+$  ions are adsorbed into the framework.

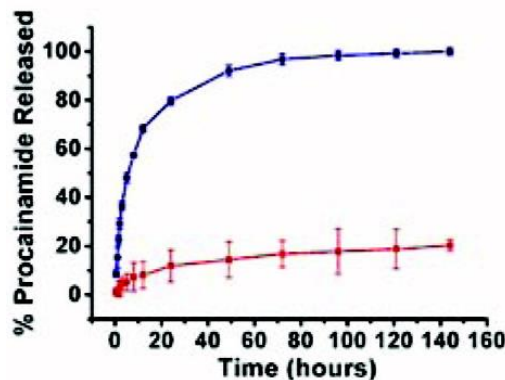


Figure 3.3. Release of procainamide- $H^+$  into 0.1 M PBS buffer (blue) and ultrapure (red) over 140 h. Adapted from reference 6 (highest available resolution).

Figure 3.3 shows the procainamide- $H^+$  loss from bio-MOF-1 into PBS buffer (blue) and ultrapure water (red). Steady release was observed into PBS over 20 h and complete loss after 72 h, proving that encapsulation within a biocompatible framework delivered the therapeutic more efficiently than through currently-used intravenous or oral administration.

In comparison to other popular nanoscale DDSs – such as micelles,<sup>7–11</sup> zeolites<sup>12–14</sup> and quantum dots<sup>4,11,15–20</sup> – MOFs boast several advantages. Organic delivery systems, such as micelles, often suffer from poor drug loadings and inefficient and uncontrolled release of therapeutic agent.<sup>21,22</sup> Inorganic delivery systems, such as zeolites and quantum dots, are hindered by low therapeutic loadings, but exhibit more controlled release of treatment due to their well-ordered structures.<sup>22</sup> MOFs can present high drug loadings as well as slow, controlled release.<sup>1,6,23–25</sup> Control of the constituent parts of the framework, *via* approaches such as the aforementioned post-synthetic modification of frameworks with targeting functionality or *via* inclusion of biocompatible metals, presents a range of opportunities to exploit the inherent high porosity and extended order within MOFs. For this work, we exploit the high drug loading capabilities and controlled release mechanisms reported previously<sup>1,22,25</sup> to examine the kinetics of pharmaceutical guest desorption from single crystals of MOFs by *in situ* infrared microspectroscopy.

### 3.1.1 Therapeutic uses of carbon monoxide

Despite the well-known toxicity and hazardous effects of carbon monoxide, it has shown promise over the last two decades as a therapeutic agent.<sup>26–28</sup> In particular, CO is appropriate for use as an anti-inflammatory and to reduce likelihood of transplant rejection and to prolong the storage of organs in transplant.

Ferrández *et al.* reported a significant reduction in manifestation of collagen-induced arthritis after treatment of mice with a CO-releasing molecule, tricarbonylchloro(glycinato)ruthenium(II) (known as CORM-3).<sup>29</sup> Reduction of PGE2 (a fatty acid produced at elevated levels by tissues during inflammation) and various interleukins (a class of glycoproteins produced to regulate immune responses) were observed following treatment, suggested diminished response by the immune system to collagen-induced arthritis.

The same CO-releasing molecule (CORM-3) was reported by Motterlini and co-workers to prolong the life of transplanted hearts in mice.<sup>30</sup> Untreated mice saw organ failure after 9 days, whereas 60% of mice receiving CORM-3 did not show any signs of rejection. The same group also reported how CORM-3 aided the successful preservation of kidneys *ex vivo*.<sup>31</sup> They stated that kidneys treated with the CO-releasing compound and stored at 4 °C displayed better blood flow, sodium and glucose reabsorption rates and glomerular (kidney) filtration rate than those stored at 4 °C but not treated.

The effect of CO on intimal hyperplasia (the thickening of the innermost layer of an artery or vein) in a porcine model was investigated by Raman *et al.* in 2006.<sup>32</sup> Reception of inhaled CO (250 ppm) both before and during balloon angioplasty led to a 51.7% reduction in scar tissue generally associated with intimal hyperplasia. Figure 3.4 below shows significantly thicker scar tissue in the arteries of a pig not treated with CO.

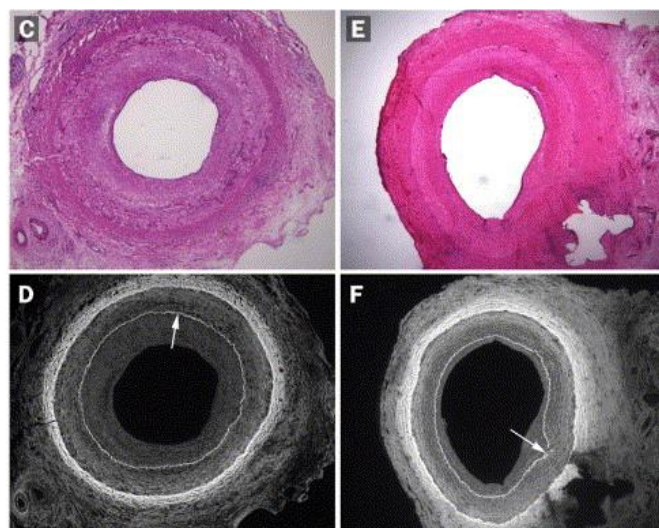


Figure 3.4. Histological analysis of pig arteries 3 weeks after angioplasty. Sections were stained (C, E) or viewed under autofluorescence (D, F). C & D show surgically injured pig artery from a pig treated with oxygen. E & F show surgically injured pig artery from a pig treated CO. Arrows indicate scar tissue. Adapted from reference 32.

Alongside the success MOFs have shown in the drug delivery arena, they are currently employed internationally as a tool to combat food waste. Decco, alongside Queens University Belfast spinout company MOF Technologies, have produced a framework that slowly releases 1-methylcyclopropene (1-MCP) to combat fruit ripening.<sup>33</sup> This keeps fruit fresh for longer and enables it to be stored for up to nine months. This commercialisation of a slow guest-release mechanism could also be employed to CO release, enabling the therapeutic benefits of the gas to be delivered in a slow, controlled manner.

## 3.2 Aims and Objectives

In this chapter, we are investigating the intrinsic diffusion of therapeutic agents in MOFs. This was studied in two scenarios – the diffusion of a pharmaceutical guest molecule from a MOF into solvent, and the diffusion of a gaseous small molecule from a MOF. The primary challenge of this chapter, however, was developing and adapting a methodology to track such diffusion, specifically, of neutral, coordinatively-innocent non-luminescent guests within single crystals. To achieve this, rather than optical spectroscopies in the visible region, we have employed infrared microspectroscopy. The objectives of this chapter are:

1. Method development for solvent-induced diffusion
2. Test method with several drug-loaded frameworks
3. Study guest release from single crystals, validating the method
4. Compare release from single crystals with data obtained from bulk crystalline powders to assess the wider applicability of the method

## 3.3 Choice of materials

A variety of MOFs, guest pharmaceuticals (shown in Figure 3.7 on pp.136) and diffusion solvents were considered for MOF $\rightarrow$ guest desorption experiments, discussed in Section 3.5.1. The FT-IR spectra recorded on an infrared microscope at DLS B22 MIRIAM for these materials are shown in Figure 3.5. Samples of each MOF shown in Figure 3.6 were loaded with each analyte shown in Figure 3.7 and screened for suitability during the first trip to Diamond Light Source B22 MIRIAM. Key features of these spectra are highlighted in Figures 3.9–3.11.

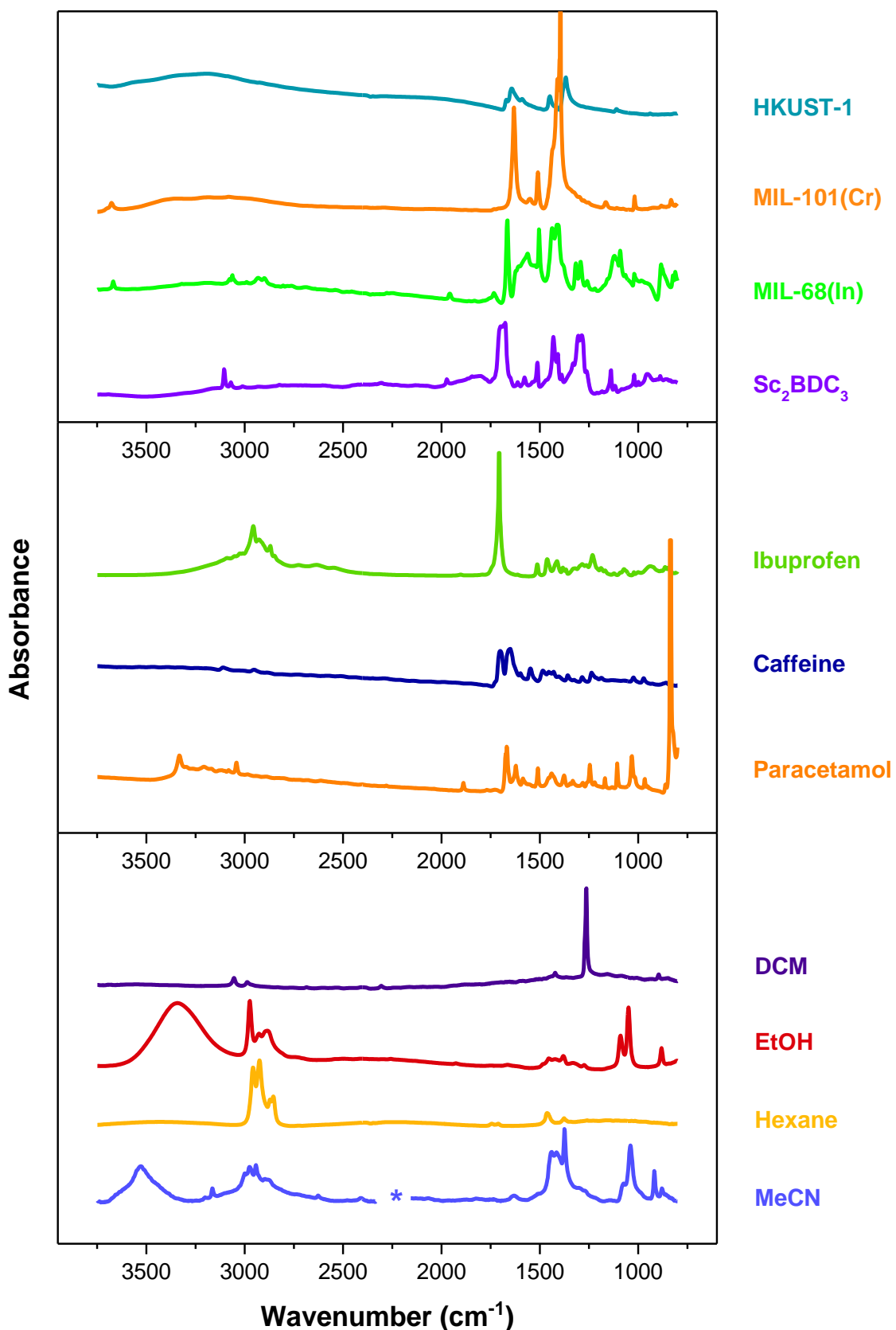
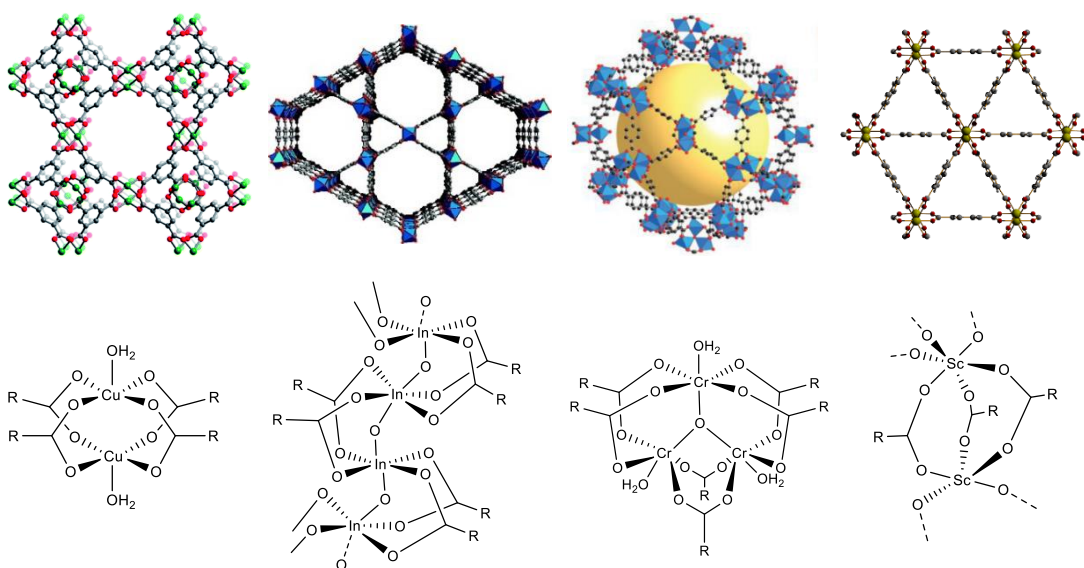


Figure 3.5. *In situ* infrared spectra of (top) metal-organic frameworks, (middle) guest pharmaceuticals and (bottom) solvents considered for desorption experiments, as indicated.  
 \* region contains  $\text{CO}_2$  background peaks, removed for clarity.

The MOFs shown in Figure 3.6 were chosen for several reasons. MIL-68(In) and  $\text{Sc}_2\text{BDC}_3$  were investigated in Chapter 2, where we focussed on tracking the binding of coordinating fluorescent guest species via UV-visible absorption and emission spectroscopies. Therefore, these two frameworks were also investigated here. HKUST-1 and MIL-101(Cr) both have literature precedent in the DDS field,<sup>1,25,34</sup> and hence were studied in this work. Portions of the crystal structures showing the pore structure and schematic representations of the metal nodes are shown in Figure 3.6.



*Figure 3.6. (Top) Crystal structures of (left-to-right) HKUST-1, MIL-68(In), MIL-101(Cr) and  $\text{Sc}_2\text{BDC}_3$ . (Bottom) Metal nodes for the frameworks shown above. Crystal structures (excluding  $\text{Sc}_2\text{BDC}_3$ ) taken from references 35–37.*

The pharmaceutical guest molecules shown in Figure 3.7 were chosen as they were readily available, uncontrolled substances that had precedent in the drug delivery arena,<sup>1,38–40</sup> and characteristic infrared spectra, which are discussed below. Caffeine, ibuprofen and paracetamol have previously been studied in the MOF–DDS field.

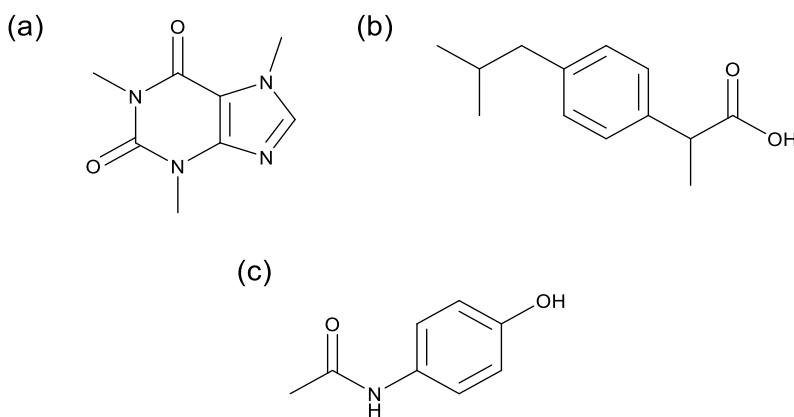


Figure 3.7. ChemDraw structures of (a) caffeine, (b) ibuprofen and (c) paracetamol.

Although the ideal medium for biological applications is obviously water or buffer solutions, the fundamental diffusion properties are important regardless of solvent choice. Some guest pharmaceuticals discussed herein have poor water solubility and are often administered as the HCl salt. To avoid complication of charged species interactions with the framework (as investigated in Chapter 2), we are in this chapter focussing on fundamental diffusion from non-aqueous solvents (shown below in Figure 3.8). Key criteria are therefore guest solubility and avoiding IR spectral overlap. The solvent IR spectra are shown in Figure 3.11 (bottom) on pp.139.

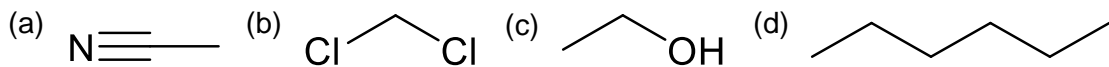


Figure 3.8. ChemDraw structures of (a) acetonitrile (*MeCN*), (b) dichloromethane (*DCM*), (c) ethanol (*EtOH*) and (d) *n*-hexane.

## 3.4 IR spectral features

### 3.4.1 MOF IR spectral features

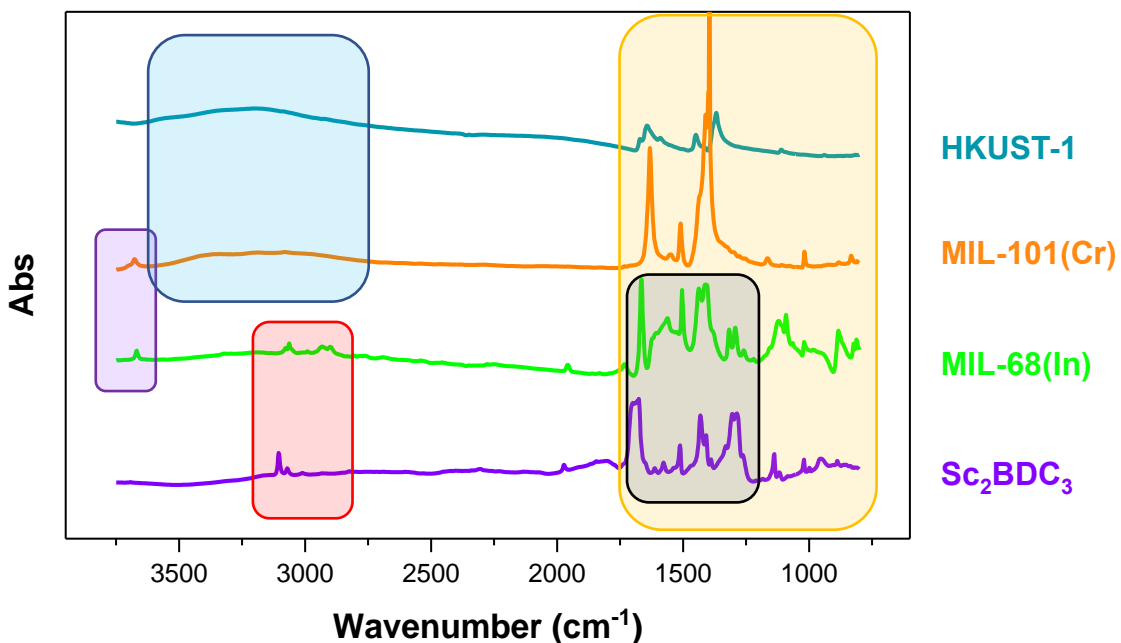


Figure 3.9. Infrared spectra of single crystals of the MOFs studied in this chapter.

Figure 3.9 shows the IR spectra of the frameworks investigated with the key features colour-coded and identified below.

#### All spectra

**Multiple peaks from 3200–2800 cm<sup>-1</sup>** – aromatic C–H

**Multiple peaks from ~1800 cm<sup>-1</sup> to lower energy** – metal-bound carboxylates, aromatic ring modes and other low energy vibrations in the fingerprint region

#### Some spectra

**Sharp peak at 3675 cm<sup>-1</sup>** – metal-bound OH groups

**Broad peak from 3600–2800 cm<sup>-1</sup>** – water (despite drying procedures). Often obscures  $\nu$ (C–H)

*N.B. Saturation was not uncommon in our experiments in region 1600–1300 cm<sup>-1</sup>, resulting from thick crystals. This phenomenon is detailed further in Section 1.7.*

### 3.4.2 Guest pharmaceutical IR spectral features

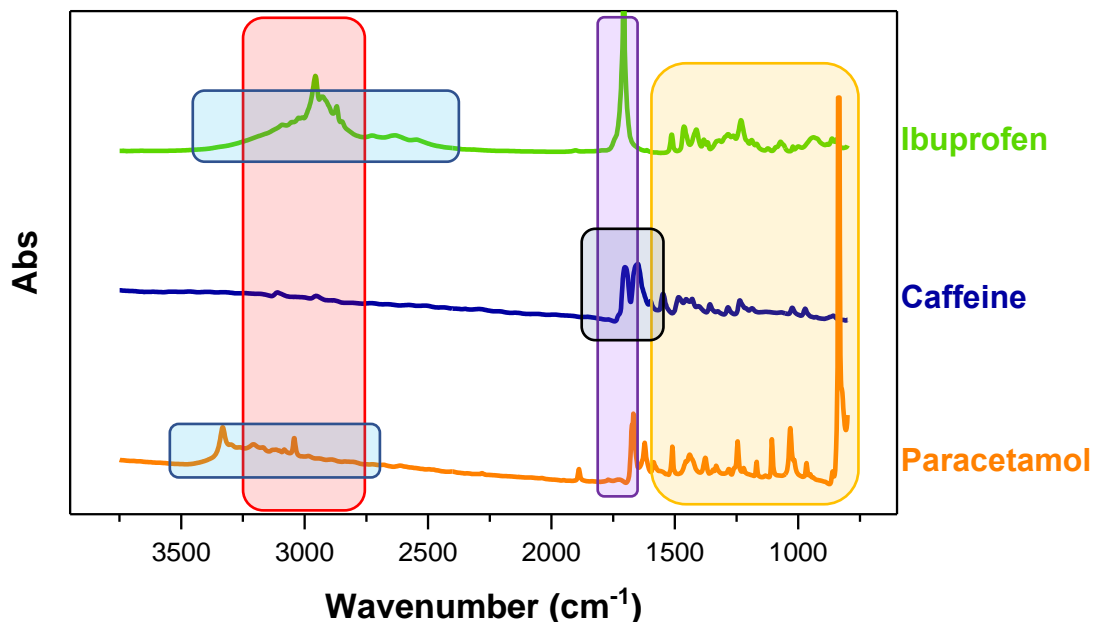


Figure 3.10. Infrared spectra of guest pharmaceuticals studied in this chapter.

Figure 3.10 shows the IR spectra of the pharmaceutical guests investigated with the key features colour-coded and identified below.

#### All spectra

**Multiple peaks from 3200–2700 cm<sup>-1</sup>** – from alkyl and aromatic C–H

**Multiple peaks from 1750–1600 cm<sup>-1</sup>** – from C=O

**Multiple peaks from ~1800 cm<sup>-1</sup> to lower energy** – from aromatic ring modes, C–N and other low energy vibrations in the fingerprint region

#### Some spectra

**Broad peak from 3450–3150 cm<sup>-1</sup>** – from N–H

**Broad peak from 3400–2450 cm<sup>-1</sup>** – from COOH group and/or water

**Sharp peak from 1700–1600 cm<sup>-1</sup>** – from C=N

### 3.4.3 Solvent IR spectral features

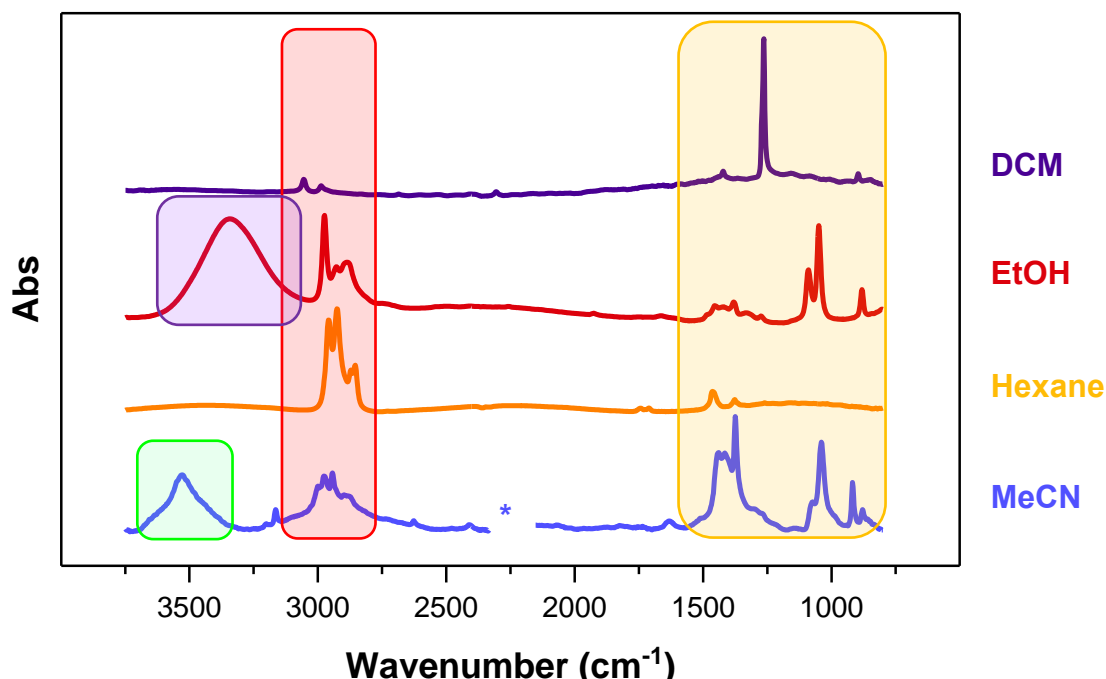


Figure 3.11. Infrared spectra of diffusion solvents used in this chapter.

Figure 3.11 shows the IR spectra of the diffusion solvents investigated with the key features colour-coded and identified below.

#### All spectra

**Multiple peaks from 3100–2800 cm<sup>-1</sup>** – from alkyl C–H

**Multiple peaks from ~1800 cm<sup>-1</sup> to lower energy** – from C–C, C–Cl and other low energy vibrations in the fingerprint region

#### Some spectra

**Broad peaks from 3700–3400 cm<sup>-1</sup>** – from C≡N

**Broad peak from 3500–3150 cm<sup>-1</sup>** – from ethanol OH group and residual water

Having identified the key spectral features of each spectrum, Figure 3.12 shows an example of the considerations applied for the experiments in this chapter (solvent, MOF, guests). Regions of interest for analytes are indicated for caffeine (blue), highlighting the lack of spectral overlap of their peaks of interest with infrared features of the solvent and framework shown. The method development is discussed in Section 3.5.1.1.

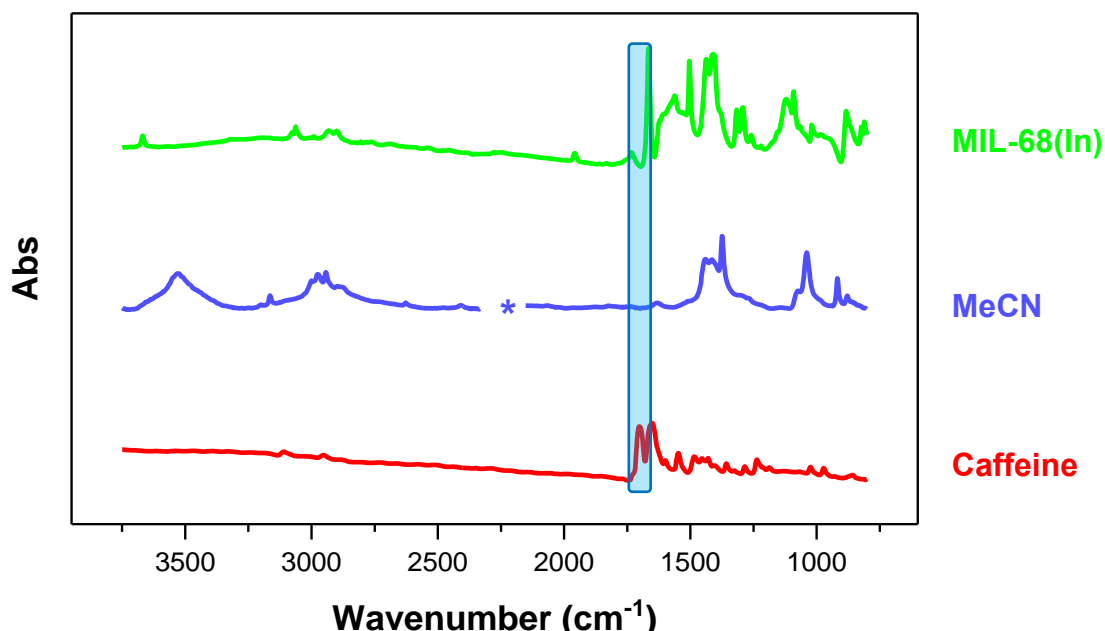


Figure 3.12. Example spectral overlap comparison, with regions of interest indicated for caffeine (blue).

\* region contains  $\text{CO}_2$  background peaks, removed for clarity.

Given these considerations, this chapter describes the method development of experiments using MeCN to track the diffusion of caffeine from single crystal and bulk crystalline powder forms of MIL-68(In), to investigate the applicability of the method to both MIL-68(In) morphologies.

## 3.5 Results and Discussion

### 3.5.1 DLS B22 MIRIAM analyte diffusion experiments

The experiments discussed in this section were carried out during two visits to DLS B22 MIRIAM. The aim of the experiments was to extract data regarding desorption kinetics of caffeine from metal-organic frameworks. Details of experimental development associated with this section are described below.

#### 3.5.1.1 Experimental development

##### 3.5.1.1.1 Extrinsically bound analyte removal

Sample preparation of MIL-68( $\text{In}$ ) $\supset$ caffeine from saturated caffeine solution in DCM (0.2 M) led to large amounts of crystallised caffeine present upon solvent evaporation. The visual similarity of crystalline caffeine and the framework crystals made locating MIL-68( $\text{In}$ ) $\supset$ caffeine crystals on the microscope difficult, and apparent there would be extrinsic caffeine on the surface of the framework.

To prevent the kinetics of caffeine loss being convoluted with extrinsic caffeine, a rapid washing protocol was developed. Samples were collected from the stock analyte solution *via* centrifugation, submerged in 0.5 mL of clean, anhydrous DCM, briefly vortex mixed, the tube centrifuged again, the supernatant decanted, the Eppendorf tube vortex mixed again (containing just framework and residual solvent) and the crystals then transferred to the Linkam cell using a 10  $\mu\text{L}$  pipette tip. This was performed rapidly to minimise extraction of analyte from the framework. As this experiment measured the diffusion rate of guest from the framework, and not the total uptake, a small loss of guest from the initial samples can be tolerated to the point at which the signal becomes too small to reliably measure.

### 3.5.1.1.2 Solvent evaporation during analyte diffusion

The Linkam cell contains a sizeable (relative to the sample size) volume of ‘dead space’. Figure 3.13 below shows a schematic of the experimental setup within the Linkam stage for these experiments. Due to the use of solvent in this experiment, we encountered several problems with evaporation of solvent around the sample.

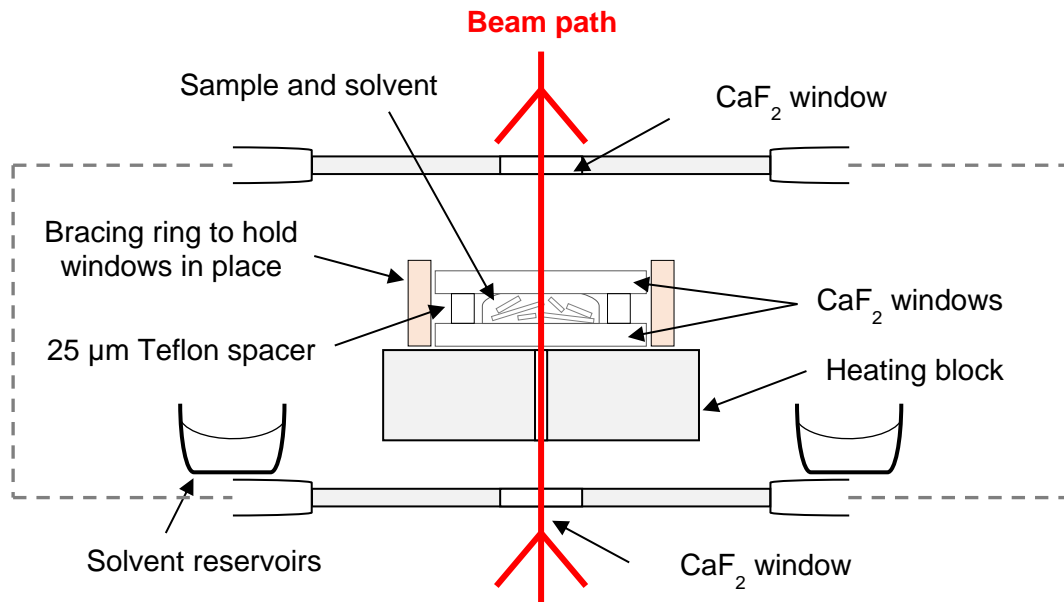


Figure 3.13. Schematic of solvent-saturated Linkam cell

To minimise solvent evaporation, solvent reservoirs ( $2 \times 2\text{ mL}$  each) were positioned in the base of the Linkam cell. A  $25\text{ }\mu\text{m}$  Teflon spacer was placed around the sample following solvent addition and an additional  $\text{CaF}_2$  window was placed on top of the spacer to create a sub-compartment within the stage.

*In situ* IR spectroscopic measurements were carried out on the B22 MIRIAM beamline at the Diamond Light Source, according to the experimental setup described in Section 1.6.

Samples were loaded on to and topped with a  $0.2 \times 16\text{ mm}$   $\text{CaF}_2$  window and enclosed within a variable-temperature gas-tight Linkam FTIR600 cell fitted with  $0.2 \times 22\text{ mm}$   $\text{CaF}_2$  top and bottom windows, with the above adaptation to combat solvent evaporation. Spectra were collected using slit sizes of  $15 \times 15\text{ }\mu\text{m}$ .

DCM and MeCN used for washings and diffusion experiments were collected from Cardiff University's in-house solvent purification system (SPS) and stored over molecular sieves under N<sub>2</sub>.

### 3.5.1.1.3 Choice of MOF and analyte

The first visit to DLS B22 MIRIAM involved screening different frameworks, analytes and solvents to find a combination with clear analyte bands to facilitate spectral processing. Two frameworks taken to B22 (MIL-68(In) and Sc<sub>2</sub>BDC<sub>3</sub>) were investigated in Chapter 2 for post-synthetic modification, whilst the other two frameworks (HKUST-1 and MIL-101(Cr)) were chosen for their drug delivery capabilities.<sup>1,23,24</sup>

Figure 3.10 on pp.138 shows the infrared spectrum of the pharmaceutical analytes. The spectra of caffeine and ibuprofen exhibit peaks that are easily monitored, enabling straightforward tracking of analyte diffusion. The spectrum of paracetamol does not contain any peaks that are as easily identifiable, and hence focus was shifted to caffeine and ibuprofen.

Out of the four solvents considered (DCM, EtOH, hexane and MeCN), the low surface tension of hexane (17.89 mN/m) prevented the positioning of a stable droplet on top of the sample. Due to the high solubility of caffeine in DCM, it was avoided to prevent caffeine diffusing from the framework too quickly. For this reason, EtOH and MeCN were the solvents employed for initial experiments exploring the unloading of analytes.

Saturated solutions of caffeine, ibuprofen and paracetamol were made up in DCM, EtOH and EtOH respectively. HKUST-1, MIL-68(In), MIL-101(Cr) and Sc<sub>2</sub>BDC<sub>3</sub> were immersed in each analyte solution and solutions were exchanged three times a day over the course of a one week to ensure maximum uptake of each analyte.

Initial experiments at B22 presented problems with several materials. Crystals of  $\text{Sc}_2\text{BDC}_3$  were large enough that insufficient light was able to be detected by the spectrometer, providing poor quality spectra. The spectrum of MIL-101(Cr) contained peaks for unreacted terephthalic acid ( $1621 \text{ cm}^{-1}$ ), and hence was unsuitable. MIL-68(Ind) showed no unreacted linker, no saturation in the region of interest and no sloping baseline. Due to limited time available on the beamline, only the loss of caffeine from MIL-68(Ind) was investigated in detail. In future, ibuprofen would be a suitable candidate for investigation.

### 3.5.1.2 Spectral analysis

The loss of caffeine from MIL-68 into MeCN was tracked at 10, 15, 20, 25, 30 and 35 °C. Spectra were analysed in OriginPro 2017, by peak integration and subsequent exponential curve fitting. Masks were applied to all data outside  $1716.4\text{--}1691.4 \text{ cm}^{-1}$  and baseline correction was applied. Three types of baseline correction were used: constant, no baseline (integral taken from  $y = 0$ ) and straight line. These are illustrated below in Figure 3.14.

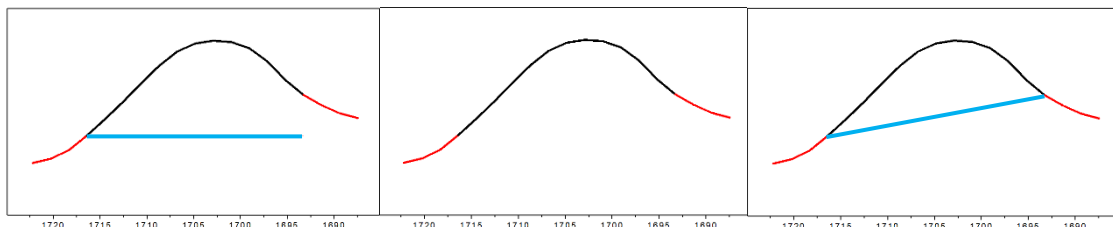


*Figure 3.14. Possible baseline corrections; (left) constant, (centre) no baseline (integral taken from  $y = 0$ ) and (right) straight line.*

Detailed baseline positions for each experimental temperature are shown overleaf in Figure 3.15. Following baseline correction, the caffeine peak was integrated between  $1710.6\text{--}1695.2 \text{ cm}^{-1}$ . These peak integrals were then plotted against time and fit to exponential curves, where  $y_0$  was fixed to 0. All fitted curves can be seen on pp.146–148. Summative curve fitting results are shown in Table 3.1 on pp.149.

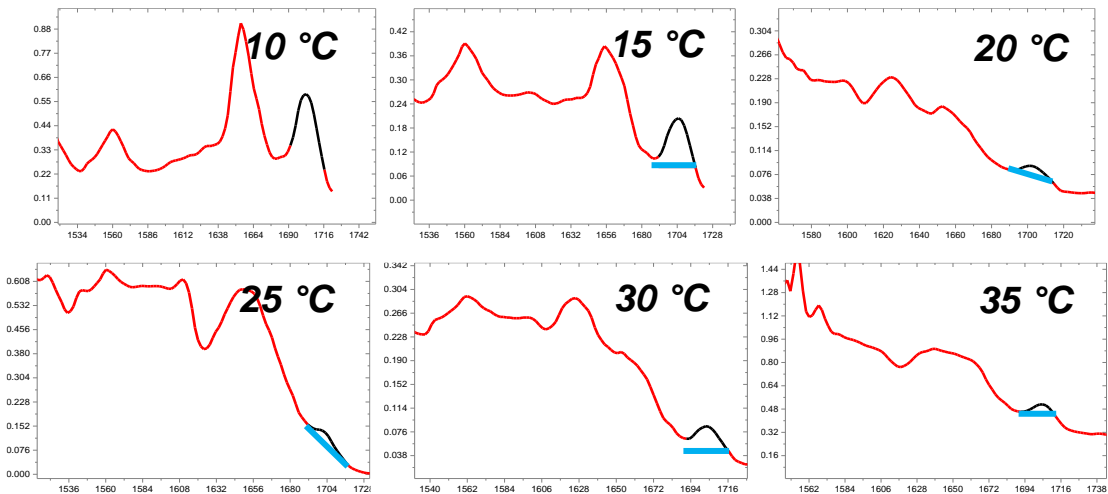


*Figure 3.15. Baseline applied to MIL-68(In)-caffeine spectra during peak integration at indicated temperatures. Baselines are coloured blue.*

**10 °C**

No baseline was applied to the 10 °C data set and peak integrals were calculated from  $y = 0$ .

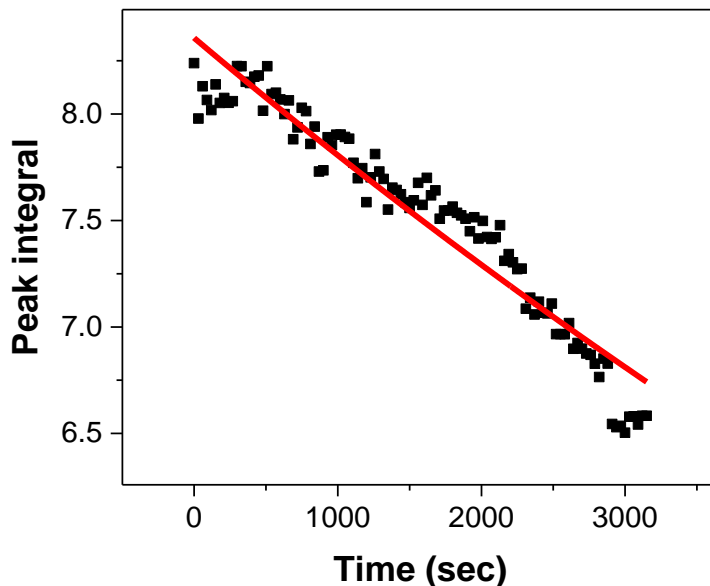


Figure 3.16. Peak integral change of 1700 cm<sup>-1</sup> caffeine carbonyl band during diffusion from MIL-68(In) at 10 °C.

**15 °C**

A constant baseline was applied to the 15 °C data set.

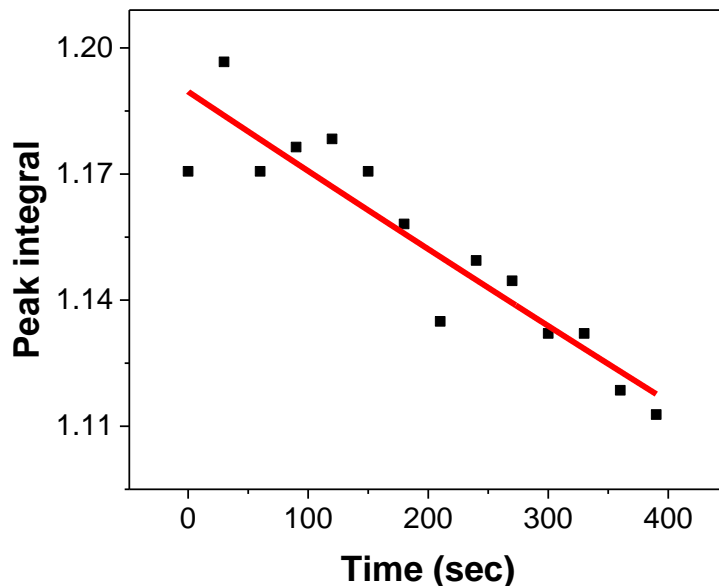


Figure 3.17. Peak integral change of 1700 cm<sup>-1</sup> caffeine carbonyl band during diffusion from MIL-68(In) at 15 °C.

## 20 °C

A straight line baseline was applied to the 20 °C data set.

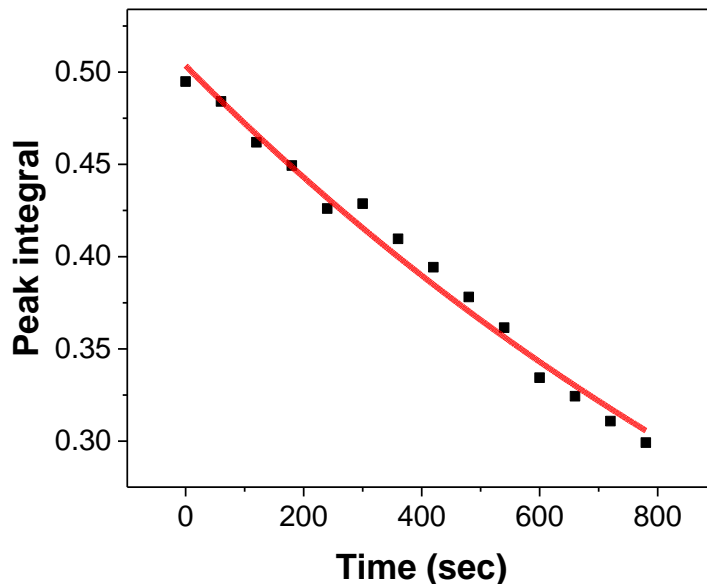


Figure 3.18. Peak integral change of  $1700\text{ cm}^{-1}$  caffeine carbonyl band during diffusion from MIL-68(In) at 20 °C.

## 25 °C

A straight line baseline was applied to the 25 °C data set.

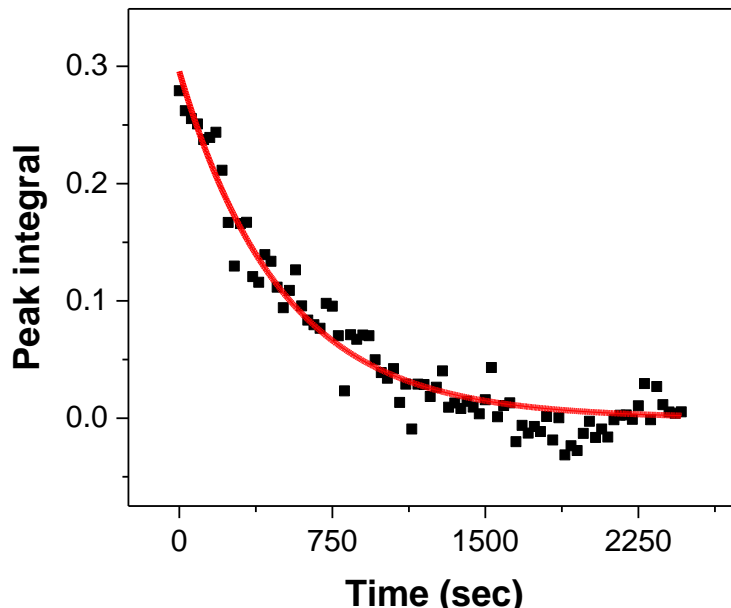


Figure 3.19. Peak integral change of  $1700\text{ cm}^{-1}$  caffeine carbonyl band during diffusion from MIL-68(In) at 25 °C.

### 30 °C

A constant baseline was applied to the 30 °C data set.

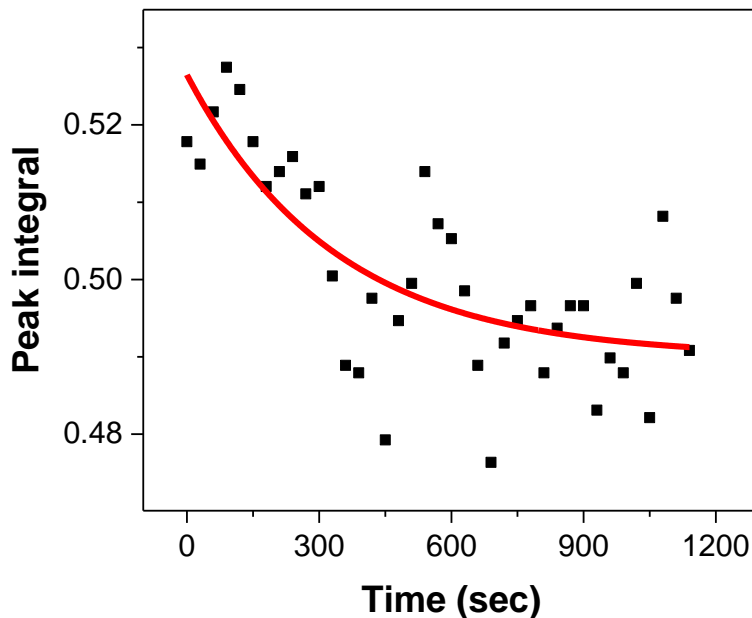


Figure 3.20. Peak integral change of  $1700\text{ cm}^{-1}$  caffeine carbonyl band during diffusion from MIL-68(Ind) at 30 °C.

### 35 °C

A straight line baseline was applied to the 35 °C data set.

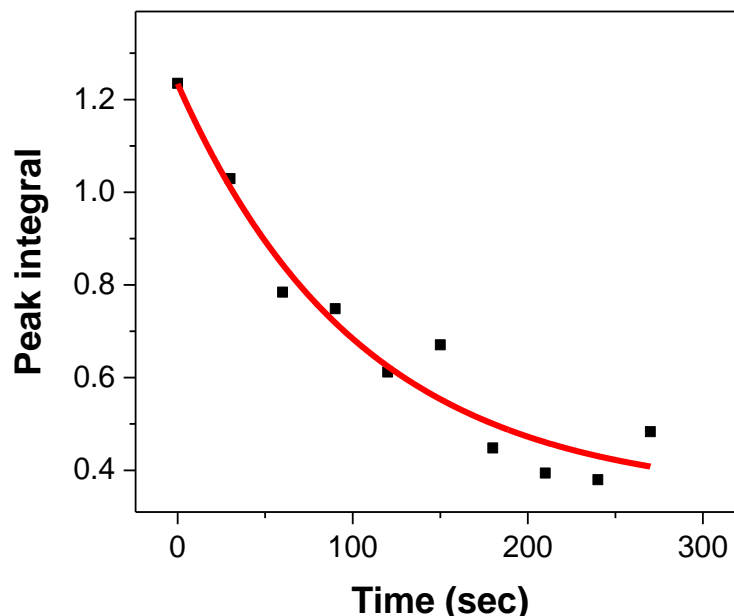


Figure 3.21. Peak integral change of  $1700\text{ cm}^{-1}$  caffeine carbonyl band during diffusion from MIL-68(Ind) at 35 °C.

Exponential decay curves were fit to the plots shown in Figures 3.16–3.21 in OriginPro 2017 using the Equation 3.1. The results from these fits are shown in Table 3.5.

$$y = y_0 + Ae^{\frac{-x}{\tau}}$$

*Equation 3.1. Exponential curve decay equation.*

*Table 3.1. Exponential curve fitting results from MIL-68(In)–caffeine diffusion experiments.*

	10 °C	15 °C	20 °C	25 °C	30 °C	35 °C
<b>A</b>	8.36 ± 0.03	1.190 ± 0.005	0.503 ± 0.005	0.296 ± 0.008	0.490 ± 0.004	0.89 ± 0.09
<b>τ</b>	14666 ± 412	6251 ± 736	1564 ± 55	501 ± 20	336 ± 138	104 ± 29
<b>Red. <math>\chi^2</math></b>	1.8 × 10 <sup>-2</sup>	9.7 × 10 <sup>-5</sup>	6.4 × 10 <sup>-5</sup>	3.2 × 10 <sup>-4</sup>	7.8 × 10 <sup>-5</sup>	4.9 × 10 <sup>-3</sup>
<b>R<sup>2</sup></b>	0.925	0.858	0.986	0.951	0.569	0.952

Values for  $\tau$  are given in minutes. As each experiment examined the relative loss of caffeine from MIL-68(In), and not the complete loss, the exponential fitting result parameter of most importance was the time component,  $\tau$ . These values are given in minutes above in Table 3.5. Use of these values in the next section is justified as we are examining the relative reduction in characteristic caffeine bands and not complete loss.

The R<sup>2</sup> values for all fits are reasonable, although we note peaks within the 10 and 15 °C spectra are still decreasing significantly within the timeframe of the experiment. Longer experimental runs would provide more reliable data regarding the diffusion process, but this was not possible due to eventual fogging of the infrared windows in the sample cell.

## Arrhenius plot

Using the reciprocal of  $\tau$  values given in Table 3.1 to generate  $k$  ( $k = 1/\tau$ ), an Arrhenius plot was constructed to calculate the  $E_a$  of caffeine diffusion. The Arrhenius plot is shown below in Figure 3.22.

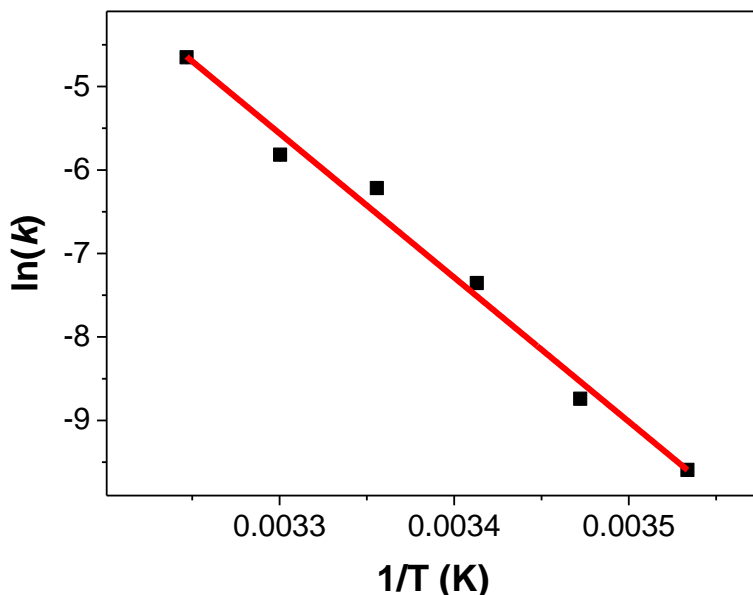


Figure 3.22. Arrhenius plot of caffeine diffusion from MIL-68(ln)⊃caffeine.  
N.B. Calculated errors are negligible (max. 0.02%) and are therefore not shown.

A linear fit of the Arrhenius plot gave a slope of  $-17265 \pm 984$ . Using the Arrhenius equation (given below in Equation 3.2);

$$k = A e^{-\frac{E_a}{RT}}$$

Equation 3.2. Arrhenius equation.

$E_a$  of  $+144 \text{ kJ mol}^{-1}$  (Calculated error  $<1 \text{ kJ mol}^{-1}$ ) was calculated for the diffusion of caffeine from MIL-68(ln)⊃caffeine (12.6 wt%). This is larger than the  $E_a$  calculated for the diffusion of ferrocene (FC) in SURMOF  $\text{Cu}_2(\text{ndc})_2(\text{dabco})$ , which was  $+90 \pm 30 \text{ kJ mol}^{-1}$ .<sup>41</sup>

Note, that the  $E_a$  of FC diffusivity was calculated during the uptake of FC into the SURMOF, as opposed to diffusion out of the framework, as in our experiment. Furthermore, the guest materials in question (caffeine and ferrocene) are significantly different. There is currently no literature evidence for the  $E_a$  of a process to be calculated from the infrared peak integrals. Therefore, despite the difference in framework and guest materials employed in the SURMOF $\supset$ FC experiment, calculating a  $E_a$  of similar magnitude in our experiments warranted its mention as a comparable example. It is still slightly surprising that caffeine diffusion is as slow as it is in our experiments given the high  $E_a$ .

### 3.5.1.3 Diffusion from bulk powder

To compare the diffusion of caffeine from single crystals of MIL-68(Indium) to the bulk crystalline powder, experiments were carried out to measure the mass of caffeine lost from a larger sample of MIL-68(Indium) $\supset$ caffeine into MeCN. All materials were subjected to the same extrinsically bound analyte removal washing procedure (discussed in Section 3.2.1.1.1), where bulk sample was vortex mixed in clean DCM, pelleted by centrifugation and the supernatant liquor decanted. Solids were then left to dry in air.

150 mg of washed MIL-68(Indium) $\supset$ caffeine was held at 15, 20, 25 or 30 °C, and 1 mL of MeCN was added. 150 mg of material was used to ensure a measurable mass of caffeine in MeCN after the shortest mixing period. These samples were vortex mixed at 1,500 rpm for 5, 10, 20, 30, 60 or 90 minutes. Based on the single crystal data, all caffeine should have desorbed after 90 minutes at room temperature. *In situ* experiments indicated that caffeine loss began immediately following solvent addition, hence the first time point taken was 5 minutes. No shorter time points were collected. Any shorter time points would exceed five minutes due to the additional time involved in the experiments (centrifugation, decanting, etc.). After the vortex mixing, the samples were then pelleted by centrifugation and the supernatant liquor carefully decanted into individual pre-weighed sample vials, ensuring that the solid bed of MIL-68(Indium) was not disturbed.

The decanted solvent was then allowed to evaporate in air overnight, before all traces of solvent were removed by drying under high vacuum for a further 16 hr. The mass of caffeine desorbed from MIL-68(Ind)–caffeine during vortex mixing was then calculated by weighing the dried sample vials. A 5 decimal place analytical balance was used to weigh sample vials pre- and post-experiment to achieve the best available precision.

Figure 3.23 shows plots of the mass of desorbed caffeine with increasing mixing time at 15, 20, 25 and 30 °C respectively.

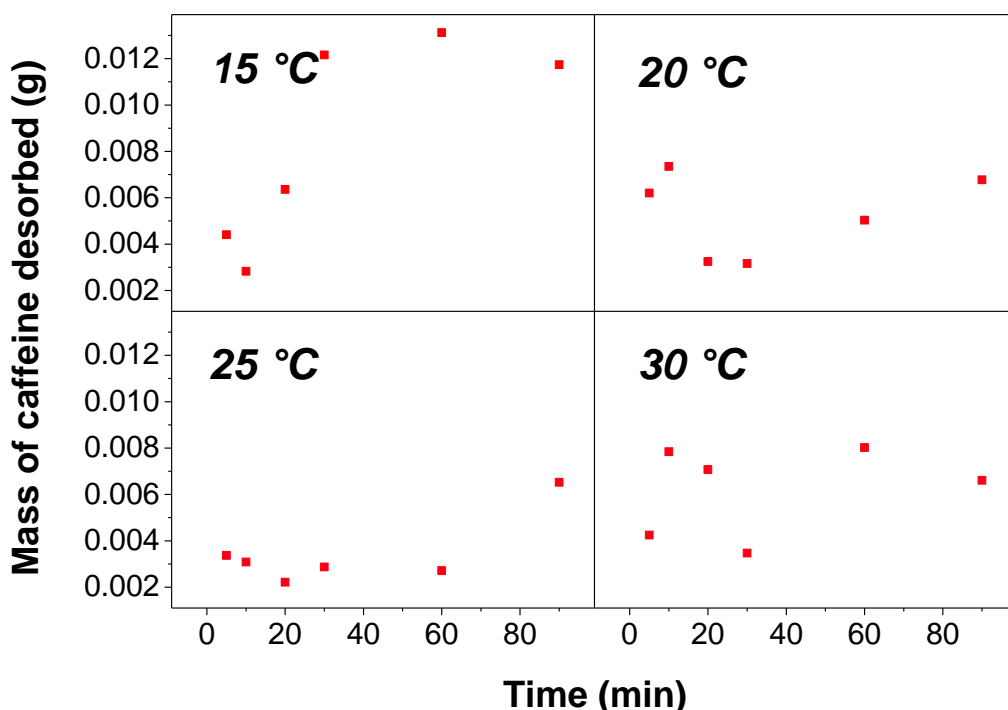


Figure 3.23. Plots of mass of caffeine desorbed from MIL-68(Ind)–caffeine at indicated temperatures. The y-axis is consistent for all plots.

The data shown in Figure 3.23 was surprising. Diffusion of the analyte from the framework should occur more quickly at higher temperatures, and subsequently more material should diffuse.

The plots in Figure 3.23 do not reflect this, where the largest mass of caffeine diffused from the framework was observed at 15 °C and the lowest amount diffused was observed at 25 °C, however the total mass of desorbed caffeine is the same order of magnitude in all cases. There are several possible reasons for these results.

The MIL-68(In) used for caffeine loading in these experiments came from several different synthetic batches. The particle size variation between these batches is not known, and therefore the rate of diffusion from different crystallite sizes would vary.

The photographs in Figure 3.24 show four supernatant caffeine solutions from MIL-68(In)-caffeine desorption experiments and four solid samples of MIL-68(In)-caffeine after desorption experiments. The volume of the supernatant solutions and amount of remaining solid both differ significantly. After centrifugation, despite the supernatant liquor being decanted, there is still a significant solvent volume present in the bed of solid. This introduces a significant source of error, as caffeine solution remaining in the solid bed will not be accounted for in the final mass.



Figure 3.24. (Left) Caffeine solutions in MeCN after MIL-68(In)-caffeine desorption experiments. (Right) Four samples of MIL-68(In)-caffeine post-desorption.

Experiments investigating the diffusion of caffeine from bulk solids were unsuccessful. Plots of desorbed caffeine at various temperatures (Figure 3.23, pp.152) suggested that the timescale of caffeine loss was between minutes and tens of minutes, which are commensurate with the results from the highly successful single crystal diffusion experiments. A better method of analysing the diffusion from bulk solids is required for any future experiments.

To prevent the residual solution remaining in the bed of solid, the use of filtered centrifuge tubes would easily separate the supernatant solution from the framework solid. Future experiments could also use  $^1\text{H}$  NMR spectroscopy to monitor the loss of analyte from the material.

This section examined the diffusion of a large pharmaceutical agent, whereas the next section of this chapter will focus on the bulk uptake and release of the much smaller gaseous therapeutic, carbon monoxide.

### 3.5.2 CO loss from NOTT-100 DRIFTS experiments

This work was carried out in collaboration with Dr Paul Webb at the University of St Andrews and alongside two undergraduate project students; Joseph Paul-Taylor and Cameron Gray. Three visits were made to Dr Webb in St Andrews; June 2017 (myself and Joseph Paul-Taylor), August 2017 (Joseph Paul-Taylor) and July 2018 (myself and Cameron Gray). Experiments carried out during visits with Joseph Paul-Taylor focussed on experimental method development. All data discussed throughout this chapter was collected in the July 2018 visit. Spectral analysis was carried out alongside Cameron Gray.

For this investigation, we were interested in framework materials that were capable of retaining CO. NOTT-100 was selected as previous studies have explored Cu-CO interactions,<sup>42,43</sup> as well as high uptake of CH<sub>4</sub> and H<sub>2</sub>.<sup>44–46</sup> The framework is synthesised from Cu(NO<sub>3</sub>)<sub>2</sub> and biphenyltetracarboxylic acid (H<sub>4</sub>BPTC), and was first reported by Yaghi and co-workers as MOF-505 with pore dimensions of 8.3 and 10.1 Å.<sup>46</sup> The crystal structure of NOTT-100 and the Cu-paddlewheel metal node are shown below in Figure 3.25.

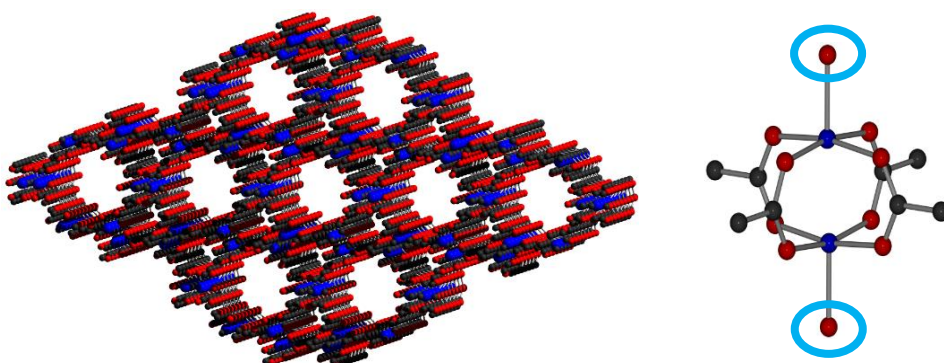


Figure 3.25. Crystal structures of (left) NOTT-100 and (right) Cu-paddlewheel metal node. Axial water molecules are circled in blue.

Experiments were carried out to track CO desorption from NOTT-100 at 0, -25, -50, -75 and -100 °C using diffuse reflectance infrared-Fourier transform spectroscopy (DRIFTS). The experimental setup in St Andrews housed a VT-DRIFTS spectrometer inside a N<sub>2</sub>-filled glovebox.

This allowed the uptake and release of CO to be investigated without interference from atmospheric water. The DRIFTS chamber is connected to a gas dosing valve that allows any gas to be controllably flowed through the sample chamber. In our experiments, a 10 ms CO dose was delivered to the N<sub>2</sub> atmosphere. The chamber was vented of excess CO using a N<sub>2</sub> flow. The chamber venting timescale was determined by dosing the sample chamber with CO (10 ms), at -100 °C, in the absence of NOTT-100 and observing how long the CO signals (2170 and 2115 cm<sup>-1</sup>) took to decay completely.

To prevent contamination of the glovebox with water, and to facilitate maximum uptake of CO into the material, NOTT-100 was activated under vacuum for 11 hr in a tube furnace at 200 °C. The activation process removed both pore-bound and node-bound water molecules (indicated in Figure 3.25), introducing additional CO binding sites throughout the material. The material was transferred to the glovebox and loaded into a custom-made silver sample holder. NOTT-100 was then activated *in situ* for 2 hr at 150 °C under N<sub>2</sub> (flowrate 50 SCCM). The material was then cooled to -100 °C (to ensure maximum uptake of gas) and the sample dosed with CO (10 ms pulse). The sample chamber was isolated for 15 minutes to allow NOTT-100 to adsorb CO. Following adsorption, the chamber was vented with N<sub>2</sub> (50 SCCM) for 5 minutes to remove gaseous CO. CO-loaded NOTT-100 was then heated from -100 °C to the appropriate temperature and IR spectra collected every 22 seconds. Figure 3.26 overleaf shows an example of the change in the spectral region of interest throughout the desorption experiments.

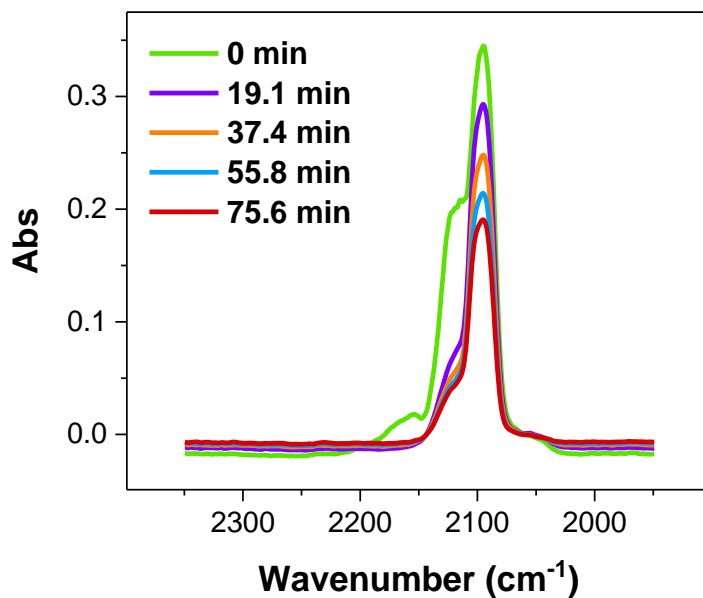


Figure 3.26. DRIFT spectra of CO-loaded NOTT-100 CO region during -100 °C desorption experiments.

During the collection of each spectrum, the IR background spectrum (activated NOTT-100, at the appropriate experiment temperature) was subtracted from the collected spectrum. Therefore, the spectra collected and subsequently analysed can be regarded as difference spectra, where the only peaks visible are CO interacting with the Cu-paddlewheel.

### 3.5.2.1 Spectral analysis

Figure 3.26 shows several overlapped peaks within the 2200–2050 cm<sup>-1</sup> region of the IR spectrum. These peaks all decay at vastly different rates. A variety of methods were employed to deconvolute the spectral region and shed light on the kinetics of decay of different Cu–CO species.

#### 3.5.2.1.1 CO region integration

To determine kinetic profiles for the loss of CO from NOTT-100, the entire 2267–1975 cm<sup>-1</sup> region was integrated in Opus software. A straight baseline was applied across the entire region and the resulting area integral plotted against time. These are plotted in Figure 3.27.

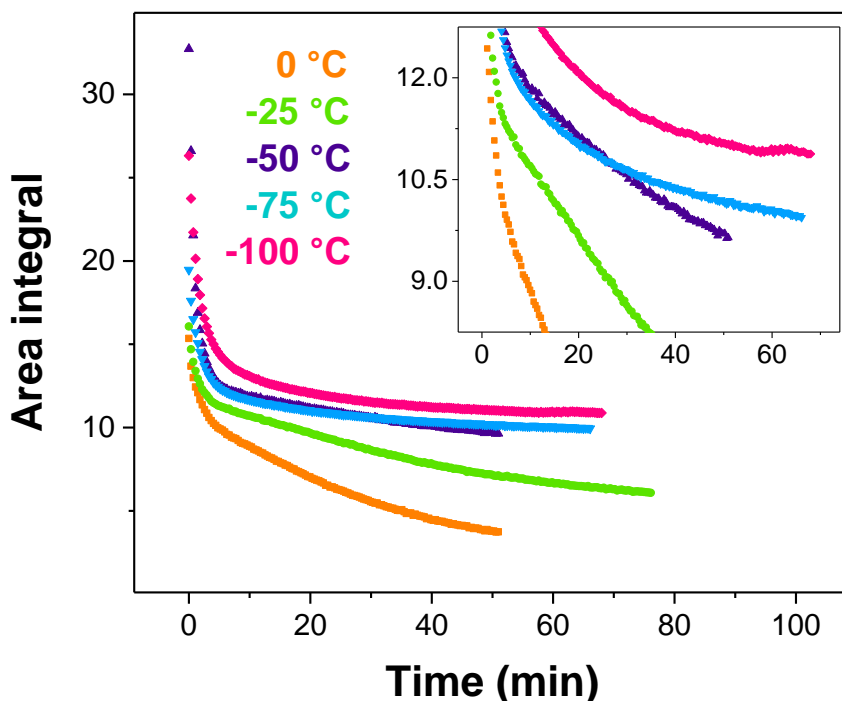


Figure 3.27. Integrated area intensity of CO-loaded NOTT-100 CO region during -100 °C desorption experiments.

Figure 3.27 shows that the CO region integral decreased more rapidly with increasing temperatures. Desorption is clearly a multicomponent process, comprised of an initial sharp drop in peak area which completes within the first 5 minutes, and a subsequent slower process. This is consistent with the change in spectral shape over time.

Simple exponential decay curves were fitted to all plots, but no meaningful kinetic information could be obtained. This is perhaps unsurprising, and suggests that CO release from NOTT-100 is not an isolated process, and CO binding sites present in the material are interacting with each other and do not release CO independently.

### 3.5.2.1.2 Peak fitting analysis

To extract data on individual peaks in the CO region, spectra were fit with Gaussian peak shapes in OriginPro 2017. The region was satisfactorily fit with six peaks; 2172, 2155, 2133, 2123, 2113 and 2096  $\text{cm}^{-1}$ . An example peak fit is shown below in Figure 3.28. One spectrum was initially fitted, then a fitting ‘theme’ was constructed and then all spectra were fit simultaneously in one batch.

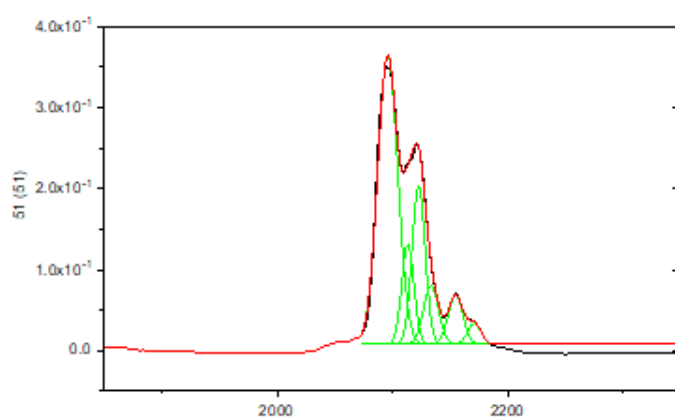


Figure 3.28. Peak analysis fit of NOTT-100 CO desorption after 44 seconds at -75 °C.

As mentioned previously, the peaks decay at vastly different rates. In particular, the higher energy peaks ( $2172$  and  $2155\text{ cm}^{-1}$ ) are lost before the end of the desolvation experiments. OriginPro is unable to fit peaks when their area falls below zero, and hence multiple themes were required to fit spectra at stages of the experiment after peak areas had reduced almost to zero. Therefore, peak positions and widths were fixed where necessary, and consequently only peak area data is presented hereafter.

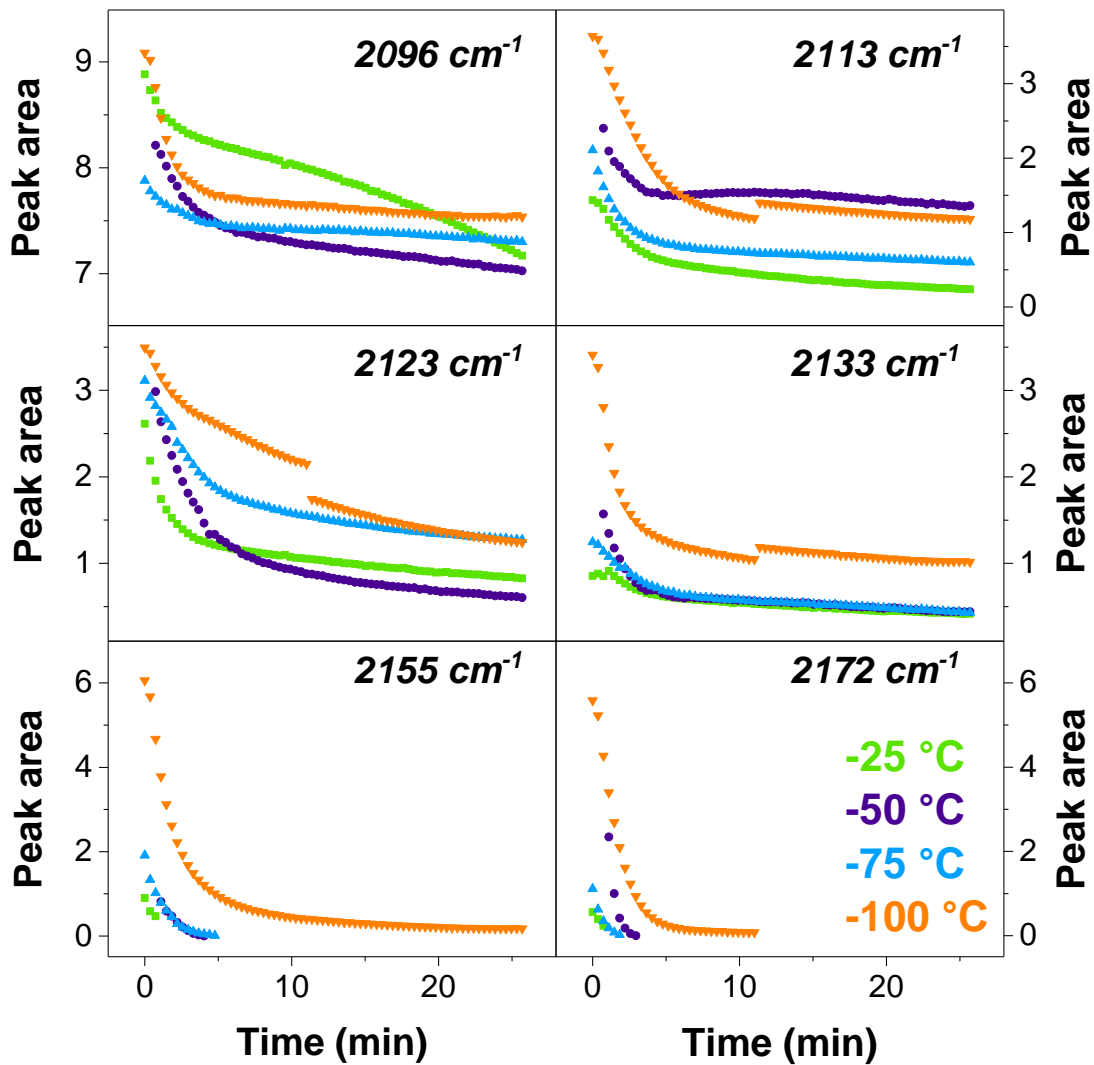


Figure 3.29. Peak area fits of indicated peaks during NOTT-100 CO desorption experiments.

Figure 3.29 shows the change in peak areas of CO–Cu bands against time at all experimental temperatures. Exponential curves were fit successfully to all plots, however no meaningful trends could be identified within the curve fitting results.

There is a markedly slower loss of CO at -100 °C than at other temperatures. Like the CO region integration, the peak area changes shown in Figure 3.29 are likely to reflect multiple, mutually dependent CO desorption processes. In particular, the steps in the 2113, 2123 and 2133 cm<sup>-1</sup> peaks in the -100 °C dataset are consistent with the idea that CO loss from one site is affecting adjacent binding sites, and the desorption from each adsorption site is not an isolated process.

### 3.5.2.1.3 Composite spectral modelling

The CO desorption process from NOTT-100 was modelled by composite spectral modelling in OriginPro 2017 (described previously in Section 1.8.3 on pp.21), using the first and last IR spectrum from each experiment to fit IR spectra collecting during CO-desorption experiments. Example composite model fit plots for 0 and -100 °C (the highest and lowest experimental temperatures) are shown below in Figure 3.30.

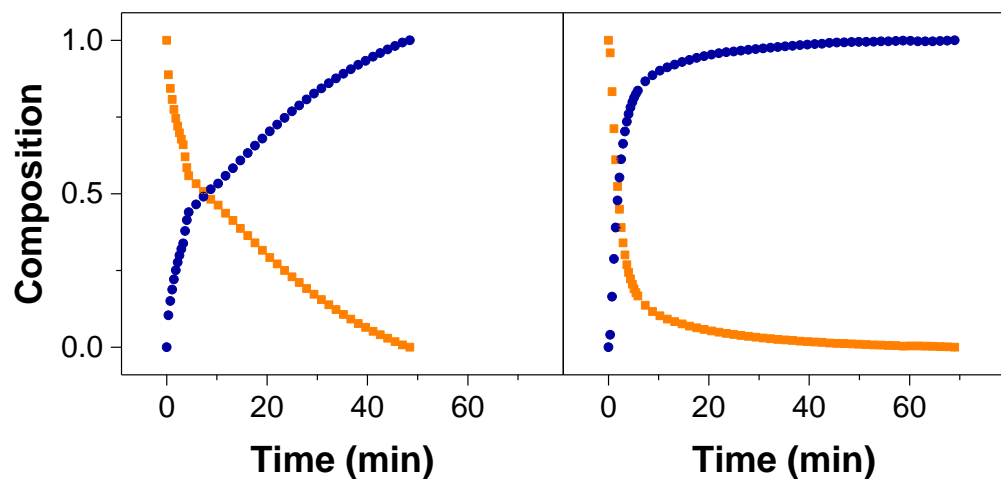


Figure 3.30. Composite model plots for CO desorption from NOTT-100 at indicated temperatures. Orange indicates CO-saturated NOTT-100 at the beginning of the experiment and blue indicates the end of the desorption experiment.

The above composite model plots clearly show at least two components to the desorption process. It is important to note that, in the 0 °C experiments, there is a two-minute lapse before the first spectrum is recorded, as the sample had to be warmed from -100 °C.

We are therefore seeing the tail loss of CO, which has not completed by the end of either experiment. In the -100 °C composition plot, we are seeing only a small proportion of the CO loss in total, and therefore kinetic information is looking at the desorption of the most easily lost CO species. These are likely to be in the pores. Due to the timescale of desorption, the processes we are observing in the 0 and -100 °C spectra are likely to be from different combinations of CO desorption processes. At the end of both desorption experiments pictured (0 and -100 °C), it is likely that only node-bound CO remains.

The initial, pore-bound CO desorption process completed after ca. 4.4 minutes at 0 °C and 7.3 minutes at -100 °C. This is anticipated, as higher temperatures would prompt more mobility in the pore-bound CO. The end of this process suggests that only node-bound CO remained in the material.

CO was loaded to the material at -100 °C, and then subsequently heated to 0 °C. During the 2-minute heating step, significant pore-bound CO is likely to have desorbed from the material. As the CO-saturated NOTT-100 model was taken as the first spectrum recorded in the desorption experiment, it is almost certainly not representing the loss of the most weakly bound CO species. The 0 °C CO-saturated model would contain less pore-bound CO than the -100 °C counterpart. This would account for the lower proportion of CO-saturated model present in the 0 °C experiment after the proposed desorption of CO from the pores.

Whilst exponential and biexponential curves were fit to the data, there were no clear kinetic trends. This is consistent with the observations from CO region integration and peak fitting analysis, and is likely due to the complex interplay of CO-bound states evolving over time. Further careful deconvolution of the peaks and comparison with computational modelling in future should enable this complex interplay of states to be fully characterised.

Any therapeutic applications of CO-loaded frameworks will be operated at either room or physiological temperature, and hence CO-desorption will be accelerated. The ideal release rate of CO would be on timescale of hours, as opposed to minutes as observed in these experiments. Therefore, the stimulated release of CO would be ideal.

The rate of CO desorption from modified NOTT-100 $\square$ **phen-spiro** (the synthesis and properties of which are explored in Chapter 2), significantly increased upon irradiation of the sample with a UV laser. The change in peak area of the  $2123\text{ cm}^{-1}$  peak is shown in Figure 3.31.

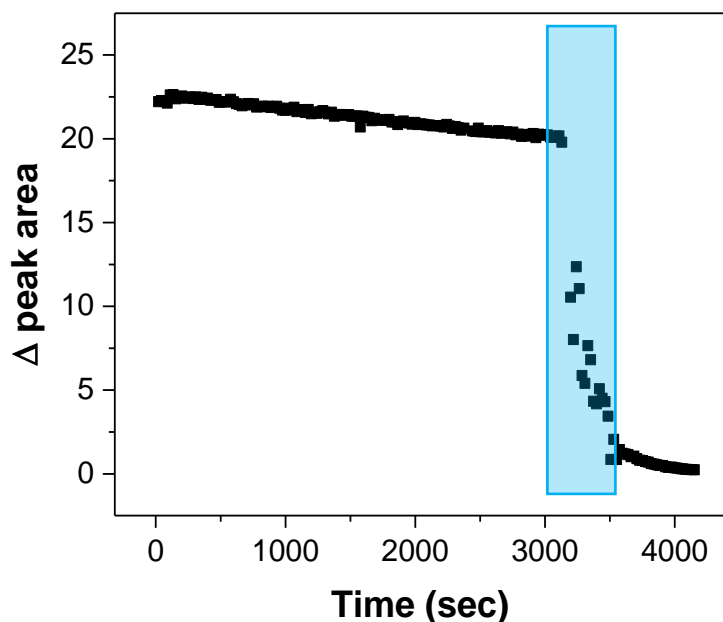


Figure 3.31. Change in peak area of  $2123\text{ cm}^{-1}$  peak during CO-desorption from NOTT-100, with UV irradiation in indicated region in blue.

Irradiation of NOTT-100 $\square$ **phen-spiro** clearly affected the release rate of CO, which is likely due to photoinduced isomerism of the **phen-spiro** photoswitch. Future experiments will investigate CO release under UV irradiation using this DRIFTS method.

### 3.5.2.1.4 Cu–CO spectral assignment

Based on computational experiments and XPS experiments reported by Petkov *et al.*, a spectral assignment of the Cu–CO region is shown below in Figure 3.32.

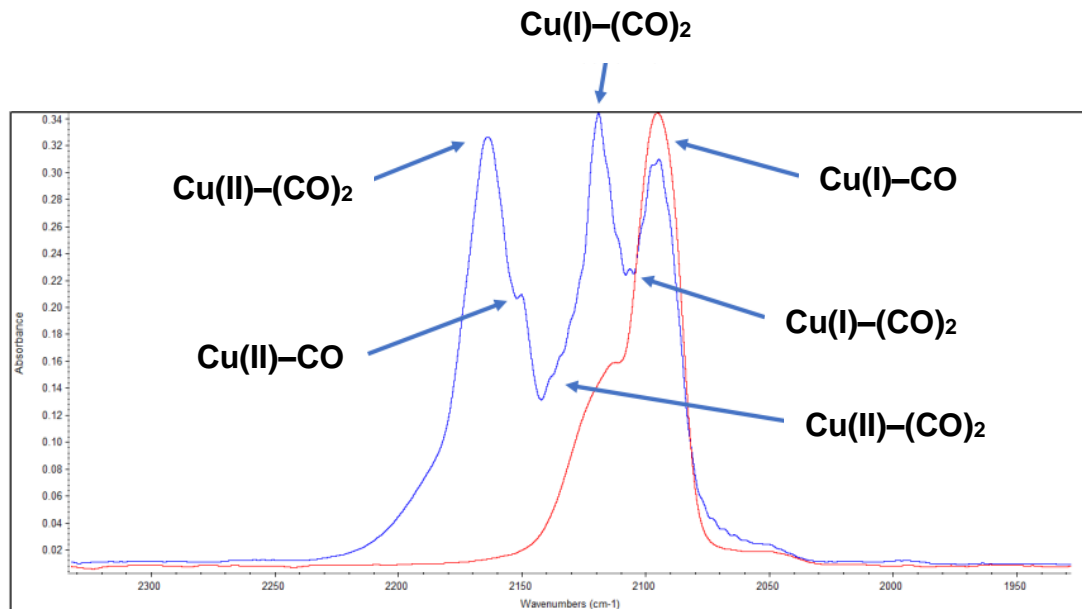


Figure 3.32. IR spectral assignment of NOTT-100-CO, based on reference 47.

The spectral assignment above is based purely on the experiments conducted by Petkov *et al.*. Peaks that should decay at the same rate (such as the two Cu(II)–(CO)<sub>2</sub> interactions at 2172 and 2133  $\text{cm}^{-1}$ ) were shown by peak fitting analysis (detailed in Section 3.5.2.2) to decay independently, further supporting the suggestion that CO desorption from different binding environments are complementary processes.

### 3.6 Conclusions and Outlook

This chapter has reported the development and implementation of two novel methodologies for tracking the loss of non-fluorescent guest molecules from metal-organic frameworks using IR spectroscopy.

The first of these methodologies can be employed to track a variety of analytes from single crystals of MOFs into surrounding media. An approach was developed to minimise solvent evaporation, by covering the sample and solvent droplet with an additional IR window. The decreasing concentration of analyte was tracked using characteristic IR bands, and an Arrhenius plot constructed. An  $E_a$  of  $+144 \pm 5.7 \times 10^{-5}$  kJ mol $^{-1}$  was calculated for the diffusion of caffeine from MIL-68(Ind). Several examples exist where  $E_a$  has been calculated using diffusion of an analyte into a framework, but, as far as we are aware, this is the first example where the diffusion of an analyte out of a framework has been used to calculate  $E_a$ . The  $E_a$  of the process is quite high, but diffusion is quite slow, which is desirable in a delivery drug system

Experiments to investigate the diffusion of caffeine from a bulk powder sample into surrounding media were attempted but did not corroborate the data calculated using the *in situ* microspectroscopic approach discussed above. Experimental adaptations, such as using filtered centrifuge tubes to collect diffusion solutions, should be employed during future experiments to remove significant sources of error.

An additional dataset for the diffusion of lidocaine from single crystals of MIL-68(Ind) $\supset$ lidocaine was also collected at DLS B22 MIRIAM, and will be analysed in the future using similar approaches detailed herein to further investigate the behaviour of coordinatively innocent guests within metal-organic frameworks.

The CO loss from activated NOTT-100 was investigated using DRIFTS, and spectra analysed through a combination of peak integration, peak fitting analysis and composite spectral modelling. Although qualitative trends could be visually observed in the data extracted from spectral analysis, such as the faster decrease in the CO region integral at higher temperatures (corresponding to quicker CO loss from the framework), simple exponential decay curves did not yield meaningful kinetic information. This is consistent with multiple CO sites within the framework, interacting with each other as CO is lost and not acting as independent species. In order to probe the loss of CO not bound to paddlewheel sites, a less rigorously activated material was examined.

Therapeutic applications of CO-loaded materials would be performed nearer to room temperature, resulting in significantly quicker CO loss, and so phototriggered release of CO is the longer-term goal. NOTT-100 $\supset$ **phen-spiro** has shown promise for the phototriggered release of CO, and further study of the release mechanism with irradiation is required. The ultimate vision for the application of these materials are treatments such as CO-release bandages to reduce inflammation, which are stored in the dark and activated by unpackaging and exposure to sunlight.

## 3.7 Experimental

All starting materials were obtained from commercial sources and used without further purification.

MOF materials were characterised using powder X-ray diffraction. PXRD patterns were collected between 4° and 40° 2θ using an X’Pert Pro PAN Analytical powder diffractometer employing a Cu-K<sub>α</sub> radiation source operating at 40 keV and 40 mA.

### 3.7.1 DLS B22 MIRIAM analyte diffusion experiments

#### ***Preparation of caffeine-loaded MIL-68(In)***

MIL-68(In) was synthesised as described in Section 2.4.4, as initially reported by Volkinger *et al.*<sup>36</sup> MIL-68(In) was immersed in saturated solutions of caffeine in bench DCM (0.2 M). Solutions were exchanged three times a day over the course of one week to ensure maximum uptake of analyte by the framework to give **MIL-68(In)⊃caffeine** (12.6 wt%).

#### ***DLS B22 MIRIAM experimental protocol***

*In situ* IR spectroscopic measurements were carried out on B22 MIRIAM beamline at the Diamond Light Source, using a Bruker Vertex 80 V FTIR interferometer with an internal broadband liquid N<sub>2</sub>-cooled MCT detector coupled to a Hyperion 3000 microscope with x15 objective. Spectra were collected using slit sizes of 15 x 15 μm. N<sub>2</sub> gas was dried through zeolite filters between the gas cylinder and mass flow controller.

DCM and MeCN used for washings and diffusion experiments were collected from Cardiff University’s in-house solvent purification system (SPS) and stored over molecular sieves under N<sub>2</sub>.

MIL-68(In) $\supset$ caffeine (1–2 mg) was collected *via* centrifugation from MIL-68(In) in analyte stock mixture (0.5 mL) and washed (as described in Section 3.2.1.1) to remove extrinsically bound analyte. Two MeCN reservoirs (ca. 2 mL each) were placed in the bottom of a variable-temperature gas-tight Linkam FTIR600 cell fitted with 0.2 x 22 mm CaF<sub>2</sub> top and bottom windows. Washed MIL-68(In) $\supset$ caffeine was loaded on to a 0.2 x 16 mm CaF<sub>2</sub> window and one drop (ca. 50  $\mu$ L) MeCN was added to the sample. The sample was surrounded by a Teflon 25  $\mu$ m spacer and an additional 0.2 x 16 mm CaF<sub>2</sub> window placed atop the sample and spacer to prevent solvent evaporation before the cell was sealed. Further details of the Linkam cell setup are discussed in Section 3.2.1. Analyte diffusion was monitored in separate experiments at 10, 15, 20, 25 and 30 °C.

### ***Spectral analysis of analyte diffusion experiments***

Infrared spectra were analysed by peak integration in OriginPro 2017. Masks were applied to data outside the region 1716.4–1691.4 cm<sup>-1</sup>. Baseline correction (constant, straight or  $y = 0$ ; discussed previously in Section 3.5.1.2) was applied and a peak indicative of caffeine was integrated between 1710.6–1695.2 cm<sup>-1</sup> and the integral plotted against time. A single spectrum was integrated initially, before an integration ‘theme’ was constructed and used to integrate all other spectra in batch. Other characteristic caffeine peaks overlap with nearby framework bands and were not chosen due to their proximity to saturated bands and subsequent difficulty obtaining reliable integrals. Exponential curves were then fit to plots of time-dependent peak integral changes, and these fitting results used to construct an Arrhenius plot.

### 3.7.2 Bulk solid caffeine desorption experiments

MeCN (1 mL) was added to pre-weighed portions of **MIL-68(Ind)⊃caffeine** ( $150 \pm 1$  mg) at  $15^\circ\text{C}$  and the samples vortex mixed at 1,500 rpm for 5, 10, 20, 30, 60 and 90 minutes. Samples were then pelleted by centrifugation (1 min at 4,200 rpm) and the supernatant liquor decanted to a pre-weighed vial. Solvent was evaporated (in air for 18 hr and then under high vacuum for 18 hr) and the mass of desorbed caffeine calculated. The experiment was repeated at 20, 25 and  $30^\circ\text{C}$ .

### 3.7.3 CO release from NOTT-100 DRIFTS experiments

*In situ* DRIFTS measurements to study the CO release from NOTT-100 were undertaken in collaboration with Dr Paul Webb at the University of St Andrews. Measurements were carried out in Sasol laboratories by Dr Webb, using a VT proprietary instrument housed in a  $\text{N}_2$ -filled glovebox. Gas lines were connected to the instrument to allow control of the sample environment.

Bulk powder NOTT-100 was synthesised by summer project student Joseph Paul-Taylor, according to the procedure described in Section 2.4.4 previously reported by Lin *et al.*<sup>45</sup>

Measurements were carried out on NOTT-100 after *ex situ* activation; where the sample was heated in a Schlenk flask at  $200^\circ\text{C}$  for 11 hr under vacuum in a tube furnace, before being transferred to the glovebox and loaded into the spectrometer. Activated NOTT-100 (ca. 100 mg) was loaded into a custom-made silver sample holder and heated at  $150^\circ\text{C}$  2 hr under  $\text{N}_2$  (flow rate 100 SCCM). CO and  $\text{N}_2$  gases were dried through zeolite filters between the gas cylinder and mass flow controller.

NOTT-100 (ca. 100 mg) was cooled to  $-100^\circ\text{C}$  and dosed with CO (10 ms pulse) in  $\text{N}_2$  (flow rate 10 SCCM). After 90 seconds, the chamber was isolated from the inflow and exhaust for 15 minutes to allow for the material to equilibrate CO.

The chamber was then reopened, N<sub>2</sub> flow rate increased (50 SCCM) and the sample heated (if necessary) to the appropriate temperature to monitor CO loss.

CO loss was monitored at -100, -75, -50, -25 and 0 °C. Cu-bound CO peaks in the range 2250-2000 cm<sup>-1</sup> were measured using single beam DRIFTS. A background spectrum (activated NOTT-100 under N<sub>2</sub>) was subtracted as part of the spectral collection process, and hence the spectra collected can be regarded as IR difference spectra.

### ***Spectral analysis.***

Spectral analysis was carried out with summer project student Cameron Gray.

Peak data was deconvoluted using peak fitting analysis in OriginPro 2017. Data was trimmed to the region 2250–2000 cm<sup>-1</sup>. Peaks were fit to a Gaussian peak shape, with some peak positions and widths values fixed to enable completion of the fitting process. Peak positions, widths and areas were initially manually varied to produce a fit that most closely resembled the spectral profile and then the fit refined until convergence was reached. One spectrum from the set was fit initially, before a fitting ‘theme’ was created in OriginPro to enable peak fitting of multiple spectra.

### 3.8 References

- 1 P. Horcajada, C. Serre, M. Vallet-Regí, M. Sebban, F. Taulelle and G. Férey, *Angew. Chemie Int. Ed.*, 2006, **45**, 5974–5978.
- 2 L. Wang, M. Zheng and Z. Xie, *J. Mater. Chem. B*, 2018, **6**, 707–717.
- 3 W. J. Rieter, K. M. Pott, K. M. L. Taylor and W. Lin, *J. Am. Chem. Soc.*, 2008, **130**, 11584–11585.
- 4 C. Ding, L. Tong, J. Feng and J. Fu, *Molecules*, 2016, **21**, 1715.
- 5 T. Feng, X. Ai, G. An, P. Yang and Y. Zhao, *ACS Nano*, 2016, **10**, 4410–4420.
- 6 J. An, S. J. Geib and N. L. Rosi, *J. Am. Chem. Soc.*, 2009, **131**, 8376–7.
- 7 Q. Zhang, N. Re Ko and J. Kwon Oh, *Chem. Commun.*, 2012, **48**, 7542.
- 8 N. Nishiyama, Y. Matsumura and K. Kataoka, *Cancer Sci.*, 2016, **107**, 867–74.
- 9 M. S. Kim, H. Hoon, G. Khang and H. B. Lee, in *NanoScience in Biomedicine*, Springer Berlin Heidelberg, Berlin, Heidelberg, 2009, pp. 388–404.
- 10 A. Madaan, P. Singh, A. Awasthi, R. Verma, A. T. Singh, M. Jaggi, S. K. Mishra, S. Kulkarni and H. Kulkarni, *Clin. Transl. Oncol.*, 2013, **15**, 26–32.
- 11 J. J. Lee, L. Saiful Yazan and C. A. Che Abdullah, *Int. J. Nanomedicine*, 2017, **12**, 2373–2384.
- 12 M. G. Rimoli, M. R. Rabaioli, D. Melisi, A. Curcio, S. Mondello, R. Mirabelli and E. Abignente, *J. Biomed. Mater. Res. Part A*, 2008, **87A**, 156–164.
- 13 E. Khodaverdi, H. A. Soleimani, F. Mohammadpour and F. Hadizadeh, *Chem. Biol. Drug Des.*, 2016, **87**, 849–857.
- 14 O. Martinho, N. Vilaça, P. J. G. Castro, R. Amorim, A. M. Fonseca, F. Baltazar, R. M. Reis and I. C. Neves, *RSC Adv.*, 2015, **5**, 28219–28227.
- 15 A. O. Choi, S. E. Brown, M. Szyf and D. Maysinger, *J. Mol. Med.*, 2008, **86**, 291–302.
- 16 K.-T. Yong, Y. Wang, I. Roy, H. Rui, M. T. Swihart, W.-C. Law, S. K. Kwak, L. Ye, J. Liu, S. D. Mahajan and J. L. Reynolds, *Theranostics*, 2012, **2**, 681–694.
- 17 Y. Wang and L. Chen, *Nanomedicine Nanotechnology, Biol. Med.*, 2011, **7**, 385–402.
- 18 C. E. Probst, P. Zrazhevskiy, V. Bagalkot and X. Gao, *Adv. Drug Deliv. Rev.*, 2013, **65**, 703–718.
- 19 S. Y. Lim, W. Shen and Z. Gao, *Chem. Soc. Rev.*, 2015, **44**, 362–381.
- 20 N. Vilaça, A. F. Machado, F. Morais-Santos, R. Amorim, A. Patrícia Neto, E. Logodin, M. F. R. Pereira, M. Sardo, J. Rocha, P. Parpot, A. M. Fonseca, F. Baltazar and I. C. Neves, *RSC Adv.*, 2017, **7**, 13104–13111.

- 21 R. B. Greenwald, Y. H. Choe, J. McGuire and C. D. Conover, *Adv. Drug Deliv. Rev.*, 2003, **55**, 217–250.
- 22 M. Ibrahim, R. Sabouni and G. Husseini, *Curr. Med. Chem.*, 2017, **24**, 193–214.
- 23 M. Giménez-Marqués, T. Hidalgo, C. Serre and P. Horcajada, *Coord. Chem. Rev.*, 2016, **307**, 342–360.
- 24 P. Horcajada, T. Chalati, C. Serre, B. Gillet, C. Sebrie, T. Baati, J. F. Eubank, D. Heurtaux, P. Clayette, C. Kreuz, J.-S. Chang, Y. K. Hwang, V. Marsaud, P.-N. Bories, L. Cynober, S. Gil, G. Férey, P. Couvreur and R. Gref, *Nat. Mater.*, 2010, **9**, 172–178.
- 25 J. Gordon, H. Kazemian and S. Rohani, *Mater. Sci. Eng. C*, 2015, **47**, 172–179.
- 26 D. R. Hess, *Respir. Care*, 2017, **62**, 1333–1342.
- 27 M. Knauert, S. Vangala, M. Haslip and P. J. Lee, *Oxid. Med. Cell. Longev.*, 2013, **2013**, 360815.
- 28 R. Motterlini and L. E. Otterbein, *Nat. Rev. Drug Discov.*, 2010, **9**, 728–743.
- 29 M. L. Ferrandiz, N. Maicas, I. Garcia-Arnandis, M. C. Terencio, R. Motterlini, I. Devesa, L. A. B. Joosten, W. B. van den Berg and M. J. Alcaraz, *Ann. Rheum. Dis.*, 2007, **67**, 1211–1217.
- 30 J. E. Clark, P. Naughton, S. Shurey, C. J. Green, T. R. Johnson, B. E. Mann, R. Foresti and R. Motterlini, *Circ. Res.*, 2003, **93**, e2-8.
- 31 A. Sandouka, B. J. Fuller, B. E. Mann, C. J. Green, R. Foresti and R. Motterlini, *Kidney Int.*, 2006, **69**, 239–47.
- 32 K. G. Raman, J. E. Barbato, E. Ifedigbo, B. A. Ozanich, M. S. Zenati, L. E. Otterbein and E. Tzeng, *J. Vasc. Surg.*, 2006, **44**, 151–158.
- 33 Authors unknown, *Nat. Chem.*, 2016, **8**, 987–987.
- 34 A. C. McKinlay, P. K. Allan, C. L. Renouf, M. J. Duncan, P. S. Wheatley, S. J. Warrender, D. Dawson, S. E. Ashbrook, B. Gil, B. Marszalek, T. Düren, J. J. Williams, C. Charrier, D. K. Mercer, S. J. Teat and R. E. Morris, *APL Mater.*, 2014, **2**, 124108.
- 35 J. A. Mason, M. Veenstra and J. R. Long, *Chem. Sci.*, 2014, **5**, 32–51.
- 36 C. Volkringer, M. Meddouri, T. Loiseau, N. Guillou, J. Marrot, G. Férey, M. Haouas, F. Taulelle, N. Audebrand and M. Latroche, *Inorg. Chem.*, 2008, **47**, 11892–11901.
- 37 A. Alshammari, Z. Jiang and K. E. Cordova, in *Semiconductor Photocatalysis - Materials, Mechanisms and Applications*, ed. W. Cao, IntechOpen, Rijeka, 2016, pp. 301–341.
- 38 S. Nagata, K. Kokado and K. Sada, *Chem. Commun.*, 2015, **51**, 8614–7.

- 39 S. Rojas, I. Colinet, D. Cunha, T. Hidalgo, F. Salles, C. Serre, N. Guillou and P. Horcajada, *ACS Omega*, 2018, **3**, 2994–3003.
- 40 X. Lian, Y. Huang, Y. Zhu, Y. Fang, R. Zhao, E. Joseph, J. Li, J.-P. Pellois and H.-C. Zhou, *Angew. Chemie Int. Ed.*, 2018, **57**, 5725–5730.
- 41 L. Heinke and C. Wöll, *Phys. Chem. Chem. Phys.*, 2013, **15**, 9295.
- 42 J. Szanyi, M. Daturi, G. Clet, D. R. Baer and C. H. F. Peden, *Phys. Chem. Chem. Phys.*, 2012, **14**, 4383.
- 43 S. Bordiga, L. Regli, F. Bonino, E. Groppo, C. Lamberti, B. Xiao, P. S. Wheatley, R. E. Morris and A. Zecchina, *Phys. Chem. Chem. Phys.*, 2007, **9**, 2676.
- 44 Y. He, W. Zhou, T. Yildirim and B. Chen, *Energy Environ. Sci.*, 2013, **6**, 2735.
- 45 X. Lin, I. Telepeni, A. J. Blake, A. Dailly, C. M. Brown, J. M. Simmons, M. Zoppi, G. S. Walker, K. M. Thomas, T. J. Mays, P. Hubberstey, N. R. Champness and M. Schröder, *J. Am. Chem. Soc.*, 2009, **131**, 2159–71.
- 46 B. Chen, N. W. Ockwig, A. R. Millward, D. S. Contreras and O. M. Yaghi, *Angew. Chemie Int. Ed.*, 2005, **44**, 4745–4749.
- 47 P. St. Petkov, G. N. Vayssilov, J. Liu, O. Shekhah, Y. Wang, C. Wöll and T. Heine, *ChemPhysChem*, 2012, **13**, 2025–2029.

---

# **Chapter 4**

## **Solvent-switchable behaviour of SHF-61**

---

## 4.1 Flexible MOFs

The stimuli-responsivity in frameworks has been explored extensively throughout the previous chapters, and the inherent responsivity of many frameworks can be accredited to their flexibility. The topic of flexible frameworks has been extensively reviewed over recent decades,<sup>1–7</sup> and these materials are easily identifiable by their characteristic S-shape gas uptake isotherms.<sup>8</sup> Investigations into the area of flexible frameworks are extensive, and hence only examples that are conceptually relevant to the work in this chapter will be introduced.

Arguably the most famous flexible framework is MIL-53(Al), reported by Loiseau, Férey and co-workers in 2005.<sup>9</sup> The as-synthesised Al-based framework, MIL-53as was heated between 275 and 420 °C to remove unreacted benzenedicarboxylic acid (BDC) linker to form MIL-53*ht*. Cooling of the sample to room temperature formed MIL-53*t*, with a significant change in pore size, from  $8.5 \times 8.5 \text{ \AA}^2$  in MIL-53as/*ht*, to  $2.6 \times 13.6 \text{ \AA}^2$  in MIL-53*t* (Figure 4.1). The switch in pore size was attributed to the formation of hydrogen-bonds between atmospheric water molecules (adsorbed during cooling to room temperature) and carboxylate groups of the BDC linkers.

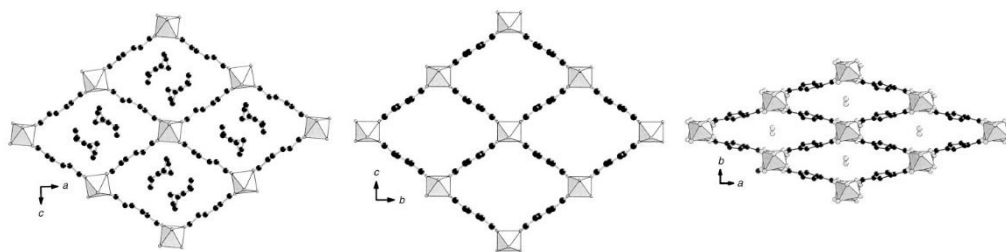


Figure 4.1. Structures of (left) MIL-53as, (middle) MIL-53*ht* and (right) MIL-53*t*. Altered pore structure is clear in right-hand figure. Adapted from reference 9.

Computational modelling and structure prediction have been used extensively to probe the behaviour of flexible frameworks, with multiple groups focussing on this aspect of structural investigation.

Manion *et al.* reported the computational design of linkers which could undergo pressure-induced conformational change,<sup>10</sup> identifying topological fragments most likely to lead to mechanical behaviour. Coudert and co-workers have gone a step further by including the behaviour of metal nodes in their calculations, whereby wine-rack flexibility in the structures of NOTT-300 and CAU-13 was predicted in 2014.<sup>11</sup> Flexibility in CAU-13 was not experimentally reported until later in 2017 by Reinsch, Stock and co-workers,<sup>12</sup> despite the initial report of the structure by the group in 2013.<sup>13</sup>

The flexibility exhibited by frameworks is often triggered by uptake of guest molecules. The guest-induced structural rearrangement of two frameworks, MIL-101(Cr) and MIL-53(Cr) was studied by Yu and co-workers.<sup>14</sup> The adsorption of carbamazepine into rigid MIL-101(Cr) and flexible MIL-53(Cr) instigated the opening of the pore in MIL-53(Cr), increasing the cell volume by 33%, as determined by Rietveld refinement of PXRD patterns. The comparison of the guest-loaded framework pores is indicated in Figure 4.2.

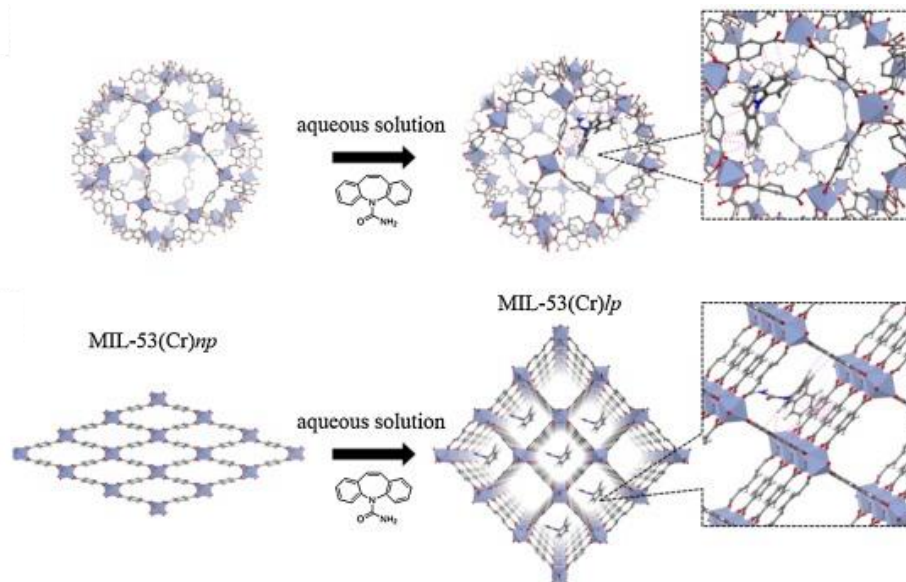


Figure 4.2. Proposed structures of (top) MIL-101(Cr) and (bottom) MIL-53(Cr) following adsorption of carbamazepine. Reproduced from reference 14.

The effect of gaseous guest uptake was investigated by Kitagawa and co-workers, who reported the synthesis of a flexible MOF,  $[\text{Cu}(\text{dhbc})_2(4,4'\text{-bpy})]\cdot\text{H}_2\text{O}$  (where dhbc = 2,5-dihydroxybenzoic acid and bpy = 4,4'-bipyridine) with a supercritical gas-induced gate-opening mechanism.<sup>15</sup> The gate-opening pressures for N<sub>2</sub>, O<sub>2</sub>, and CO<sub>2</sub> were 50, 35 and 0.4 atmospheres (atm), and the gate-closing pressures were 30, 25 and 0.2 atm, respectively.

Framework flexibility can also impact guest uptake in a number of ways. The changes in accessible pore volume upon guest uptake in MIL-88 and MCF-15 had been reported previously,<sup>5,16</sup> but the direct comparison was reported in a 2018 review by Zhang, Chen and co-workers.<sup>4</sup>

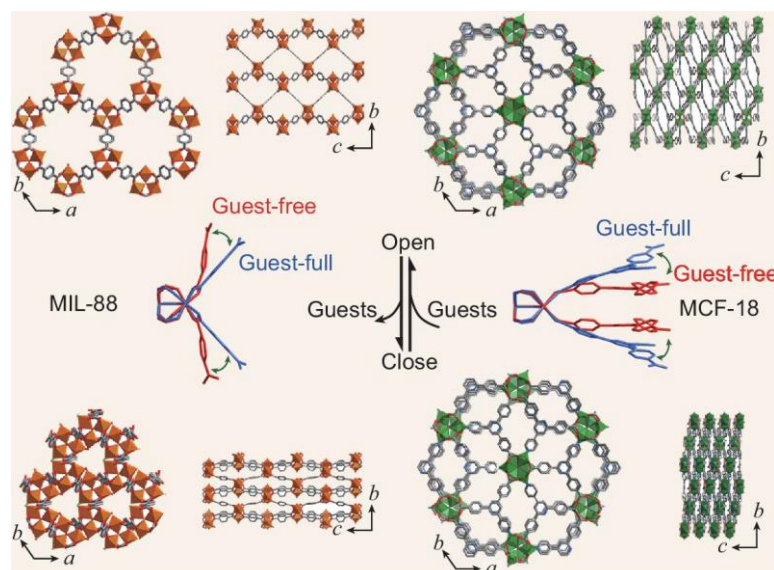


Figure 4.3. Distortion of the classic  $\text{M}_3(\mu_3\text{-O})(\text{ldc})_3(\text{L}^T)_3$  cluster, leading to the reversed breathing directions for MIL-88 and MCF-18.  $\text{ldc}$  = linear dicarboxylic acid;  $\text{L}^T$  = terminating ligand. Reproduced from reference 4.

Both materials adopt the same overall formula,  $\text{M}_3(\mu_3\text{-O})(\text{ldc})_3(\text{L}^T)_3$ . In MIL-88, the framework shortens along the c-axis and expands in the ab-plane, accommodating more guests into the pores. In contrast, MCF-18 expands along the c-axis and contracts in the ab-plane to accommodate more guests, as illustrated in Figure 4.3. Although the volumetric breathing amplitude of MCF-18 (105%) is significantly smaller than MIL-88 (230%), the axial breathing amplitude of MCF-18 (121%) is larger than for MIL-88 (100%).<sup>17</sup>

A Zn-based framework,  $\text{Zn}_2(\text{BDC})_2(\text{DABCO})$ , reported by Kim and co-workers, originally in 2004 and subsequently in 2016,<sup>18,19</sup> exhibited anisotropic thermal expansion along the *a*- and *b*-axes (Figure 4.4). The breathing behaviour was stabilised by strengthening of the  $\text{CH}\cdots\pi$  interactions between the guest benzene molecule and neighbouring BDC linkers, caused by closer proximity upon cooling.

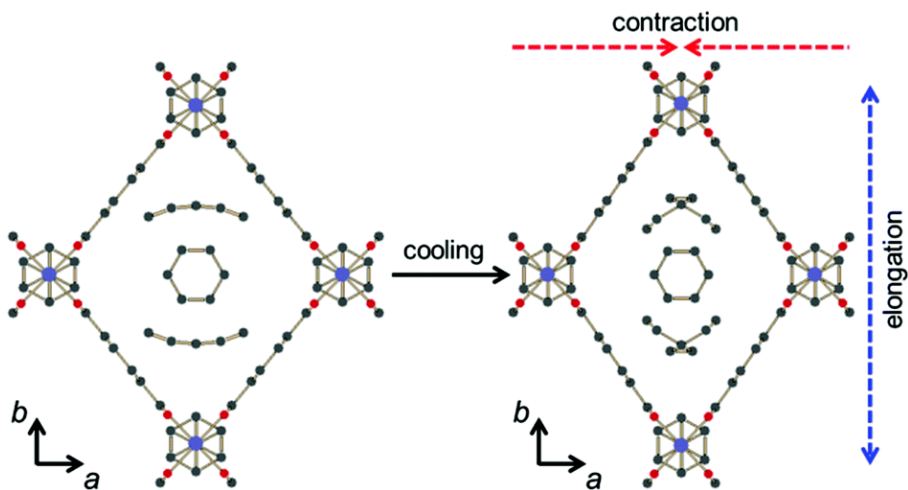


Figure 4.4. The structure of  $\text{Zn}_2(\text{BDC})_2(\text{DABCO})\cdot\text{benzene}$  at 298 (left) and 100 K (right). Reproduced from reference 19.

Anisotropic thermal expansion was observed consistently upon cooling in this framework, when DMF-loaded and when no guests were present. Thermal expansion triggered by changes in guest molecules is a topic commonly reported by members of the MOF community.<sup>20,21</sup>

Carrington *et al.* reported a solvent-switchable, breathing framework, SHF-61, which will form the basis of work within this chapter. The framework is introduced further in Section 4.3.

## 4.2 Aims & Objectives

This chapter investigates the behaviour of a flexible framework, SHF-61, in which solvent environment is the main stimulus to prompt structural change. Previous reports on the material by the Brammer group at the University of Sheffield have used single crystal X-ray diffraction (SCXRD) and isotherm experiments to probe the behaviour of the pore structure. In this work, infrared microspectroscopy was used to study states of the material derived from the inherent flexible nature of the framework. All experiments were carried out at Diamond Light Source B22 MIRIAM, and all experiments and subsequent analysis were carried out in collaboration with the Brammer group at the University of Sheffield. The insight into the material gained from SCXRD and IR experiments differs. Although IR provides real-time monitoring of material behaviour, it does not provide any structural information, which must be inferred from the IR spectra. The objectives of this chapter are:

1. Develop experimental method to study solvent-switchability of flexible frameworks
2. Determine open- and closed-pore structures through desolvation of materials SHF-61-CHCl<sub>3</sub> and SHF-61-DMF
3. Examine the effect of resolvation of open- and closed-pore structures with a variety of solvents
4. Evaluate cyclability of breathing behaviour by repeated desolvation
5. Investigate CO<sub>2</sub> uptake in both pore structures

### 4.3 Results and Discussion

This project was carried out in collaboration with the Brammer group at the University of Sheffield. Two visits (September 2016 and April 2018) to B22 MIRIAM at Diamond Light Source, UK were made with Professor Lee Brammer, Dr Timothy Easun, Dr Elliot Carrington, Mr Daniel Watkins, Mr Stephen Dodsworth and Mr Feifan Lang. Data analysis was undertaken in partnership with Daniel Watkins. We worked together on the processing, analysis and interpretation of the SHF-61-DMF desolvation/resolvation experiments, and the cyclopentanone study. I carried out all of the data processing, analysis and interpretation of the desolvation and resolvation of SHF-61-CHCl<sub>3</sub> and analysis of CO<sub>2</sub> loading of both SHF-61 frameworks myself.

SHF-61-DMF is a framework constructed from an octahedral In-node (Figure 4.6a, overleaf), 2-aminoterephthalic acid and Me<sub>2</sub>NH<sub>2</sub><sup>+</sup> cations, first reported in 2012 by Yuan *et al.* for highly selective separation of CO<sub>2</sub> and CH<sub>4</sub>.<sup>22</sup>

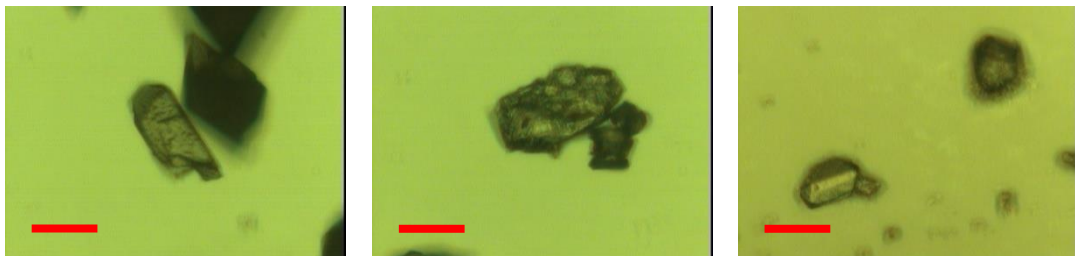
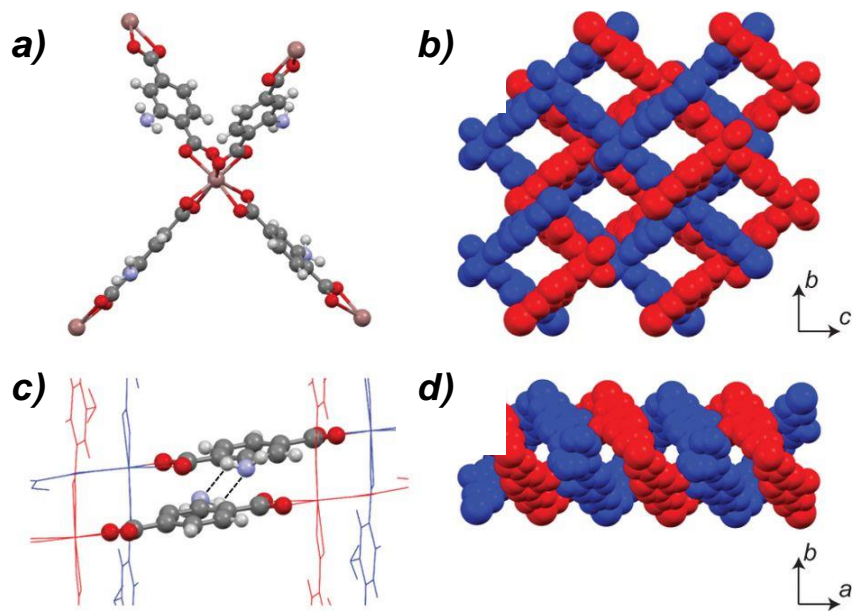


Figure 4.5. Microscope images of desolvated SHF-61-DMF (left) and SHF-61-CHCl<sub>3</sub> (centre and right) collected at x15 magnification. Scale bar represents 60 µm.

Carrington *et al.* reported the flexibility and solvent-induced structural shifting of the material in 2017. They reported the formation of brown octahedron-shaped crystals from DMF and post-synthetic exchange of DMF solvent molecules with CHCl<sub>3</sub> to yield SHF-61-CHCl<sub>3</sub>. The synthesis of this material is further described in Section 4.5.1. Microscope images of SHF-61 collected during experiments at B22 MIRIAM are shown in Figure 4.5, which show crystals of various morphologies.

The framework has a pseudo wine-rack structure, consisting of two doubly interpenetrated nets (Figure 4.6b) with one-dimensional channels running through the material (Figure 4.6d). Hydrogen-bonding interactions are present between the amino groups of the 2-aminoterephthalic acid linker of the two nets (Figure 4.6c).



*Figure 4.6. a) In(O<sub>2</sub>CR)<sub>4</sub> tetrahedral network node. b) View down the *a*-axis that shows lozenge-shaped channels. c) Hydrogen-bonding interaction between the amino groups of adjacent networks. d) View down the *c*-axis that shows the helical arrangement of the two interpenetrated networks along the channel axis (*a*-axis). Reproduced from reference 23.*

Figure 4.7 illustrates the breathing behaviour of SHF-61, where Carrington *et al.* observed contraction of the material pores upon desolvation from DMF. Desolvation from CHCl<sub>3</sub> resulted in only a small pore contraction.

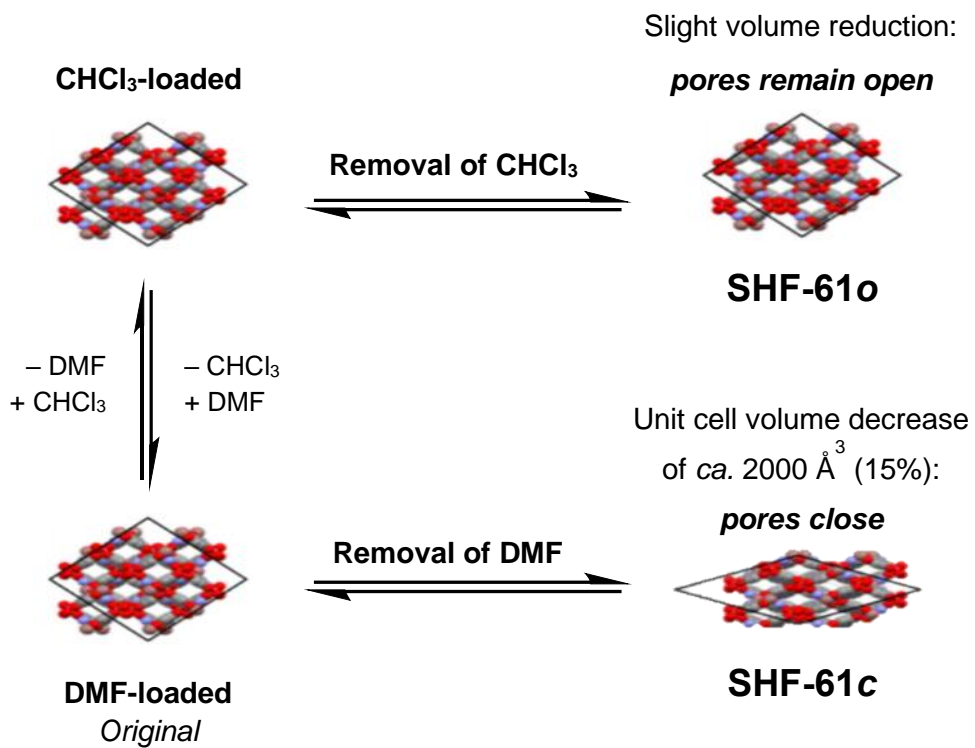


Figure 4.7. Overview of guest-related flexibility of SHF-61. Adapted from reference 23.

*In situ* infrared experiments were carried out at DLS B22 MIRIAM, described in Section 4.5.2, to monitor the desolvation, resolvation and CO<sub>2</sub> uptake of single crystals of the material. SHF-61 was desolvated from either CHCl<sub>3</sub> or DMF, and resolvated with CHCl<sub>3</sub>, cyclopentanone (CyP) or DMF. CyP was included to mirror single crystal X-ray diffraction (SCXRD) investigations being carried out by the Brammer group, but SCXRD data is still being processed by the Brammer group and is therefore not included in this thesis. IR data collected was analysed to further corroborate the previously reported ‘continuous breathing’ mechanism.

The ‘continuous breathing’ mechanism in SHF-61 results ultimately in closed- and open-pore structures, as illustrated in Figure 4.7. The following discussion will refer to frameworks desolvated from either DMF or  $\text{CHCl}_3$  as closed-pore or open-pore structures respectively. Throughout the discussion, any frameworks desolvated from DMF will be referred to as ‘SHF-61c’ and from  $\text{CHCl}_3$  as ‘SHF-61o’.

### 4.3.1 Approaches to spectral analysis

Several methods of interpreting the peak changes in the IR spectra were employed. These methods are briefly outlined in this section, before discussion of the individual experimental results in Sections 4.3.2 – 4.3.5.4.

#### 4.3.1.1 Peak fitting analysis

In order to deconvolute the overlapping peaks in the IR spectra (identified in Figure 4.8) of various SHF-61 structures, peak fitting analysis was carried out.

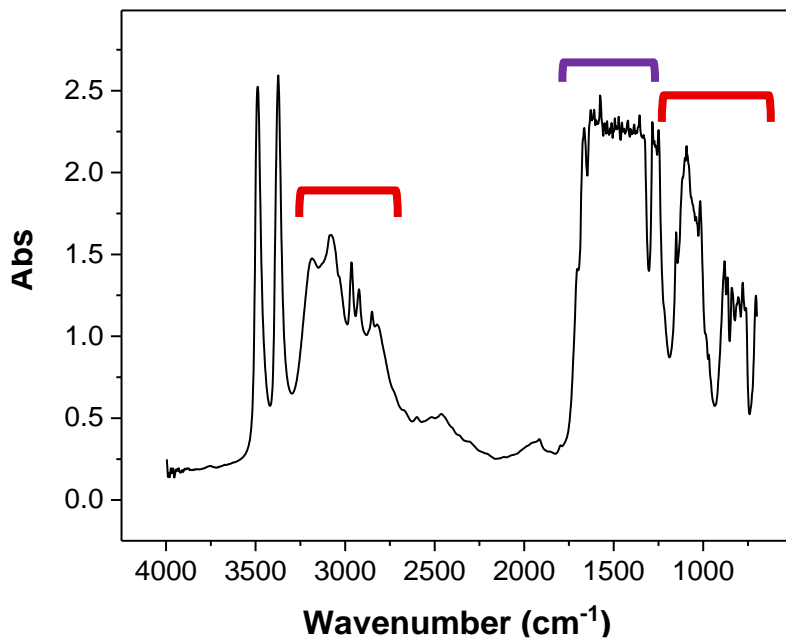
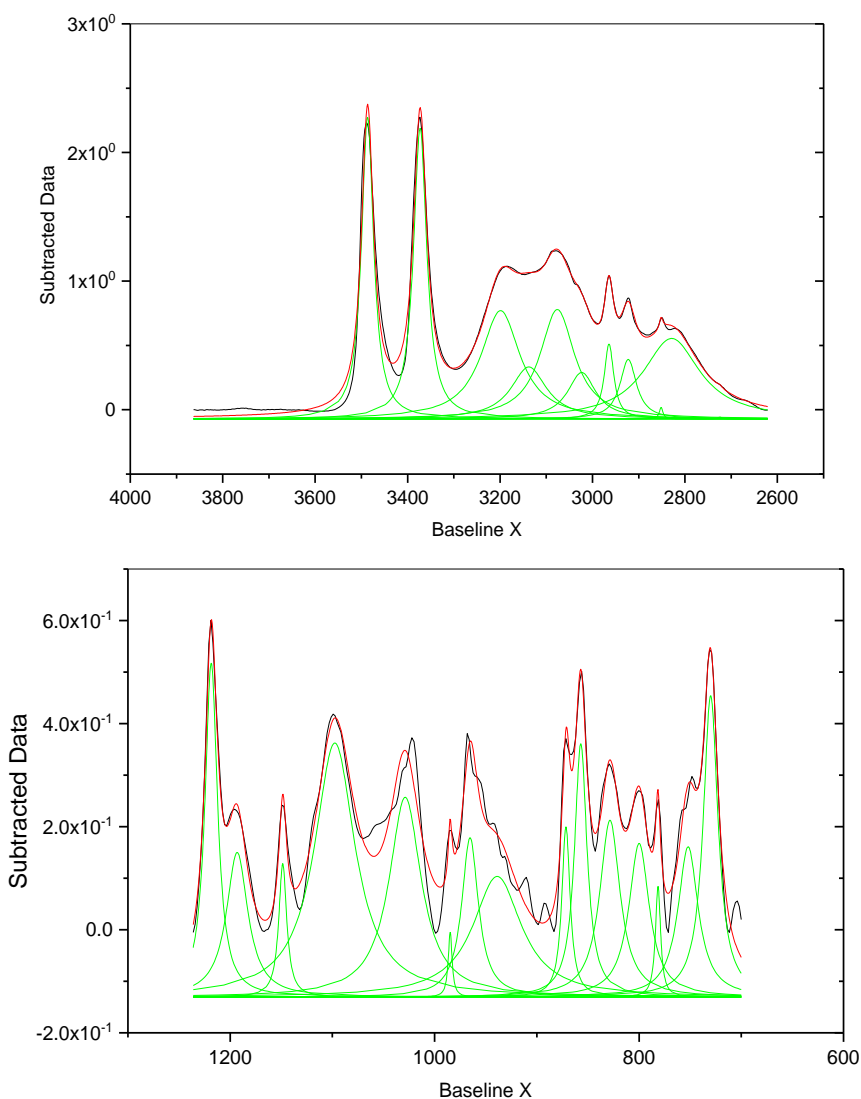


Figure 4.8. Example spectrum of SHF-61- $\text{CHCl}_3$  after desolvation at 120 °C. Regions indicated in red require deconvolution due to overlapping peaks; region indicated in purple is saturated.

Peaks were fit to a Lorentzian shape, as standard for infrared peaks.<sup>24–27</sup> Example fits for the spectra are shown in Figure 4.9.



*Figure 4.9. Example spectral fits for SHF-61-CHCl<sub>3</sub> at higher energy (top) and lower energy (bottom).*

Due to the saturation frequently present in the region indicated in purple in Figure 4.8 (ca. 1750–1237 cm<sup>-1</sup>) in each spectrum, we focussed on higher (3865–2617 cm<sup>-1</sup>) and lower energy (1236–700 cm<sup>-1</sup> for experiments involving CHCl<sub>3</sub> and CyP; 1706–700 cm<sup>-1</sup> for experiments involving DMF) regions of the spectra for peak fitting. The region between 2617–1237 cm<sup>-1</sup> was omitted due to an absence of diagnostic peaks between 2617–1830 cm<sup>-1</sup> and saturation (described in Section 1.7) between 1830–1237 cm<sup>-1</sup>.

Baseline correction was applied to all spectra to mitigate scattering effects. Example baseline corrections for high and low energy regions are shown in Figure 4.10.

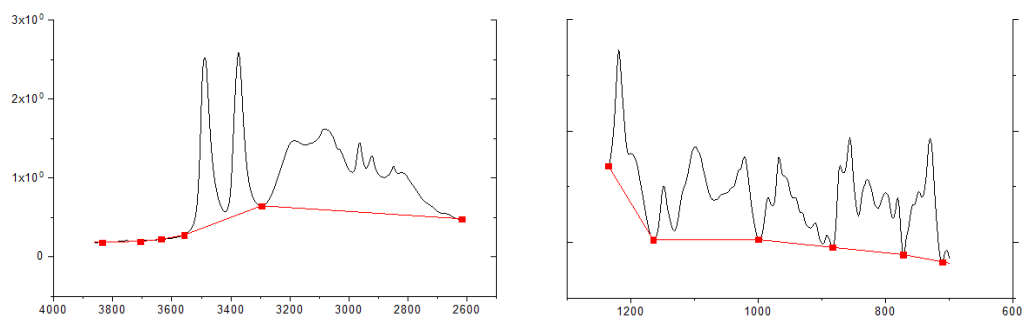


Figure 4.10. Example baseline corrections for SHF-61-CHCl<sub>3</sub>.

Baseline corrections were kept as simple as possible. Following baseline subtraction and selecting initial peak positions, peak fit properties (peak position, areas, width, etc.) refine until convergence. If fits failed to converge, peak widths and positions can be fixed. Where values were fixed, these parameters were not used to characterise changes in the crystal.

#### 4.3.1.2 Peak integration

Peak integration was employed when failure to converge during peak fitting analysis was not solved by fixing peak properties. Peak integration provided the integral of the peak, but no peak positions, and hence is potentially less informative than peak fitting analysis. Figure 4.11 shows an example IR spectrum where peak integration was employed, focussed on the CyP ν(CO) bands, collected during the CyP-resolvation of SHF-61 o.

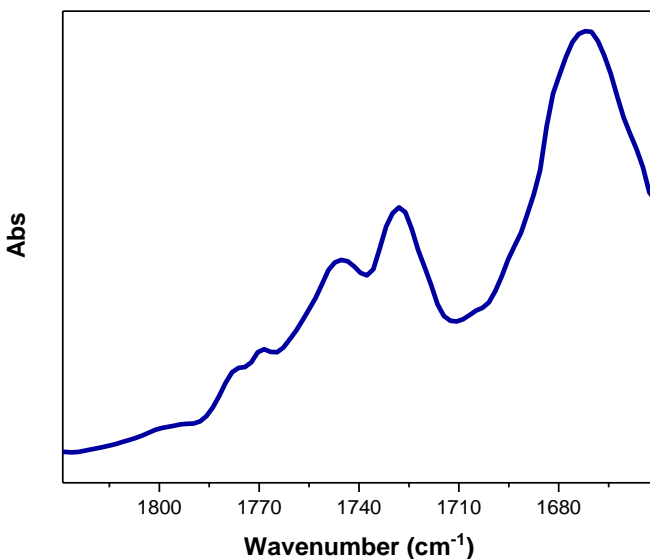


Figure 4.11. Infrared spectra collected during CyP-resolvation of SHF-61o, focussed on CyP  $\nu(\text{CO})$  band region.

Figure 4.12 shows an example of the baseline correction applied during peak integration of the CyP bands resolvation of SHF-61o. During resolvation experiments, baseline rises (caused by regions of increasing saturation due to adjacent solvent bands) made baseline point selection challenging, and therefore simple, straight line baselines are applied.

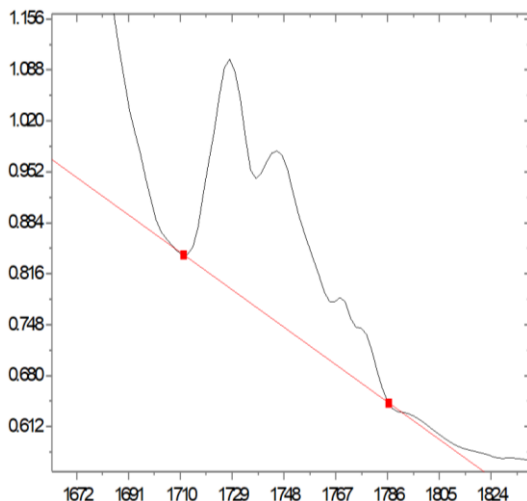
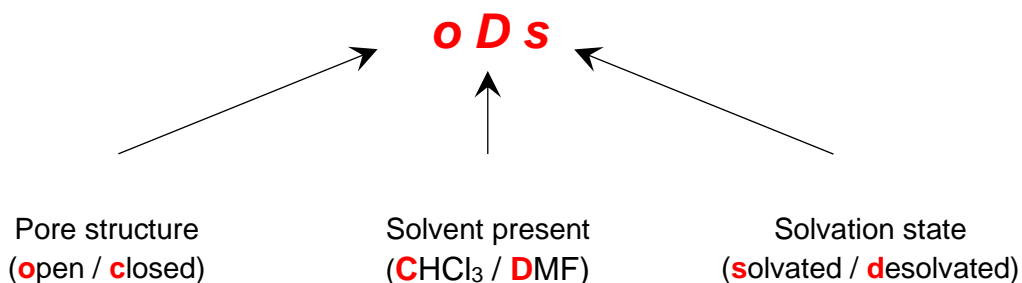


Figure 4.12. Baseline applied to integration process of CyP  $\nu(\text{CO})$  bands during resolvation of SHF-61o with CyP.

Following baseline subtraction, integration boundaries were selected and the peak integrals were calculated.

### 4.3.1.3 Composite spectral modelling

Composite spectral modelling was employed to identify the various pore geometry and solvation states present during experiments. As peak fitting analysis identified the  $\nu(\text{NH})$  regions as being most informative, composite spectral modelling analysis was confined to the spectral region 3599–3311 cm<sup>-1</sup>. In order to avoid overfitting the data, the minimum number of spectral models were used in each case to achieve a satisfactory fit. For the SHF-61 system, we defined a variety of model spectra, each representing a different solvation and pore state. A naming protocol was established for the states, describing the pore structure, parent solvent and solvation state:



Crystallographic experiments have defined four end states across the SHF-61 CHCl<sub>3</sub> and DMF structures: solvated (with CHCl<sub>3</sub> or DMF) and desolvated (open- or closed-pore):

*oCs* – open-pore, CHCl<sub>3</sub> solvated

*oDs* – open-pore, DMF solvated

*od* – open-pore, desolvated

*cd* – closed-pore, desolvated

Furthermore, the closed form can be partially solvated, with either CHCl<sub>3</sub> or DMF, so two additional states have also been defined:

*cCs* – closed-pore, partially CHCl<sub>3</sub> solvated

*cDs* – closed-pore, partially DMF solvated

Spectra of the final desolvated states and those collected during resolvation experiments were collected at ambient temperature (27 °C) to ensure that any spectral differences were not artefacts of temperature. These models can therefore be directly compared. Spectra collected throughout desolvation time series were collected at the experimental temperature, and this is indicated where appropriate. After the collection of time series, the sample was returned to ambient temperature and a new background and sample spectrum recorded. The sample was then heated to the next temperature stage.

There is not currently crystallographic data to support conclusions drawn from CyP experiments, but the same approach to model selection has been used for this system. The model list above is not exclusive since additional models were employed in specific cases, highlighted as appropriate in the text below.

### 4.3.2 Desolvation of SHF-61

Desolvation of single crystals of SHF-61-CHCl<sub>3</sub> and SHF-61-DMF, to form SHF-61*o* and SHF-61*c* was carried out in a Linkam FTIR600 stage, described and pictured in Section 1.6 and Figure 1.13 (pp.13) respectively. Samples of SHF-61-CHCl<sub>3</sub> and SHF-61-DMF were heated under a constant N<sub>2</sub> flow of 100 SCCM sequentially at a variety of temperatures, detailed in Table 4.1 below. Time series of spectra were collected during the desolvation experiments every 30 seconds for SHF-61-CHCl<sub>3</sub> and every 60 seconds for SHF-61-DMF at each temperature.

Following heating for the times indicated in Table 4.1, the stage was returned to ambient temperature (27 °C) and new background and sample spectra recorded between each temperature. No spectrum was recorded following heating of SHF-61-CHCl<sub>3</sub> at 100 °C due to user error.

*Table 4.1. Times for which SHF-61-DMF and SHF-61-CHCl<sub>3</sub> were held at specified temperatures during desolvation experiments. \*The detector required a liquid N<sub>2</sub> fill at this stage and therefore we had to wait for the detector temperature to stabilise before further collection.*

T (°C / K)	Time held at temperature (minutes)	
	CHCl <sub>3</sub>	DMF
27 / 300	30	30
40 / 313	20	20
60 / 333	20	20
80 / 353	20	20
100 / 373	*130	20
120 / 393	80	20
150 / 423	-	80

Desolvation was deemed to be complete for SHF-61-CHCl<sub>3</sub> (to form SHF-61**o**) and SHF-61-DMF (to form SHF-61**c**) upon loss of the CHCl<sub>3</sub> δ(CH) bend at 1220 cm<sup>-1</sup> and DMF carbonyl ν(CO) stretch at 1670 cm<sup>-1</sup> for each framework respectively.

Spectra for desolvation experiments were analysed by peak fitting analysis to extract changes in peak position and area for each peak of interest. Peak position and area data were extracted *via* this method for time series collected at each temperature, as per Table 4.1, and for additional room temperature spectra collected following each heating stage. Although trends were discernible during data processing, they were often inconsistent between spectral series collected at different temperatures. Inconsistencies were observed for several reasons, including (but not limited to); baseline shifts due to change in experimental temperature, crystal position shifts during the experiment, and the temperature sensitivity of IR peaks.

The largest and most identifiable peak position and area changes are the  $\nu(\text{NH})$  bands in the region of 3486 and 3370  $\text{cm}^{-1}$ . The  $\nu(\text{NH})$  stretches of SHF-61- $\text{CHCl}_3$  and SHF-61-DMF, solvated (blue) and desolvated (red), are shown in Figure 4.13.

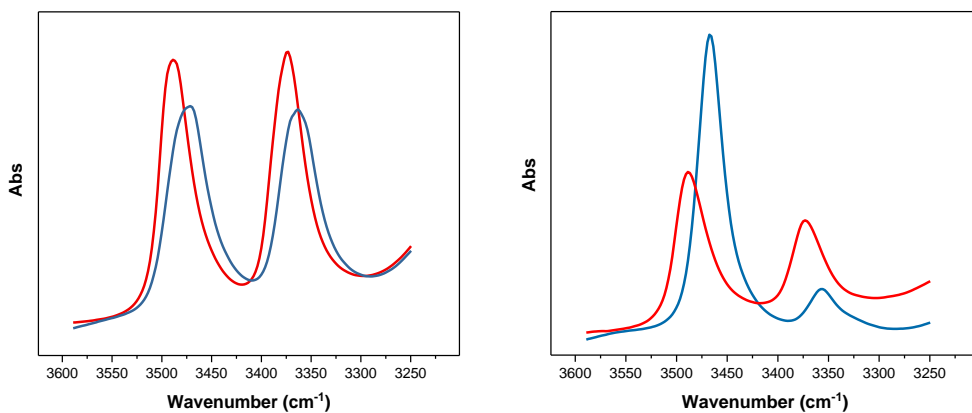


Figure 4.13. IR spectra of solvated (blue) and desolvated (red) crystals of SHF-61- $\text{CHCl}_3$  (left) and SHF-61-DMF (right).

Changes in peak area and position observed upon desolvation are shown in Table 4.2 and Figure 4.14. Greater changes in peak area and position were observed for desolvation of SHF-61-DMF (forming SHF-61c) than SHF-61- $\text{CHCl}_3$  (forming SHF-61o), due to the increased strength of interactions present between DMF molecules and the  $\text{NH}_2$  group of the linker than for  $\text{CHCl}_3$ , as illustrated in Figure 4.15.

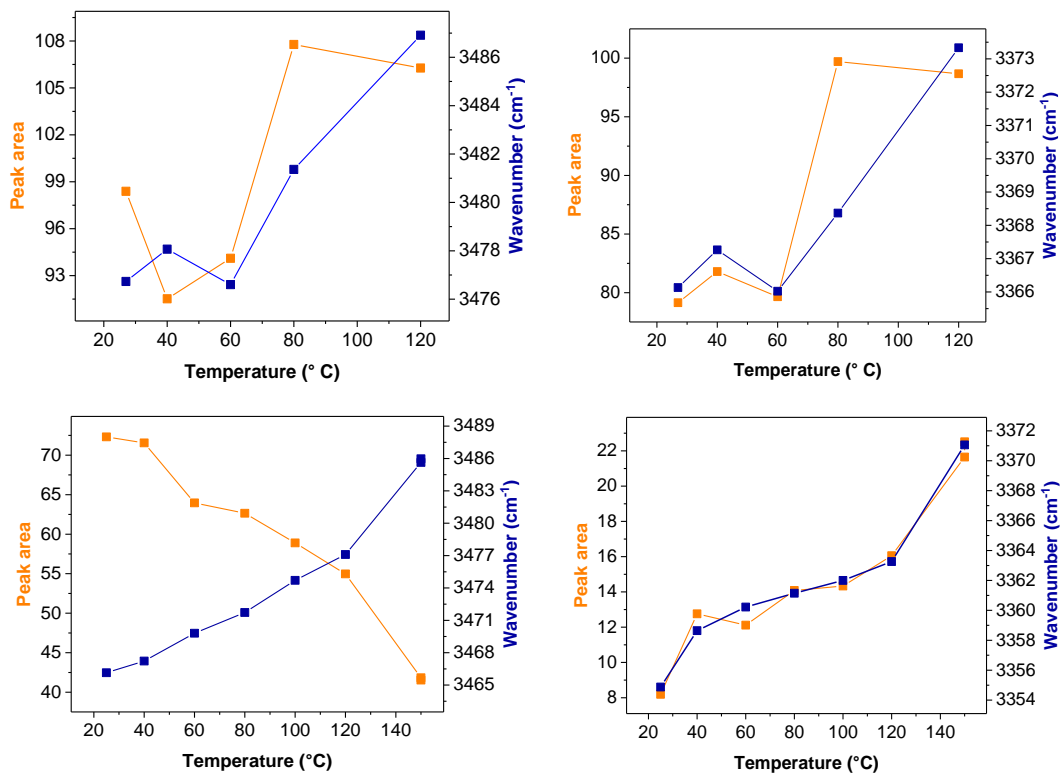


Figure 4.14. Peak area (orange) and position (blue) changes of SHF-61-CHCl<sub>3</sub> (top) and SHF-61-DMF (bottom) higher energy (left) and lower energy (right)  $\nu(\text{NH})$  following heating.

Table 4.2. Peak area and position changes for SHF-61 upon desolvation.

Framework	$\nu_{\text{initial}}$ (cm <sup>-1</sup> )	$\nu_{\text{final}}$ (cm <sup>-1</sup> )	$\Delta\nu$ (cm <sup>-1</sup> )	$A_{\text{initial}}$	$A_{\text{final}}$	$\Delta A$
SHF-61-DMF( <b>c</b> )	3465	3480	+15	69.7	40.0	-29.7
	3352	3368	+16	3.6	15.0	+11.4
SHF-61-CHCl <sub>3</sub> ( <b>o</b> )	3475	3485	+10	89.4	79.8	-9.6
	3363	3371	+8	72.4	54.6	-17.8

As desolvation occurs and the host-guest interactions are reduced/removed, the N–H bond is strengthened and hence the peak shifts to higher energy.

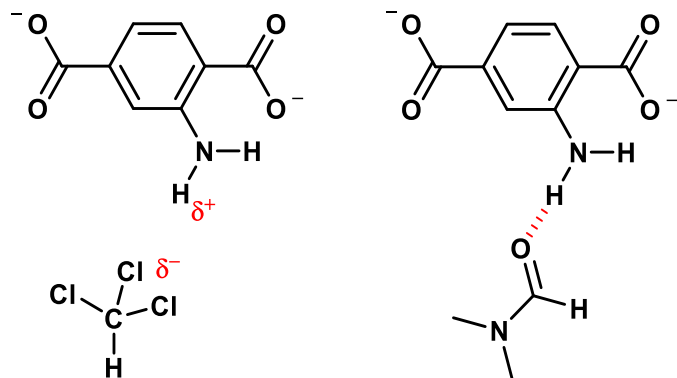


Figure 4.15. Illustration of solvent interactions with 2-aminoterephthalate linker in SHF-61.

One particular aim of the spectral deconvolution by peak fitting was to identify a peak which indicated the closure of the pore structure. This would allow the extent of pore closure to be monitored in real-time at high spatial resolution. Unfortunately, a single peak could not be identified, and hence alternative methods of spectral analysis were investigated.

Composite spectral modelling was employed to determine composition of model states in each desolvation spectrum. The model spectra were taken from the following points during the experiments;

*oCs* – before SHF-61-CHCl<sub>3</sub> desolvation experiment

*oDs* – before SHF-61-DMF desolvation experiment

*od* – after SHF-61-CHCl<sub>3</sub> desolvation experiment

*cd* - after SHF-61-DMF desolvation experiment

*cDs* – generated by subtraction of *cd* from *oDs* at point immediately prior to pore opening (75 minutes)

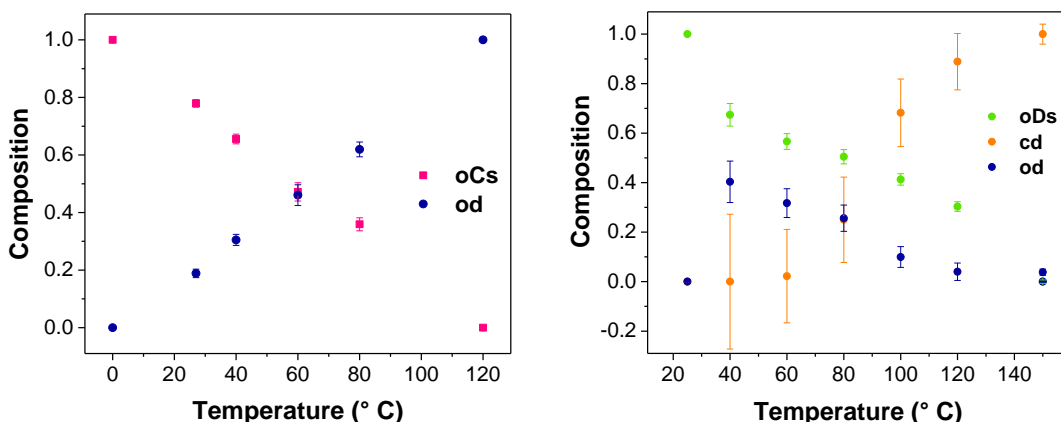


Figure 4.16. Spectral composition plots of SHF-61-CHCl<sub>3</sub> (left) and SHF-61-DMF (right) during staged desolvation experiments.

Only two model states were needed to fit the SHF-61-CHCl<sub>3</sub> desolvation spectra: open-pore, CHCl<sub>3</sub> solvated (*oCs*) and open-pore, desolvated (*od*). Figure 4.16 shows a straightforward progression from the *oCs* form to the *od* form.

The desolvation process of SHF-61-DMF better fits to more states. Conceptually the crystal could be comprised of open-pore, DMF solvated (*oDs*); closed-pore, DMF solvated (*cDs*); open-pore desolvated (*od*) and closed-pore, desolvated (*cd*) states. Despite this, the spectra were satisfactorily fit to only three model spectra (*oDs*, *od* and *cd*) without need for the *cDs* state (Figure 4.16). Indeed, Figure 4.17 shows the spectral modelling outcome when the spectra were fit to four models, where the *cDs* state dominates from 40 to 120 °C. This unrealistically suggests that reduction in the pore size occurs during heating at 27 °C, which is inconsistent with crystallographic experiments. The error bars associated with this model are also very large.

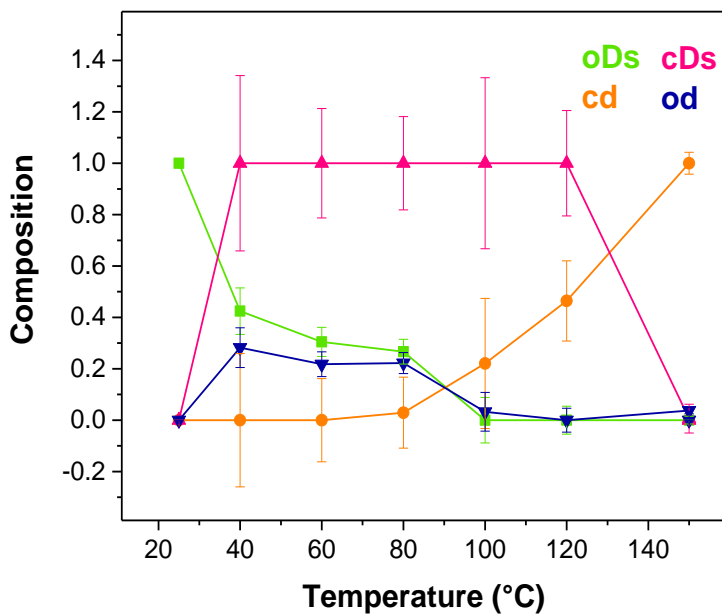


Figure 4.17. Spectral composition plot of SHF-61-DMF during staged desolvation experiments, when fit to four models.

The more informative modelling outcome when the spectra are fit to three models (*oDs*, *cd* and *od*) as shown in Figure 4.16. Since the state omitted from the model fitting is *cDs* (closed-pore, DMF-solvated), we can propose that pore closure is initiated locally by DMF loss; the *cDs* state is not observed throughout the desolvation process (shown schematically in Figure 4.18).

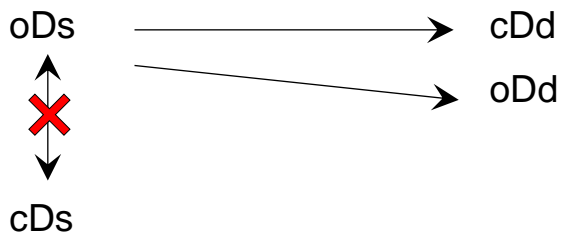


Figure 4.18. Transition of DMF model states

### 4.3.3 Resolvation of SHF-61*o* and SHF-61*c*

Resolvation of SHF-61 (desolvated as discussed in Section 4.3.2) was carried out at room temperature in the same Linkam FTIR600 stage detailed previously (Figure 1.13, pp.13). SHF-61*c* was resolvated with DMF, since this solvent has been observed (by crystallography) to reopen the structure, and different samples of SHF-61*o* were resolvated individually with CHCl<sub>3</sub>, CyP and DMF. A bubbler containing CHCl<sub>3</sub>, CyP or DMF was attached to the stage and pre-dried N<sub>2</sub> gas flowed through the bubbler (rate 5 SCCM) to deliver a solvent-saturated vapour flow to the desolvated sample in the cell environment. Infrared spectra were collected every 30 seconds for CHCl<sub>3</sub> resolvation of SHF-61*o*, every 19 seconds for CyP resolvation of SHF-61*o*, every 19 seconds for DMF resolvation of SHF-61*o* and every 60 seconds for DMF resolvation of SHF-61*c* during resolvation experiments.

The resolvation processes of SHF-61 were initially deconvoluted using peak fitting analysis in OriginPro 2017, as described for the analysis of infrared spectra from desolvation experiments in Section 4.2.1.1. Similarly to desolvation experiments, spectra were split into a higher energy section (3865–2617 cm<sup>-1</sup>) and lower energy section (1236–700 cm<sup>-1</sup> for experiments involving CHCl<sub>3</sub> and CyP; 1706–700 cm<sup>-1</sup> for experiments involving DMF) regions of the spectrum and each band was fitted to a Lorentzian peak shape. Trends in the  $\nu(\text{NH})$  and respective solvent regions during resolvation experiments were examined and are discussed hereafter.

To enable direct comparison of the states present in SHF-61 systems during resolvation, composite spectrum modelling was also carried out on the resolvation spectra. Composite spectrum modelling has been introduced in more detail in Section 4.2.1.2.

### 4.3.3.1 Resolvation of SHF-61c with DMF

Figure 4.19 shows a photograph of the particular SHF-61c crystal resolvated during this experiment, which is ca.  $80 \times 40 \mu\text{m}$ . Note, the black lines are the glass knife edge aperture. Speckled appearance of apertures is due to dirt, which is present on the aperture glass and not the sample.



Figure 4.19. Photograph of SHF-61c measured in this experiment (indicated), collected *in situ* on the IR microscope. Aperture size is  $20 \times 20 \mu\text{m}$ .

The shifts in peak position and area for the  $\nu(\text{NH})$  bands pre- and post-resolvation of SHF-61c with DMF are shown below in Figure 4.20 and Table 4.3. Resolvation experiments were stopped once the peak positions of the  $\nu(\text{NH})$  bands no longer appeared to be shifting.

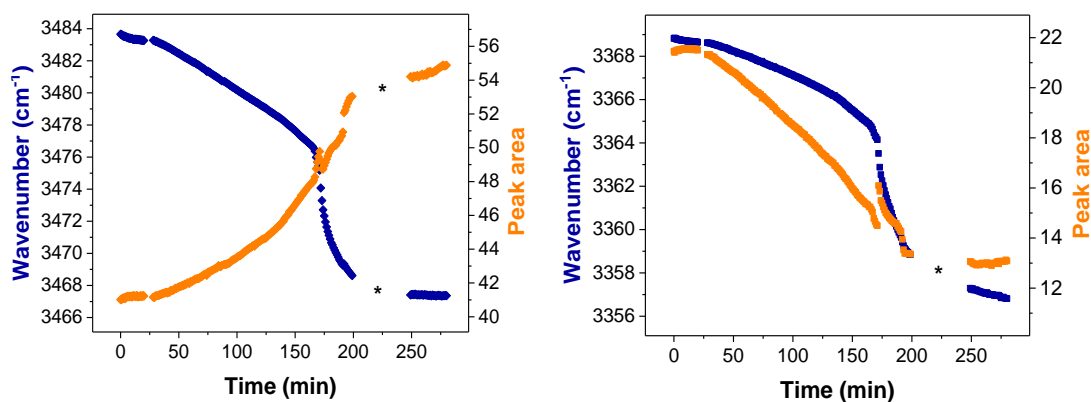


Figure 4.20. Peak area and position changes of SHF-61c following resolvation with DMF for (left) higher energy and (right) lower energy  $\nu(\text{NH})$  peaks. Data is absent for 199–249 mins (indicated by \*) due to a detector coolant fill on the microscope spectrometer.

Figure 4.20 and changes in peak absorbance values in Table 4.3 show a clear change in the peak ratios and positions of the N–H bands following resolvation with DMF. There is a greater peak shift and area change observed in the higher energy  $\nu(\text{NH})$  peak, indicating that resolvation with DMF has a larger effect on the asymmetric N–H stretching mode. The peaks did not return to the original solvated SHF-61-DMF positions ( $3465$  and  $3352\text{ cm}^{-1}$ ), likely due to the significantly larger solvent volume present in the original sample. These samples were originally synthesised in DMF, meaning pores were completely saturated. Resolvation of the desolvated material with DMF vapour, although effective in this experiment, clearly does not saturate the framework to the same extent as during synthesis.

*Table 4.3. Changes in  $\nu(\text{NH})$  bands after resolvation of SHF-61c with DMF.*

Framework	$\nu_{\text{initial}}$ ( $\text{cm}^{-1}$ )	$\nu_{\text{final}}$ ( $\text{cm}^{-1}$ )	$\Delta\nu$ ( $\text{cm}^{-1}$ )	$A_{\text{initial}}$	$A_{\text{final}}$	$\Delta A$
SHF-61c-DMF	3484	3467	-17	41.0	55.6	+15.6
	3369	3356	-13	21.5	11.8	-9.7

Composite spectral modelling was used to examine the states present during the resolvation process. The model spectra were taken from the following points during the experiments;

*oDs* – before SHF-61-DMF desolvation experiment

*od* – after SHF-61-CHCl<sub>3</sub> desolvation experiment

*cd* - after SHF-61-DMF desolvation experiment

*cDs* – subtraction of *cd* from *oDs* at point immediately prior to pore opening

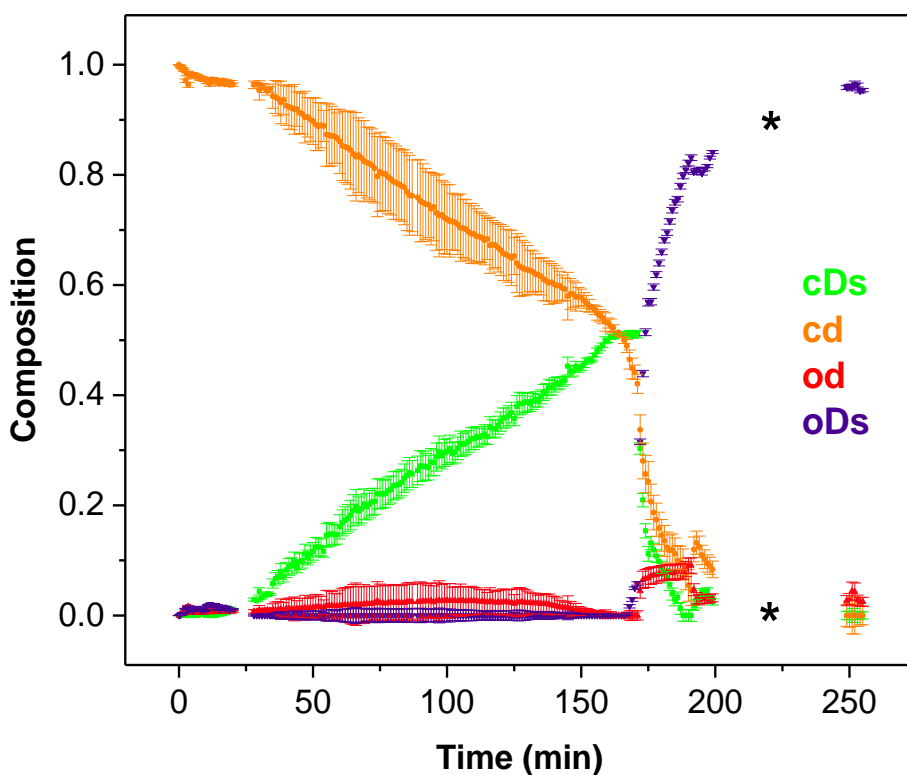
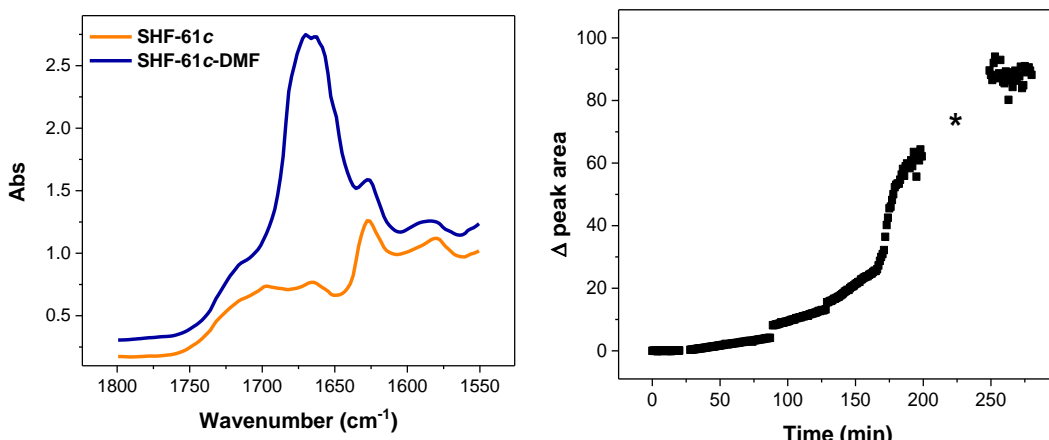


Figure 4.21. Composition plot of spectra during SHF-61c-DMF resolvation experiment. Data is absent for 199–249 mins (indicated by \*) due to a detector coolant fill on the microscope spectrometer.

The plot in Figure 4.21 shows that four models are required to fit the spectra, and the pore structure is clearly dynamic. The changes seen in several models around 75 minutes indicate a gated pore mechanism. The closed-pore, DMF solvated (*cDs*) state increases steadily until reaching approximately 50% of the total composition at ca. 175 mins, when there is then a sharp decrease. This decrease is accompanied by a sharp increase of the open-pore, DMF solvated (*oDs*) state, indicating that the material is resolvated sufficiently to induce expansion of the pore structures. There is, at the same time, a small increase in the amount of open-pore, desolvated (*od*) state, which subsequently decreases as the remainder of the pore resolvates.

This is significant, as it suggests that, unlike in desolvation experiments discussed in Section 4.3.2, local changes in DMF occupancy are influencing the wider framework structure. Note, that composite spectral modelling only reflects changes in the  $\nu(\text{NH})$  region of the spectrum, and therefore does not reflect the uptake and behaviour of DMF in any other parts of the structure.

Figure 4.22 show the growth of the DMF carbonyl stretch at ca.  $1660\text{ cm}^{-1}$  in the IR spectrum (left), and the change in peak area of the band (right).



*Figure 4.22. (Left) Infrared spectra of DMF  $\nu(\text{CO})$  stretch ( $1700\text{--}1650\text{ cm}^{-1}$ ) in SHF-61c (orange) and SHF-61c-DMF (blue). (Right) Change in peak area of  $1660\text{ cm}^{-1}$  DMF carbonyl peak during DMF-resolvation of SHF-61c. Data is absent for SHF-61c-DMF resolvation for the period 199–249 mins (indicated by \*) due to a detector coolant fill on the microscope spectrometer.*

The spectral composition plot in Figure 4.21 shows that at ca. 175 minutes, sufficient DMF–NH<sub>2</sub> interactions are occurring to instigate pore opening. In Figure 4.22 (right), at 175 minutes, the DMF  $\nu(\text{CO})$  stretch is approximately a third of its total intensity. Therefore, approximately one more third of the total DMF uptake can interact with amine groups as the structure opens, and the final third is (by inference) occupying pore space but not directly bonding to the amine groups. These are reasonable assumptions as the amine sites will saturate before the pore volume saturates, and because the open-pore form has greater volume than the closed form.

This confirms that the changes in  $\nu(\text{NH})$  are in direct correlation with the introduction of DMF to the framework amine groups, and hence should be interpreted together. Note, that following the liquid N<sub>2</sub> detector fill (signified by \*), the peak area and position stabilised. The slope of the plots in Figures 4.21 and 4.22 all increase sharply approximately 150 minutes into the resolvation experiments.

### 4.3.3.2 Resolvation of SHF-61o with DMF

Figure 4.23 shows a photograph of the particular SHF-61o crystal resolvated during this experiment, which is ca.  $40 \times 30 \mu\text{m}$ .

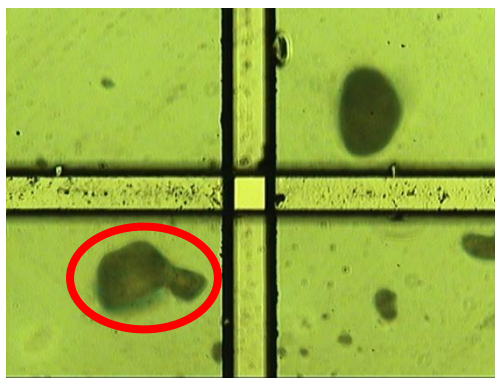


Figure 4.23. Photograph of SHF-61o (indicated), collected *in situ* on the IR microscope. Aperture size is  $20 \times 20 \mu\text{m}$ .

Table 4.4 shows peak position and area changes following resolvation of SHF-61o with DMF. The resolvation of the material with DMF resulted in a peak shift of both  $\nu(\text{NH})$  to lower energies. Peaks did not return to the original SHF-61-DMF  $\nu(\text{NH})$  positions, and, surprisingly, shifted further past them. A greater peak shift was observed for the asymmetric peak shift, as it was during the DMF-resolvation of the closed-pore structure. An increase in peak area was observed for the higher energy asymmetric peak, and a decrease for the lower energy symmetric peak.

Table 4.4. Changes in  $\nu(\text{NH})$  bands after resolvation of SHF-61o with DMF.

Framework	$\nu_{\text{initial}}$ ( $\text{cm}^{-1}$ )	$\nu_{\text{final}}$ ( $\text{cm}^{-1}$ )	$\Delta\nu$ ( $\text{cm}^{-1}$ )	$A_{\text{initial}}$	$A_{\text{final}}$	$\Delta A$
SHF-61o-DMF	3472	3458	-14	30.3	38.2	+7.9
	3360	3349	-11	26.5	24.7	-1.8

To analyse the change in the DMF  $\nu(\text{CO})$  stretch (Figure 4.24 (right), ca.  $1650 \text{ cm}^{-1}$ ), peak integration was used, as peak fitting analysis was unable to reach convergence.

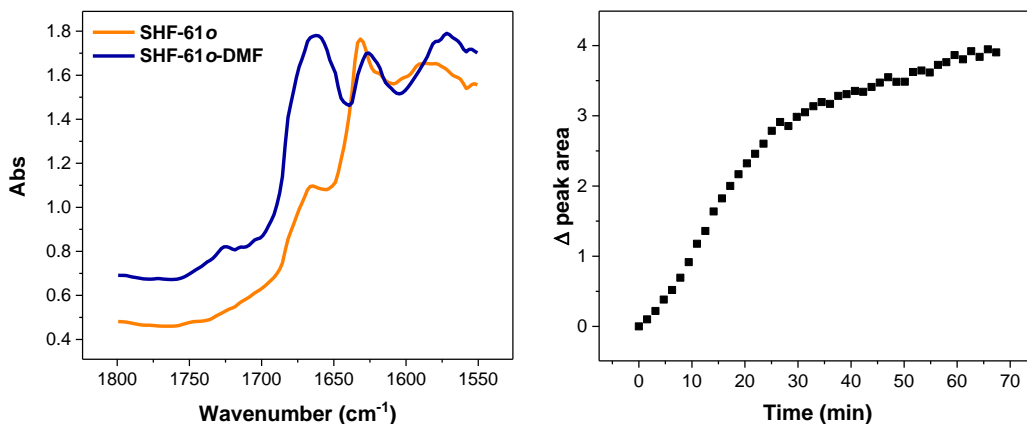


Figure 4.24. (Left) Infrared spectra of DMF  $\nu(\text{CO})$  stretch ( $1700\text{--}1650\text{ cm}^{-1}$ ) in SHF-61o (orange) and SHF-61o-DMF (blue). (Right) Change in peak area of  $1660\text{ cm}^{-1}$  DMF  $\nu(\text{CO})$  band during SHF-61o DMF-resolvation.

Figure 4.24 (left) shows IR spectra of SHF-61o and SHF-61o-CHCl<sub>3</sub>, with a clear growth of the DMF  $\nu(\text{CO})$  peak at around 1660 cm<sup>-1</sup>. Baseline positions were difficult to determine for the treatment of this series of spectra, due to the growth of the DMF  $\nu(\text{CO})$  stretch raising the baseline in the region surrounding the peak. A straight line baseline was therefore applied, and the peak integrated across the range 1660.5–1668.2 cm<sup>-1</sup>.

The plot of  $\nu(\text{CO})$  peak area change in Figure 4.24 (right) shows an initial accelerated increase in peak area in the first 7 minutes of resolvation. The rate of peak area growth then increases further at ca. 30 minutes. This second accelerated growth rate could be attributed to a cooperative resolvation effect, where additional DMF (at ca. 30 minutes) is able to resolvate the framework more easily following the initial introduction of solvent in the first 7 minutes. The change in peak area suggests that the resolvation process has two components (pre- and post-30 minutes). The initial, faster process (until 30 minutes) is likely to be the initial interaction of DMF with the N–H groups of the aminoterephthalic acid linker. The slower process is likely to be resolvation of the framework pores after all interactions with amine groups have been satisfied.

The reason for the first 7 minutes of accelerated uptake are unclear. Although we have proposed the cooperative resolvation effect seen between 7 – 30 minutes, we have no further evidence to support this.

To relate the change in carbonyl band with the change specifically in the  $\nu(\text{NH})$  region, composite spectral modelling was performed on the resolvation spectra. Resolvation of SHF-61<sup>o</sup> with DMF required only two model spectra to fit – open-pore, desolvated (*od*) and open-pore, DMF-solvated (*oDs*), as the pore is already open and hence no closed-pore model components are required.

The model spectra were taken from the following points during the experiments;

*oDs* – before SHF-61-DMF desolvation experiment

*od* – after SHF-61-CHCl<sub>3</sub> desolvation experiment

The spectral composition plot of SHF-61<sup>o</sup> DMF-resolvation experiments is shown below in Figure 4.25.

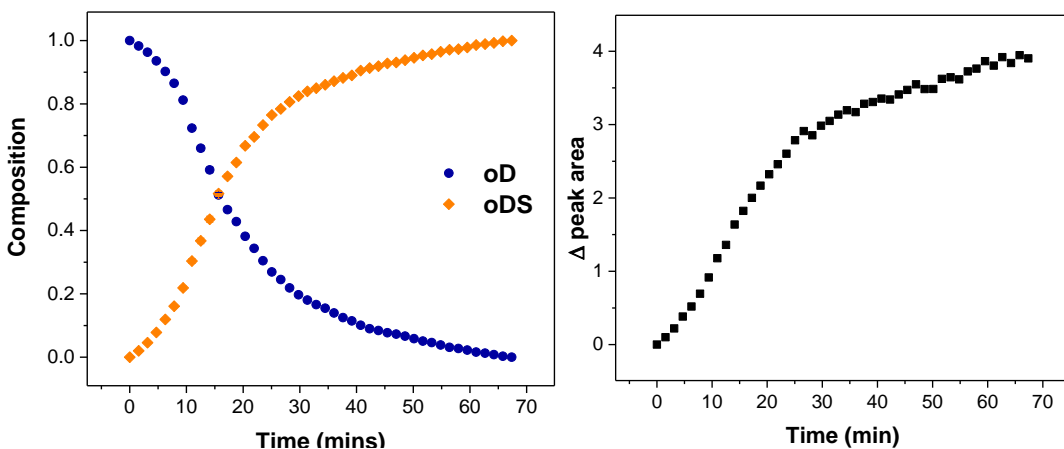


Figure 4.25. (Left) Composition plot of spectra during SHF-61<sup>o</sup>-DMF resolvation experiment. (Right) Change in peak area of 1660 cm<sup>-1</sup> DMF  $\nu(\text{CO})$  band during SHF-61<sup>o</sup> DMF-resolvation.

Figure 4.25 (left) shows a two-component progression, where the first 30 minutes occur at a faster rate than the subsequent 40 minutes. This is likely to be DMF initially interacting with the NH<sub>2</sub> groups of framework, followed by filling of the framework pores.

The peak profiles of the *od* model and 1660 cm<sup>-1</sup> peak area change are incredibly similar, corroborating the assumptions that the first 30 minutes of resolvation are responsible for saturating the DMF–NH<sub>2</sub> interaction sites, and the remainder of the resolvation experiment filling the pore space. While the rise in the *od* model appears to be levelling off by the end of this experiment, the peak integral of the DMF band is still rising, which is consistent with the continued resolvation of the rest of the pore space after saturation of the amine sites. Quantitative assessment of the kinetics was attempted, using mono and biexponential curve fitting, but no satisfactory fits could be achieved. This is perhaps unsurprising, as the DMF resolvation experiments discussed in Section 4.3.3.1 indicate that the amine and other pore sites in the framework are not independent of each other when it comes to solvent binding.

#### 4.3.3.3 Resolvation of SHF-61o with CHCl<sub>3</sub>

Figure 4.26 shows a photograph of the particular SHF-61o crystal resolvated during this experiment, which is ca. 80 x 50 µm.

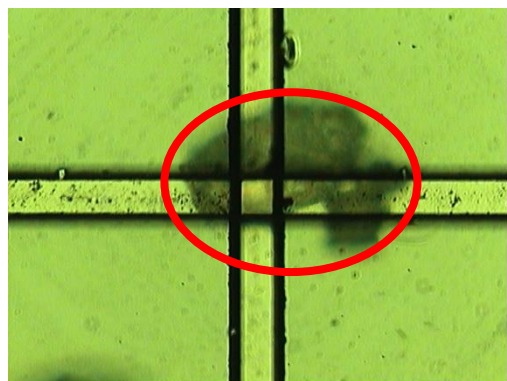


Figure 4.26. Photograph of SHF-61o measured in this experiment (indicated), collected *in situ* on the IR microscope. Aperture size is 20 x 20 µm.

Figure 4.27 shows the changes in peak position and area of the ν(NH) bands following resolvation of SHF-61o with CHCl<sub>3</sub>. Changes in peak position and area for ν(NH) bands pre- and post-resolvation are shown below in Table 4.5.

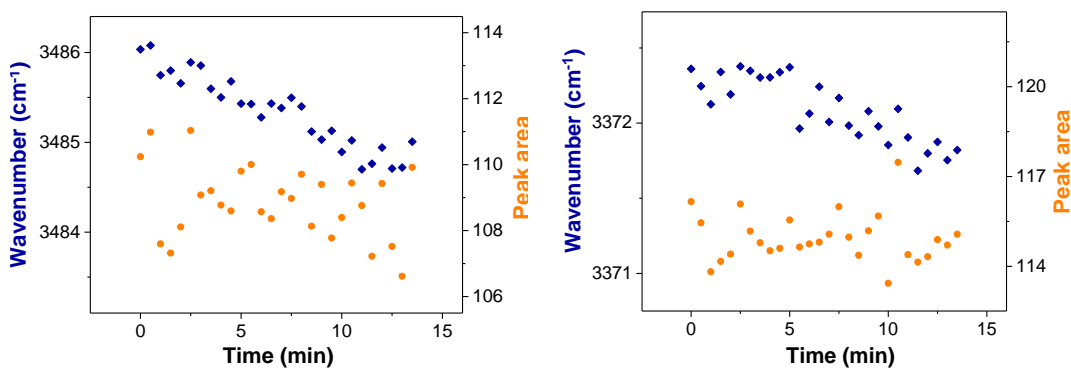


Figure 4.27. Peak area and position changes of SHF-61o following resolvation with  $\text{CHCl}_3$  for (left) higher energy and (right) lower energy  $\nu(\text{NH})$  peaks.

As can be seen from both Figure 4.27 above and Table 4.5, the changes in peak position and area are significantly smaller for resolvation with  $\text{CHCl}_3$  than for the resolvation with DMF, as discussed previously. This is attributed to the comparatively lower hydrogen-bonding strength between the amino group and  $\text{CHCl}_3$  than for DMF. Peak positions did not return to those in pre-desolvated SHF-61- $\text{CHCl}_3$  ( $3475$  and  $3363\text{ cm}^{-1}$ ), and this is predicted to be due to resolvation with vapour-phase  $\text{CHCl}_3$  not saturating the material as fully as during the post-synthetic solvent-exchange procedure.

Table 4.5. Changes in  $\nu(\text{NH})$  bands after resolvation of SHF-61o with  $\text{CHCl}_3$ .

Framework	$\nu_{\text{initial}}$ (cm <sup>-1</sup> )	$\nu_{\text{final}}$ (cm <sup>-1</sup> )	$\Delta\nu$ (cm <sup>-1</sup> )	$A_{\text{initial}}$	$A_{\text{final}}$	$\Delta A$
SHF-61o- $\text{CHCl}_3$	3486	3485	-1	110.2	109.9	-0.3
	3372	3372	0	116.2	115.1	-1.1

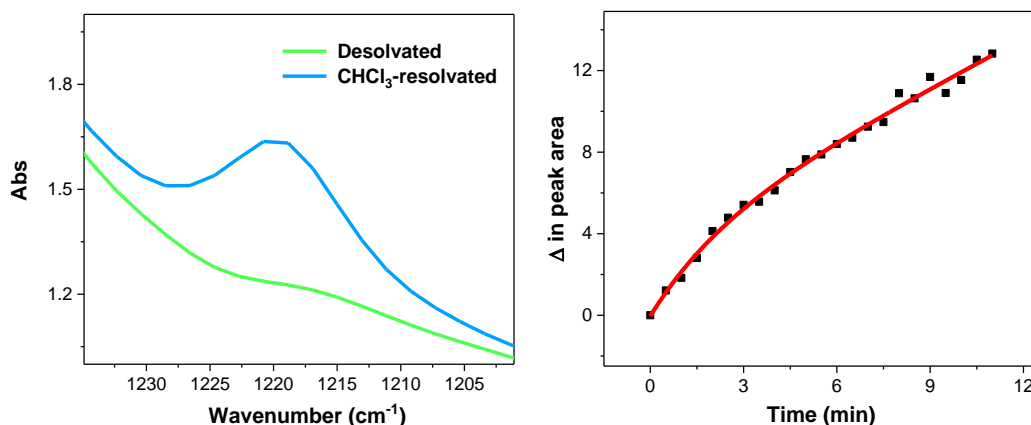


Figure 4.28. (Left) Desolvated (green) and  $\text{CHCl}_3$ -resolvated (blue) SHF-61 o. Peak at  $1230\text{--}1215\text{ cm}^{-1}$  is indicative of  $\delta(\text{CH})$  bend. (Right) Peak area of  $1220\text{ cm}^{-1}$   $\text{CHCl}_3 \delta(\text{CH})$  bend during SHF-61  $\text{CHCl}_3$ -resolvation fit to a biexponential curve (red).

The peak shown above in Figure 4.28 (left), characteristic of the  $\delta(\text{CH})$  bend in  $\text{CHCl}_3$ , was fit to a Lorentzian peak shape in OriginPro 2017. The only data used for fit was up until 12 minutes, due to the crystal moving during the data collection, affecting the increase of the band. The peak area increased with time, as shown in Figure 4.28 (right), and a biexponential curve fit to this data appears to show a two-component process. The first 3 minutes occurred more quickly than the subsequent 11 minutes, indicating a fast process as  $\text{CHCl}_3$  interacts with the amine groups of the framework linker. The second process is likely to be the framework pores filling after interactions all amino groups have been filled.

Composite spectral modelling was employed to investigate changes in the  $\nu(\text{NH})$  bands. The only states needed to fit during SHF-61- $\text{CHCl}_3$  resolvation were open-pore,  $\text{CHCl}_3$  solvated (*oCs*) and open-pore, desolvated (*od*). The model spectra were taken from the following points during the experiments;

- oCs* – before SHF-61- $\text{CHCl}_3$  desolvation experiment
- od* – after SHF-61- $\text{CHCl}_3$  desolvation experiment

The spectral composition plot of SHF-61 o DMF-resolvation experiments is shown below in Figure 4.29.

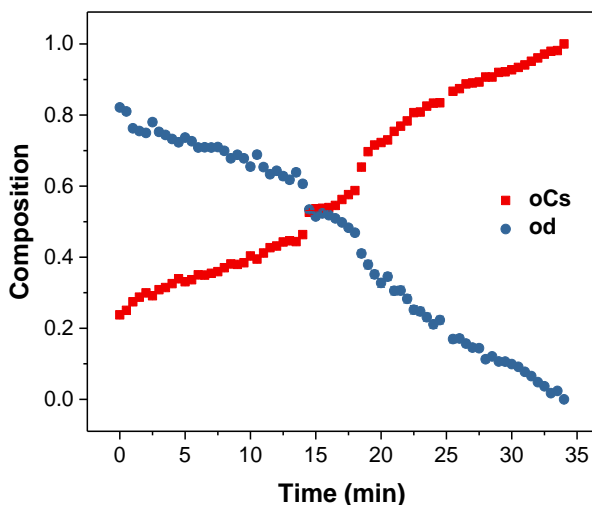


Figure 4.29. Composition plot of spectra during SHF-61o-CHCl<sub>3</sub> resolvation experiment.

Figure 4.29 shows a decrease of the initially superior *od* state and an increase of the *oCs* state to maximum with time. Due to repositioning of the crystal at ca. 15 minutes during this resolvation experiments, the analysis of the spectral composition plot is less straightforward, however does show a clear changeover between the *od* and *oCs* states.

#### 4.3.3.4 Resolvation of SHF-61o with CyP

Figure 4.30 shows a photograph of the particular SHF-61o crystal resolvated during this experiment, which is ca. 50 x 40 µm.

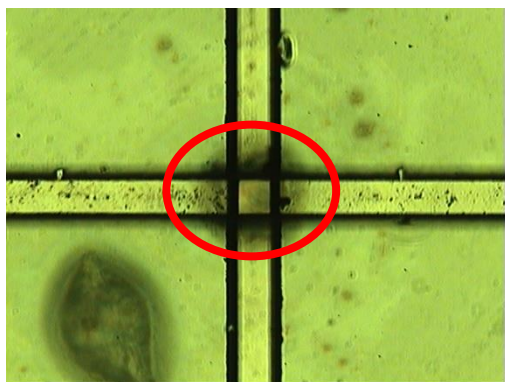


Figure 4.30. Photograph of SHF-61o measured in this experiment (indicated), collected *in situ* on the IR microscope. Aperture size is 20 x 20 µm.

The resolvation of SHF-61 $\bullet$  with CyP resulted in the peak position and area changes shown in Table 4.6. These shifts are significantly smaller than those observed following resolvation with DMF, likely due to weaker hydrogen-bonding interactions with the NH<sub>2</sub> group.

Table 4.6. Changes in  $\nu(\text{NH})$  bands after resolvation of SHF-61 $\bullet$  with CyP.

Framework	$\nu_{\text{initial}}$ (cm <sup>-1</sup> )	$\nu_{\text{final}}$ (cm <sup>-1</sup> )	$\Delta\nu$ (cm <sup>-1</sup> )	$A_{\text{initial}}$	$A_{\text{final}}$	$\Delta A$
SHF-61 $\bullet$ -CyP	3485	3481	-4	84.6	90.4	+5.8
	3368	3366	-2	28.6	27.0	-1.6

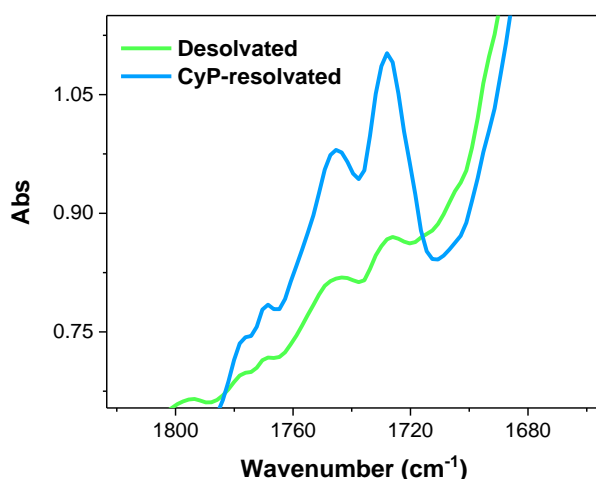


Figure 4.31. (Left) Infrared spectra of CyP  $\nu(\text{CO})$  stretches (1750–1710 cm<sup>-1</sup>) in SHF-61 $\bullet$  (green) and SHF-61 $\bullet$ -CyP (blue).

Figure 4.31 shows the IR spectrum of SHF-61 $\bullet$  and SHF-61 $\bullet$ -CyP (green and blue respectively), showing two peaks growing in intensity with resolvation. Peak integrals were calculated by peak integration, and not peak area fitting, as the fit would not converge. Baseline correction was applied to all spectra and is illustrated in Figure 4.32.

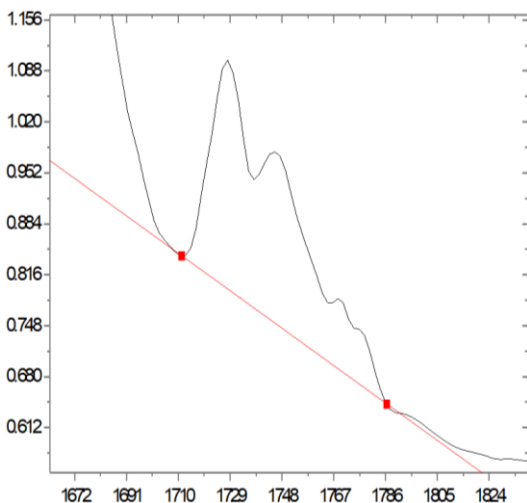


Figure 4.32. Baseline applied to integration process of CyP  $\nu(\text{CO})$  stretches during resolvation of SHF-61o with CyP.

The peak integrals of these bands ( $1727$  and  $1744\text{ cm}^{-1}$ ) are shown in Figure 4.33, with accompanying biexponential fit curves. These increases appear to be a two-component process.

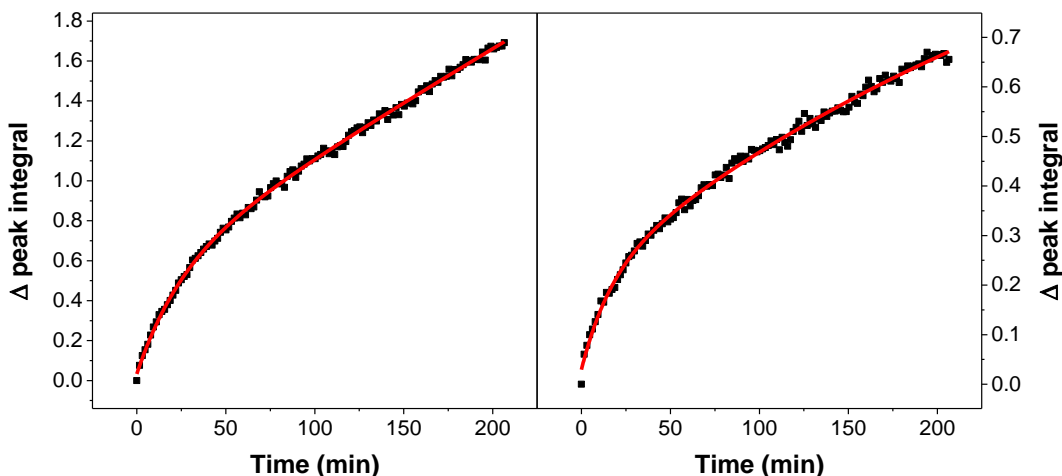


Figure 4.33. (Left)  $1727\text{ cm}^{-1}$  and (right)  $1744\text{ cm}^{-1}$  CyP  $\nu(\text{CO})$  stretches fit to biexponential curve fits (red) during SHF-61o CyP-resolvation.

To investigate the changes in the  $\nu(\text{NH})$  region of the spectrum, composite spectral modelling was employed. Two model spectra were required to fit the CyP-resolvation of SHF-61o; open-pore, CyP solvated (*oCys*) and open-pore, desolvated (*od*).

The model spectra were taken from the following points during the experiments;

- oCys – after resolvation of SHF-61<sup>o</sup> with CyP
- od – after SHF-61-CHCl<sub>3</sub> desolvation experiment

Figure 4.34 shows the composition plot for CyP resolvation of SHF-61<sup>o</sup> spectra.

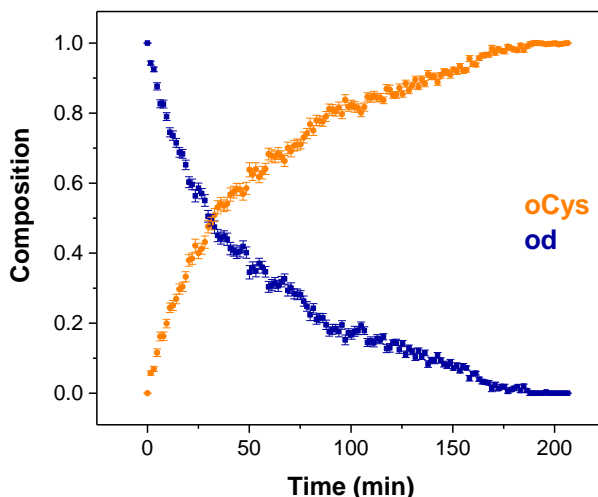


Figure 4.34. Composition plot of spectra during SHF-61<sup>o</sup>-CyP resolvation experiment.

The composition plot in Figure 4.34 shows a switch of states between oCys and od. Biexponential fit curves for the above composition plots are shown in Figure 4.35.

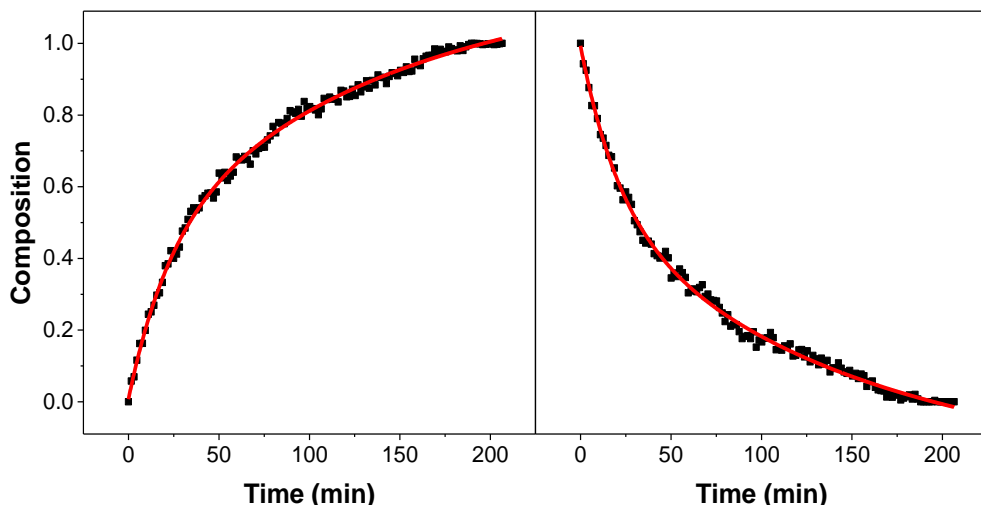


Figure 4.35. (Left) oCys and (right) od model composition fit to biexponential curves (red) during SHF-61<sup>o</sup> CyP-resolvation.

Although biexponential curves were fit successfully to all plots shown in Figures 4.33 and 4.35, the curves fit to the model composition plots (Figure 4.35) do not clearly possess two components. In contrast, the biexponential curves fit to the CyP  $\nu(\text{CO})$  stretches (Figure 4.33) do imply two-component processes, which would suggest CyP–NH<sub>2</sub> interaction saturation followed by pore filling. This could suggest that the interactions between guest CyP and NH<sub>2</sub> groups are not as strong as those observed for DMF and CHCl<sub>3</sub>, and hence do not instigate as much of a change in the NH region, or that CyP–NH<sub>2</sub> interactions and subsequent pore filling processes are not as strictly defined in this system.

### 4.3.3.5 Comparison of results from resolvation experiments

The solvent resolvation experiments carried out as the basis of discussion in Section 4.3.3 resulted in a variety of peak position and area changes of the  $\nu(\text{NH})$  bands. These changes depended on the solvent used for resolvation and the pore structure (open or closed) that was being resolvated. Peak changes for all resolvation experiments are shown below in Table 4.7.

*Table 4.7. Changes in  $\nu(\text{NH})$  bands (top) after resolvation experiments (April 2018) and (bottom) after desolvation experiments (September 2016).*

Framework	$\nu_{\text{initial}}$ (cm $^{-1}$ )	$\nu_{\text{final}}$ (cm $^{-1}$ )	$\Delta\nu$ (cm $^{-1}$ )	$A_{\text{initial}}$	$A_{\text{final}}$	$\Delta A$
SHF-61 $\text{c}$ -DMF	3484	3467	-17	41.0	55.6	+14.6
	3369	3356	-13	21.5	11.8	-9.7
SHF-61 $\text{o}$ -DMF	3472	3458	-14	30.3	38.2	+7.9
	3360	3349	-11	26.5	24.7	-1.8
SHF-61 $\text{o}$ -CHCl $_3$	3486	3485	-1	110.2	109.9	-0.3
	3372	3372	0	116.2	115.1	-1.1
SHF-61 $\text{o}$ -CyP	3485	3481	-4	84.6	90.4	+5.8
	3368	3366	-2	28.6	27.0	-1.6
SHF-61-DMF desolvation	3465	3480	+15	69.7	40.0	-29.7
	3352	3368	+16	3.6	15.0	+11.4
SHF-61-CHCl $_3$ desolvation	3475	3485	+10	89.4	79.8	-9.6
	3363	3371	+8	72.4	54.6	-17.8

The largest peak shifts were observed following resolvation with DMF; 17 and 13 cm<sup>-1</sup> shifts to lower energy for the higher and lower energy bands respectively following resolvation of the closed-pore form, and 14 and 11 cm<sup>-1</sup> shifts for the open-pore form. This indicates that interactions between DMF and the NH<sub>2</sub> groups are the stronger than for CHCl<sub>3</sub> and CyP.

Larger peak changes are seen in both peak position and area for the closed-pore structure than the open-pore structure following resolvation of structures with DMF. This is consistent with the structural reopening of the pore upon DMF resolvation of the closed form, as the environment surrounding the NH<sub>2</sub> groups changes drastically, which is reflected in the peak properties.

As mentioned earlier, the peak properties following resolvation did not return to the original, pre-desolvation values. This would indicate that the solvent-switching behaviour of the SHF-61 pore is not binary, and the degree of solvation of the material contributes to the position of the v(NH) bands. Note, that each of the de/resolvation experiments detailed in Table 4.7 were performed independently, and over two visits to DLS B22 MIRIAM (September 2016 and April 2018) and hence small variations in peak position and area (specifically between SHF-61c and SHF-61-DMF, and SHF-61o and SHF-61-CHCl<sub>3</sub>) are anticipated. An additional factor affecting the extent of positional and area shift is residual water, present within the framework pre-desolvation and in the solvent used for resolvation. Trace water will affect the extent of peak change, due to the strong hydrogen-bonding character of water. The amount of water present in both scenarios is unknown and hence the impact it has cannot easily be quantified. This has also been a significant challenge in the crystallographic experiments on this material.

#### 4.3.4 Desolvation of resolvated SHF-61o

After resolvation of SHF-61o with CHCl<sub>3</sub>, CyP or DMF, samples were subsequently desolvated at 120 °C to examine the reversibility of these processes. Spectra were collected every 19 seconds in all desolvation experiments. All data discussed in this section was collected during the DLS B22 MIRIAM visit in April 2018.

All peak positions and areas for desolvation of resolution experiments were deconvoluted using peak area fitting in Origin 2017, as described in Sections 1.8.1 and 4.3.1.1. Similarly to the previously discussed de/resolvation experiments, spectra were split into a higher energy (3865–2617 cm<sup>-1</sup>) and lower energy (1236–700 cm<sup>-1</sup> for experiments involving CHCl<sub>3</sub> and CyP; 1706–700 cm<sup>-1</sup> for experiments involving DMF) region of the spectrum and bands was fit to a Lorentzian peak shape. v(NH) and respective solvent band changes are discussed hereafter.

##### 4.3.4.1 Desolvation of SHF-61o-DMF

Table 4.8 shows the peak changes observed following desolvation of SHF-61o-DMF, and the peak changes observed after original desolvation of SHF-61-DMF. Original desolvation of SHF-61-DMF, carried out in September 2016 at DLS B22 MIRIAM, led to the formation of closed-pore SHF-61c. Surprisingly, desolvation of SHF-61o-DMF, in April 2018, did not reproduce the same large peak position and area shifts, as highlighted in Table 4.8. Reasoning for this result is discussed later in this section.

Table 4.8. Changes in  $\nu(\text{NH})$  bands (top) after desolvation of SHF-61o-DMF (April 2018) and (bottom) after desolvation of SHF-61-DMF (September 2016).

Framework	$\nu_{\text{initial}}$ (cm $^{-1}$ )	$\nu_{\text{final}}$ (cm $^{-1}$ )	$\Delta\nu$ (cm $^{-1}$ )	$A_{\text{initial}}$	$A_{\text{final}}$	$\Delta A$
SHF-61o-DMF	3472	3478	+6	32.9	30.7	-2.2
	3361	3367	+6	24.9	24.4	-0.5
SHF-61-DMF	3465	3480	+15	69.7	40.0	-29.7
	3352	3368	+16	3.6	15.0	+11.4

Figure 4.36 below shows the peak area change of the 1660 cm $^{-1}$  DMF  $\nu(\text{CO})$  carbonyl band during desolvation experiments of SHF-61o-DMF, with the associated biexponential curve fit shown in red.

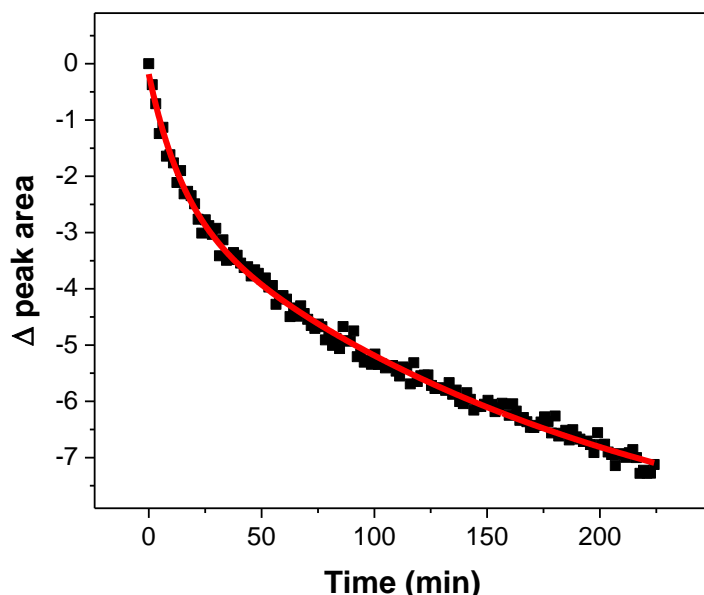


Figure 4.36. Peak area of 1660 cm $^{-1}$  DMF  $\nu(\text{CO})$  stretch fit to a biexponential curve (red) during SHF-61o-DMF desolvation experiments.

The fit curve suggests a two-component process. The first process is likely desorption of the weakly-bound DMF in the framework pores, whilst the longer, slower process is likely the cessation of stronger DMF–NH interactions.

Composite spectral modelling was used to examine the states present during the desolvation experiments. The model spectra were taken from the following points during experiments;

- $oDs$  – before SHF-61 **o**-DMF desolvation experiment
- $od$  – end of SHF-61 **o**-DMF desolvation experiment

The composite modelling plot is shown below in Figure 4.37.

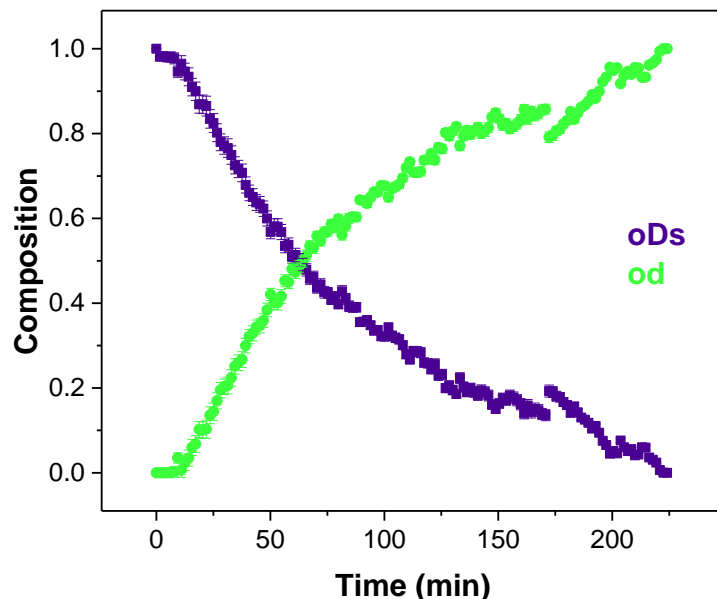


Figure 4.37. Composition plot of spectra during desolvation of SHF-61 **o**-DMF.

The above plot in Figure 4.37 indicates a switch of state maximum, where the open-pore, DMF-solvated ( $oDs$ ) state progresses from maximum to zero, and *vice versa* for the open-pore, desolvated ( $od$ ) state. There is no experimental reasoning for the small jump in the data at around 175 minutes but it is consistent with the jumps seen in other examples when the crystal has shifted in the beam. Biexponential curve fits of the composite modelling plots are shown in Figure 4.38.

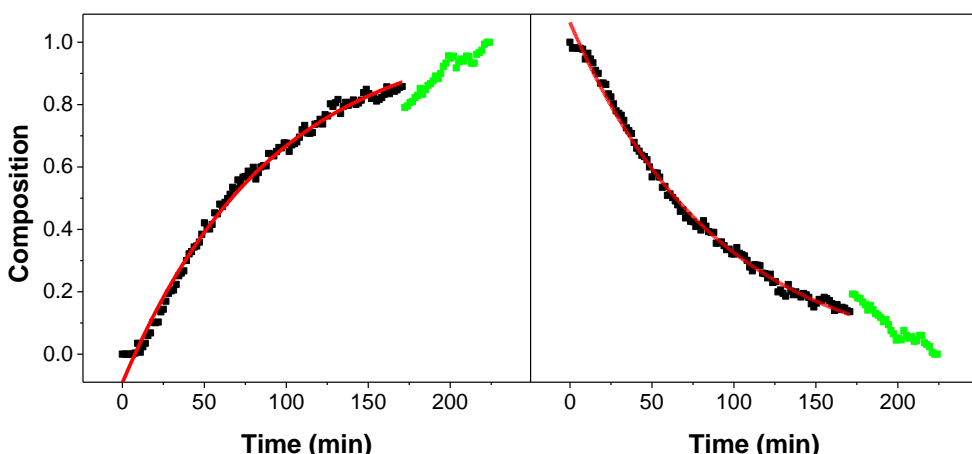


Figure 4.38. Biexponential curve fits (red) of (left) od and (right) oDs model composition during desolvation of SHF-61o-DMF.

Data marked in green was excluded from the fitting process.

Given the expectation of various states present in systems involving the desolvation from DMF, the presence of only two states (and small accompanying error bars) suggests that pore closure does not occur in this experiment. This observation is concurrent with the small peak position and area shifts, compared to the initial SHF-61-DMF desolvation data collected in September 2016. The exponential curve fits do not overwhelmingly suggest a two-component desolvation process, suggesting that the desolvation process of DMF-resolved SHF-61 is not identical to the desolvation of parent SHF-61-DMF. We note that this measurement was performed on a different crystal to the first, and hence crystal size effects cannot be ruled out.<sup>28</sup>

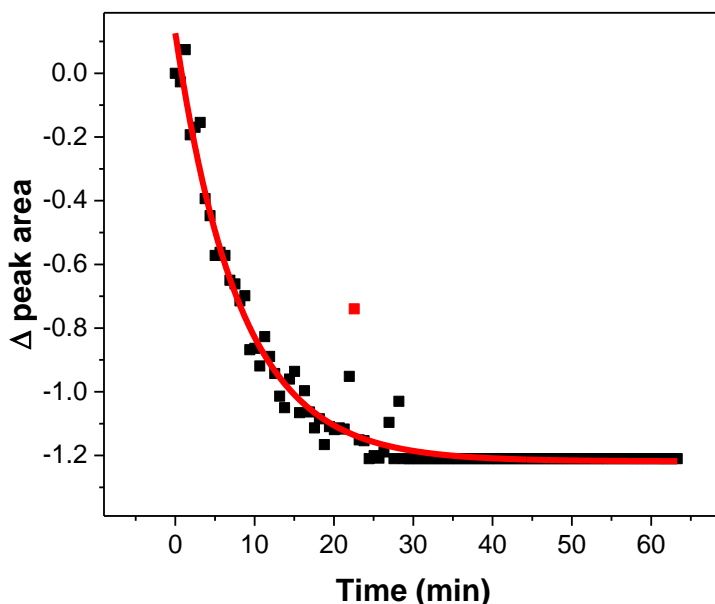
#### 4.3.4.2 Desolvation of SHF-61o-CHCl<sub>3</sub>

Table 4.9 shows the peak changes observed following desolvation of SHF-61o-CHCl<sub>3</sub> in April 2018, and the peak changes observed after original desolvation of SHF-61-CHCl<sub>3</sub> to form SHF-61o in September 2016. Similarly to the desolvation of SHF-61o-DMF discussed earlier in this section, desolvation of SHF-61o-CHCl<sub>3</sub> did not reproduce the same peak shift or area change, as highlighted in Table 4.9.

*Table 4.9. Changes in  $\nu(\text{NH})$  bands (top) after desolvation of SHF-61o-DMF (April 2018) and (bottom) after desolvation of SHF-61-DMF (September 2016).*

Framework	$\nu_{\text{initial}}$ (cm $^{-1}$ )	$\nu_{\text{final}}$ (cm $^{-1}$ )	$\Delta\nu$ (cm $^{-1}$ )	$A_{\text{initial}}$	$A_{\text{final}}$	$\Delta A$
SHF-61o-CHCl <sub>3</sub>	3486	3491	+5	75.6	78.4	+2.8
	3371	3374	+3	16.2	15.5	-0.7
SHF-61-CHCl <sub>3</sub>	3475	3485	+10	89.4	79.8	-9.6
	3363	3371	+8	72.4	54.6	-17.8

Figure 4.39 below shows the change in peak area and associated biexponential fit of the 1220 cm $^{-1}$  CHCl<sub>3</sub>  $\delta(\text{CH})$  bend during the desolvation of SHF-61o-CHCl<sub>3</sub>. The two-component decrease in peak area can be seen throughout the course of the experiment. The first 15 minutes of the desolvation process is likely attributable to the CHCl<sub>3</sub> in the pore, while the second process is the loss of CHCl<sub>3</sub>–NH<sub>2</sub> interactions. Note, that a boundary was applied to prevent any peak parameters falling below zero, and hence further changes in the peak area were not observed after ca. 22 minutes.



*Figure 4.39. Biexponential curve fit (red) of 1220 cm $^{-1}$  CHCl<sub>3</sub>  $\delta(\text{CH})$  bend peak integral during SHF-61o-CHCl<sub>3</sub> desolvation experiments.  
The point marked in red was excluded from fitting.*

Composite spectral modelling was used to examine the states present during the desolvation experiments. The model spectra were taken from the following points during experiments;

*oCs* – before SHF-61 *o*-DMF desolvation experiment  
*od* – end of SHF-61 *o*-CHCl<sub>3</sub> desolvation experiment

The composite modelling plot is shown below in Figure 4.40.

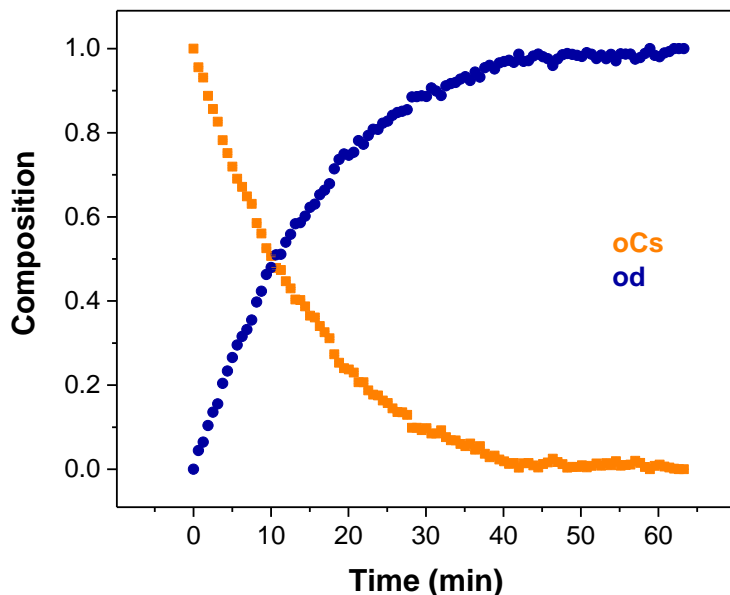


Figure 4.40. Composition plot of spectra during desolvation of SHF-61 *o*-CHCl<sub>3</sub>.

Figure 4.40 shows an exponential increase in the open-pore, desolvated (*od*) model as the open-pore, CHCl<sub>3</sub>-solvated (*oCs*) model decreases. The decrease in *oCs* matches the loss of CHCl<sub>3</sub> observed in Figure 4.39. Biexponential curves are fit to these composition plots in Figure 4.41 overleaf.

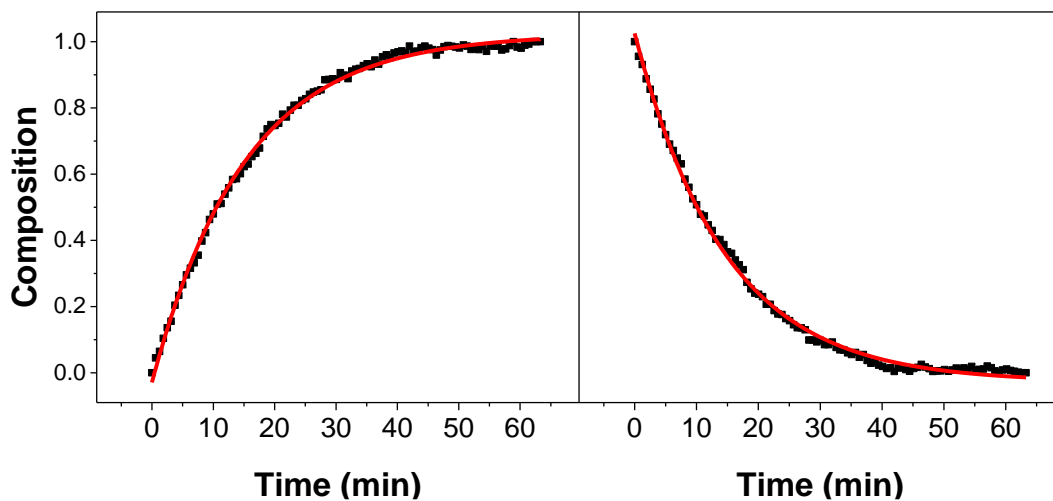


Figure 4.41. Biexponential curve fits (red) of oCs (left) and od (right) model composition plots during desolvation of **SHF-61o-CHCl<sub>3</sub>**.

The biexponential fit curves for the model composition plots indicate an initial process, which completes at ca. 25 minutes, and likely corresponds to the loss of CHCl<sub>3</sub> from the framework pore. The next component reflects a slower process, which is likely the loss of CHCl<sub>3</sub>-NH<sub>2</sub> interactions.

#### 4.3.4.3 Desolvation of SHF-61o-CyP

The changes in peak position and peak area for the  $\nu(\text{NH})$  bands following desolvation of SHF-61o-CyP are shown below in Table 4.10.

Table 4.10. Changes in  $\nu(\text{NH})$  bands (top) after desolvation of SHF-61o-DMF (April 2018) and (bottom) after desolvation of SHF-61-DMF (September 2016).

Framework	$\nu_{\text{initial}}$ (cm <sup>-1</sup> )	$\nu_{\text{final}}$ (cm <sup>-1</sup> )	$\Delta\nu$ (cm <sup>-1</sup> )	$A_{\text{initial}}$	$A_{\text{final}}$	$\Delta A$
SHF-61o-CyP	3480.3	3480.6	+0.3	83.1	78.1	-5.0
	3365.1	3366.2	+1.1	26.3	27.5	+1.2

On comparison to the changes observed for desolvation of SHF-61 $\bullet$ -DMF and SHF-61 $\bullet$ -CHCl<sub>3</sub>, the changes seen upon desolvation of the CyP structure are significantly smaller. This would suggest that cyclopentanone is a significantly weaker H-bond acceptor than CHCl<sub>3</sub> and DMF; no directly comparable literature values for this could be found. Figure 4.42 shows the peak area changes of the 1727 and 1740 cm<sup>-1</sup> CyP carbonyl bands during the desolvation of SHF-61 $\bullet$ -CyP, with accompanying biexponential curve fits.

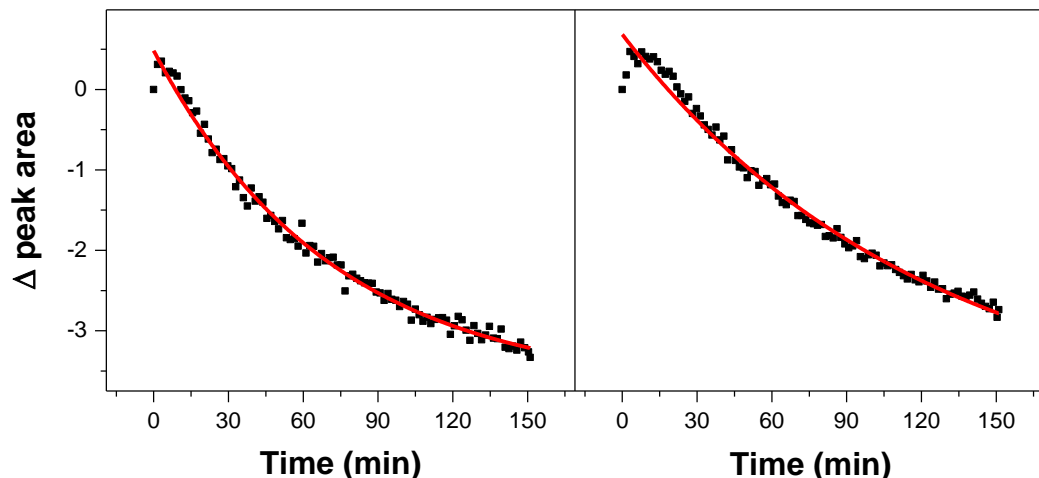


Figure 4.42. Biexponential curve fits (red) of (left) 1727 cm<sup>-1</sup> and (right) 1744 cm<sup>-1</sup> CyP  $\nu(\text{CO})$  stretches during desolvation of SHF-61 $\bullet$  CyP.

Figure 4.42 shows decrease of both the 1727 and 1744 cm<sup>-1</sup> CyP  $\nu(\text{CO})$  stretches during the desolvation experiment, however the curves suggest a single component process.

Composite spectral modelling was used to examine the states present during the desolvation experiments. The model spectra were taken from the following points during experiments;

*oCys* – before SHF-61 $\bullet$ -DMF desolvation experiment  
*od* – end of SHF-61 $\bullet$ -CHCl<sub>3</sub> desolvation experiment

The composite modelling plot is shown overleaf in Figure 4.43.

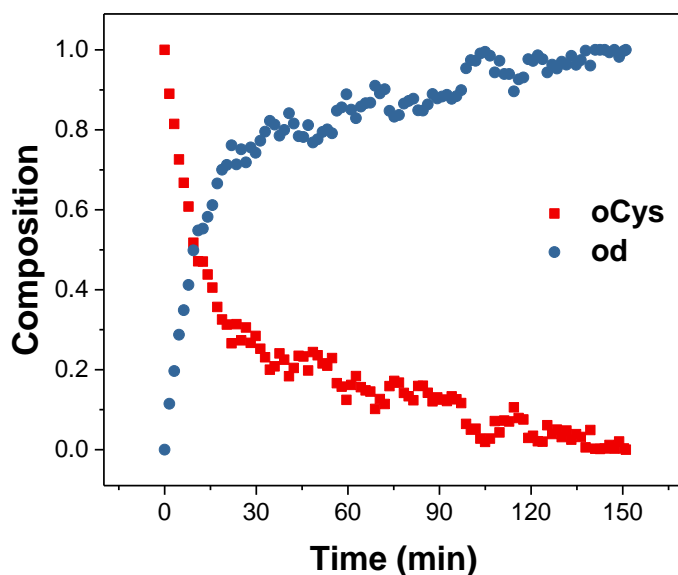


Figure 4.43. Composition plot of spectra during desolvation of SHF-61o-CyP.

Figure 4.43 shows a rise of open-pore, desolvated (*od*) state, and vice versa for the open-pore, CyP-solvated (*oCys*) state. Biexponential curves were fit to these plots, and are shown in Figure 4.44.

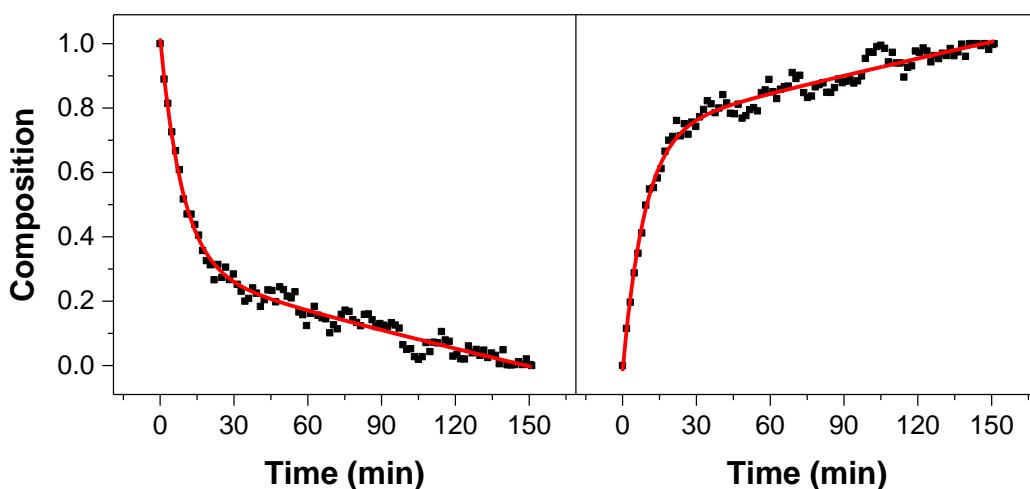


Figure 4.44. Biexponential curve fits (red) of *oCys* (left) and *od* (right) model composition during desolvation of SHF-61o CyP.

The fit curves for these plots clearly indicate two-component processes. The first 20 minutes of the desolvation process likely indicates the desolvation of CyP from the pore. This process occurred significantly faster than the second component of the desolvation process, which likely reflects the loss of CyP–NH<sub>2</sub> interactions throughout the structure.

#### 4.3.4.4 Comparison of results from desolvation of resolvated SHF-61<sup>o</sup> experiments

Peak shifts and area changes following the desolvation of CHCl<sub>3</sub>--, CyP- and DMF-resolvated SHF-61<sup>o</sup> were significantly smaller than changes observed following desolvation of SHF-61-CHCl<sub>3</sub> in September 2016 (Table 4.11).

*Table 4.11. Changes in  $\nu(\text{NH})$  bands after desolvation of resolvated SHF-61<sup>o</sup> materials.*

Framework	$\nu_{\text{initial}}$ (cm <sup>-1</sup> )	$\nu_{\text{final}}$ (cm <sup>-1</sup> )	$\Delta\nu$ (cm <sup>-1</sup> )	$A_{\text{initial}}$	$A_{\text{final}}$	$\Delta A$
SHF-61 <sup>o</sup> -DMF	3472.0	3478.4	+6.4	32.9	30.7	-2.2
	3360.6	3366.6	+6.0	24.9	24.4	-0.5
SHF-61 <sup>o</sup> -CHCl <sub>3</sub>	3486.3	3490.5	+4.2	75.6	78.4	+2.8
	3370.7	3374.0	+3.3	16.2	15.5	-0.7
SHF-61 <sup>o</sup> -CyP	3480.3	3480.6	+0.3	83.1	78.1	-5.0
	3365.1	3366.2	+1.1	26.3	27.5	+1.2
<hr/>						
SHF-61-CHCl <sub>3</sub> desolvation	3475	3485	+10	89.4	79.8	-9.6
	3363	3371	+8	72.4	54.6	-17.8

There are two possible explanations for this. Firstly, resolvation of the framework with DMF or CyP has a sustained effect on the open-pore framework, and subsequent desolvation of DMF- and CyP-resolvated frameworks did not return the material to the same state observed in desolvated SHF-61-CHCl<sub>3</sub>. Secondly, the framework may not be robust enough to withstand multiple de/resolvations, and reduced impact of desolvation is reflective of material fatigue. Multiple solvent cycling of this material was not studied by Carrington *et al.*<sup>23</sup>

Resolvation experiments, discussed in Section 4.2.2, saw similar biexponential fitting results from  $\nu(\text{NH})$  band composite spectral modelling and solvent band area/integration, clearly corroborating the role solvents play in  $\nu(\text{NH})$  shifts. Unfortunately, desolvation of resolvated SHF-61<sup>o</sup> experiments did not corroborate the solvation mechanism as clearly as the resolvation experiments.

Finally, crystal size effects have been seen to play a significant role in the changes of other flexible frameworks.<sup>28</sup> These have not been controlled here, which is why quantitative assessments of the rate of change have not been discussed further.

### 4.3.5 CO<sub>2</sub> loading in SHF-61

Our collaborators, Carrington *et al.*, reported interesting pore behaviour upon CO<sub>2</sub> loading of the material. Uptake of CO<sub>2</sub> in the closed-pore structure of activated SHF-61c did not induce pore opening. This resulted in significantly lower CO<sub>2</sub> uptake for desolvated SHF-61c (298 K, 1.46 mmol g<sup>-1</sup> at 4.5 bar; 2.43 mmol g<sup>-1</sup> at 18 bar) than for desolvated SHF-61o (298 K, 4.45 mmol g<sup>-1</sup> at 4.5 bar; 6.5 mmol g<sup>-1</sup> at 19.5 bar). CO<sub>2</sub> isotherm data collected as part of the initial 2017 study by Carrington *et al.* is shown in Figure 4.45.

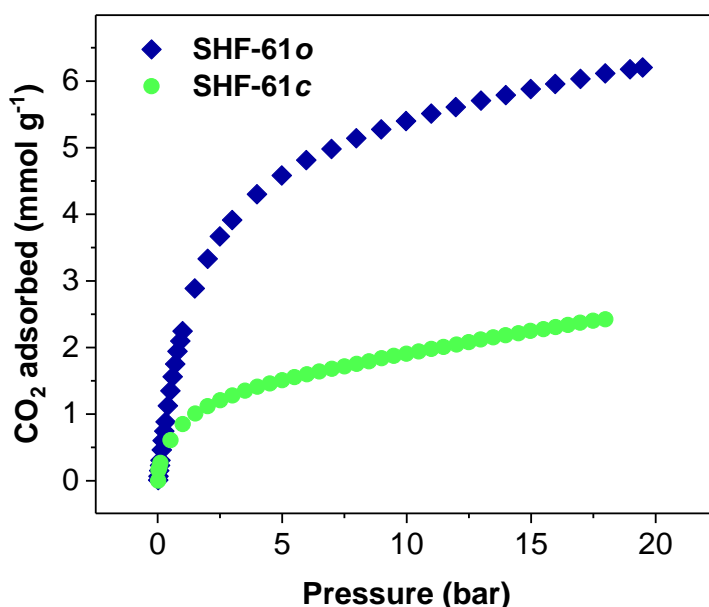


Figure 4.45. Gravimetric CO<sub>2</sub> isotherms at 298 K of desolvated SHF-61o (blue) and SHF-61c (green).

CO<sub>2</sub> loading of single crystals of SHF-61-CHCl<sub>3</sub> and SHF-61-DMF was carried out in a Linkam FTIR600 stage, described and pictured in Section 1.6 and Figure 1.13 (pp.13) respectively, and monitored by IR. Pre-dried CO<sub>2</sub> and N<sub>2</sub> gases were delivered to activated SHF-61 single crystals *via* separate mass flow controllers and mixed in a single inlet tube. Specific partial pressures of CO<sub>2</sub> (0.2, 0.4, 0.6, 0.8 and 1.0 bar) were delivered and at each partial pressure a new background and sample spectrum collected after allowing the cell to equilibrate for 10 minutes.

#### 4.3.5.1 Spectral analysis by peak fitting

The  $\nu(\text{NH})$  bands shift as  $\text{CO}_2$  is adsorbed into the framework, as shown for SHF-61- $\text{CHCl}_3$  in Figure 4.46.

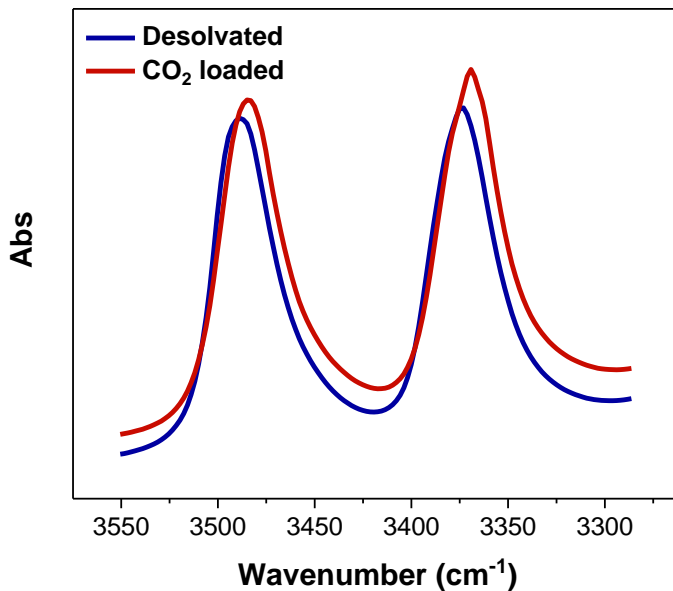


Figure 4.46. IR spectrum of desolvated SHF-61- $\text{CHCl}_3$  (blue) and  $\text{CO}_2$ -loaded SHF-61- $\text{CHCl}_3$ .

The effect of  $\text{CO}_2$  loading on  $\nu(\text{NH})$  was investigated by peak fitting analysis. Figure 4.47 shows the position of each  $\nu(\text{NH})$  stretch at different partial pressures of  $\text{CO}_2$ . Table 4.12 contains the peak position and area changes following  $\text{CO}_2$  loading.

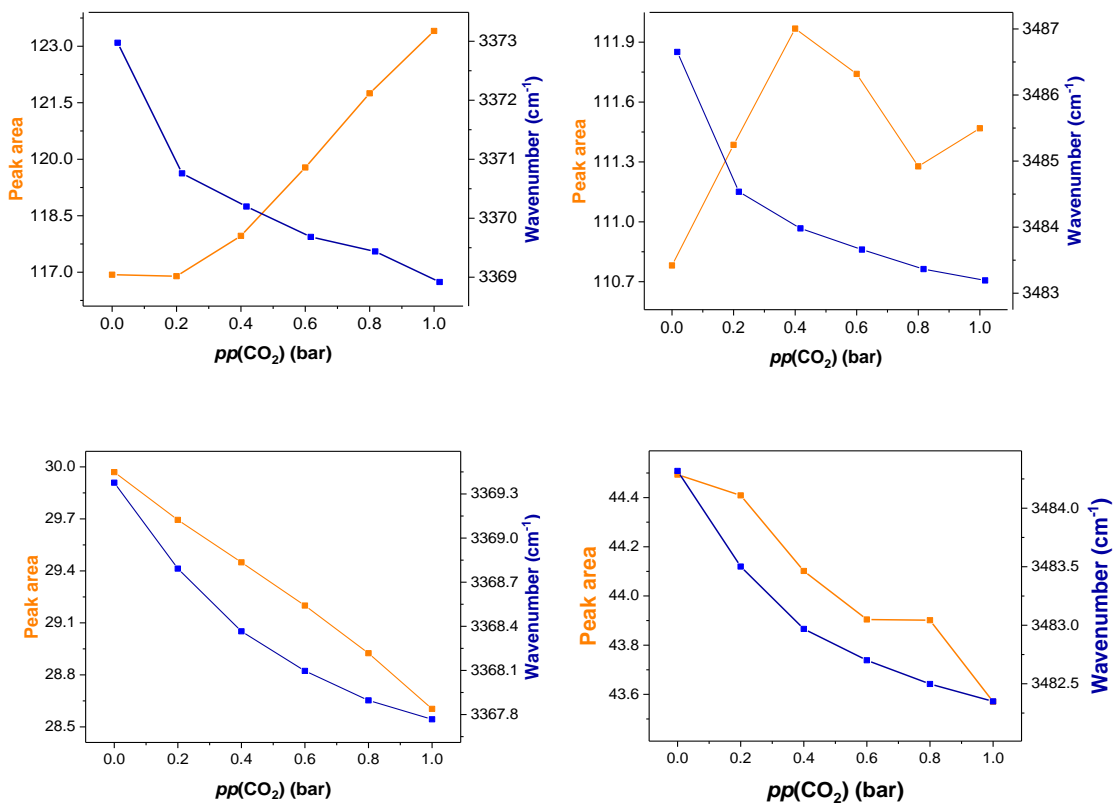


Figure 4.47. Peak area (orange) and position (blue) changes of SHF-61o (top) and SHF-61c (bottom) higher energy (left) and lower energy (right)  $\nu(\text{NH})$  following  $\text{CO}_2$  sorption.

The positional shift of both stretches is greater in SHF-61o than SHF-61c, where total peak shifts (for both higher and lower energy bands) to lower energy of 7.5 and 3.6  $\text{cm}^{-1}$  were observed for SHF-61o and SHF-61c respectively. The initial positions of the desolvated  $\nu(\text{NH})$  bands in SHF-61o are at a higher wavenumber than in the (closed) SHF-61-DMF desolvated framework.

*Table 4.12. Changes in  $\nu(\text{NH})$  bands in SHF-61o (top) and SHF-61c (bottom) after  $\text{CO}_2$  loading.*

Framework	$\nu_{\text{initial}}$ ( $\text{cm}^{-1}$ )	$\nu_{\text{final}}$ ( $\text{cm}^{-1}$ )	$\Delta\nu$ ( $\text{cm}^{-1}$ )	$A_{\text{initial}}$	$A_{\text{final}}$	$\Delta A$
SHF-61o	3487	3483	-4	110.8	111.5	+0.7
	3373	3369	-4	116.9	123.4	+6.5
SHF-61c	3484	3482	-2	44.5	43.6	-0.9
	3369	3368	-1	30.0	28.6	-1.4

Crystallographic experiments by the Brammer group highlighted that adsorption of  $\text{CO}_2$  up to 1 bar into the closed-pore structure did not induce opening of the pore. It is therefore surprising that the  $\nu(\text{NH})$  band positions of the  $\text{CO}_2$ -loaded frameworks are similar in both cases. The greater shift for  $\nu(\text{NH})$  in SHF-61o on adsorption of  $\text{CO}_2$  is therefore a consequence of both the increased amount of  $\text{CO}_2$  adsorbed by this material compared to the closed-pore structure and the initially higher energy  $\nu(\text{NH})$  band positions.

In both SHF-61o and SHF-61c  $\text{CO}_2$  uptake experiments, the spectra show increasing  $\text{CO}_2$  combination bands as the partial pressure rises. These are highlighted in the infrared spectrum of 1 bar  $\text{CO}_2$ -loaded SHF-61o, shown in Figure 4.48. These combination bands have been observed in other studies and are visible in these spectra at  $3693$  and  $3589 \text{ cm}^{-1}$ .<sup>29–31</sup> These bands are intrinsically weak and, due to overlap with the amine bands and adjacent OH stretches, peak fitting analysis was difficult. Therefore, they were investigated using simple peak integration.

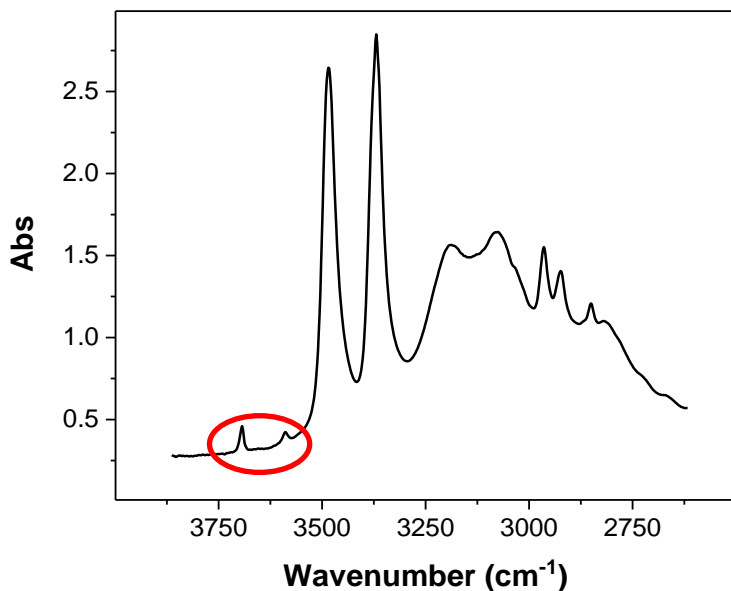


Figure 4.48. Infrared spectrum (3700–2500 cm<sup>-1</sup>) of CO<sub>2</sub>-loaded SHF-61-CHCl<sub>3</sub>, with CO<sub>2</sub> combination bands indicated (red circle).

#### 4.3.5.2 Spectral analysis by peak integration

Prior to peak integration, the same baseline correction was applied to each spectrum, shown in Figure 4.49. The combination bands were then integrated between 3608.3–3567.8 and 3712.5–3672.0 cm<sup>-1</sup>, and the resulting integrals are shown in Figure 4.50.

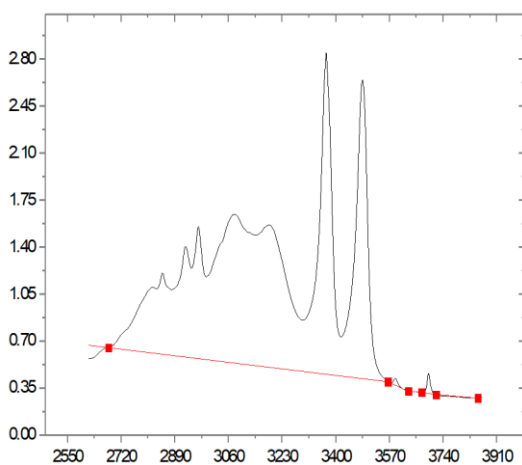


Figure 4.49. Baseline correction applied during peak integration of CO<sub>2</sub> combination bands in SHF-61-CHCl<sub>3</sub>.

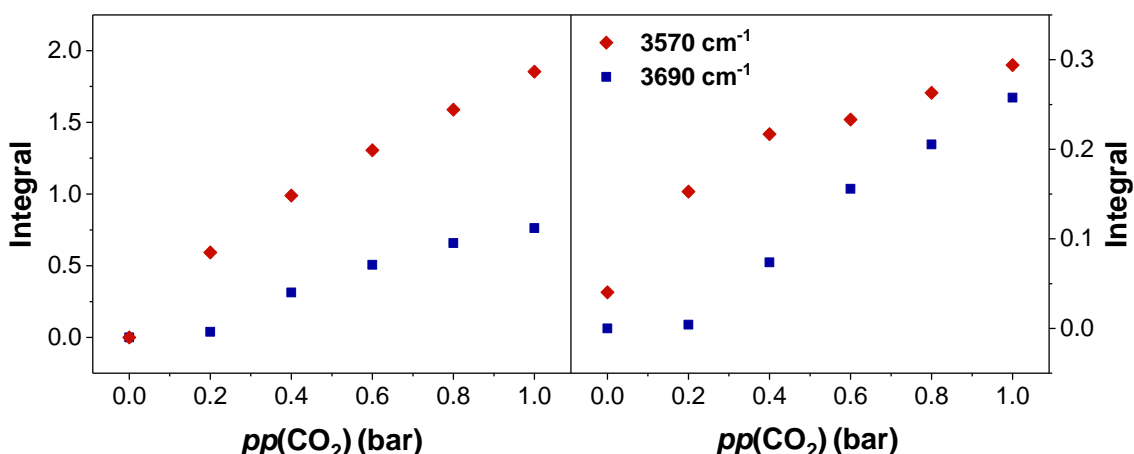


Figure 4.50. Plots of  $\text{CO}_2$  combination band integral in SHF-61- $\text{CHCl}_3$  (left) and SHF-61-DMF (right) at varying partial pressures of  $\text{CO}_2$ . Note, difference in y-axis scale.

When measured by gas sorption experiments, the uptake of  $\text{CO}_2$  in SHF-61- $\text{CHCl}_3$  is greater than in SHF-61-DMF due to the open pore structure. This is also clearly observed in the infrared peak integral plots of Figure 4.50, where the peak integrals for the  $\text{CO}_2$  combination bands are significantly larger in SHF-61- $\text{CHCl}_3$  than for SHF-61-DMF.

Figure 4.50 bears resemblance to the shape of a gas sorption isotherm. In a gas sorption experiment, in excess of 50 mg of sample is required, whereas in this experiment, we have successfully recreated the isotherm shape using a single crystal of material.

#### 4.3.5.3 Spectral analysis by composite modelling

Composite spectral modelling was used to examine the states present during  $\text{CO}_2$  loading. The model spectra were taken from the following points during experiments;

*od* – before  $\text{CO}_2$  loading into SHF-61 **o**

*oC* – after 1 bar  $\text{CO}_2$  loading into SHF-61 **o**

*cd* – before  $\text{CO}_2$  loading into SHF-61 **c**

*cC* – after 1 bar  $\text{CO}_2$  loading into SHF-61 **c**

Bounds were applied to each composite modelling analysis to prevent composition values being greater than 1 or less than 0. The composite modelling plots for SHF-61 $\text{o}$ -CO<sub>2</sub> and SHF-61 $\text{c}$ -CO<sub>2</sub> are shown below in Figure 4.51.

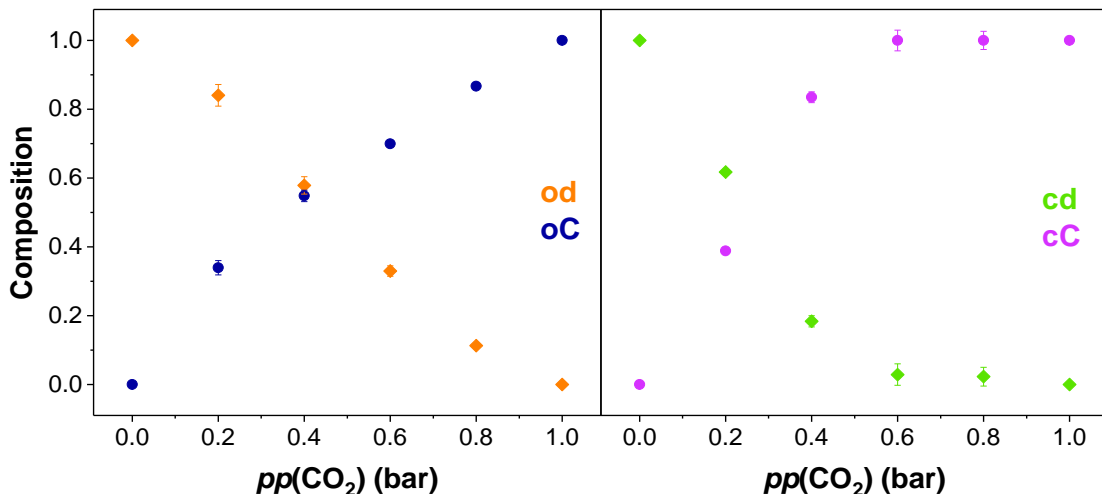


Figure 4.51. Composition plot of spectra during CO<sub>2</sub> uptake into (left) SHF-61 $\text{o}$  and (right) SHF-61 $\text{c}$ .

The change of spectral composition in SHF-61 $\text{c}$  was greater until 0.6 bar CO<sub>2</sub> than in SHF-61 $\text{o}$ , and the closed-pore, CO<sub>2</sub>-loaded state (cC) state reached a maximum at this pressure. The shape of the closed-pore, CO<sub>2</sub>-loaded state (cC) composition almost resembles the shape of a gas uptake isotherm. The change in spectral composition does not reach a plateau in SHF-61 $\text{o}$  as the partial pressure of CO<sub>2</sub> increases to 1 bar. This indicates that the closed-pore SHF-61 $\text{c}$  NH<sub>2</sub> bands interact with CO<sub>2</sub> and saturate at a lower pressure than required in SHF-61 $\text{o}$ , suggesting that the open-pore structure can accommodate more CO<sub>2</sub> at higher pressures up to 1 bar.

#### 4.3.5.4 Comparison of results from CO<sub>2</sub> uptake experiments

CO<sub>2</sub> uptake experiments in SHF-61 were successfully monitored by IR, where a similar, but not identical, peak profile was produced by the integration of the 3570 cm<sup>-1</sup> CO<sub>2</sub> combination band (Figure 4.52). This is particularly significant, as gas isotherms often require ca. 50 mg of material, whereas this isotherm shape has been reproduced from one single crystal of material.

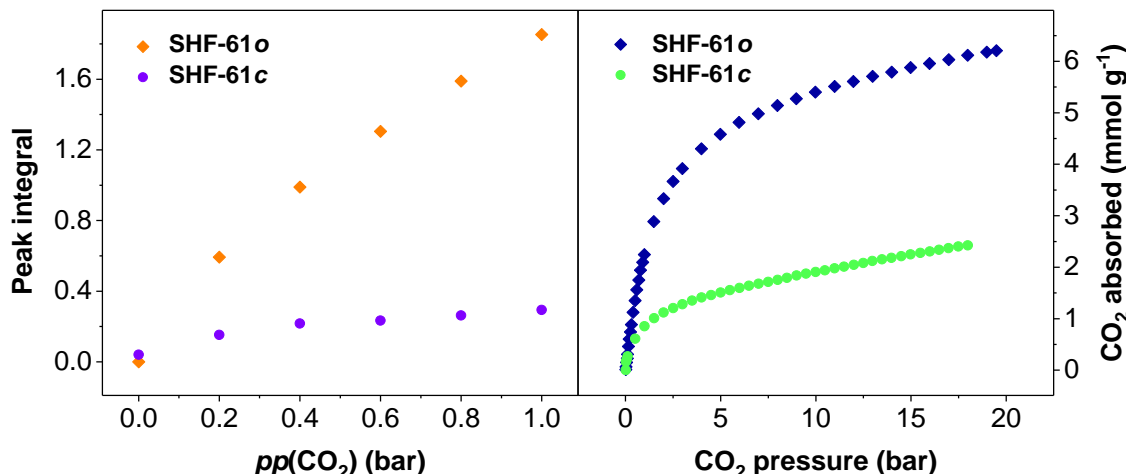


Figure 4.52. (Left) Peak integrals of 3570 cm<sup>-1</sup> peak during CO<sub>2</sub> uptake in SHF-61o (orange) and SHF-61c (purple). (Right) Volumetric CO<sub>2</sub> isotherms of SHF-61o (blue) and SHF-61c (green).

The peak profiles extracted from composite spectral modelling do not exactly match the gravimetric CO<sub>2</sub> uptake curves. These plots, and the small differences between the calculated peak integrals and gravimetric CO<sub>2</sub> uptake curves, indicate that although CO<sub>2</sub> is preferentially adsorbing at NH sites at low partial pressures, other binding sites must be present which contribute to the overall adsorption isotherm shape. This effect is observed to a greater extent in SHF-61o than SHF-61c due to the significantly increased CO<sub>2</sub> uptake properties of the open-pore material.

## 4.4 Conclusions and Outlook

The desolvation of SHF-61-CHCl<sub>3</sub> and SHF-61-DMF (to form open-pore SHF-61**o** and closed-pore SHF-61**c** respectively) saw greater position shifts in the  $\nu(\text{NH})$  peaks on desolvation from DMF than CHCl<sub>3</sub>. This was attributed to greater strengthening of the N–H bond after desolvation from DMF than from CHCl<sub>3</sub>, due to the greater hydrogen-bond acceptor character of DMF. Composite spectral modelling of the desolvation process of SHF-61-DMF did not require the closed-pore, DMF-solvated (*cDs*) model. This suggested that the pore closure is instigated by localised desolvation of DMF and is not an effect of DMF removal from the whole system. As such, the removal of solvent from the material results in localised pore closure, whilst the remainder of DMF-solvated areas remain open. These experiments corroborate crystallographically observed data.

The investigation into the effect of resolvation of SHF-61**c** and SHF-61**o** with a variety of solvents did not return the materials to their exact pre-desolvated states. This could be due to two reasons. Firstly, the amount of solvent in the pre-desolvated materials saturated the structure, due to the sheer excess present during synthesis or post-synthetic solvent exchange. Alternatively, the interactions of residual water present in the resolvation solvents are having a significant impact on the position of the  $\nu(\text{NH})$  bands. The resolvation timescale also varies significantly, and this could be attributed to the difference in sizes for the crystals selected for each experiment. Further experiments would examine the resolvation of both SHF-61**o** and SHF-61**c** with other solvents, including iPrOH and H<sub>2</sub>O. This data will corroborate crystallographic experiments already undertaken and currently being processed by the Brammer group, and would expound upon how the pore breathing mechanism is affected by solvents with different hydrogen bond forming capabilities.

Subsequent desolvation of resolvated SHF-61 did not return peak positions to the peak positions originally observed following SHF-61-CHCl<sub>3</sub> desolvation. There are several possible explanations for this effect. Firstly, resolvation of SHF-61**o** with DMF and CyP may have had a sustained effect on the framework pores. The second reason for inconsistent peak positions could be framework

instability towards this repeated desolvation and resolvation cycling at elevated temperatures. Finally, the effects of crystal size variation and the role this plays is not yet understood.

Evaluation of the composite spectrum modelling following CO<sub>2</sub> uptake into SHF-61<sup>o</sup> and SHF-61<sup>c</sup> shows that SHF-61<sup>c</sup> preferentially adsorbs more CO<sub>2</sub> at lower partial pressures than the open-pore structure. Integration of CO<sub>2</sub> combination bands that grow with increasing CO<sub>2</sub> partial pressures nearly recreates an adsorption isotherm shape. This is particularly notable, as we have been able to recreate this adsorption isotherm from only one single crystal of material. Hence, we have obtained from our measurements both the overall CO<sub>2</sub> sorption isotherm and the site-specific adsorption isotherm of the amine-binding site in a single crystal. In order to examine the binding nature of different gases with the NH groups present, competitive gas binding experiments will be carried out using SO<sub>2</sub> as well as CO<sub>2</sub>, as explored by Savage *et al.* in 2016.<sup>32</sup>

Infrared microspectroscopy has proved a valuable technique to not only corroborate experimental data from crystallographic measurements, but also to identify pore and solvation states within the framework that could not be observed crystallographically. A combination of approaches to IR spectral analysis has identified changes in different spectral regions that are indicative of pore de- and resolvation. Collaboration with a computational chemist (currently underway) will identify particular areas of the infrared spectrum that can provide yet more data than the current regions that have been examined within the scope of this project.

## 4.5 Experimental

All SHF-61 materials were provided by Daniel Watkins, Elliot Carrington and Stephen Dodsworth of the Brammer Group at the University of Sheffield, with whom all this work was carried out in collaboration. Syntheses are described below. All reagents for these syntheses were purchased from Sigma-Aldrich or Alfa Aesar and were used without further purification. All infrared spectral analysis was done in partnership with Daniel Watkins. All solvents used for resolution experiments ( $\text{CHCl}_3$ , cyclopentanone, DMF,  $\text{H}_2\text{O}$  or  $\text{iPrOH}$ ) were anhydrous (except  $\text{H}_2\text{O}$ ) and sourced from Sigma-Aldrich. Elemental analyses were recorded on a Perkin Elmer 24000 CHNS/O Series II Elemental Analyser using combustion in pure oxygen.

*In situ* IR spectroscopic measurements were carried out on B22 MIRIAM beamline at the Diamond Light Source, using a Bruker Vertex 80 V FTIR interferometer with an internal broadband liquid  $\text{N}_2$ -cooled MCT detector coupled to a Hyperion 3000 microscope with x15 objective. A sample of SHF-61 was loaded on to a 0.5 x 16 mm ZnSe window and enclosed within a variable-temperature gas-tight Linkam FTIR600 cell fitted with 0.5 x 22 mm ZnSe top and bottom windows. Spectra were collected using aperture sizes of 20 x 20  $\mu\text{m}$ .  $\text{CO}_2$  and  $\text{N}_2$  gases were dried through zeolite filters between the gas cylinder and mass flow controller.

### 4.5.1 Synthesis of SHF-61 materials

#### **Synthesis of ( $\text{Me}_2\text{NH}_2$ )[In(ABDC)<sub>2</sub>]<sub>x</sub>DMF<sub>y</sub>H<sub>2</sub>O (SHF-61-DMF).<sup>23</sup>**

DMF (10 mL) was added to a mixture of  $\text{InCl}_3$  (0.1106 g, 0.5 mmol) and 2-aminoterephthalic acid ( $\text{H}_2\text{ABDC}$ ) (0.092 g, 0.5 mmol) and stirred until fully dissolved. The solution was then transferred to a 125 mL Teflon-lined steel autoclave and placed inside a temperature-controlled oven. The temperature was ramped to 130 °C at 1 °C/min and maintained for 24 h before cooling to room temperature at a rate of 0.1 °C/min. The solvent was decanted off and the brown crystals of SHF-61-DMF were transferred and stored in fresh DMF.

Yield: 46 %. Elemental analysis calculated for  $(\text{Me}_2\text{NH}_2)[\text{In}(\text{ABDC})_2] \cdot 1.75\text{DMF} \cdot 1.25\text{H}_2\text{O}$ : C, 41.70; H, 4.93; N, 9.94. Found C, 41.69; H, 4.93; N, 9.92

### **Solvent Exchange of $(\text{Me}_2\text{NH}_2)[\text{In}(\text{ABDC})_2]$ .**

Single crystals of SHF-61-DMF (50 mg, 0.01 mmol) were placed in anhydrous  $\text{CHCl}_3$  (1 mL) for 1-2 weeks.  $\text{CHCl}_3$  was replaced daily yielding  $\text{CHCl}_3$ -exchanged MOF **SHF-61-CHCl<sub>3</sub>**. Elemental analysis calculated for  $(\text{Me}_2\text{NH}_2)[\text{In}(\text{ABDC})_2] \cdot 1.25\text{CHCl}_3 \cdot 0.65\text{H}_2\text{O}$ : C, 34.00; H, 3.08; N, 6.18. Found C, 33.73; H, 3.08; N, 5.84

### **4.5.2 B22 MIRIAM experiments**

#### ***Staged desolvation experiments.***

Spectra of SHF-61-CHCl<sub>3</sub> were collected every 30 seconds under 100 SCCM N<sub>2</sub> flow at: 27, 40, 60, 80, 100 and 120 °C, to give **SHF-61o**.

Spectra of SHF-61-DMF were collected every 60 seconds under 100 SCCM N<sub>2</sub> flow at: 27, 40, 60, 80, 100, 120 and 150 °C to give **SHF-61c**. Time for each heating stage are shown in Table 4.13. After holding at each temperature, samples were returned to ambient temperature

(27 °C) and a spectrum recorded.\*

T (°C)	t (min) CHCl <sub>3</sub>	t (min) DMF
27	30	30
40	20	20
60	20	20
80	20	20
100	130	20
120	80	20
150	-	80

Table 4.13. Timescales for staged heating of SHF-61

\*With the exception of SHF-61-CHCl<sub>3</sub> after heating at 100 °C.

### ***Resolvation/desolvation experiments.***

To monitor resolvation and desolvation of the materials from different solvents, a bubbler containing the solvent of interest ( $\text{CHCl}_3$ , cyclopentanone (CyP), or DMF) was incorporated between the  $\text{N}_2$  mass flow controller and Linkam cell to deliver a saturated atmosphere of solvent vapour in  $\text{N}_2$  to the sample environment. The flow rate was set to 1-2 bubbles per second (5 SCCM), slow enough to ensure vapour saturation in the gas flow.

Experiments investigated the resolvation of SHF-61<sup>o</sup> were carried out after activation of the material at 120 °C. This temperature was chosen to ensure solvent removal but no interference with the  $\text{Me}_2\text{NH}_2^+$  framework cation. Samples were activated *ex situ*, away from the infrared microscope under a steady flow of house  $\text{N}_2$  for a minimum of 200 minutes, and the cell was then transferred to the microscope for resolvation experiments. Spectra were collected every 30 seconds (for data collected in 2016) or every 19 seconds (for data collected in 2018) during resolvation until no further change in solvent peak intensity was observed.

Subsequent desolvation of the resolvated materials was carried out at 120 °C for all solvents. Spectra were collected every 19 seconds during re-desolvation at elevated temperatures until solvent peaks were no longer observable. An additional spectrum was collected following return of the sample to 27 °C.

### ***$\text{CO}_2$ uptake experiments.***

$\text{CO}_2$  adsorption in activated open- and closed-pore structure materials was measured by delivery of a mixture of  $\text{N}_2$  and  $\text{CO}_2$  gases *via* separate mass flow controllers mixed into a single inlet pipe. The partial pressure of  $\text{CO}_2$  delivered was controlled by varying the volumetric flow of the two gases. Partial pressures of 200 (20%  $\text{CO}_2$  in  $\text{N}_2$ ), 400, 600, 800 and 1000 mbar of  $\text{CO}_2$  were delivered and SHF-61 allowed to equilibrate in each case for 10 minutes. Spectra were recorded at 27 °C at each equilibrated partial pressure of  $\text{CO}_2$ .

### 4.5.3 Spectral analysis

Infrared spectra were analysed by a combination of peak fitting, peak integration and composite spectral regression modelling in OriginPro 2017. Spectral analysis procedure is described more throughout Sections 1.8 and 4.3.

For peak fitting, data were trimmed to a range of 3865–700 cm<sup>-1</sup> and split into regions of 3865–2619, 1236–903 (1706–903 for experiments involving DMF de/resolvation) and 903–700 cm<sup>-1</sup>. Due to peak saturation, masks were applied to data in the ranges 957–925 and 843–792 cm<sup>-1</sup> to exclude these regions from peak fitting and 2617–1236 cm<sup>-1</sup> was excluded for experiments involving CHCl<sub>3</sub> and CyP. Experiments involving DMF had an additional mask applied to data in the range 1637–1180 cm<sup>-1</sup> due to saturation. Baseline points were manually selected and baseline subtraction applied to the spectrum. Peaks were fit to a Lorentzian peak shape, with some peak positions and widths values fixed to enable completion of the fitting process (see Section 4.3). Peak positions, widths and areas were initially manually varied to produce a fit that most closely resembled the spectral profile and then the fit refined until convergence was reached. One spectrum from the set was fit initially, before a fitting ‘theme’ was created in OriginPro to enable peak fitting of multiple spectra.

Peak integration was used in place of peak fitting when fits would not converge, particularly to determine the integrals of solvent bands. Baseline correction was applied, if appropriate, after assessing peak shape and nearby spectral overlap by eye. A summary of the approach used (peak area fitting vs peak integration) to deconvolute peaks for specific solvent bands is shown in Appendix 2.

Composite spectral regression modelling allows a spectrum to be fit with multiple spectral models, yielding each spectrum as a percentage composition of the chosen models. The model spectra chosen for each state of the system can be found throughout Section 4.3. A non-linear curve fit function was constructed in OriginPro, which dictated the number of spectral models to fit each spectrum to. On fitting the models to each spectrum, bounds were applied that prevented any model being a negative component of the fit.

Composite models and some peak areas were fit to biexponential curves in OriginPro. These were carried out in order to investigate whether timescales and line shapes were similar across composite modelling and peak fitting analysis, and corroborate results extracted from the two different analysis methods in different regions of the infrared spectrum.

## 4.6 References

- 1 D.-D. Zhou, Z.-J. Liu, C.-T. He, P.-Q. Liao, H.-L. Zhou, Z.-S. Zhong, R.-B. Lin, W.-X. Zhang, J.-P. Zhang and X.-M. Chen, *Chem. Commun.*, 2015, **51**, 12665–12668.
- 2 A. Schneemann, V. Bon, I. Schwedler, I. Senkovska, S. Kaskel and R. A. Fischer, *Chem. Soc. Rev.*, 2014, **43**, 6062–6096.
- 3 K. Yang, G. Zhou and Q. Xu, *RSC Adv.*, 2016, **6**, 37506–37514.
- 4 J.-P. Zhang, H.-L. Zhou, D.-D. Zhou, P.-Q. Liao and X.-M. Chen, *Natl. Sci. Rev.*, 2018, **5**, 907–919.
- 5 J.-P. Zhang, P.-Q. Liao, H.-L. Zhou, R.-B. Lin and X.-M. Chen, *Chem. Soc. Rev.*, 2014, **43**, 5789–5814.
- 6 A. P. Katsoulidis, D. Antypov, G. F. S. Whitehead, E. J. Carrington, D. J. Adams, N. G. Berry, G. R. Darling, M. S. Dyer and M. J. Rosseinsky, *Nature*, 2019, **565**, 213–217.
- 7 T. D. Bennett, A. K. Cheetham, A. H. Fuchs and F.-X. Coudert, *Nat. Chem.*, 2016, **9**, 11–16.
- 8 F.-X. Coudert, M. Jeffroy, A. H. Fuchs, A. Boutin and C. Mellot-Draznieks, *J. Am. Chem. Soc.*, 2008, **130**, 14294–14302.
- 9 T. Loiseau, C. Serre, C. Huguenard, G. Fink, F. Taulelle, M. Henry, T. Bataille and G. Férey, *Chem. - A Eur. J.*, 2004, **10**, 1373–1382.
- 10 C. Manion, R. Arlitt, M. I. Campbell, I. Turner, R. Stone and P. A. Greaney, *Dalton Trans.*, 2016, **45**, 4338–4345.
- 11 A. U. Ortiz, A. Boutin and F.-X. Coudert, *Chem. Commun.*, 2014, **50**, 5867–70.
- 12 H. Reinsch, J. Benecke, M. Etter, N. Heidenreich and N. Stock, *Dalton Trans.*, 2017, **46**, 1397–1405.
- 13 F. Niekiel, M. Ackermann, P. Guerrier, A. Rothkirch and N. Stock, *Inorg. Chem.*, 2013, **52**, 8699–8705.
- 14 Y. Gao, K. Liu, R. Kang, J. Xia, G. Yu and S. Deng, *J. Hazard. Mater.*, 2018, **359**, 248–257.
- 15 R. Kitaura, K. Seki, G. Akiyama and S. Kitagawa, *Angew. Chemie Int. Ed.*, 2003, **42**, 428–431.
- 16 Y.-S. Wei, K.-J. Chen, P.-Q. Liao, B.-Y. Zhu, R.-B. Lin, H.-L. Zhou, B.-Y. Wang, W. Xue, J.-P. Zhang and X.-M. Chen, *Chem. Sci.*, 2013, **4**, 1539.
- 17 C. Serre, C. Mellot-Draznieks, Surblé. S., N. Audebrand, Y. Filinchuk and G. Férey, *Science*, 2007, **315**, 1828–1831.
- 18 D. N. Dybtsev, H. Chun and K. Kim, *Angew. Chemie Int. Ed.*, 2004, **43**, 5033–6.

- 19 Y. Kim, R. Haldar, H. Kim, J. Koo and K. Kim, *Dalton Trans.*, 2016, **45**, 4187–4192.
- 20 H.-L. Zhou, R.-B. Lin, C.-T. He, Y.-B. Zhang, N. Feng, Q. Wang, F. Deng, J.-P. Zhang and X.-M. Chen, *Nat. Commun.*, 2013, **4**, 2534.
- 21 H.-L. Zhou, Y.-B. Zhang, J.-P. Zhang and X.-M. Chen, *Nat. Commun.*, 2015, **6**, 6917.
- 22 B. Yuan, D. Ma, X. Wang, Z. Li, Y. Li, H. Liu and D. He, *Chem. Commun.*, 2012, **48**, 1135–1137.
- 23 E. J. Carrington, C. A. McAnally, A. J. Fletcher, S. P. Thompson, M. Warren and L. Brammer, *Nat. Chem.*, 2017, **9**, 882–889.
- 24 L. Chen and M. Garland, *Appl. Spectrosc.*, 2003, **57**, 323–330.
- 25 S. A. Kirillov, in Novel Approaches to the Structure and Dynamics of Liquids: Experiments, Theories and Simulations, Springer Netherlands, Dordrecht, 2004, pp. 193–227.
- 26 J. T. Reilly, J. M. Walsh, M. L. Greenfield and M. D. Donohue, *Spectrochim. Acta Part A Mol. Spectrosc.*, 1992, **48**, 1459–1479.
- 27 H. Keles, A. Naylor, F. Clegg and C. Sammon, *Analyst*, 2014, **139**, 2355–2369.
- 28 S. Ehrling, I. Senkovska, V. Bon, J. D. Evans, P. Petkov, Y. Krupskaya, V. Kataev, T. Wulf, A. Krylov, A. Vtyurin, S. Krylova, S. Adichtchev, E. Slyusareva, M. S. Weiss, B. Büchner, T. Heine and S. Kaskel, *J. Mater. Chem. A*, DOI:10.1039/C9TA06781G.
- 29 P. A. Gerakines, W. A. Schutte, J. M. Greenberg and E. F. van Dishoeck, *Astron. Astrophys.*, 1995, **296**, 810–818.
- 30 S. A. Sandford and L. J. Allamandola, *Astrophys. J.*, 1990, **355**, 357.
- 31 E. Quirico and B. Schmitt, *Icarus*, 1997, **127**, 354–378.
- 32 M. Savage, Y. Cheng, T. L. Easun, J. E. Eyley, S. P. Argent, M. R. Warren, W. Lewis, C. Murray, C. C. Tang, M. D. Frogley, G. Cinque, J. Sun, S. Rudić, R. T. Murden, M. J. Benham, A. N. Fitch, A. J. Blake, A. J. Ramirez-Cuesta, S. Yang and M. Schröder, *Adv. Mater.*, 2016, **28**, 8705–8711.

## 5 Concluding remarks

---

As a result of work described in this thesis, we are now able to collect IR spectra of MOF single crystals during desolvation and resolvation, and in the presence of gases. We have even developed the capability to perform these measurements within droplets of solvent. We have successfully monitored both guest uptake and release, as well as binding interactions between guests and the frameworks, and monitored structural change in the frameworks during guest interactions. These guests are not just small molecule gases, but include larger molecules, including caffeine and cyclopentanone.

Complementary to IR microspectroscopy experiments, CLSM has been used to spatially map guest diffusion within MOF single crystals. While the work described in this thesis has focussed on known materials, the novel post-synthetic modification of materials with photoswitches has also been discussed. The solid-state behaviour of these photoswitches has been probed, integrating photolysis with more routine characterisation and imaging techniques to examine the changes in our systems.

Our work examining the diffusion of therapeutic guests from MOFs has enabled us to study the loss of caffeine from single crystals into a single drop of solvent at several temperatures. From these studies, we calculated an  $E_a$  for this diffusion process. The investigation into the loss of Cu-bound CO from a framework has shed light on the multiple CO binding sites and the co-dependency of each of these sites.

IR microspectroscopic experiments investigating the solvent-induced breathing of SHF-61 have identified the gated resolvation of the material in real-time, which was unobservable by single crystal X-ray diffraction. CO<sub>2</sub> loading into the desolvated frameworks has enabled us to recreate the shape of a gas isotherm, both throughout the material and exclusively at amine binding sites.

The investigation into the MOF-bound photoswitches explored in this thesis clearly has scope for further study. The inclusion of other techniques, such as Raman spectroscopy, will enable full characterisation and understanding of the photophysical behaviour of these functional materials. The work detailed herein has paved the way for further studies into the phototriggered release of guest molecules from MOFs. By combining our newly developed method of tracking guest diffusion within MOFs using IR microspectroscopy, and the proven photoswitching of MOF-bound spirooxazine moieties, the promising avenues into the design of truly functional materials can now be explored.

## 6 Appendix

---

### 6.1 Appendix 1 (Chapter 2)

*Table A2.1. Attempted combinations for NOTT-100 single crystal synthesis*

Mass ( $\text{H}_4\text{BPTC}$ ) (mg)	Mass ( $(\text{Cu}(\text{NO}_3)_3 \cdot 3\text{H}_2\text{O}$ ) (mg)	Acid	Vol. (acid) ( $\mu\text{L}$ )	Vol. ( $\text{H}_2\text{O}$ ) (mL)	Vol. (DMF) (mL)	Vol. (EtOH) (mL)	Mass ( $L\text{-PrOH}$ ) (mg)	$T$ (°C)
13.87	20.29	Benzoic	10	1	2	0	0	0
13.87	20.29	Benzoic	30	1	2	0	0	0
13.87	20.29	Benzoic	50	1	2	0	0	0
13.87	20.29	Formic	10	1	2	0	0	0
13.87	20.29	Formic	30	1	2	0	0	0
13.87	20.29	Formic	50	1	2	0	0	0
13.87	20.29	$\text{H}_2\text{SO}_4$	8	1	2	0	0	0
13.87	20.29	$\text{H}_2\text{SO}_4$	14	1	2	0	0	0
13.87	20.29	$\text{H}_2\text{SO}_4$	20	1	2	0	0	0
13.87	20.29	$\text{H}_2\text{SO}_4$	30	1	2	0	0	0
13.87	20.29	$\text{H}_2\text{SO}_4$	30	1	2	0	0	0
13.87	20.29	$\text{H}_2\text{SO}_4$	30	0	0	0	3	0
13.87	20.29	$\text{H}_2\text{SO}_4$	30	1	0	0	2	0
13.87	20.29	$\text{H}_2\text{SO}_4$	30	1	1	0	1	0
13.87	20.29	$\text{H}_2\text{SO}_4$	30	1	2	0	0	311
13.87	20.29	$\text{H}_2\text{SO}_4$	30	1	2	0	0	55
13.87	20.29	$\text{H}_2\text{SO}_4$	30	0	3	0	0	311
13.87	20.29	$\text{H}_2\text{SO}_4$	30	0	3	0	0	80
13.87	20.29	$\text{H}_2\text{SO}_4$	30	1	2	0	0	311
13.87	20.29	$\text{H}_2\text{SO}_4$	30	1	2	0	0	120
13.87	20.29	$\text{H}_2\text{SO}_4$	30	0	3	0	0	311
13.87	20.29	$\text{H}_2\text{SO}_4$	30	0	3	0	0	55
13.87	20.29	$\text{H}_2\text{SO}_4$	30	0	3	0	0	311
13.87	20.29	$\text{H}_2\text{SO}_4$	30	0	3	0	0	80
13.87	20.29	$\text{H}_2\text{SO}_4$	30	0	3	0	0	311
13.87	20.29	$\text{H}_2\text{SO}_4$	30	1	1	0	0	120
13.87	20.29	$\text{H}_2\text{SO}_4$	30	1	1	0	0	55
13.87	20.29	$\text{H}_2\text{SO}_4$	30	1	0	0	0	2
13.87	20.29	$\text{H}_2\text{SO}_4$	30	0	0	0	0	55
13.87	20.29	$\text{H}_2\text{SO}_4$	40	1	2	0	0	0
13.87	20.29	$\text{H}_2\text{SO}_4$	40	1	2	0	0	0

Mass (H <sub>4</sub> BPTC) (mg)	Mass (Cu(NO <sub>3</sub> ) <sub>3</sub> ·3H <sub>2</sub> O) (mg)	Acid	Vol. (acid) (μL)	Vol. (H <sub>2</sub> O) (mL)	Vol. (DMF) (mL)	Vol. (DMSO) (mL)	Vol. (EtOH) (mL)	Mass (L-ProH) (mg)	T (°C)
13.87	20.29	H <sub>2</sub> SO <sub>4</sub>	50	1	2	0	0	0	65
13.87	20.29	H <sub>2</sub> SO <sub>4</sub>	50	1	2	0	0	0	55
6.94	10.15	HCl	8	1	2	0	0	0	65
2.77	4.06	HCl	8	1	2	0	0	0	65
1.39	2.03	HCl	8	1	2	0	0	0	65
13.87	20.29	HCl	8	0	2	1	0	0	65
13.87	20.29	HCl	8	0.5	2	0.5	0	0	65
13.87	20.29	HCl	10	1	2	0	0	0	65
13.87	20.29	HCl	15	1	2	0	0	0	65
13.87	20.29	HCl	20	1	2	0	0	0	65
13.87	20.29	HCl	30	1	2	0	0	0	55
13.87	20.29	HCl	30	1	2	0	0	0	65
13.87	20.29	HCl	40	1	2	0	0	0	55
13.87	20.29	HCl	40	1	2	0	0	0	65
13.87	20.29	HCl	45	1	2	0	0	0	55
13.87	20.29	HCl	45	1	2	0	0	0	311
13.87	20.29	HCl	45	1	2	0	0	0	80
13.87	20.29	HCl	45	1	2	0	0	0	311
13.87	20.29	HCl	45	0	3	0	0	0	55
13.87	20.29	HCl	45	0	3	0	0	0	311
13.87	20.29	HCl	45	0	3	0	0	0	80
13.87	20.29	HCl	45	0	3	0	0	0	311
13.87	20.29	HCl	50	1	2	0	0	0	55
13.87	20.29	HCl	50	1	2	0	0	0	65
13.87	20.29	HNO <sub>3</sub>	30	1	2	0	0	0	65
13.87	20.29	HNO <sub>3</sub>	30	1	2	0	0	0	55
13.87	20.29	HNO <sub>3</sub>	30	1	2	0	0	0	276
13.87	20.29	HNO <sub>3</sub>	30	1	2	0	0	0	55
13.87	20.29	HNO <sub>3</sub>	30	1	2	0	0	0	276
13.87	20.29	HNO <sub>3</sub>	30	0	3	0	0	0	120
13.87	20.29	HNO <sub>3</sub>	30	0	3	0	0	0	55
13.87	20.29	HNO <sub>3</sub>	30	0	3	0	0	0	276
13.87	20.29	HNO <sub>3</sub>	30	0	3	0	0	0	80
13.87	20.29	HNO <sub>3</sub>	30	0	3	0	0	0	276

Mass (H <sub>4</sub> BPTC) (mg)	Mass (Cu(NO <sub>3</sub> ) <sub>3</sub> ·3H <sub>2</sub> O) (mg)	Acid	Vol. (acid) (μL)	Vol. (H <sub>2</sub> O) (mL)	Vol. (DMF) (mL)	Vol. (DMSO) (mL)	Vol. (EtOH) (mL)	Mass (L-PrOH) (mg)	T (°C)
13.87	20.29	HNO <sub>3</sub>	40	1	2	0	0	0	65
13.87	20.29	HNO <sub>3</sub>	40	1	2	0	0	0	55
13.87	20.29	HNO <sub>3</sub>	50	1	2	0	0	0	65
13.87	20.29	HNO <sub>3</sub>	50	1	2	0	0	0	55
13.87	20.29	HNO <sub>3</sub>	60	1	2	0	0	0	55
13.87	20.29	HNO <sub>3</sub>	75	1	2	0	0	0	55
13.87	20.29	HNO <sub>3</sub>	90	1	2	0	0	0	55
13.87	20.29	HNO <sub>3</sub>	90	1	2	0	0	0	276
13.87	20.29	HNO <sub>3</sub>	90	1	2	0	0	0	80
13.87	20.29	HNO <sub>3</sub>	90	1	2	0	0	0	120
13.87	20.29	HNO <sub>3</sub>	90	0	3	0	0	0	276
13.87	20.29	HNO <sub>3</sub>	90	0	3	0	0	0	80
13.87	20.29	HNO <sub>3</sub>	90	0	3	0	0	0	120
13.87	20.29	Salicylic	10	1	2	0	0	0	55
13.87	20.29	Salicylic	30	1	2	0	0	0	55
13.87	20.29	Salicylic	50	1	2	0	0	0	55

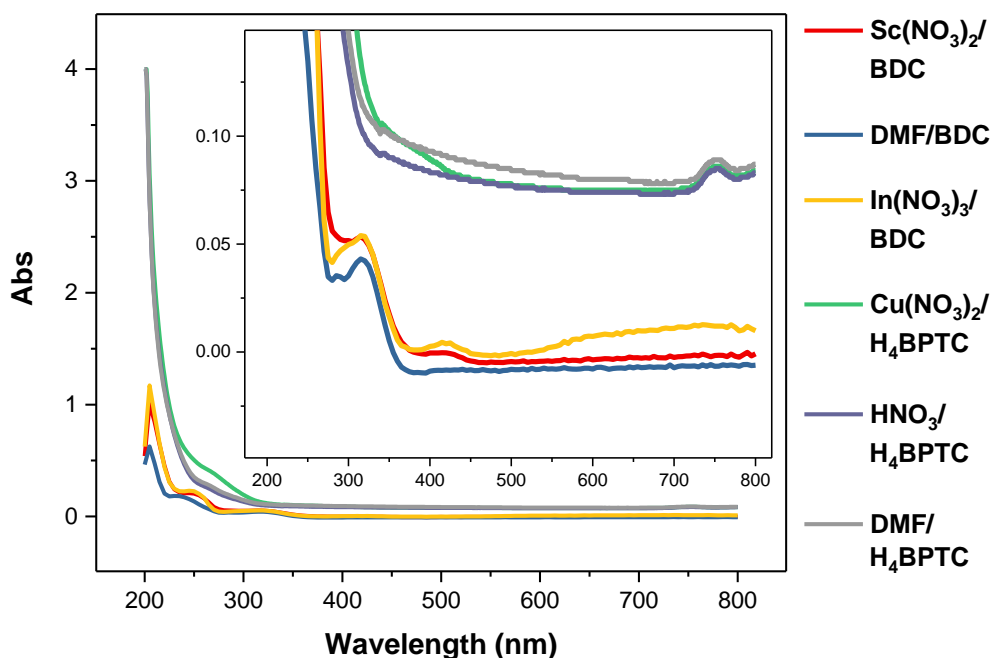


Figure A2.1. Solution-phase UV-VIS spectra of metal salt-, solvent- and modulator-linker combinations of indicated MOF constituents in MeOH.

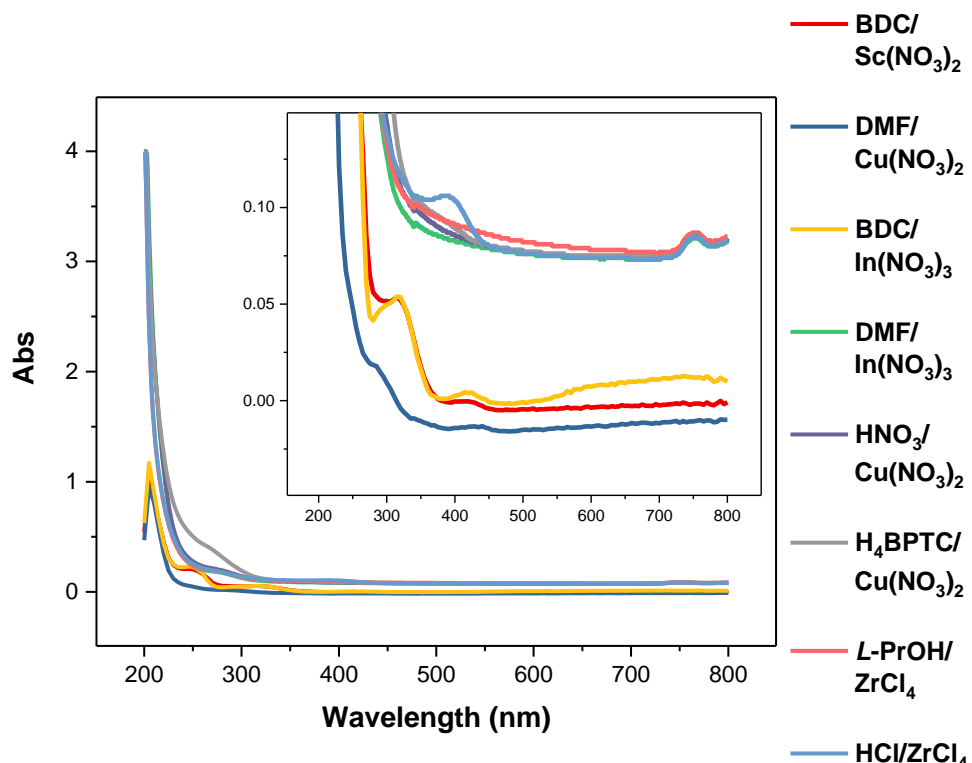


Figure A2.2. Solution-phase UV-VIS spectra of linker-, solvent- and modulator-metal salt combinations of indicated MOF constituents in MeOH.

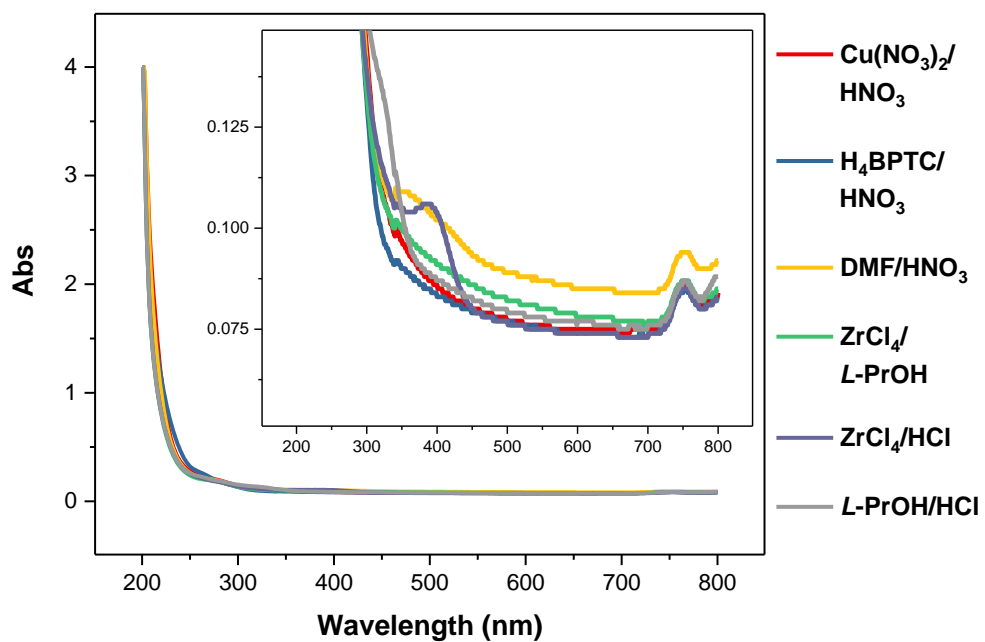


Figure A2.3. Solution-phase UV-VIS spectra of metal salt-, linker-, solvent-modulator combinations of indicated MOF constituents in MeOH.

Table A2.2. Peak positions for  $\lambda_{max}$  of **7-DCCA** peaks in UV-VIS-DR spectra during timed modification experiments.

Time (h)	$\lambda$ (nm)	Time (h)	$\lambda$ (nm)
1	418.3	1	429.2
4	430.9	4	437.4
8	418.9	8	436.3
16 (a)	414.3	16	432.6
16 (b)	420.7	24	429.5
32	414.3	48	426.8
48	420.6	72	426.8
56	422.5		
72 (a)	417.4		
72 (b)	389.9		
80	418.7		
96 (a)	416.1		
96 (b)	430		
104	452.7		
120	413.2		

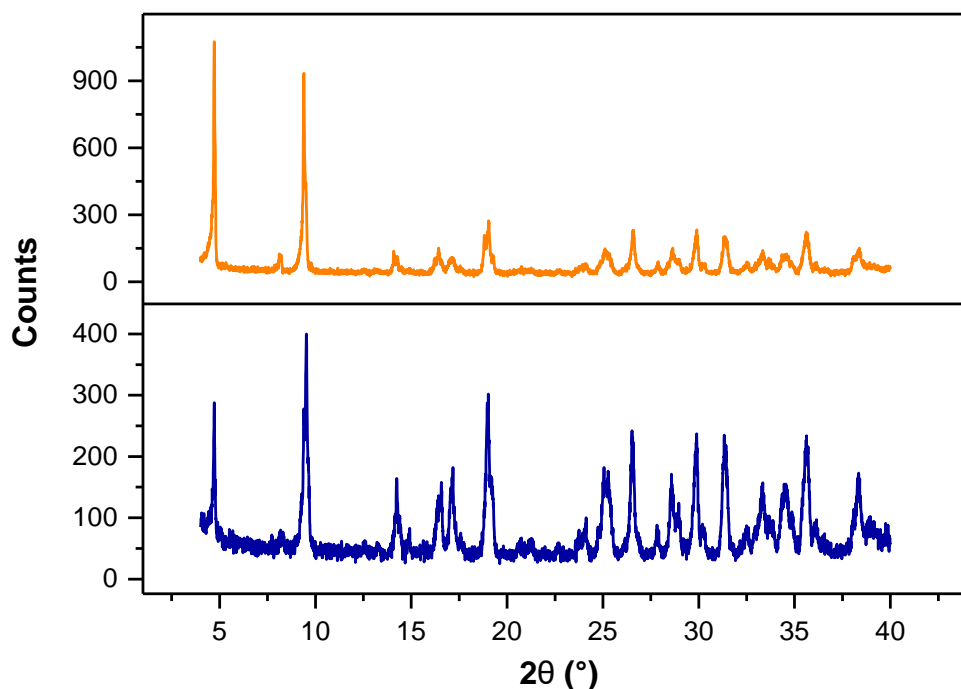


Figure A2.4. PXRD patterns of MIL-68(ln) collected from (orange) control and (blue) **7-DCCA** SALE experiments.

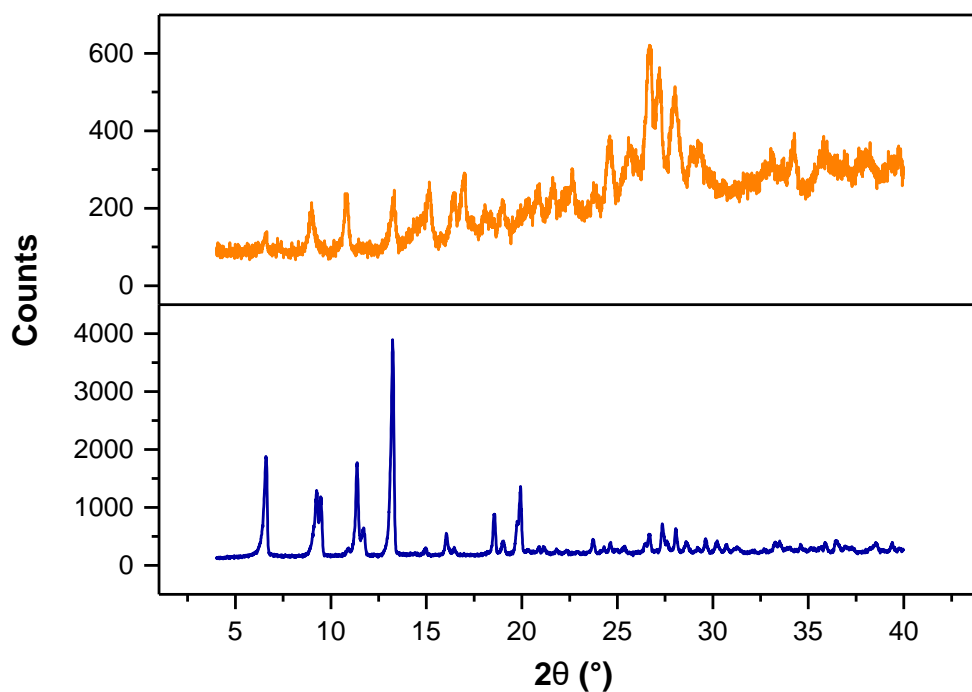


Figure A2.5. PXRD patterns of NOTT-100 collected from (orange) control and (blue) **7-DCCA** SALE experiments.

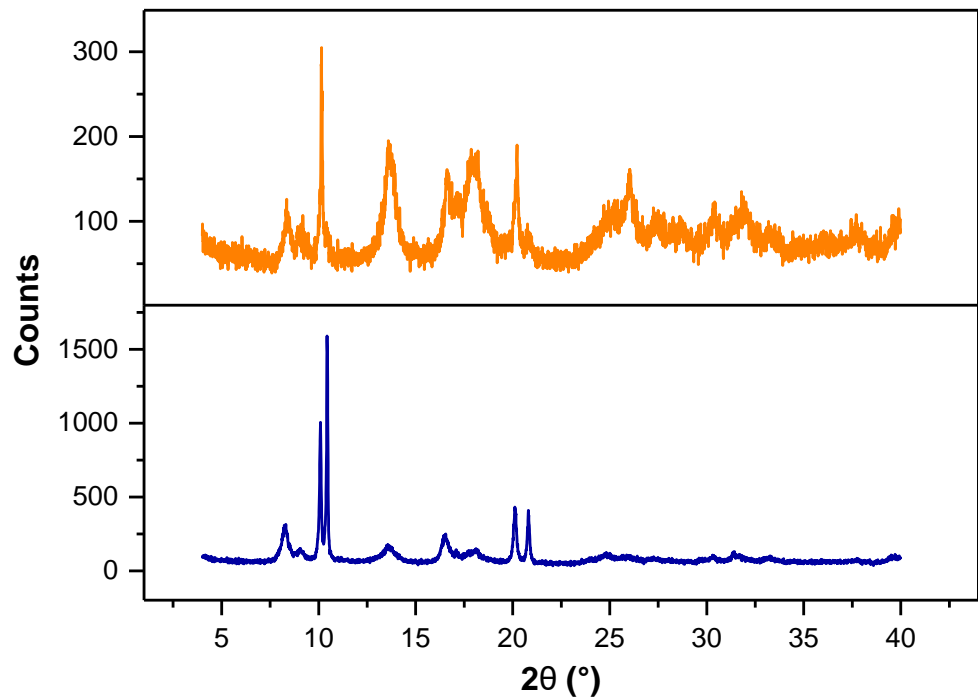


Figure A2.6. PXRD patterns of  $\text{Sc}_2\text{BDC}_3$  collected from (orange) control and (blue) **7-DCCA** SALE experiments.

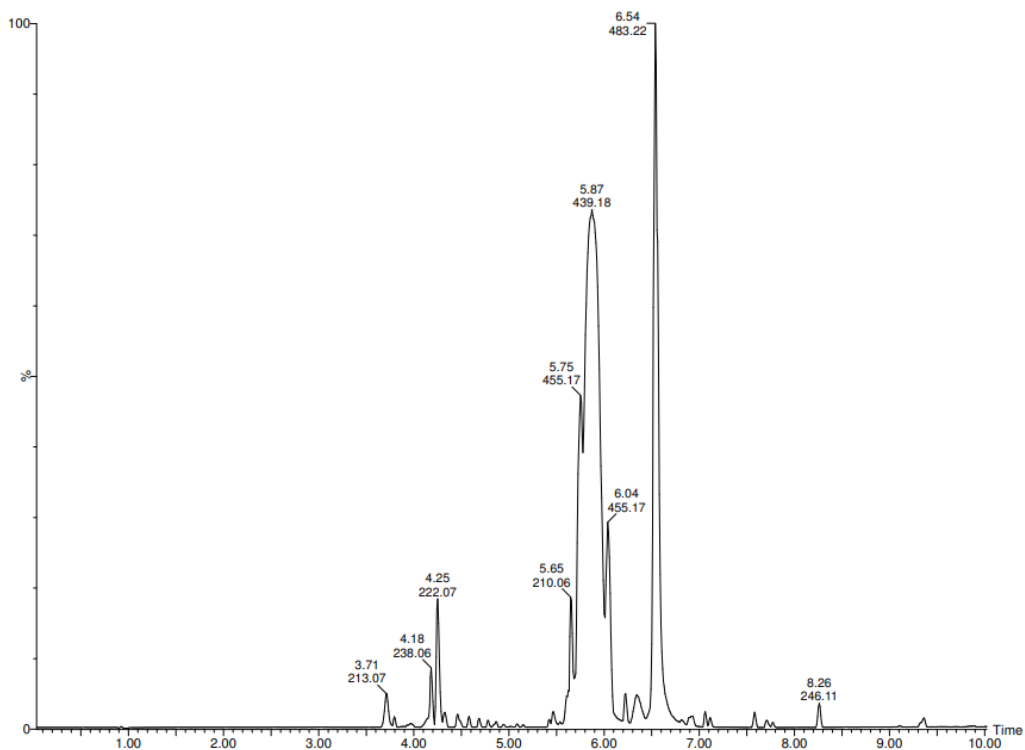


Figure A2.7. LC-MS trace of crude **phen-spiro**.

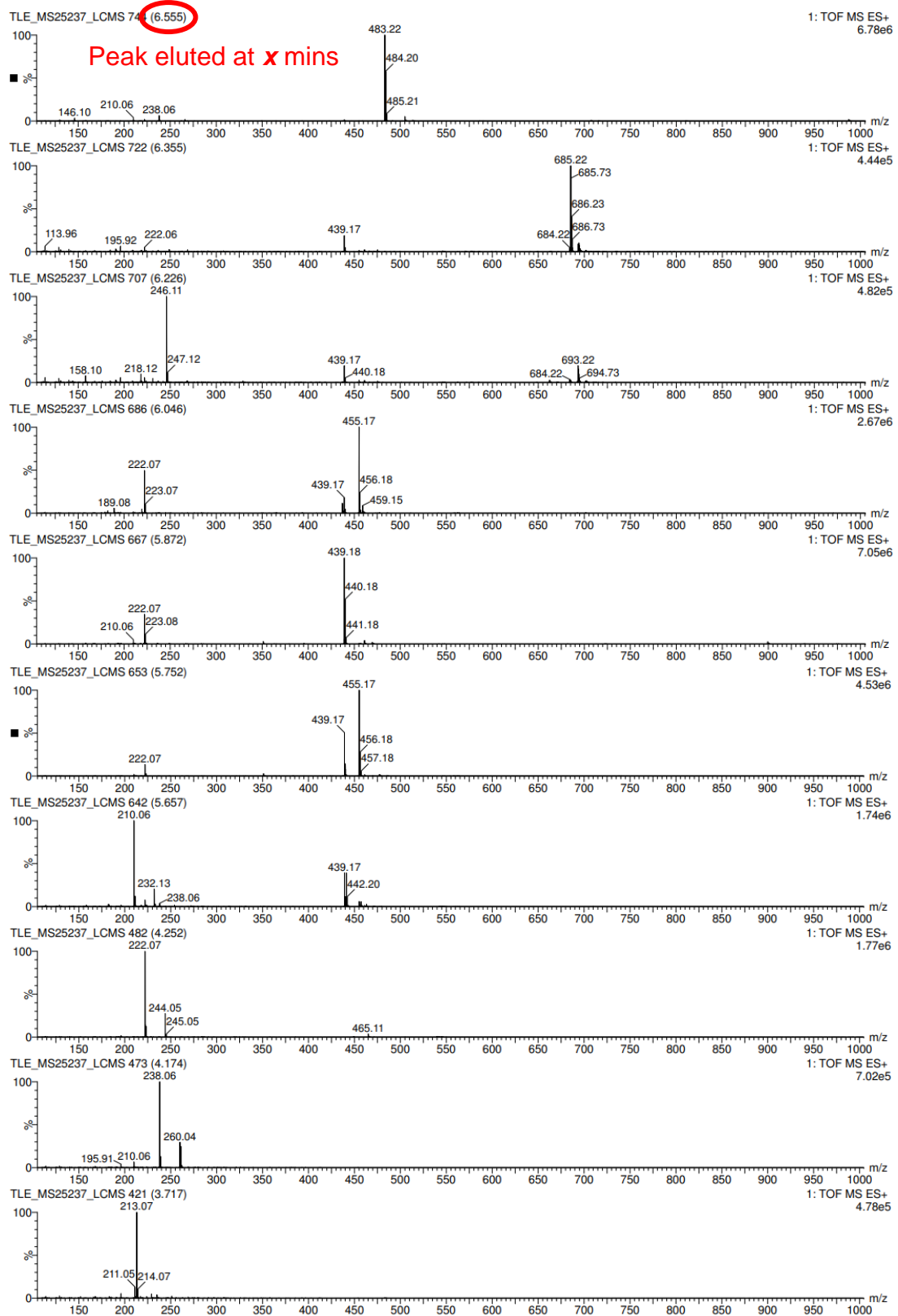


Figure A2.8. MS fragments of crude phen-spiro LC trace.

*Table A2.3. Assignment of MS fragments in crude **phen-spiro**.*

LC-MS peak (min)	Fragment ( <i>m/z</i> )	Adduct
6.555	483.22	PS + 2Na – H
6.355	439.17	PS + H
	685.22	PPC + 3H (3+)
6.226	246.11	PPC + Na
	439.17	PS + H
	693.22	PPC + 2H + H
6.046	455.17	PS + NH <sub>4</sub>
5.872	439.18	PS + H
5.752	455.17	PS + NH <sub>4</sub>
5.657	439.17	PS + H

## 6.2 Appendix 2 (Chapter 4)

*Table A4.1. Peak analysis approach used for solvent bands during SHF-61 re/desolvation experiments.*

Framework	Solvent	Experiment	Band ( $\text{cm}^{-1}$ )	Peak analysis approach
SHF-61 <b>c</b>	DMF	Resolvation	1660	Fitting
SHF-61 <b>o</b>	CHCl <sub>3</sub>	Resolvation	1220	Fitting
SHF-61 <b>o</b>	CyP	Resolvation	1730	Integration
SHF-61 <b>o</b>	DMF	Resolvation	1660	Integration
SHF-61 <b>o</b> -CHCl <sub>3</sub>		Desolvation	1220	Fitting
SHF-61 <b>o</b> -CyP		Desolvation	1730	Fitting
SHF-61 <b>o</b> -DMF		Desolvation	1660	Fitting